

FEDERAL UNIVERSITY OF ESPÍRITO SANTO  
TECHNOLOGIC CENTER  
GRADUATE PROGRAM IN ELECTRICAL ENGINEERING

ARNALDO GOMES LEAL JUNIOR

DOCTORAL THESIS

---

**POLYMER OPTICAL FIBER SENSORS FOR HEALTHCARE DEVICES:  
FROM MATERIAL ANALYSIS TO PRACTICAL APPLICATIONS**

---

VITÓRIA

2018

FEDERAL UNIVERSITY OF ESPÍRITO SANTO  
TECHNOLOGIC CENTER  
GRADUATE PROGRAM IN ELECTRICAL ENGINEERING

DOCTORAL THESIS

---

**POLYMER OPTICAL FIBER SENSORS FOR HEALTHCARE DEVICES:  
FROM MATERIAL ANALYSIS TO PRACTICAL APPLICATIONS**

---

*Author:* Arnaldo Gomes Leal Junior

*Advisors:*

Prof. Dr. Anselmo Frizera Neto

Prof. Dr. Maria José Pontes

Dr. Carlos Alberto Ferreira Marques

*Thesis submitted to the Graduate Program in Electrical Engineering from the Technology Center of the Federal University of Espírito Santo, as partial requirement for the degree of Doctor in Electrical Engineering*

*in the*

Graduate Program in Electrical Engineering

Federal University of Espírito Santo

VITÓRIA

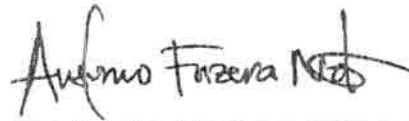
2018

ARNALDO GOMES LEAL JUNIOR

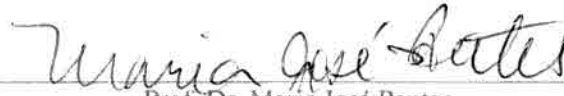
**Polymer Optical Fiber Sensors for Healthcare Devices: From the Material Analysis to Practical Applications**

*Thesis presented to the Graduate Program in Electrical Engineering of the Federal University of Espirito Santo, as a partial requirement for the degree of Doctor in Electrical Engineering.*

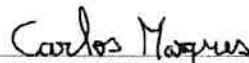
Date: 12-17-2018



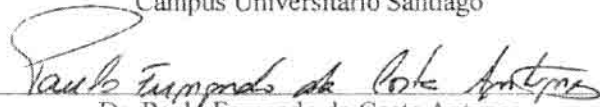
Prof. Dr. Anselmo Frizera Neto  
Advisor, Graduate Program in Electrical Engineering  
Federal University of Espirito Santo



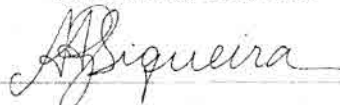
Prof. Dr. Maria José Pontes  
Co-Advisor, Graduate Program in Electrical Engineering  
Federal University of Espirito Santo



Dr. Carlos Alberto Ferreira Marques  
Co-Advisor, Instituto de Telecomunicações  
Campus Universitário Santiago



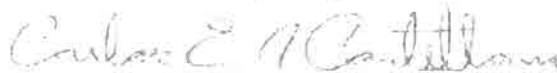
Dr. Paulo Fernando da Costa Antunes  
Physics Department & IBN and Instituto de Telecomunicações  
Universidade de Aveiro



Prof. Dr. Adriano Alineida Gonçalves Siqueira  
Escola de Engenharia de São Carlos  
Universidade de São Paulo



Prof. Dr. Moisés Renato Nunes Ribeiro  
Graduate Program in Electrical Engineering  
Federal University of Espirito Santo



Prof. Dr. Carlos Eduardo Schmidt Castellani  
Universidade Federal do Espírito Santo

VITÓRIA

2018

## Abstract

Advances in medicine and improvements to quality of life have led to an increase in the life expectancy of the general population. An ageing world population has placed demands on the use of assistive technology and in particular towards novel robotic assistance and rehabilitation devices. In order to achieve their functionalities, such robotic devices highly rely on sensors systems, which indicate the necessity of novel sensing solutions to cope with the continuously increasing performance standards of healthcare devices.

Besides the electromagnetic field immunity, polymer optical fiber (POF) sensors have additional advantages due to its material features such as high flexibility, lower Young's modulus (enabling high sensitivity), higher elastic limits and impact resistance. Such advantages are well aligned with the instrumentation requirements of many healthcare devices and in movement analysis. Aiming at these advantages, this Thesis presents the development of POF sensors for healthcare devices. The sensors are developed using two different (and complementary) approaches: (i) Intensity variation-based sensors for low-cost and portable systems; (ii) Fiber Bragg gratings (FBGs), which were inscribed using a femtosecond laser through the direct write plane-by-plane inscription method, with the goal of taking advantage of the multiplexing capabilities and high precision of FBGs.

Even though POFs presented the aforementioned advantages on sensing applications, polymers by their very own nature are viscoelastic materials, which do not have constant response with stress or strain. Such behavior leads to creep, hysteresis and nonlinearities on POF sensors when the fiber is under stress or strain. In order to compensate these effects, first, a dynamic mechanical analysis is made on two different POF materials: polymethyl methacrylate (PMMA) and cyclic transparent optical polymer (CYTOP) for the characterization of the viscoelastic effects on these fibers. After knowing the material properties, compensation techniques for undesirable effects on POF sensors e.g. hysteresis and nonlinearities, are proposed and validated in different conditions for both intensity variation-based sensors (using PMMA POFs) and FBGs (using CYTOP fibers), obtaining reliable sensors for dynamic measurements of temperature, humidity, strain, force and curvature. Then, both intensity variation- and FBG-based sensors are applied on the instrumentation of exoskeletons, active orthosis and smart walkers. In addition, two instrumented insoles were proposed: one for gait phase estimation in a functional electric stimulation system for gait assistance and the other for plantar pressure monitoring and ground reaction forces assessment using an innovative multiplexing technique for intensity variation-based sensors, resulting in a highly customizable and low-cost system with 15 pressure points.

The proposed characterization method for POF materials, compensation techniques and applications in healthcare devices proposed in this Thesis pave the way for novel instrumentation approaches in robotic assistance devices using the proposed flexible sensors, which can be especially desirable not only in the rigid robots presented, but also in soft robotics applications.

**Keywords:** Polymer Optical Fiber, Fiber Bragg Gratings, Optical Fiber Sensors, Viscoelasticity, Dynamic Mechanical Analysis, Wearable Robots, Smart Walkers.

## Resumo

Avanços na medicina e na qualidade de vida levaram à um aumento na expectativa de vida da população em geral. O envelhecimento da população mundial promove demandas em relação ao uso de tecnologias assistivas, em particular, em relação à novos dispositivos robóticos para reabilitação e assistência. Para atingir suas funcionalidades, estes dispositivos robóticos dependem dos seus sistemas de sensores, indicando a necessidade de novas soluções de sensoriamento para lidar com o aumento contínuo nos padrões de desempenho dos dispositivos de apoio à saúde.

Além da imunidade à interferências eletromagnéticas, sensores baseados em fibras ópticas poliméricas (POF, do inglês *polymer optical fibers*) possuem vantagens adicionais relacionadas as propriedades do material, tais como flexibilidade, menor módulo de Young (permitindo maior sensibilidade), maiores limites elásticos e resistência à impactos. Tais vantagens estão de acordo com os requerimentos para instrumentação de muitos dispositivos de apoio à saúde e em análise de movimento. Visando essas vantagens, esta Tese apresenta o desenvolvimento de sensores baseados em POFs para dispositivos de apoio à saúde. Os sensores são desenvolvidos utilizando duas abordagens diferentes (e complementares): (i) sensores baseados em variação de intensidade para sistemas portáteis e de baixo custo; (ii) Redes de Bragg em fibra (FBG, do inglês *fiber Bragg gratings*) que foram gravadas usando laser de femtosegundo através do método de gravação direta plano-a-plano com o objetivo de aproveitar as vantagens de alta capacidade de multiplexação e alta precisão dos sensores baseados em FBGs.

Embora POFs apresentem as vantagens supracitadas para aplicações em sensores, polímeros, por sua própria natureza, são materiais viscoelásticos que não possuem resposta constante em relação à tensões ou deformações mecânicas. Este comportamento resulta em fluência, histerese e não-linearidades na resposta dos sensores em POF quando a fibra está submetida à tensões ou deformações mecânicas. Para compensar esses efeitos, primeiro, uma análise mecânica dinâmica é realizada em POFs de dois diferentes materiais: polimetil metacrilato (PMMA) e polímero óptico transparente cíclico (CYTOP, do inglês *cyclic transparente optical polymer*) para a caracterização dos efeitos viscoelásticos nessas fibras. Após conhecer as propriedades do material, técnicas de compensação para os efeitos indesejados em sensores baseados em POF e.g. histerese e não-linearidades, são propostas e validadas em diferentes condições para sensores baseados em variação de intensidade (usando fibras de PMMA) e FBGs (usando fibras CYTOP), obtendo sensores confiáveis para medições dinâmicas de temperatura, umidade, deformação, força e curvatura. Então, os sensores baseados em variação de intensidade e FBGs são aplicados na instrumentação de exoesqueletos, órteses ativas e andadores inteligentes. Além disso, duas palmilhas instrumentadas são propostas: uma para estimar fases da marcha em sistemas para auxílio à locomoção baseados em estimulação elétrica funcional e outra para monitoramento de pressão plantar e forças de reação do solo usando uma inovadora técnica de multiplexação para sensores baseados em variação de intensidade, resultando num sistema altamente customizável e de baixo custo com 15 pontos de medição de pressão plantar.

Os métodos de caracterização propostos para os materiais das fibras, as técnicas de compensação e as aplicações em dispositivos de apoio à saúde propostas nesta Tese preparam o caminho para novas abordagens de instrumentação em dispositivos robóticos usando os sensores flexíveis propostos, algo que desejável não só para os robôs rígidos apresentados, mas também em aplicações de robótica flexível.

**Palavras-chave:** Fibra óptica polimérica, Redes de Bragg em fibra, Sensores em fibra óptica, Viscoelasticidade, Análise mecânica dinâmica, Robôs vestíveis, Andadores inteligentes.

## Acknowledgements

I believe this work is not just a product of my own efforts, but whether the contributions, help and support of many people around me. In the first place, I would like to thank my father (Arnaldo Leal), my mother (Marleide Leal) and my little brother (Marcelo Leal) for all the support during my entire life. I wish to express my gratitude to my Advisor Prof. Dr. Anselmo Frizera Neto, who aroused my interest in optical fiber sensors and introduced me at the LABTEL group, where I met my Co-Advisor Maria José Pontes who gives me all the support I needed on my research and I am very grateful for that. Furthermore, I also would like to thank my Co-Advisor Carlos Alberto Ferreira Marques for all the support on the research. In summary, I thank all my advisors for the patience, support, friendship, and, most important, to introduce me to this awesome research field.

I also would like to thank all my friends for all the support and understanding. Special thanks for those whom helped me on the development of all the works presented in this PhD: Manuel Sanchez, Laura Vargas, Thomaz Botelho, Mário Jimenez and, especially, Leticia Munhoz and Camilo Diaz for the support, friendship and patience. In addition, I am grateful for all my friends and colleagues from not only LABTEL, but also from all the Graduate Program in Electrical Engineering of UFES. I am grateful for all the collaborators in this work, especially Antreas Theodosiou and Kyriacos Kalli for providing the FBGs used in this Thesis. LabPetro – UFES (Laboratório de Pesquisa e Desenvolvimento de Metodologias para Caracterização de Óleos Pesados) for the use of the DMA equipment and LAFEC (Department of Physical Education - Federal University of Espírito Santo) for the use of the force platform.

This research is financed by CAPES (88887.095626/2015-01) – financing code 001, FAPES (72982608), CNPq (304192/2016-3 and 310310/2015-6) and FCT through the fellowship SFRH/BPD/109458/2015, program UID/EEA/50008/2013 by the National Funds through the Fundação para a Ciência e a Tecnologia / Ministério da Educação e Ciência, and the European Regional Development Fund under the PT2020 Partnership Agreement.

# Contents

<b>Chapter 1. Introduction .....</b>	<b>23</b>
1.1. Motivation .....	23
1.2. Research Objectives and Contributions .....	26
1.3. Publications .....	27
1.3.1. Journal Articles .....	27
1.3.2. Conference Papers .....	30
1.3.3. Book Chapters .....	31
1.4. Organization of the Thesis .....	31
<b>Chapter 2. Theoretical Background.....</b>	<b>33</b>
2.1. Polymer Optical Fibers Overview .....	33
2.2. POF-based Sensors .....	36
2.2.1. Intensity Variation-based Sensors Review .....	36
2.2.2. Fiber Bragg Gratings-based Sensors Review .....	38
<b>Chapter 3. Mechanical Characterization of Different POFs .....</b>	<b>42</b>
3.1. Introduction .....	42
3.2. Dynamic Mechanical Analysis .....	42
3.3. DMA on PMMA Solid Core POF .....	43
3.4. Dynamic Characterization of CYTOP Fibers.....	46
3.4.1. Experimental Analysis.....	46
3.4.2. Results and Discussion .....	47
3.5. Final Remarks.....	49
<b>Chapter 4. Intensity Variation-based Sensors.....</b>	<b>50</b>
4.1. Introduction .....	50
4.2. Curvature Sensor .....	50
4.2.1. Experimental setup .....	51
4.2.2. Compensation Technique Based on Viscoelastic Features.....	51
4.3. Temperature and Humidity Sensors .....	55
4.3.1. POF Microclimate Sensors Operation Principle.....	56
4.3.2. Experimental Setup.....	56
4.3.3. Results and Discussion .....	57
4.4. Multiplexing Technique for Quasi-distributed Sensors Arrays in Polymer Optical Fiber Intensity Variation-based Sensors.....	61
4.4.1. Operation Principle and Experimental Setup .....	62
4.4.2. Results and Discussion .....	64
4.5. Final Remarks.....	67
<b>Chapter 5. Fiber Bragg Gratings-based Sensors .....</b>	<b>69</b>

5.1.	Introduction .....	69
5.2.	FBG Inscription Using fs Laser.....	69
5.3.	Influence of Thermal Treatments and Compensation Techniques in FBGs Responses.....	70
5.3.1.	Experimental Setup.....	70
5.3.2.	Results and Discussion .....	72
5.4.	Compensation Method for Temperature cross-sensitivity in Transverse Force Sensors.....	77
5.4.1.	Experimental Setup and Operation Principle .....	77
5.4.2.	Results and Discussion .....	79
5.5.	Development and Dynamic Compensation of FBG-based Curvature Sensors .....	83
5.5.1.	Theoretical Background and Compensation Technique .....	83
5.5.2.	Experimental Setup.....	85
5.5.3.	Results and Discussion .....	85
5.6.	Final Remarks.....	89
<b>Chapter 6.</b>	<b>POF Sensors Applications in Healthcare Devices.....</b>	<b>90</b>
6.1.	Introduction .....	90
6.2.	Assistive Devices Employed on Sensors Applications .....	91
6.2.1.	Advanced Lower Limb Orthosis for Rehabilitation (ALLOR) .....	91
6.2.2.	Active Knee Orthosis Driven by a SEA .....	91
6.2.3.	Smart Walker.....	92
6.3.	Intensity Variation-based Sensors Applications in Healthcare Devices.....	93
6.3.1.	Angle Measurements in Lower Limb Exoskeletons.....	93
6.3.2.	Angle and Torque Measurements in a SEA Spring.....	96
6.3.3.	POF-Embedded, 3D-printed Support for Microclimate and Human-Robot Interaction Forces Assessment in Wearable Devices .....	103
6.3.4.	Smart Walker Instrumentation and Health Assessment .....	109
6.3.5.	3D-printed POF Insole: Application of Multiplexing Techniques in Low-cost Intensity Variation-based Sensors .....	115
6.4.	FBG-based Sensors Applications in Healthcare Devices .....	125
6.4.1.	FBG-embedded 3D-printed Support for Human-robot Interaction Forces in a Lower Limb Exoskeleton .....	125
6.4.2.	FBG Array Application in a SEA's Spring .....	130
6.4.3.	FBG Array on Multiparameter Measurements in Smart Walker.....	136
6.5.	Final Remarks.....	143
<b>Chapter 7.</b>	<b>Conclusions and Future Works.....</b>	<b>145</b>
7.1.	Summary.....	145
7.2.	Future Works .....	146
<b>Appendix A.</b>	<b>Analytical Model for Intensity Variation POF Sensors Based on Macrobending</b>	<b>147</b>
<b>Appendix B.</b>	<b>Sensitive Zone Parameters Evaluation .....</b>	<b>155</b>
<b>Appendix C.</b>	<b>Compensation Technique Based on Angular Velocity .....</b>	<b>164</b>
<b>Appendix D.</b>	<b>Torque Characterization .....</b>	<b>170</b>

<b>Appendix E. POF-based Insole for In-shoe GRF Measurements During FES-assisted Gait.....</b>	<b>172</b>
<b>Appendix F. Influence of the Stress-optic Effect on POF Intensity Variation-based Sensors...</b>	<b>180</b>
<b>Appendix G. Results of Intensity Variation-based Microclimate and Force Sensors Characterizations</b>	<b>182</b>
<b>Appendix H. Characterization of the FBG Array Embedded in TPU Structure for Human-robot Interaction Forces Assessment .....</b>	<b>184</b>
<b>Appendix I. Numerical Analysis of the FBG Array on the Torsional Spring .....</b>	<b>189</b>
<b>Bibliography</b>	<b>191</b>

## List of Figures

Figure 1-1 Overview of the robotic devices and monitored parameters.....	26
Figure. 2-1 Cross-sectional view of a polymer optical fiber (figure out of scale).....	33
Figure 2-2 Comparison between SI and GI profile [76].....	34
Figure 2-3 Cross-sectional view of the mPOFs with 3-rings hexagonal structure [86]. .....	35
Figure 2-4 Attenuation (in dB/km) of PMMA and CYTOP fibers .....	36
Figure 2-5 Self-referencing system for compensation of environmental and light source deviations [111]...	37
Figure 2-6 Periodic variation of the refractive index with respect to the fiber z-axis (fiber length). .....	38
Figure 2-7 A typical phase mask technique inscription setup for POFBGs (this case using a 248 nm KrF laser). Figure inset shows a FBG inscribed using this setup. ....	38
Figure 2-8 Historical evaluation of the inscription times using UV laser (CW and nanosecond pulsed). .....	39
Figure 2-9 Application fields using FBGs inscribed in POFs. ....	41
Figure 3-1 Schematic view of the POF sample positioning in the DMA. ....	43
Figure 3-2 Temperature sweep on the solid-core PMMA fiber.....	44
Figure 3-3 Storage modulus for frequencies between 0.01 Hz and 21 Hz with different temperatures.....	44
Figure 3-4 POF creep recovery tests with loads of 0.5 N to 2 N.....	45
Figure 3-5 POF curvature sensor stress response with two strain cycles. ....	46
Figure 3-6 POF curvature sensor stress response with two strain cycles. ....	46
Figure 3-7 (a) Stress-strain curve for the CYTOP without FBGs in a strain range of 0-6%. (b) Stress-strain curves for Young's modulus calculation for CYTOPs with and without FBGs. ....	47
Figure 3-8 (a) CYTOP's storage modulus as a function of the temperature. (b) Frequency response in 4 different temperatures (30°C, 40°C, 50°C and 60°C). ....	48
Figure 3-9 Loss factor on the range of 27°C to 130°C.....	48
Figure 3-10 Master curve for the FBG inscribed in CYTOP fiber.....	49
Figure 4-1 Schematic view of the POF sensor under curvature. ....	50
Figure 4-2 Prototype employed on the dynamic tests of the curvature POF sensors. ....	51
Figure 4-3 POF sensor response estimated by the model and linear regression.....	52
Figure 4-4 (a) POF sensor response without the application of the compensation equation and (b) POF sensor response with the compensation equation. ....	54
Figure 4-5 (a) Comparison of the measured hysteresis and RMSE with and without the compensation technique. (b) Comparison of the linearity at the flexion and extension movements with and without the compensation technique. ....	55
Figure 4-6 Experimental setup for POF humidity and temperature sensors tests. ....	57
Figure 4-7 RH characterization of POF sensors. ....	58
Figure 4-8 Temperature characterization of POF sensors. ....	59
Figure 4-9 POF sensor's response for temperature and humidity tests. ....	60
Figure 4-10 Improved response time with the etching on the POF humidity sensor based on induced stress- optic effect.....	61
Figure 4-11 Schematic representation of the proposed multiplexing technique for intensity variation-based sensors. ....	62

Figure 4-12 Experimental setup for (a) multiplexing technique validation with the array of 3 curvature sensors. (b) Validation for a multi-parameter application.....	64
Figure 4-13 POF sensor array characterization for 3-DOF angle measurement (a) signal acquired by the photodetectors when each LED is active and (b) linear regression for the angle characterization with each sensor.....	65
Figure 4-14 Sensor response in the 3-DOF validation test.....	66
Figure 4-15 Experimental characterization of each sensor for multi-parameter application.....	66
Figure 4-16 (a) Responses of the three sensors acquired by the photodetector 1. (b) Angle, force and temperature measurements using the proposed multiplexing technique acquired for 210 seconds. ....	67
Figure 5-1 Schematic representation of the experimental setup used in the gratings inscription. The insets show a magnified view of the CYTOP with and without FBG. ....	69
Figure 5-2 Schematic representation of the POF connectorization. ....	70
Figure 5-3 Experimental setup employed for (a) temperature characterization, (b) strain characterization and (c) transverse force characterization, the inset shows the assembly of the POFBG between the plates. ....	71
Figure 5-4 Reflection spectra of the POFBGs before and after the annealing (a) at low humidity (b) under hot water. ....	73
Figure 5-5 Increasing and decreasing temperature response of POFBGs with and without different thermal treatments. The region of high hysteresis is also indicated in the figure.....	73
Figure 5-6 Response of POFBGs with and without different thermal treatments for sequential strain cycles. ....	74
Figure 5-7 Response of POFBGs with and without different thermal treatments for sequential transverse force cycles. ....	75
Figure 5-8 Temperature compensated response for the sample annealed at low humidity. ....	76
Figure 5-9 Strain compensated response for the sample annealed under water. ....	77
Figure 5-10 Transverse force compensated response for the sample annealed under water. ....	77
Figure 5-11 Experimental setup employed for transverse force and temperature variations. ....	78
Figure 5-12 POFBG wavelength shift as a function of the transverse force at 30°C and 40°C. ....	79
Figure 5-13 POFBG wavelength shift with respect to the temperature increase.....	80
Figure 5-14 CYTOP fiber Young's modulus variation as a function of temperature. ....	80
Figure 5-15 POFBG wavelength shift with respect to the transverse force for different temperature conditions. ....	81
Figure 5-16 Comparison between sensor transverse force sensitivity and CYTOP Young's modulus variations with respect to the temperature variation. ....	82
Figure 5-17 Compensated and uncompensated transverse force responses of POFBG sensors at different temperatures. ....	83
Figure 5-18 Schematic illustration of the frequency effect on the sensor sensitivity and linearity for two different frequencies; where $h_1$ and $h_2$ are the hysteresis for the frequencies 1 and 2, respectively. Analogously, $s_1$ and $s_2$ are the sensitivities for frequencies 1 and 2, respectively.....	84
Figure 5-19 Block diagram of the sensitivity compensation (block $m_1$ ), hysteresis compensation (block $m_2$ ) and the correlation equation that results in the angle output (block $m_3$ ).....	84
Figure 5-20 Experimental setup for the POFBG curvature sensor characterization. ....	85
Figure 5-21 (a) POFBG curvature sensor response for three different frequencies (0.50 Hz, 1.32 Hz and 4.49 Hz). (b) Comparison between the sensor sensitivity and Young's modulus variations with respect to frequency. ....	86

Figure 5-22 (a) Flexion and extension cycles at 0.5 Hz with the sensitivity of each cycle. (b) Hysteresis variation as a function of the frequency. (c) Sensitivity difference between flexion and extension cycles at each frequency. ....	87
Figure 5-23 Measured angles for flexion and extension cycles after applying the compensation technique..	88
Figure 5-24 RMSE of the compensated and uncompensated responses at each tested frequency. ....	88
Figure 5-25 Hysteresis of the compensated and uncompensated responses at each tested frequency. ....	89
Figure 6-1 Overview of the applications developed in this Chapter and their relation with the developments presented in previous chapters.....	90
Figure 6-2 ALLOR orthotic device positioned on the chair for flexion/extension cycles.....	91
Figure 6-3 Rotary Series Elastic Actuator for an active knee orthosis. ....	92
Figure 6-4 Back view of the spring with the encoder used for comparison purposes. ....	92
Figure 6-5 Overview of the SW used for the POF sensors implementation – UFES Cloud Walker. ....	93
Figure 6-6 POF curvature sensor positioned on the ALLOR through 3D-printed supports.....	93
Figure 6-7 Subject with the exoskeleton before the experiment. The hip passive joint as well as the POF curvature sensor and reference arm are not connected at the time of the picture was taken. ....	94
Figure 6-8 POF sensor response (vertical axis) and potentiometer response (horizontal axis) for the first cycle of the rehabilitation exercise.....	95
Figure 6-9 POF sensor response and potentiometer response for the 5 different angular velocities tested. Regions 1, 2, 3, 4 and 5 refer to the angular velocities of 0.05 rad/s, 0.10 rad/s, 0.16 rad/s, 0.21 rad/s and 0.26 rad/s respectively. ....	95
Figure 6-10 Error between the POF sensor and the potentiometer on the vertical axis. The potentiometer angle is presented on the horizontal axis. The shaded part of the error represents the standard deviation of the error in each velocity at each cycle. ....	96
Figure 6-11 Experimental setup for the POF sensor validation. ....	97
Figure 6-12 Equivalent strain of the spring submitted to a 15 Nm torque. The points a and b are more suitable for the POF sensor positioning. ....	97
Figure 6-13 (a) Schematic drawing of the POF sensor attached on the spring and (b) Photograph of the spring with the 3D printed supports for the POF sensor positioning. ....	98
Figure 6-14 Comparison between compensated and uncompensated responses of the POF sensor when the spring is deflected in 10°. ....	99
Figure 6-15 Calibration curve of the POF curvature sensor. ....	99
Figure 6-16 POF curvature sensor response for successive loading/unloading cycles and encoder measurements. ....	100
Figure 6-17 POF sensor output power variation with different refractive indexes and the linear compensation for refractive indexes higher than 1.3 RIU. ....	101
Figure 6-18 Torque estimated by the POF torque sensor for successive loading/unloading cycles and torque estimated by the encoder and POF curvature sensor with the application of the spring constant. ....	102
Figure 6-19 (a) POF sensors fabrication. (b) Schematic representation of the instrumented shank support. (c) Pictures of the front and back views of the developed prototype.....	104
Figure 6-20 Block diagram for the temperature, humidity and force responses of the proposed sensor system. ....	106
Figure 6-21 Experimental setup for validation of the proposed sensor system.....	106
Figure 6-22 Experimental setup for exoskeleton application. ....	107

Figure 6-23 (a) Force sensors validation under different temperature and humidity conditions for short (top) and long (bottom) term tests. (b) Validation of the force and microclimate sensors embedded in the 3D-printed shank support.....	108
Figure 6-24 Force, temperature and humidity measured in the application of the proposed shank support in an exoskeleton for rehabilitation exercises. ....	109
Figure 6-25 Schematic representation of the SW employed and the developed sensors.....	110
Figure 6-26 Schematic illustration of the proposed SpO <sub>2</sub> sensor. ....	111
Figure 6-27. Overview of the POF-based smart textile and the loadings acting on it during the gait.....	112
Figure 6-28 SW embedded oximetry sensor response for (a) SpO <sub>2</sub> measurement and (b) HR assessment. ....	113
Figure 6-29 Heart and breathing rates measurement with the POF-based smart textile. ....	113
Figure 6-30 POF-based smart textile response for BR and gait cadence. ....	114
Figure 6-31 Block diagram of the POF sensors implementation in the smart walker. ....	114
Figure 6-32 (a) SpO <sub>2</sub> measurements in the SW implementation. (b) BR measurement. (c) HR measurement. (d) Gait cadence estimation. ....	115
Figure 6-33 Foot anatomical areas and regions of the sensors positions, where each circle represents the sensor positioning. ....	117
Figure 6-34 Insole components, assembly and POF sensitive zone, where the ‘c’ is the sensitive zone length. ....	117
Figure 6-35 (a) Schematic illustration of the insole connection, data acquisition and LEDs numbering. (b) Photograph of the device positioned on a subject. ....	118
Figure 6-36 (a) Linear regression of sensors 1 to 8 as a function of the applied pressure and force. (b) Linear regression of sensors 9 to 15 with respect to the applied pressure and force. (c) Response as a function of time of sensors 11 to 15 when a loading is applied to sensor 13. F1 and F2 are the applied forces of 40 N and 80 N, respectively.....	120
Figure 6-37 Plantar pressure at each part of the foot and pressure map of subject 1. ....	121
Figure 6-38 (a) Insole positioning on the force platform, direction of the movements and R2 obtained for each subject on the estimation of GRF, CoPx and CoPy. (b) Comparison between the responses of force platform and instrumented insole for test 2 of subject 3. ....	122
Figure 6-39 (a) GRF and plantar pressure for female subject with 46 kg body mass. Solid line represents the mean GRF and shaded curve represents the standard deviation of 5 cycles. (b) Normalized GRF and plantar pressure measurements for all 20 participants. Solid line represents the mean GRF and shaded curve represents the standard deviation.....	123
Figure 6-40 (a) Block diagram of the proposed method for 3D-printed, FBG-embedded flexible support fabrication. (b) Schematic representation of the assembled flexible support. ....	127
Figure 6-41 (a) Reflected spectrum of the FBG array without applied force and after a transverse force application 40 N. (b) Picture of the fabricated flexible shank supports with embedded FBGs (without the elastic bands). Figure inset shows the schematic representation of the fiber connectorization method (further discussed in Section 5.2).....	127
Figure 6-42 Exoskeleton for knee rehabilitation exercises with the 3d-printed flexible supports positioned on the shank region.....	128
Figure 6-43 Block diagram of the force estimation for FBGs 1 and 2 with compensation of creep and temperature effects. ....	129
Figure 6-44 Validation tests for FBGs 1 and 2 at different forces and temperatures, where tests 1-3 were made at 25°C, 4 and 5 at 35°C and the remainder (6 and 7) at 45°C.....	130
Figure 6-45 (a) Responses of the FBGs embedded in shank support 1 and 2 for extension (FBG 1) and flexion (FBG 2) cycles. (b) Human-robot interaction force measurement with the FBG-embedded, 3D-printed flexible supports. ....	130

Figure 6-46 Front view of the spring with the FBG sensors positions. ....	131
Figure 6-47 Mean and standard deviation of the FBGs responses as a function of the applied strain. ....	132
Figure 6-48 (a) Wavelength shift for the 8 FBGs and simulated strain on the region of each FBG. (b) Wavelength shift at each region of the spring as a tool for shape reconstruction of the device under deformation. ....	133
Figure 6-49 FBGs responses as a function of the applied torque on the spring. ....	134
Figure 6-50 Torque estimated after the sensor fusion between 8 FBGs compared with the applied torque. The RMSE and covariance matrix values are also presented. ....	135
Figure 6-51 (a) Force application points and wavelength shift at each region of the spring at 2 transverse force cases. (b) Wavelength shift of each FBG at flexion/extension torques and transverse force conditions. ....	136
Figure 6-52 (a) Finite element analysis on the SW's support bar for two loading conditions: forces applied only on y-axis and forces applied on z-axis. (b) Positions of the FBGs on the SW structure. ....	137
Figure 6-53 (a) FBGs array spectrum recovered in Micron Optics sm 125 FBG interrogator after the POF connectorization and after the application of an axial strain on the fiber. (b) FBGs array spectrum obtained in I-MON 512 spectrometer used on the sensors characterization and implementation on the SW. (c) Wavelength shift as a function of the strain for FBGs 1, 2, 4 and 5. (d) Temperature response for FBG 3. (e) Wavelength shift of FBG 1 under oscillatory loadings at 3 different frequencies (0.5 Hz, 1.5 Hz and 3.5 Hz), where the solid line is the mean and the shaded line is the standard deviation of three tests performed at each frequency. (f) FBG response in the frequency domain for each dynamic test. ....	139
Figure 6-54 (a) Path performed by the user (x and y directions) in the FBGs array implementation tests. (b) Temporal variation of the x and y directions of the path. (c) Comparison between FBGs 1 and 2 with y-axis of the force sensor placed on the SW's right handle. (d) Comparison between FBGs 4 and 5 with y-axis of the force sensor placed on the SW's left handle. (e) Temperature response and wavelength shift of FBG 3 during the test. ....	140
Figure 6-55 (a) FBGs array, LRF and accelerometer responses in the frequency domain for floor condition 1. (b) FBGs array, LRF and accelerometer responses in the frequency domain for floor condition 2. (c) FBGs array, LRF and accelerometer responses in the frequency domain for floor condition 3. ....	141
Figure 6-56 Schematic representation of the SW implementation in a structured environment using the proposed FBG array for instrumentation of healthcare devices. ....	143
Figure A-1 Section view of the POF sensor analyzed. ....	147
Figure A-2 Polymer optical fiber under the bending stress condition. ....	150
Figure A-3 Results for the quasi-static test of the POF with 25 mm section length. ....	153
Figure A-4 Calculated and measured values for five cycles of POF flexion and extension with 1.5 rad/s...	154
Figure B-1 Experimental setup for dynamic test of the optical fiber curvature sensor. ....	155
Figure B-2 Equipment to create the POF sensor sensitive zone. ....	156
Figure B-3 Typical stress-strain curve for a viscoelastic material. ....	157
Figure B-4 (a) Hysteresis and sensitivity for sensitive zone length of 3.25 mm through 31.66 mm. (b) Linearity for different POF sensor section length. The correlation coefficient with the second-degree polynomial is 0.9948. ....	158
Figure B-5 (a) Hysteresis and sensitivity for sensitive zone depth of 0.6 mm through 1.09 mm. The results can be approximated by a second-degree polynomial. (b) Linearity for different POF sensor section depth. The correlation coefficient with the second-degree polynomial is 0.9806. ....	160
Figure B-6 (a) Hysteresis and sensitivity for different POF sensor sensitive zone roughness (samples 14-20), which is represented as the sandpaper grit size. (b) Linearity for different POF sensor sensitive zone roughness. ....	161

Figure B-7 (a) Hysteresis and sensitivity of the sensor with different curvature radii. The correlation coefficient between the results for the sensitivity analysis is 0.9888 and 0.9852 for the hysteresis analysis. (b) Linearity of the sensor with different curvature radii. The correlation coefficient between the results is 0.9843. ....	162
Figure B-8 POF curvature sensor response with optimized sensitive zone parameters and curvature radius	163
Figure C-1 Dynamic compensation technique block diagram. ....	165
Figure C-2 POF curvature sensor response for constant angular velocity of 0.09 rad/s. (a) Response with the compensation technique. (b) Response without the compensation technique. ....	168
Figure D-1 POF under torsion stress. ....	170
Figure D-2 POF response under different torques. ....	171
Figure E-1 Bottom of the insole with the POF sensors positions. ....	173
Figure E-2 Viscoelastic compensation technique applied on sensor 2. ....	173
Figure E-3 Signal attenuation of the sensors under compression loads and the sensitivity of each sensor. ...	174
Figure E-4 POF sensors for in-shoe measurement of vertical GRF. ....	175
Figure E-5 Experimental setup for the quasi-static tests with the POF insole and the force platform. ....	175
Figure E-6 POF sensors response and force platform measurement for the quasi-static tests with the male subject. ....	176
Figure E-7 Gait cycle analysis with the POF insole, where HS is the heel strike, MA is the maximum weight acceptance, FF is the flat foot phase, HO is heel off and TO, toe off. ....	177
Figure E-8 In-shoe monitoring of sequential gait cycles. ....	178
Figure E-9 FES system for gait assistance ....	178
Figure E-10 POF insole for the gait phase detection during the FES assisted gait. ....	179
Figure F-1 POF sensor response in 0 to 100° bend with angular velocity 0.0561 rad/s. The dashed line represents the angle of 90°. ....	180
Figure F-2 POF sensor response on static tests with curvature angle between 0° and 100°. ....	181
Figure G-1 (a) Temperature characterization for the microclimate sensors. (b) Humidity response for the microclimate sensors. All results normalized with respect to the initial power. ....	182
Figure G-2 (a) Temperature characterization for the force sensors. (b) Humidity response for the force sensors. ....	183
Figure G-3 Force characterization under different temperature and humidity conditions for Force sensor 1 and Force sensor 2. ....	183
Figure G-4 Creep/relaxation tests with force sensors 1 and 2. ....	184
Figure H-1 Experimental setup for the FBG sensors (embedded in the TPU structure) characterization. ....	185
Figure H-2 Force characterization of FBG 1 (embedded in the shank flexible support 1) and FBG 2 (embedded in the shank flexible support 2) at constant temperature of 25 °C. ....	186
Figure H-3 Temperature characterization of FBG 1 (embedded in the shank flexible support 1) and FBG 2 (embedded in the shank flexible support 2). ....	186
Figure H-4 (a) Force characterization at different temperatures for FBG 1. (b) Force characterization at different temperatures for FBG 2. (c) Force sensitivity as a function of the temperature for FBGs 1 and 2. ....	187
Figure H-5 Creep response and exponential regression for FBG 1 and 2 for 5 minutes. ....	188
Figure I-1 Equivalent strain (m/m) on the spring under (a) flexion and (b) extension. ....	189
Figure I-2 Equivalent strain (m/m) on the spring under a transverse force of 5 N. ....	189

## List of Tables

Table 2-1 POFBG inscription times with different materials.....	40
Table 4-1 Parameters applied on the simultaneous measurement of temperature and relative humidity.....	60
Table 5-1 POF performance parameters in temperature tests. ....	74
Table 5-2 POF performance parameters in strain cycles.....	74
Table 5-3 POF performance parameters in transverse force cycles. ....	75
Table 5-4 POF performance parameters in transverse force cycles. ....	82
Table 6-1 RMSE and hysteresis of each cycle with and without the compensation technique.....	94
Table 6-2 POF sensor properties. ....	100
Table 6-3 Body mass estimated by the instrumented insole for each subject. ....	121
Table 6-4 Linear regression and torque response of each FBG.....	134
Table A-1 POF sensor parameters.....	152
Table B-1 POF Sensor sensitive zone characteristics.....	157
Table C-1 Parameters employed on the dynamic compensation technique .....	165
Table C-2 Comparison between the sensor with compensation and without technique.....	169
Table E-1 POF sensors design parameters. ....	174

## List of Abbreviations and Acronyms

ABS	Acrylonitrile Butadiene Styrene
ALLOR	Advanced Lower Limb Orthosis for Rehabilitation
BDK	Benzyl Dimethyl Ketal
BR	Breath rate
COC	Cyclic Olefin Copolymers
CoP	Center of Pressure
CMOS	Complementary Metal-Oxide Semiconductors
CYTOP	Cyclic Transparent Optical Polymer
CW	Continuous Wave
DC	Direct Current
DMA	Dynamic Mechanical Analysis
DoF	Degree of Freedom
FBG	Fiber Bragg Grating
FEM	Finite Element Method
FES	Functional Electrical Stimulation
FFT	Fast Fourier Transform
fs	Femtosecond
GI	Graded Index
GRF	Ground Reaction Force
HR	Heart rate
IMU	Inertial Measurement Unit
LC	Light Coupler
LED	Light Emitting Diode
LIDAR	Light Detection and Ranging
LRF	Laser Range Finder
MEMs	Micro-Electro-Mechanical systems
MMF	Multimode Fiber

mPOF	Microstructured Polymer Optical Fiber
NA	Numerical Aperture
OFDR	Optical Frequency-Domain Reflectometry
OTDR	Optical Time-Domain Reflectometry
PC	Polycarbonate
PD	Photodiode
PMMA	Poly (Methyl Methacrylate)
POF	Polymer Optical Fiber
POFBG	Polymer Optical Fiber Bragg Gratings
PLA	Poly(lactic Acid)
PPG	Photoplethysmography
$R^2$	Correlation Coefficient
RH	Relative Humidity
RMSE	Root Mean Squared Error
SEA	Series Elastic Actuator
SHM	Structural Health Monitoring
SMF	Single Mode Fiber
SI	Step Index
SW	Smart Walker
TOPAS	Thermoplastic Olefin Polymer of Amorphous Structure
TPU	Thermoplastic Polyurethane
TS	Trans-4-Stilbenemethanol
TTS	Time-Temperature Superposition
UV	Ultraviolet
WLF	Williams-Landel-Ferry

## List of Symbols

$\alpha$	Angle
$\alpha_e$	Extension Angle
$\alpha_f$	Flexion Angle
$\alpha_T$	Thermal expansion coefficient
$\alpha_p$	Fiber Attenuation coefficient
$\beta$	Constant
$\delta$	Phase Lag
$\varepsilon$	Strain
$\varepsilon_{ref}$	Reference Strain
$\eta$	Polymer Viscosity
$\theta_b$	Angle corrected by the fiber bending
$\theta_c$	Critical Angle
$\theta_i$	Incident Angle
$\theta_l$	Lower Bound Angle
$\theta_{max}$	Acceptance Angle
$\theta_p$	Angle of propagation
$\theta_t$	Transmitted Angle
$\theta_u$	Upper Bound Angle
$\lambda$	Wavelength
$\lambda_B$	Bragg Wavelength
$\nu^*$	Poisson's Ratio
$\sigma_0$	Stress on static condition
$\sigma(t)$	Stress on dynamic condition
$\tau$	Relaxation Time
$\tau_{1,2}$	Time constant
$\tau_0$	Applied torque
$\xi$	Thermo-optic coefficient

$\omega$	Angular Velocity
$\Delta n_z$	Refractive Index Variation
$\Delta B_i$	Changes of coefficients in optical indicatrix
$\Delta T$	Temperature variation
$\Delta RH$	Relative humidity variation
$A$	Modulation period
$a$	Core radius
$a_T$	Time-Temperature Shift Factor
$c$	Sensitive Zone Length
$d$	Fiber diameter
$d\theta$	Element Angle
$d\Omega$	Element solid angle
$d_s$	Spacing between the fibers
$dP$	Element power radiated
$dS$	Element Section
$f$	Frequency
$h$	Hysteresis
$n_1$	Refractive Index of the less refractive medium
$n_2$	Refractive Index of the more refractive medium
$n_c$	Core Refractive Index
$n_{cl}$	Cladding Refractive Index
$n_{ext}$	External Refractive Index
$n_{eff}$	Effective refractive index
$p$	Sensitive Zone Depth
$q_{11}$	Stress-Optic Tensor Coefficient
$r_{PL}$	Reflection of parallel rays
$r_{PP}$	Reflection of perpendicular rays
$r_T$	Reflection coefficient
$SF$	Force sensitivity

$s_T$	Temperature sensitivity
$t$	Time
$y_{1,2}$	Weight of each exponential
$x$	Distance between the bended portion and the center of the fiber
$C_1$	Material Constant 1
$C_2$	Material Constant 2
$C_{cp}$	Strain response to a unit stress input
$E^*$	Dynamic Young's Modulus
$E_a^*$	Uncorrected dynamic Young's modulus
$E_0$	Static Young's Modulus
$E$	Young's modulus
$F$	Force
$G$	Shear modulus
$I$	Identity matrix
$I_x$	Inertia moment
$K_{x,x}$	Sensitivity parameter
$L$	POF Length
$L_o$	Light Source Radiance
$N$	Number of internal reflections
$N_m$	Number of Modes
$NA$	Numerical Aperture
$P_0$	Static Power
$P_l$	Power at $0^\circ$
$P_{in}$	Input Power
$P_o$	Output Power
$P_s$	Sensitive Zone Power
$P_e$	Effective photoelastic constant
$V$	Normalized Frequency
$R$	Curvature Radius

$R^2$	Correlation coefficient
$S_c$	Fiber core cross sectional area
$S_o$	Maximum area of removed material
$T$	Torque
$T_r$	Temperature
$T_{ref}$	Reference Temperature
$V_{comp,1}^e$	Hysteresis Compensated Voltage for Extension
$V_{comp,2}^e$	Error Compensated Voltage for Extension
$V_{comp,1}^f$	Hysteresis Compensated Voltage for Flexion
$V_{comp,2}^f$	Error Compensated Voltage for Flexion
$V_{meas}$	Measured Voltage
$Y_{max}$	Maximum point on the hysteretic curve
$Y_{min}$	Minimum point on the hysteretic curve
$Y_{mp}$	Midpoint of the hysteretic curve

# Chapter 1. Introduction

## 1.1. Motivation

The continuous increase of the life expectancy due to improvements in the quality of life and advances in medicine as well as the increasing interest in family planning and birth control policies in developed countries have led to a rapid and progressive increase on ageing of the world's population [1]. According to the World Health Organization, by 2020 the number of elderly people (over 60 years) will be higher than the children below 5 years [2]. The population ageing also results in increase of clinical conditions that affect the human locomotion such as stroke, spinal cord injury, Parkinson's disease and weakness of the skeletal muscles [3]. This scenario has pushed the boundaries for novel therapeutic methods and assistance devices for patients with locomotor impairment, which also result in the development of novel devices with the aim of monitoring parameters for human health assessment [4]. In addition, different devices for gait assistance and rehabilitation have been proposed [5], [6].

In order to offer independence and attenuate the effects of the human gait disorders, different gait assistance devices have been proposed throughout the years, e.g., prostheses [7], exoskeletons [8], orthosis [9] and smart walkers (SWs) [5]. The latter is generally used as a supporting device in the patients bipedestration, which aids in their balance and, thus, improving the mobility [5]. SWs present actuators and electronic components aiming to provide a better assistance to the users, where the functionalities of such devices include autonomous control with possibility of shared or manual control as well, sensorial feedback, higher safety and the possibility of monitoring the user's state [10]. Among the wearable robotic devices for gait rehabilitation, lower limb exoskeletons show advantages over conventional rehabilitation therapies related to their higher repeatability in the rehabilitation exercises, possibility of treatment customization and quantitative feedback of the patient's recovery [11]. In addition, wearable robots control strategies for human-robot cognitive interaction enable using exoskeletons as assistance devices for daily activities, which include the gait assistance [12].

The monitored parameters for human health assessment include foot plantar pressure, which provides important data regarding the human health condition [13]. With the plantar pressure assessment, it is possible to obtain a foot pressure distribution map, which plays an important role on the monitoring of foot ulcerations (of particular importance for diabetes patients). In addition, foot pressure maps enable measurements of foot-function indexes such as arch index, which provide the evaluation of the arch type of each individual that is also related to injuries in runners [14]. Furthermore, the dynamic evaluation of the foot plantar pressure can also aid clinicians on the gait related pathologies diagnosis [15]. The gait cycle is divided into two main phases: stance and swing, which present many subdivisions [16]. The subdivisions of the stance phase can be detected by the plantar pressure variation and it is critical for the control of wearable devices for gait assistance [17], [18]. Additionally, the measurement and analysis of joint angles can provide benefits for clinicians and therapists, since it is used on the evaluation and quantification of surgical interventions and rehabilitation exercises [19]. In addition, such measurements can be applied for training athletes [20] and the kinematic data have been employed on the control of neural prostheses [21]. Furthermore, wearable sensors can be used on healthcare applications [22]. To that extent, significant advances in sensor technology, wireless communications and data analysis have enabled a change of scenario, where the health condition assessment is not limited to clinical environments [23]. Thus, it is also possible to monitor different physiological parameters for patients at home, which is especially desirable for the elderly population and people with locomotor disabilities [4]. Among many important physiological parameters, abnormalities on the heart rate (HR) and breathing rate (BR) are important indicators of some cardiovascular diseases [24], fatigue [25], apnea [25] and respiratory abnormalities [26].

In order to achieve their functionalities, exoskeletons highly rely on sensors systems, which generally are potentiometers and encoders for the joint angles assessment that have to be carefully attached to the device's joints due to their sensitivity to misalignments [6]. For this reason, these sensors need mechanical supports precisely attached to the robot, which result in a less compact system [18]. Another commonly employed sensor technology is based on inertial measurement units (IMUs), but they need regular calibration [27]. In addition, the high sensitivity to electromagnetic fields can be regarded as an important disadvantage in wearable robots applications in which electric actuators are constantly activated [18].

Similarly, the electronic strain gauges employed in the assessment of human-robot force/torque interaction and actuator dynamics also have sensitivity to electromagnetic fields, need frequency calibration and require a careful attachment to the structure, where the strain/force will be measured [28].

Microclimate conditions in the interface of the human body and the exoskeleton supports are also important parameters in wearable devices. Humidity and temperature must be monitored to minimize the injuries or pressure ulcers and improve the patient's comfort while using the wearable device [6]. The electronic sensors employed in these applications usually lack in linearity or, in some cases, can present low accuracy and stability [6].

Most of the disadvantages of the aforementioned electronic sensors are especially undesirable in soft wearable robotics, where robots are combined with soft materials for the development of novel actuators [29] and wearable solutions [30]. Such systems present the advantages of low weight and being inherently compliant with the user due to the soft/flexible materials used [31]. Thus, the sensors for these systems are constantly submitted to larger strains or deflections of the soft structure, which inhibit the application of non-flexible electronic sensors [22]. In order to achieve the flexibility requirements of some sensors' systems, different flexible electronic sensors have been proposed [22]. However, these sensors still have sensitivity to electromagnetic fields and generally need complex manufacturing techniques.

Different control strategies for human-robot interaction proposed for SW are summarized in [10] and require different types of sensors. The sensors for the SW instrumentation can be divided into four main groups: force sensors for upper limbs strategies, sensors for kinematic assessment of the gait, odometry sensors and sensors for environment interaction of the SW. In the human-robot interaction considered in this Thesis, the SW tracks the human position to minimize the differences in their orientations and distances [32]. In this case, the orientation is obtained through IMUs positioned in the user's hip and the cadence is obtained with a laser range finder (LRF) that detects the legs of the user, whereas two 3D force sensors are applied on the detection of the user's movement intention [33]. Moreover, a light detection and ranging (LIDAR) can be used on the environment localization and mapping.

For physiological parameters monitoring, several electronic sensors based on different approaches such as piezo-electric films, dry textile electrodes, flexible capacitive electrodes (among others) have been proposed throughout the years. Such technologies are summarized in some published review works [4], [22]. However, in general, as electronic sensors are sensitive to electromagnetic interferences, it inhibits their application in magnetic resonance imaging (MRI) [34] and can also present inaccuracies related to electromagnetic field produced on the constant activation of electric motors in wearable robots.

For the plantar pressure and ground reaction forces (GRFs) monitoring, there are three major techniques for foot plantar pressure assessment: imaging technologies [35], force/pressure distribution platforms [36] and instrumented insoles [37]. Imaging technologies generally employ expensive equipment and complex signal processing [13]. In addition, these issues scale when the analysis is made in computed tomography machines, which, besides the high cost, inhibits the dynamic analysis of the plantar pressure [35].

As a more affordable option with the possibility of performing dynamic analysis, force platforms are used on the plantar pressure assessment. These platforms generally have a matrix of pressure sensing elements arranged in a rigid and flat platform [13]. Even though they provide measurements of the foot plantar pressure and 3D dynamics, they also lack in portability, restricting the tests to laboratory or clinical environments, where there is a limitation on the number of steps per trial. This drawback inhibits the application on wearable robotics, remote and home health monitoring, which is a trend on healthcare applications with the advances in wireless sensor and communication technologies [38]. Another drawback of force platforms is the so-called foot targeting effect, where the users alter their natural gait pattern in order to correctly place the foot on the platform, which leads to inaccuracies on the analysis [39]. Consequently, it leads to the necessity of hidden the platform on the ground and repeating the test until a natural gait pattern is obtained with the foot placed within the platform boundaries [36].

Instrumented insoles became a feasible option to the force platforms with the possibility of being used inside a shoe, thereby resulting in a portable device to be assessed outside the laboratory environment, for remote health monitoring and wearable robotics applications [13]. In addition, another advantage of instrumented insoles is the possibility of monitoring the plantar pressure during daily activities with the natural gait pattern of the users. However, mainly due to the sensor technology employed (generally electronic sensors), such insoles can present instability on the measurement (with false positives and false negatives) and lack of resistance to the impact loads that commonly occurs in the gait cycle [40]. Another issue of

instrumented insoles is the number of sensors, which resulted in a low spatial resolution for the plantar pressure analysis [13]. The human foot has 15 pressure areas that support most of the body weight as discussed in [37]. Thus, an ideal sensor system for complete monitoring of the plantar pressure needs 15 sensors positioned on each of those 15 critical points. However, previous works generally aim to a system simplification and the number of sensors is generally 5 to 7 sensors distributed on the foot [13]. Even though a higher number of sensors can be achieved with sensors based on smart textiles and custom fabrics, they generally present performance limitations such as low repeatability, hysteresis, creep and nonlinearities [13].

As an emerging sensor technology, optical fiber sensors present the intrinsic advantages of lightweight, compactness, chemical stability, immunity to electromagnetic field and multiplexing capabilities [41]. These advantages make optical fiber sensors an intrinsically safe technology for industrial [42], medical [43] and structural health monitoring [44] applications. Additionally, optical fiber sensors are employed on the measurement of several parameters like angle [45], refractive index [46], temperature [47], humidity [48], acceleration [49], pressure [50], breathing rate [51] and oxygen saturation [52]. In addition, the features of optical fibers enable their embedment in textiles for sensing applications [51], [53] and also the creation of optical fiber-based textiles, the so-called photonics textiles [52].

There are two major types of optical fibers, silica and polymer optical fibers (POFs). Besides their higher optical power attenuation when compared with silica fibers, POFs present advantages over silica fibers related to their material features. Such advantages include higher flexibility, lower Young's modulus, higher strain limits, fracture toughness and impact resistance [41]. Furthermore, POFs enable a safer operation in smart textiles, since silica fibers can break more easily than POFs and present a risk for the users when there is a breakage due to the glass punctures that might cause injuries [51].

The advantages of POFs are also well aligned with the requirements for soft robotics applications, which make POFs suitable for the embedment in these novel soft structures. One of the technologies that have enabled the development of such novel wearable flexible systems with lower relative cost is the 3D printing, which is an additive layer manufacturing process, where a hot or melted polymer is injected layer-by-layer [54]. The materials generally used in 3D printing are polylactic acid (PLA) or acrylonitrile butadiene styrene (ABS) with the possibility of using flexible materials such as thermoplastic polyurethane (TPU). To that extent, optical fiber sensors can be embedded in 3D-printed structures for structural health monitoring (SHM) [55] and plantar pressure sensing platforms [56].

However, it is noteworthy that the POF material features are twofold. On the one hand, the lower Young's modulus of POFs and higher strain limits enable developing sensors with higher dynamic range and much higher sensitivity when compared with the ones in silica fibers [57]. On the other hand, polymers are viscoelastic materials, which do not present a constant relation with stress or strain [17]. Furthermore, viscoelastic materials present a hysteretic response between stress and strain [18] and this may be a source of hysteresis and nonlinearities in POF sensors [58]. In addition, viscoelastic materials have a variation of their Young's modulus in response to different parameters such as strain cycle frequency, temperature and relative humidity [59]. Therefore, it is necessary to understand and characterize the POF viscoelastic response to propose a compensation of the viscoelastic effects and obtain a more reliable measurement of any POF sensor based on direct stress or strain on the fiber (such as curvature sensor [60], strain [61] and force [40] sensors) prior to their applications in healthcare devices and movement analysis.

There are a few optical fiber-based techniques to measure temperature and strain, such as fiber Bragg gratings (FBGs) [62], interferometers [63] and nonlinear effects [64]. However, the complexity of signal processing, implementation and the cost of the interrogation equipment are critical disadvantages [65]. On intensity variation-based sensors, the variation of the sensing parameter leads to an output power attenuation. The advantages of this approach are its low cost and simplicity in signal processing [66]. Although these sensors may present errors on the measurement due to the variation of the light source power and environmental conditions, techniques based on self-referencing schemes [67] or dual-wavelength compensation [65] can be applied to reduce these errors. Aiming at the development of low-cost and portable sensor systems, intensity variation is one of the techniques used on the sensors' development in this Thesis.

However, intensity variation-based sensors have another important drawback due to the lack of multiplexing capabilities in this approach. In order to overcome the limitations of intensity variation-based sensors and considering recent advances in FBG inscription in POFs [68], another sensing technique used in this Thesis is to use uniform FBGs due to their multiplexing capabilities, which makes it possible to inscribe long arrays with increasing number of sensors in the same fiber for quasi-distributed and multiparameter

applications [69]. FBGs are periodic modulations of the fiber core's refractive index. Different gratings can be inscribed in the same fiber by just modifying the period of this refractive index modulation, with each grating acting as a wavelength selective filter, reflecting light at a discrete wavelength that is directly proportional to the inscribed period. Changes to the period as a result of external perturbations are recovered as wavelength-encoded data. This offers a huge advantage as the data is an absolute quantity and may be recovered even if the signal is temporarily interrupted. FBGs can be fabricated using the methods discussed in [68], through the ultraviolet (UV) laser irradiation with a phase mask [70] or direct write in the fiber core using a femtosecond (fs) laser [71]. A lot of progress have been achieved in POFs made of different materials [72]. Among those materials for POFs, the cyclic transparent optical polymer (CYTOPs) offer advantages over other materials, such as poly methyl methacrylate (PMMA) and cyclic olefin copolymers (COC), due to their lower optical losses, particularly in the 1550 nm wavelength region [73]. This advantage enables the employment of commercially available optical components, which are generally designed to work within the 1550 nm wavelength region. Thus, FBGs inscribed in CYTOP fiber are good candidates for practical sensing applications. However, such fibers present multimode operation, which can inhibit their application as sensors and in long arrays. Theodosiou et al [74] proposed a direct write, plane-by-plane inscription method with optimized inscription parameters using a fs laser, where it is possible to control the coupling between the grating and core modes, leading to a single peak spectrum, which can be regarded as an important advance towards practical sensing applications with FBGs inscribed in POF.

Figure 1-1 shows a schematic representation of the robotic devices (lower limb exoskeleton and SW) and monitored parameters, which not only outline the aforementioned parameters and devices, but also show the sensors developed throughout this Thesis with different sensing approaches.



Figure 1-1 Overview of the robotic devices and monitored parameters.

## 1.2. Research Objectives and Contributions

The general objective of this Doctoral Thesis is the development of novel sensors systems based on POFs using two different approaches: intensity variation and FBGs for the instrumentation of assistive devices (SW, orthosis and exoskeletons) as well as for movement analysis purposes.

In order to achieve these objectives, an extensive investigation of the POF materials is necessary, since they have direct influence on the sensor dynamic range and performance. The influence of thermal and

chemical treatments on POF materials are also evaluated, since these treatments can enhance the sensor performance.

In addition, the evaluation of the material viscoelasticity also enables the development of novel compensation techniques for POF sensors and different approaches aiming on the enhancement of POF sensors for the assessment of angle, force, pressure, strain, temperature, humidity and physiological parameters. These lead to the contributions of this Thesis listed as following:

- Development of a characterization methodology for mechanical and viscoelastic properties of POFs;
- Mechanical characterization of POFs with different materials, structures and thermochemical treatments;
- Characterization of the fs laser inscription influence on POF material properties;
- Development of an analytical model for POFs optical power variation under dynamic bending;
- Development of compensation techniques for creep response, hysteresis, nonlinearities, temperature and humidity dependency on POF sensors responses;
- Development of POF sensors for angle, temperature, humidity, force, pressure, HR, BR and torque with enhanced capabilities;
- Development of a novel multiplexing technique for intensity variation-based sensors;
- Application of the POF sensors in exoskeletons, orthosis, SW and Functional Electrical Stimulation (FES) systems for gait assistance;
- Development of portable wearable sensors and instrumented insoles.

### 1.3. Publications

In the time frame of the Thesis, about 50 journal papers (J), 10 conference works (C) and 4 book chapters (B) were either published, accepted or under review. These works also include the collaboration with other researchers and international groups. The works are divided into the ones used in the Thesis (marked as T) and the ones from collaborations and parallel researches (marked as P). In addition, there are also 4 patent applications under consideration on the university. The list of publications is presented in the following sections.

#### 1.3.1. Journal Articles

[J1 -T] A. G. Leal-Junior, C. R. Díaz, C. Marques, M. J. Pontes, and A. Frizera, “Multiplexing technique for quasi-distributed sensors arrays in polymer optical fiber intensity variation-based sensors,” *Opt. Laser Technol.*, vol. 111, 2019.

[J2-P] A. G. Leal-Junior, C. R. Díaz, C. Leitão, M. J. Pontes, C. Marques, and A. Frizera, “Polymer optical fiber-based sensor for simultaneous measurement of breath and heart rate under dynamic movements,” *Opt. Laser Technol.*, vol. 109, no. August 2018, pp. 429–436, 2019.

[J3-T] A. G. Leal-Junior, A. Frizera, and M. José Pontes, “Sensitive zone parameters and curvature radius evaluation for polymer optical fiber curvature sensors,” *Opt. Laser Technol.*, vol. 100, pp. 272–281, 2018.

[J4-P] A. G. Leal-Junior, C. Marques, A. Frizera, and M. J. Pontes, “Multi-interface level in oil tanks and applications of optical fiber sensors,” *Opt. Fiber Technol.*, vol. 40, pp. 82–92, Jan. 2018.

[J5-T] A. G. Leal-Junior, A. Frizera, C. Marques, M. R. A. Sanchez, W. M. dos Santos, A. A. G. Siqueira, M. V. Segatto, and M. J. Pontes, “Polymer Optical Fiber for Angle and Torque Measurements of a Series Elastic Actuator’s Spring,” *J. Light. Technol.*, vol. 36, no. 9, pp. 1698–1705, May 2018.

[J6-P] A. Leal-Junior, A. Frizera-Neto, C. Marques, and M. Pontes, “A Polymer Optical Fiber Temperature Sensor Based on Material Features,” *Sensors*, vol. 18, no. 2, p. 301, Jan. 2018.

[J7-P] C. A. F. Marques, R. Min, A. Leal Junior, P. Antunes, A. Fasano, G. Woyessa, K. Nielsen, H. K. Rasmussen, B. Ortega, and O. Bang, “Fast and stable gratings inscription in POFs made of different materials with pulsed 248 nm KrF laser,” *Opt. Express*, vol. 26, no. 2, p. 2013, Jan. 2018.

[J8-T] A. G. Leal, C. Marques, A. Frizera, and M. J. Pontes, “Dynamic Mechanical Analysis on a PolyMethyl Methacrylate (PMMA) Polymer Optical Fiber,” *IEEE Sens. J.*, vol. 18, no. 6, pp. 1–1, 2018.

- [J9-P] A. Leal-Junior, A. Frizera, C. Marques, and M. José Pontes, "Polymer-optical-fiber-based sensor system for simultaneous measurement of angle and temperature," *Appl. Opt.*, vol. 57, no. 7, p. 1717, Mar. 2018.
- [J10-P] A. G. Leal-Junior, A. Frizera, C. Marques, M. R. A. Sánchez, T. R. Botelho, M. V. Segatto, and M. J. Pontes, "Polymer optical fiber strain gauge for human-robot interaction forces assessment on an active knee orthosis," *Opt. Fiber Technol.*, vol. 41, no. December 2017, pp. 205–211, 2018.
- [J11-P] A. G. Leal-Junior, A. Frizera, and M. J. Pontes, "Compensation technique for environmental and light source power variations applied in a polymer optical fiber curvature sensor for wearable devices," *Res. Biomed. Eng.*, vol. 34, no. 1, pp. 37–44, 2018.
- [J12-P] C. Marques, A. Leal-Junior, R. Min, M. Domingues, C. Leitão, P. Antunes, B. Ortega, and P. André, "Advances on Polymer Optical Fiber Gratings Using a KrF Pulsed Laser System Operating at 248 nm," *Fibers*, vol. 6, no. 1, p. 13, 2018.
- [J13-T] A. G. Leal-Junior, A. Frizera, C. Marques, and M. J. Pontes, "Viscoelastic features based compensation technique for polymer optical fiber curvature sensors," *Opt. Laser Technol.*, vol. 105, pp. 35–40, 2018.
- [J14-T] A. G. Leal-Junior, A. Frizera, and M. J. Pontes, "Dynamic Compensation Technique for POF Curvature Sensors," *J. Light. Technol.*, vol. 36, no. 4, pp. 1112–1117, 2018.
- [J15-T] A. G. Leal-Junior, A. Frizera, L. M. Avellar, C. Marques, and M. J. Pontes, "Polymer Optical Fiber for In-Shoe Monitoring of Ground Reaction Forces during the Gait," *IEEE Sens. J.*, vol. 18, no. 6, pp. 2362–2368, 2018.
- [J16-P] A. Leal-Junior, A. Frizera, M. J. Pontes, A. Fasano, G. Woyessa, O. Bang, and C. A. F. Marques, "Dynamic mechanical characterization with respect to temperature, humidity, frequency and strain in mPOFs made of different materials," *Opt. Mater. Express*, vol. 8, no. 4, p. 804, Apr. 2018.
- [J17-T] A. Leal-Junior, A. Frizera-Neto, C. Marques, and M. Pontes, "Measurement of Temperature and Relative Humidity with Polymer Optical Fiber Sensors Based on the Induced Stress-Optic Effect," *Sensors*, vol. 18, no. 3, p. 916, Mar. 2018.
- [J18-P] A. Leal-Junior, A. Frizera, M. José Pontes, P. Antunes, N. Alberto, M. Fátima Domingues, H. Lee, R. Ishikawa, Y. Mizuno, K. Nakamura, P. André, and C. Marques, "Dynamic mechanical analysis on fused polymer optical fibers: Towards sensor applications," *Opt. Lett.*, vol. 43, no. 8, pp. 1754–1757, 2018.
- [J19-P] A. G. Leal-Junior, C. Marques, M. R. N. Ribeiro, and M. J. Pontes, "FBG-Embedded 3D Printed ABS Sensing Pads: The Impact of Infill Density on Sensitivity and Dynamic Range in Force Sensors," *IEEE Sens. J.*, vol. 1748, no. c, pp. 1–1, 2018.
- [J20-P] A. Leal-Junior, L. Vargas-Valencia, W. M. dos Santos, F. Schneider, A. A. G. Siqueira, M. J. Pontes, and A. Frizera, "POF-IMU sensor system: A fusion between inertial measurement units and POF sensors for low-cost and highly reliable systems," *Opt. Fiber Technol.*, 2018.
- [J21-T] A. Leal-Junior, A. Frizera, C. Marques, and M. J. Pontes, "Mechanical properties characterization of polymethyl methacrylate polymer optical fibers after thermal and chemical treatments," *Opt. Fiber Technol.*, vol. 43, no. March, pp. 106–111, 2018.
- [J22-P] A. Leal-Junior, A. Frizera, H. Lee, Y. Mizuno, K. Nakamura, C. Leitão, M. Fátima Domingues, N. Alberto, P. Antunes, P. André, C. Marques, and M. José Pontes, "Design and characterization of a curvature sensor using fused polymer optical fibers," *Opt. Lett.*, vol. 43, no. 11, p. 2539, Jun. 2018.
- [J23-P] A. Leal-Junior, A. Frizera, H. Lee, Y. Mizuno, K. Nakamura, T. Paixão, C. Leitão, M. F. Domingues, N. Alberto, P. Antunes, P. André, C. Marques, and M. J. Pontes, "Strain, temperature, moisture, and transverse force sensing using fused polymer optical fibers," *Opt. Express*, vol. 26, no. 10, p. 12939, May 2018.
- [J24-P] A. G. Leal-Junior, A. Frizera, R. Min, M. J. Pontes, A. Fasano, G. T. Woyessa, O. Bang, and C. Marques, "Influence of the cladding structure in PMMA mPOFs mechanical properties for strain sensors applications," *IEEE Sens. J.*, vol. 18, no. 14, 2018.
- [J25-T] A. Leal-Junior, A. Theodosiou, C. Díaz, C. Marques, M. Pontes, K. Kalli, and A. Frizera-Neto, "Polymer Optical Fiber Bragg Gratings in CYTOP Fibers for Angle Measurement with Dynamic Compensation," *Polymers (Basel)*, vol. 10, no. 6, p. 674, 2018.

- [J26-T] A. G. Leal-Junior, A. Theodosiou, C. Marques, M. J. Pontes, K. Kalli, and A. Frizera, “Thermal Treatments and Compensation Techniques for the Improved Response of FBG Sensors in POFs,” *J. Light. Technol.*, vol. 36, no. 17, 2018.
- [J27-T] A. G. Leal-Junior, A. Theodosiou, C. Marques, M. J. Pontes, K. Kalli, and A. Frizera, “Compensation Method for Temperature Cross-Sensitivity in Transverse Force Applications With FBG Sensors in POFs,” *J. Light. Technol.*, vol. 36, no. 17, pp. 3660–3665, Sep. 2018.
- [J28-P] R. Min, B. Ortega, A. Leal-Junior, and C. Marques, “Fabrication and Characterization of Bragg Grating in CYTOP POF at 600-nm Wavelength,” *IEEE Sensors Lett.*, vol. 2, no. 3, pp. 1–4, 2018.
- [J29-T] A. G. Leal-Junior, A. Frizera, L. Vargas-Valencia, W. M. dos Santos, A. P. L. Bo, A. A. G. Siqueira, and M. J. Pontes, “Polymer Optical Fiber Sensors in Wearable Devices: Toward Novel Instrumentation Approaches for Gait Assistance Devices,” *IEEE Sens. J.*, vol. 18, no. 17, pp. 7085–7092, Sep. 2018.
- [J30-P] A. Leal-Junior, A. Frizera, C. Díaz, C. Marques, M. Ribeiro, and M. J. Pontes, “Material features based compensation technique for the temperature effects in a polymer diaphragm-based FBG pressure sensor,” *Opt. Express*, vol. 26, no. 16, p. 20590, Aug. 2018.
- [J31-P] A. G. Leal-Junior, A. Frizera, L. M. Avellar, and M. J. Pontes, “Design considerations, analysis, and application of a low-cost, fully portable, wearable polymer optical fiber curvature sensor,” *Appl. Opt.*, vol. 57, no. 24, p. 6927, Aug. 2018.
- [J32-P] A. G. Leal-Junior, C. Marques, M. R. N. Ribeiro, M. J. Pontes, and A. Frizera, “FBG-Embedded 3-D Printed ABS Sensing Pads: The Impact of Infill Density on Sensitivity and Dynamic Range in Force Sensors,” *IEEE Sens. J.*, vol. 18, no. 20, 2018.
- [J33-P] M. R. A. Sanchez, A. G. Leal-Junior, M. V. Segatto, C. Marques, W. M. dos Santos, A. A. G. Siqueira, and A. Frizera, “Fiber Bragg grating-based sensor for torque and angle measurement in a series elastic actuator’s spring,” *Appl. Opt.*, vol. 57, no. 27, p. 7883, 2018.
- [J34-P] A. Leal-Junior, A. Theodosiou, A. Frizera-Neto, M. J. Pontes, E. Shafir, O. Palchik, N. Tal, S. Zilberman, G. Berkovic, P. Antunes, P. André, K. Kalli, and C. Marques, “Characterization of a new polymer optical fiber with enhanced sensing capabilities using a Bragg grating,” *Opt. Lett.*, vol. 43, no. 19, p. 4799, 2018.
- [J35-T] A. G. Leal-Junior, A. Frizera, and M. J. Pontes, “Analytical model for a polymer optical fiber under dynamic bending,” *Opt. Laser Technol.*, vol. 93, pp. 92–98, 2017.
- [J36-T] A. Leal Junior, A. Frizera Neto, M. J. Pontes, and T. R. Botelho, “Hysteresis compensation technique applied to polymer optical fiber curvature sensor for lower limb exoskeletons,” *Meas. Sci. Technol.*, Oct. 2017.
- [J37-P] A. R. Prado, A. G. Leal-Junior, C. Marques, S. Leite, G. L. De Sena, L. C. Machado, A. Frizera, M. R. N. Ribeiro, and M. J. Pontes, “Polymethyl methacrylate (PMMA) recycling for the production of optical fiber sensor systems,” *Opt. Express*, vol. 25, no. 24, 2017.
- [J38-P] C. A. R. Diaz, A. G. Leal-Junior, P. S. B. Andre, P. F. da C. Antunes, M. J. Pontes, A. Frizera-Neto, and M. R. N. Ribeiro, “Liquid Level Measurement Based on FBG-Embedded Diaphragms With Temperature Compensation,” *IEEE Sens. J.*, vol. 18, no. 1, pp. 193–200, Jan. 2018.
- [J39-P] D. Vilarinho, A. Theodosiou, C. Leitão, A. Leal-Junior, M. Domingues, K. Kalli, P. André, P. Antunes, and C. Marques, “POFBG-Embedded Cork Insole for Plantar Pressure Monitoring,” *Sensors*, vol. 17, no. 12, p. 2924, Dec. 2017.
- [J40-P] A. G. Leal-Junior, C. A. R. Díaz, A. Frizera, C. Marques, M. R. N. Ribeiro, and M. J. Pontes, “Simultaneous measurement of pressure and temperature with a single FBG embedded in a polymer diaphragm,” *Opt. Laser Technol.*, vol. 112, no. July 2018, pp. 77–84, 2019.
- [J42-T] A. G. Leal, C. R. Diaz, M. F. Jimenez, C. Leitao, C. Marques, M. J. Pontes, and A. Frizera, “Polymer Optical Fiber Based Sensor System for Smart Walker Instrumentation and Health Assessment,” *IEEE Sens. J.*, vol. 1748, no. c, pp. 1–1, 2018.
- [J42-P] C. Diaz, A. G. Leal Junior, C. Marques, C. Leitao, P. S. de Brito Andre, P. Antunes, M. J. Pontes, A. Frizera-Neto, and M. Ribeiro, “Combined Bending and Torsion Sensing by Induced Birefringence in Distributed Bragg Reflector Laser,” *J. Light. Technol.*, vol. 8724, no. c, pp. 1–1, 2018.

[J43-T] A. Leal-Junior, A. Theodosiou, C. Díaz, C. Marques, M. Pontes, K. Kalli, and A. Frizera-Neto, “Fiber Bragg Gratings in CYTOP Fibers Embedded in a 3D-Printed Flexible Support for Assessment of Human-Robot Interaction Forces,” *Materials (Basel)*, vol. 11, no. 11, p. 2305, Nov. 2018.

[J44-T] A. G. Leal-Junior, C. R. Díaz, M. J. Pontes, C. Marques, and A. Frizera, “Polymer optical fiber-embedded, 3D-printed instrumented support for microclimate and human-robot interaction forces assessment,” *Opt. Laser Technol.*, vol. 112, no. November 2018, pp. 323–331, 2019.

[J45-P] A. Leal-Junior, J. Casas, C. Marques, M. Pontes, and A. Frizera, “Application of Additive Layer Manufacturing Technique on the Development of High Sensitive Fiber Bragg Grating Temperature Sensors,” *Sensors*, vol. 18, no. 12, p. 4120, 2018.

[J46-T] A. G. Leal-Junior, A. Theodosiou, C. Diaz, C. Marques, M. J. Pontes, K. Kalli, A. Frizera, “Simultaneous Measurement of Axial Strain, Bending and Torsion with a Single Fiber Bragg Grating in CYTOP Fiber,” *Journal of Lightwave Technology* (**accepted in 11-21-2018**)

[J47-P] C. Broadway, R. Min, A. Leal-Junior, C. Marques, C. Caucheteur, “Towards commercial polymer fiber Bragg grating sensors: review and applications,” *Journal of Lightwave Technology* (**accepted in 11-16-2018**)

[J48-T] Leal-Junior, Arnaldo; Diaz, Camilo; Marques, Carlos; Pontes, Maria José; Frizera, Anselmo. Polymer Optical Fiber-Embedded, 3D-printed POF insole: development and applications of a low-cost, highly customizable device for plantar pressure and ground reaction forces monitoring. *Scientific Reports* (**submitted in 11-19-2018**)

[J49-T] Leal-Junior, Arnaldo; Theodosiou, Antreas; Min, Rui; Casas, Jonathan; Diaz, Camilo; dos Santos, Wilian; Pontes, Maria José; Siqueira, Adriano; Marques, Carlos; Kalli, Kyriacos; Frizera, Anselmo. Quasi-Distributed Sensing on a Series Elastic Actuator’s Spring using FBG arrays inscribed in CYTOP Fibers. *Journal of Lightwave Technology* (**submitted in 12-03-2018**)

[J50-T] Leal-Junior, Arnaldo; Theodosiou, Antreas; Diaz, Camilo; Jimenez, Mario; Min, Rui; Pontes, Maria José; Kalli, Kyriacos; Marques, Carlos; Frizera, Anselmo. Polymer optical fiber Bragg grating arrays inscribed with ultrafast laser – a practical route to healthcare devices instrumentation. *Light: Science and Applications* (**under submission process**)

[J51-P] Zubel, Michal; Fasano, Andrea; Woyessa, Getinet; Min, Rui; Leal-Junior, Arnaldo; Theodosiou, Antreas; Marques, Carlos; Rasmussen, Henrik; Bang, Ole; Ortega, Beatriz; Kalli, Kyriacos; Frizera-Neto, Anselmo; Pontes, Maria José; Sugden, Kate. Bragg gratings inscribed in solid-core microstructured few-moded polymer optical fiber drawn from 3D-printed polycarbonate preform. *Optics Express* (**under submission process**)

### 1.3.2. Conference Papers

[C1-P] A. G. Leal-Junior; A. Frizera, H. Lee, Y. Mizuno, C. Leitão, M. Domingues, P. F. C. Antunes, K. Nakamura, P.S.B André, C. Marques, M. J. PONTES, “Sensors applications of polymer optical fibers submitted to the fuse effect,” In: *Asia-Pacific Optical Sensors Conference APOS 2018*, 2018, Matsue. *Asia-Pacific Optical Sensors Conference APOS 2018*, 2018.

[C2-P] A. G. Leal-Junior, A. Frizera, M. Pontes, P. F. C. Antunes, N. Alberto, M. Domingues, H. Lee, R. Ishikawa; Y. Mizuno, K. Nakamura, P. S. B. André, C. Marques, “Recycling of polymer optical fibers damaged by fuse effect: dynamic mechanical analysis for sensing applications”, In: *Asia-Pacific Optical Sensors Conference APOS 2018*, 2018, Matsue. *Asia-Pacific Optical Sensors Conference APOS 2018*, 2018.

[C3-P] P. S. B. André, M. Domingues, C. Marques, N. Alberto, C. Leitão, C. Tavares, A. G. Leal-Junior, A. Frizera, M. J. Pontes, P. F. C. Antunes, “From the catastrophic fuse effect to low-cost fiber sensors: SMF and POF applications,” In: *Asia-Pacific Optical Sensors Conference APOS 2018*, 2018, Matsue. *Asia-Pacific Optical Sensors Conference APOS 2018*, 2018.

[C4-P] A. G. Leal-Junior, L. M. Avellar, A. Frizera, M. J. Pontes, “Aplicação de fibras ópticas poliméricas em um sistema portátil para detecção de eventos da marcha,” In: *Encontro nacional de engenharia biomecânica*, 2018, Águas de Lindóia. *Anais do encontro nacional de engenharia biomecânica - ENEBI 2018*, 2018.

[C5-P] A. G. Leal-Junior, A. Frizera, C. Marques, M. J. Pontes, “Water-oil interface level sensor based on FBG-embedded multi-diaphragms system,” In: OSA 26<sup>th</sup> International Conference on Optical Fibre Sensors OFS-26, 2018, Lausanne.

[C6-P] A. Leal-Junior, A. Frizera, M. J. Pontes, “Hysteresis compensation technique for POF curvature sensors. In: 25th International Conference on Optical Fiber Sensors”, 2017, Jeju. org.crossref.xschema.\_1.Title@fb5d188, 2017. p. 103232U.

[C7-P] A. G. Leal-Junior, G. Santi, L. Valencia, A. Frizera, M. J. Pontes, C. Munaro, “Sistema para Medição de Ângulos Baseado em Fibra Óptica Polimérica e Giroscópio,” In: SBAI 2017 - Simpósio Brasileiro de Automação Inteligente, 2017, Porto Alegre. Anais do Simpósio Brasileiro de Automação Inteligente - SBAI 2017, 2017. v. 1. p. 1-6.

[C8-P] L. M. Avellar, A. G. Leal-Junior, T. Botelho, A. Frizera, “Sistema Embarcado para Análise de Parâmetros Cinéticos e Cinemáticos do Pé Durante a Marcha,” In: SBAI 2017 - Simpósio Brasileiro de Automação Inteligente, 2017, Porto Alegre. Anais do Simpósio Brasileiro de Automação Inteligente - SBAI 2017, 2017. v. 1. p. 1-6.

[C9-P] A. G. Leal-Junior, L. Valencia, A. Frizera, M. J. Pontes, “Sensor Fusion between Inertial Measurement Units and Polymer Optical Fiber Curvature sensors for Joint Angle Assessment,” In: IX Congreso Iberoamericano de Tecnología de Apoyo a la Discapacidad, 2017, Bogotá. Actas del IX Congreso Iberoamericano de Tecnología de Apoyo a la Discapacidad, 2017. v. 1. p. 88-94.

[C10-P] A. G. Leal-Junior, A. Frizera, M. J. Pontes, “Polymer Optical Fiber Curvature Sensor: a Review and Hysteresis Analysis,” In: XXI Congresso Brasileiro de Automática - CBA 2016, 2016, Vitória-ES. Anais do XXI Congresso Brasileiro de Automática - CBA 2016, 2016. p. 1-6.

### 1.3.3. Book Chapters

[B1-P] A. G. Leal Junior, L. Webster, A. Frizera, M. J. Pontes, “Quasi-static Tests on a Low Cost Polymer Optical Fiber Curvature Sensor,” Biosystems & Biorobotics. 1ed.: Springer International Publishing, 2017, v., p. 1427-1431.

[B2-P] A. G. Leal Junior, A. Frizera, C. Marques, M. J. Pontes, “Development of Polymer Optical Fiber Sensors for Lower Limb Exoskeletons Instrumentation,” Wearable Robotics: Challenges and Trends. 1ed.: Springer International Publishing, 2019.

[B3-P] A. G. Leal Junior, A. Theodosiou, A. Frizera, M. Domingues, C. Leitão, K. Kalli, P. André, P. Antunes, M. J. Pontes, C. Marques, “Polymer Optical Fiber Sensors Approaches for Insole Instrumentation,” Wearable Robotics: Challenges and Trends. 1ed. Springer International Publishing, 2019.

[B4-P] A. G. Leal Junior, D. Vilarinho, M. F. Domingues, A. Theodosiou, C. Tavares, N. Alberto, C. Leitão, K. Kalli, A. Frizera-Neto, P. Antunes, P. André, C. Marques, “Fiber Bragg gratings based sensors for foot plantar pressure analysis,” Biodevices 2018 (submitted in 06-08-2018)

## 1.4. Organization of the Thesis

This Thesis is divided into six chapters as follows. Chapter 1 presents the motivation and introductory aspects of the works developed in this Thesis.

Chapter 2 provides the theoretical background of this work. Some knowledge prior to the understanding of following chapters, such as optical fiber properties, materials and state of the art review are presented in this chapter.

Thereafter, an overview of polymers viscoelasticity and the characterization of the fibers used in the remainder of the Thesis are presented in Chapter 3, where the dynamic mechanical characterizations are performed on the PMMA fibers in order to evaluate their viscoelastic properties and dependency with parameters such as temperature, humidity and frequency. In this chapter the characterization of the CYTOP fibers is also presented, where the material response of this fiber is analyzed with respect to frequency and temperature and the fiber glass transition temperature is also discussed. In addition, the effect of the grating inscription (using fs laser at 517 nm) on the material properties is also assessed in Chapter 3.

In Chapter 4, the development of intensity variation-based sensors is depicted, where the analytical model, design parameters and compensations techniques are discussed and validated.

Chapter 5 presents the development of FBG-based sensors inscribed in CYTOP fibers. The analyses of the thermal treatments and compensation techniques on the response of temperature, strain, force and curvature sensors are performed.

Applications in wearable robots, movement analysis and SW are presented in Chapter 6 using intensity variation-based sensors. Then, also in Chapter 6, FBG arrays are applied on lower limb exoskeleton for human-robot interaction forces assessment, series elastic actuator's (SEA) spring for multipoint torque/strain measurements and on a SW for multiparameter sensing, where the parameters include strain, temperature, vibration, gait temporal parameters and force.

Finally, in Chapter 7, the conclusions are outlined and future works as well as new research topics are presented and discussed.

## Chapter 2. Theoretical Background

### 2.1. Polymer Optical Fibers Overview

Solid core POFs have a circular cross-section with three layers: the core, cladding. In addition, commercial solid core fibers also have a jacket (or overcladding). Most of the optical signal is propagated through the core section, which has a higher refractive index than the cladding. Light intensity losses happen due to absorption and frustrated total internal reflection when in contact with a surface [66]. For this reason, the core is surrounded by a cladding layer with a refractive index lower than the one found at core. The jacket provides mechanical protection for the POF and it is usually made of polyethylene [75]. Figure. 2-1 shows the POF cross sectional area of a solid core fiber.

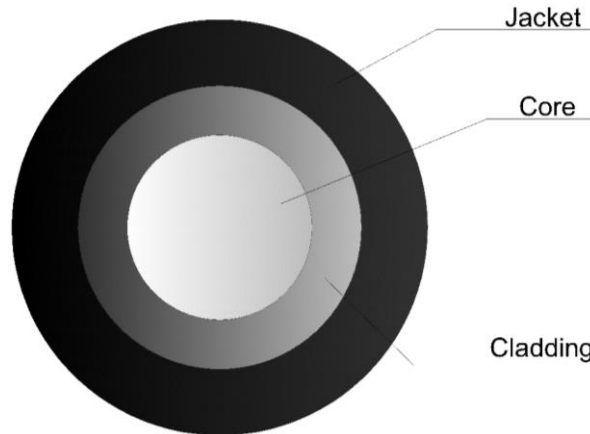


Figure. 2-1 Cross-sectional view of a polymer optical fiber (figure out of scale).

The light propagates with total internal reflection in an optical fiber and it follows the well-known Snell law presented in Eq. 2.1.

$$\frac{\sin(\theta_i)}{\sin(\theta_t)} = \frac{n_2}{n_1} \quad (2.1)$$

where  $n_2$  is the refractive index of the more refractive medium, whereas  $n_1$  is the refractive index of the less refractive medium. Furthermore,  $\theta_i$  is the incidence angle and  $\theta_t$  is the transmitted angle. The Snell law can be applied to estimate the critical angle of the light propagation inside the fiber, which is the incident angle when the transmitted angle is  $90^\circ$ .

Moreover, in an optical fiber, only the light rays with angles lower than the acceptance angle are propagated inside the fiber. The acceptance angle ( $\theta_{\max}$ ) is a function of the core refractive index ( $n_{co}$ ), external refraction index ( $n_{ext}$ ) and the critical angle ( $\theta_c$ ) as shown in Eq. 2.2.

$$\frac{\sin(\theta_{\max})}{\sin(\theta_c)} = \frac{n_{co}}{n_{ext}} \quad (2.2)$$

Additionally, the acceptance angle is important to determine the optical fiber numerical aperture (NA) which is the sine of the acceptance angle and it represents the amount of light that an optical system can receive through the acceptance cone [76]. POFs have higher NA than silica fibers. POFs have higher signal attenuation and higher modal dispersion, which leads to smaller bandwidth, since there is a time difference between the light propagation with angles close to  $0^\circ$  and propagation with angles close to the critical angle [66].

The core has two major types of refractive index profiles: step index profile (SI) and graded index profile (GI). In a step index profile, the core is homogenous and presents a uniform refraction index. On the other hand, graded index profile fibers have a distribution gradient of the core refractive index, which increases with the distance between the fiber axis and its extremity. Moreover, due to this refractive index variation in a GI

profile, the ray propagation does not occur in a straight line [66]. Figure 2-2 shows a comparison between SI and GI profiles, where perfluorinated POFs with GI profiles have lower power attenuation than SI POFs. However, the fabrication of such GI profile is more costly than the one of the SI. There is also a multistep profile created to present an alternative to the GI profile, which is difficult to manufacture. This fiber presents a multi-layer profile and every layer has its own refractive index, resulting in a non-straight ray propagation [76].

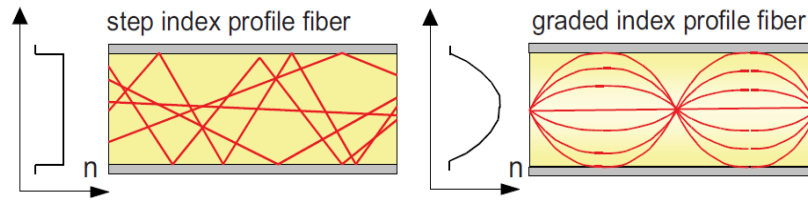


Figure 2-2 Comparison between SI and GI profile [76].

The high attenuation is the main drawback of the PMMA POFs compared with silica fibers, as mentioned earlier in this document, since higher numerical aperture leads to a higher attenuation. There are two mechanisms for the light attenuation in an optical fiber: extrinsic and intrinsic processes. Intrinsic losses are inherent of the fiber composition. The two major intrinsic losses are radiation absorption due to electronic transitions on the atomic bonds and Rayleigh scattering, which is determined by fluctuations on the material composition, density, and orientation, which happen due to the material anisotropy [66]. Extrinsic losses are caused by factors that can be controlled (but not always eliminated) in the manufacture process, installation or by environmental control. The most common extrinsic losses are caused by impurities absorption, micro fractures, structural imperfections and radiation losses due micro and macrobends [76].

Optical fibers are also classified in single mode and multimode waveguides. This classification relates the number of propagation modes inside the fiber. An optical fiber is multimode if its normalized frequency is higher than 2.405, otherwise it is single mode [76]. Equation 2.3 presents the normalized frequency ( $V$ ) as a function of the core radius ( $a$ ), wavelength ( $\lambda$ ) and numerical aperture ( $NA$ ).

$$V = \frac{2\pi a}{\lambda} NA \quad (2.3)$$

The number of modes ( $N$ ) on a step index fiber is presented in Eq. 2.4.

$$N_m = \frac{V^2}{2} \quad (2.4)$$

Typical value of the number of modes for wavelength of 650 nm is 2.8 million in a conventional step index POF with PMMA core with 0.98 mm of diameter [76]. Each mode represents one particular solution of the Maxwell equation. Since it has so many modes and POF sensor generally do not have long lengths of fiber, the geometrical optics approach can be employed on the sensor analysis [66].

Contrasting with the aforementioned solid core POFs, microstructured polymer optical fibers (mPOFs) present a pattern of holes throughout the fiber [77], [78]. Such pattern has a defined geometry and pitch between the holes, where the ratio between the hole diameter and pitch defines its modal operation. If the ratio between the hole diameter and pitch is lower than 0.43, the mPOF is endlessly single-mode [26], which means that the POF is single mode at all frequencies [80]. Another advantage of mPOFs is the possibility of holding gas or a biological sample in the holes for evanescent-wave sensing [81]. For these reasons, mPOFs are extensively employed in different sensing applications, especially those involving FBGs due to their endlessly single-mode operation [76], [82], [83]. A typical mPOF made of PMMA with 3 ring hexagonal structure is shown in Figure 2-3. In addition, the first single mode POF was proposed in 1991 by [84]. Then, after some years of research - summarized in the review work by Zubia and Arrue [75], a single mode step index POF was reported in [85], which had a core made of TOPAS and a cladding of Zeonex for humidity insensitive and high temperatures operation when compared to other POFs, where the operating temperature is lower than 110°C [85].

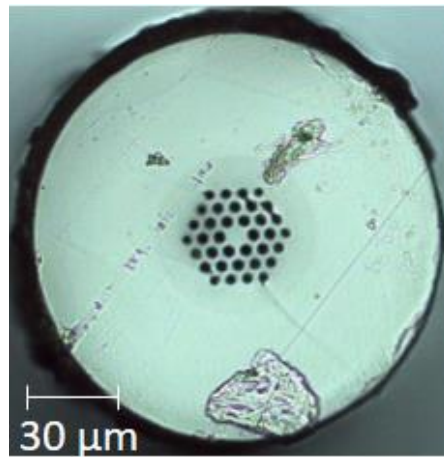


Figure 2-3 Cross-sectional view of the mPOFs with 3-rings hexagonal structure [86].

Of all POF materials, PMMA is yet the most employed material in POF production [87]. However, PMMA has a low glass transition temperature ( $T_g$ ) compared to some of the other polymer materials for fiber fabrication, such as polycarbonate (PC), which can limit its application at higher temperatures [88]. Furthermore, the higher moisture absorption capability of PMMA can harm its application in temperature or strain sensing where a humidity cross-sensitivity is undesirable [80].

In order to mitigate the issue of humidity cross-sensitivity, POFs made of cyclic olefin copolymer such as TOPAS grade 8007 [80], [89] and 5013 [79], [85] and cyclic olefin homopolymer such as Zeonex 480R [90] can be employed. Gratings inscribed in fiber made of these materials demonstrated a humidity sensitivity at least 30 times lower than that of PMMA polymer optical FBGs (POFBGs). However, the glass transition temperature can vary significantly among different grades of TOPAS. For instance, TOPAS 8007 presents  $T_g$  of only 78°C, which is even lower than the PMMA glass transition temperature (110°C) [89] and which implies that fiber cleaving parameters are quite different for POFs made of PMMA and TOPAS [91]. The low glass transition temperature of TOPAS 8007 fibers severely limits the range of temperature sensing. In order to overcome this, POFs made of another grade of TOPAS with a  $T_g$  of 134 °C was demonstrated [79], [85]. Another polymer material employed for high temperature and strain sensing is Zeonex 480R, which has a  $T_g$  of 138°C. Zeonex 480R material presents further advantages compared to TOPAS 5013 such as superior drawability that allow a more robust fabrication of microstructures in the fiber [90].

Both TOPAS and Zeonex have low loss at THz frequencies and have been applied extensively in this field as well [92]–[94]. In addition to the aforementioned POF materials, PC polymer can also be used for fiber fabrication [95]. PC has a  $T_g$  of 145°C, which is higher than TOPAS 5013 and Zeonex 480R [88]. Furthermore, PC POFs can withstand higher stresses when compared with PMMA and TOPAS POFs [88]. For these POFs, the use in the 1550 nm region is limited to a few centimeters and, for this reason, most of POFBGs are inscribed in the 850 nm wavelength region [57]. In order to tackle the limitations imposed by the higher attenuation of POFs, graded-index CYTOP fibers have been proposed [73]. In CYTOPs, the carbon-fluoride bonds replace carbon-hydrogen in the polymer backbone, resulting in much lower losses in near infrared (especially in 1550 nm) when compared with PMMA POFs [73]. In addition, this material also has low dispersion [73] and these advantages have led to the rapid widespread of CYTOPs as commercial solutions for POFs. Since these are the POFs used in this Thesis, Figure 2-4 shows the attenuation of the PMMA and CYTOP fibers, the silica fiber's attenuation is shown for comparison purposes.

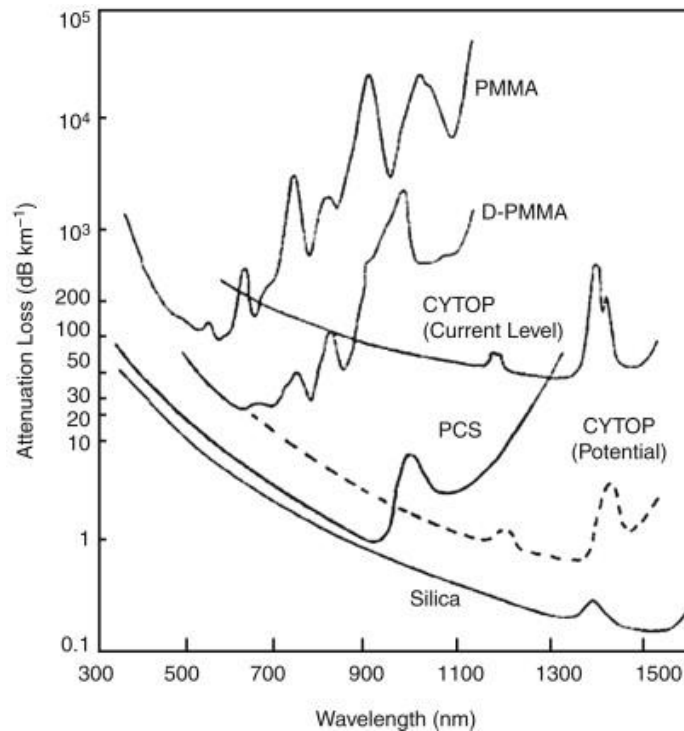


Figure 2-4 Attenuation (in dB/km) of PMMA and CYTOP fibers

## 2.2. POF-based Sensors

The application of optical fibers as sensors has been studied throughout the years. There are several applications of optical fiber sensors in different fields such as SHM [96], industrial processes [42], biomedicine [43] and detection of chemical compounds [97]. Even though there are many other sensing approaches using optical fibers (such as interferometers [98], nonlinear effects [64] and surface Plasmon resonance [99]), this section is focused on the developments of intensity variation- and FBG-based sensors, since they are the ones used in this Doctoral Thesis.

### 2.2.1. Intensity Variation-based Sensors Review

Regarding intensity variation-based POF sensors, they can be employed to evaluate the beam dispersion and phase deviation for measurement as in a turbidity sensor [66]. However, most of the POF intensity variation-based sensors take advantage of the polymer flexibility to measure the transmission losses on a bending fiber. Both macro and microbending power losses are applied for sensing applications. Fegadolli et al. [100] take advantage of microbending power loss to develop force detection platform. The rectangular platform is comprised of a lower fixed plate and an upper movable plate, both fixed and moving plates have cylindrical rods placed throughout its length. The optical fiber lies between the two parts, when force is applied on the movable part, the POF is squeezed and the signal attenuation is detected and processed. Applying the same work principle, Chen et al. [101] proposed a breathing sensor. The sensor is embedded on seat cushion or bed and detects the body vibration during breathing. The sensor proven to be capable of detecting body vibration with maximum error of the frequency measurement less than 0.2 Hz and the frequency measurement range can be up to 2000 Hz. The same principle of the microbending sensor can be employed for macrobending POF sensor. Kuang et al. [102] developed a dual cyclic bending based sensor to measure displacements. The working principle and sensor configuration is the same as proposed by [101] and [100], but with larger dimensions. It was also investigated the relationship between plates' displacement and force applied on the plates, power loss relationship with number of rollers, rollers radii and curvature radius. Furthermore, it was obtained the curvature radius variation with the plate's relative displacement. All the results obtained proved the feasibility of this sensor for measuring the displacement in industrial applications.

Another industrial application for POF based sensor is the liquid level measurement. Hou et al. [103] designed and tested a liquid level detection fiber, which comprises of two twisted in parallel POFs without the cladding and jacket parts. One of the fibers receives the light and another one is a passive fiber. Since the two fibers are bended, a radiation loss occurs, and the light is transmitted to the passive fiber. A 660 nm light

emitting diode (LED) is placed at one end of the active fiber, at the other end is placed a power meter. While the passive fiber has a power meter at both ends. The forward coupling power is measured in the passive fiber. The power meter response on the active fiber end can compensate the input power deviations, which is a measurement error source if it is not compensated. Differences in the environment refractive index cause a variation on the forward coupling power, therefore the sensor is able to detect if it is immersed on water. The same configuration for a liquid level sensor is presented in [104]. Furthermore, a calibration curve correlating the forward coupling power and the liquid level for three different media was obtained in this work. Moraleda et al. [67] developed a macrobending based temperature sensor. The working principle is based on variations of the optical fiber numerical aperture due to bending radius and temperature changes. If the bending radius is constant, the changes on the numerical aperture are caused by the temperature. The sensor works between 27.2 °C and 50.2 °C with a sensitivity for a 2 mm bend radius of  $1.29 \times 10^{-3} \text{ } ^\circ\text{C}^{-1}$ .

SHM is also an important application for POF based sensors. Antunes et al. [105] presented an accelerometer based on the misalignment between two POF. One fiber is fixed on an inertial mass supported by an L-shaped aluminum cantilever beam, which is connected to a support through a leaf spring. The other fiber is fixed directly on the support. Furthermore, the fibers have a relative displacement of 0.5mm in the vertical direction. External acceleration is encoded by measuring the change of the fibers coupling efficiency caused by additional misalignment between the two fibers due to the inertial mass movement under external acceleration. Results proved the suitability of this sensor for civil engineering SHM applications. Vallan et al. [106] developed a macrobending curvature sensor positioned on a cantilever. In order to achieve curvature pattern in the cantilever, a shaker is positioned on a rectangular cantilever tip. The sensor characterization exhibits a 454 mV/m sensitivity and maximum detectable curvature radius of about 284 m. In [107], the POF curvature sensor was investigated in a trapezoidal cantilever.

As mentioned earlier, biomedical and rehabilitation applications with POF sensors have been widely studied. Dunne et al. [108] developed a wearable garment-integrated curvature sensor for monitoring the seated spinal posture and a two-leaved decision tree model for posture classification evaluates the subject posture. System posture classification is compared with the classification from a visual analysis of professionals. However, the lack of agreement between the eight professionals presents a problem for system evaluation and for long-term monitoring of seated posture. Williams et al. [109] also investigates the spinal curvature. The investigation is limited to lumbar curvature though. Results of the lumbar monitoring are compared to a video-based method and good accuracy is obtained. Donno et al. [110] developed a POF goniometer capable of measure higher angles (up to 90°). Dynamical tests were conducted in three frequencies: 0.1Hz, 1.25Hz, and 5Hz with good correlation between the POF sensor and the reference potentiometer. The proposed goniometer can be applied for knee joint angle measurement by athletes to test and train their exercises and to physiotherapy rehabilitation. Bilro et al. [111] presented a similar approach to knee angle monitoring. However, the sensor is characterized in quasi-static tests and it is evaluated with a video-based system, which accounts only the movements on the sagittal plane. It was also presented the wireless prototype of this POF sensor.

One drawback of the signal intensity modulation optical fiber sensors is its larger sensitivity to external perturbations e.g. temperature, microbending, source power deviations, among others. It results on indistinguishable variation on the received signal from that produced by actual modification of the measurand [112]. Since these deviations can provide errors in measurement, self-referencing systems were developed [67], [111]. Such approach lowers the temperature, humidity and source power deviations to acceptable values (Figure 2-5). This system comprises of a sensor fiber and a reference fiber with the same properties as the sensor fiber. The sensor response is normalized with respect to the reference fiber for compensation of temperature, humidity and light source power deviations.

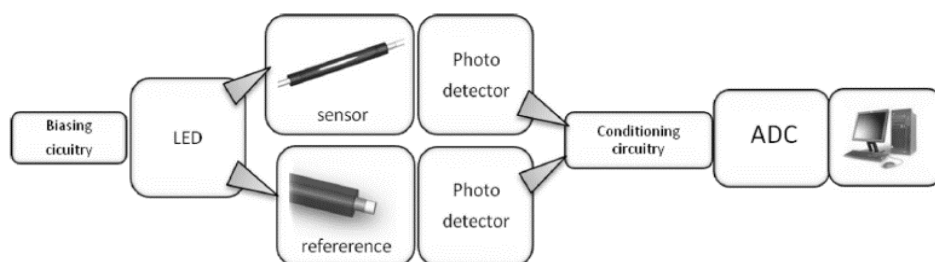


Figure 2-5 Self-referencing system for compensation of environmental and light source deviations [111].

## 2.2.2. Fiber Bragg Gratings-based Sensors Review

### 2.2.2.1. FBG Inscription in POFs

FBGs are created through a refractive index modulation when the fiber is exposed to a periodic intensity pattern (see Figure 2-6), where a specific wavelength (the Bragg wavelength) is reflected [68]; this is essentially a wavelength selective mirror. Such a grating structure can be obtained by using lasers to modify the optical fiber, and this can take several forms, such as ultraviolet (UV) laser irradiation through, holographic techniques, phase mask [68] or direct-write of the grating pattern in the fiber core using a fs laser [74]. The Bragg wavelength ( $\lambda_B$ ) depends on the material effective refractive index ( $n_{eff}$ ) and modulation period ( $\Lambda$ ) as shown in Eq. 2.5.

$$\lambda_B = 2n_{eff} \Lambda \quad (2.5)$$

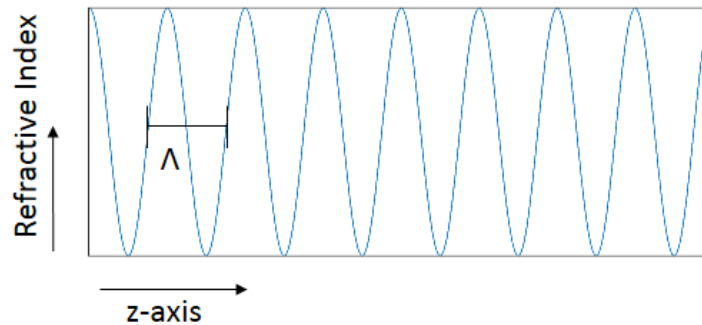


Figure 2-6 Periodic variation of the refractive index with respect to the fiber z-axis (fiber length).

Peng *et al.* reported the first POFBG inscribing with 325 nm continuous wave (CW) He-Cd and 248nm pulsed Krypton Fluoride (KrF) lasers, although a period ablation was reported with the KrF laser [113]. A typical setup for POFBG inscription is presented in Figure 2-7. As a result, He-Cd lasers were for many years the preferred option for grating inscription in POFs. At first POFBGs were inscribed in the 1550 nm region mainly due to equipment availability associated with telecommunications applications [114], [115]. However, the majority of POF has higher attenuation in the 1550 nm wavelength region and as a logical consequence grating inscription oriented itself towards lower wavelengths. Considerable progress in low cost interrogation using complementary metal-oxide semiconductors (CMOS), made inscription in the 850 nm region more attractive [80].

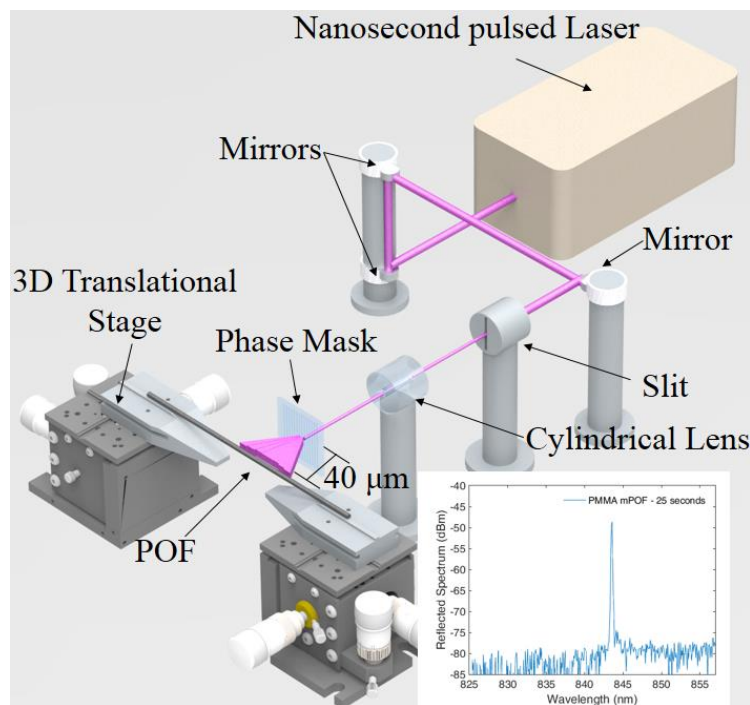


Figure 2-7 A typical phase mask technique inscription setup for POFBGs (this case using a 248 nm KrF laser). Figure inset shows a FBG inscribed using this setup.

Inscription in the 800-900 nm region using He-Cd lasers quickly became the rule and not the exception, while KrF lasers received little attention. Inscription at the beginning of the investigation of FBGs in POFs could be as long as 100 minutes and hinder commercial production due to the relatively high cost and stability requirements [116]. However, Bundalo *et al.* showed that inscription can be achieved in 7 minutes, even in microstructured fibers, while delivering improved grating stability [117].

Pre-inscription annealing has also generated further progress, as it leads to molecular alignment relaxation that reduces the internal stresses of the fiber that were generated during manufacturing [118]. Furthermore, annealed samples presented higher photosensitivity in a preform study [119]. Finally, pre-inscription annealing has been shown to reduce inscription time [119].

Dopants such as trans-4-stilbenemethanol (TS) and benzyl dimethyl ketal (BDK) can also positively influence grating production. Since the first FBG in TS doped fiber [120], TS has been shown to reduce inscription times to one second, increasing grating reflectivity and with minor etching deliver gratings with 97% reflectivity [121]–[123]. While TS is uniquely used for step-index fiber, BDK has been used to improve photosensitivity in mPOF [124]. Following on from the work of Bundalo [117], a recent advance demonstrated inscriptions in 4 minutes [124]. Pospori *et al.* have also demonstrated how the customization of inscription parameters such as annealing time can lead to more sensitive FBGs [124].

In recent years, KrF lasers are receiving greater attention since improvements in polymer photosensitivity characterization and analysis were observed. As with He-Cd lasers, pre-inscription annealing has been shown to improve the results using KrF lasers. Inscription times in the region of 7 seconds have been reported for PMMA mPOFs, a significant improvement compared to times for non-annealed samples [119]. KrF lasers intrinsically deliver lower inscription times, some as low as several ns [70]. This inscription method appears favorable towards production as a single 15 ns pulse can inscribe a grating, reducing the potential costs for mass production [59]. Following this development, pulse duration reductions were sought as this parameter was judged the new constraint, being the minimum optical power achievable for production. A Nd:YAG laser with an 8 ns pulse duration and lower pulse energy has recently been shown to have generated an FBG in BDK-doped mPOF, the current fastest time to date [125]. Indeed, the cost of this laser is approximately 5 times less than that of KrF lasers, where the maintenance costs are also lower. Figure 2-8 presents the historical evolution of the POFBGs inscription time with the phase mask technique, where some reasons or breakthroughs related to such evolution are presented. The goal here is to present the evolution inscription time reduction throughout the years.

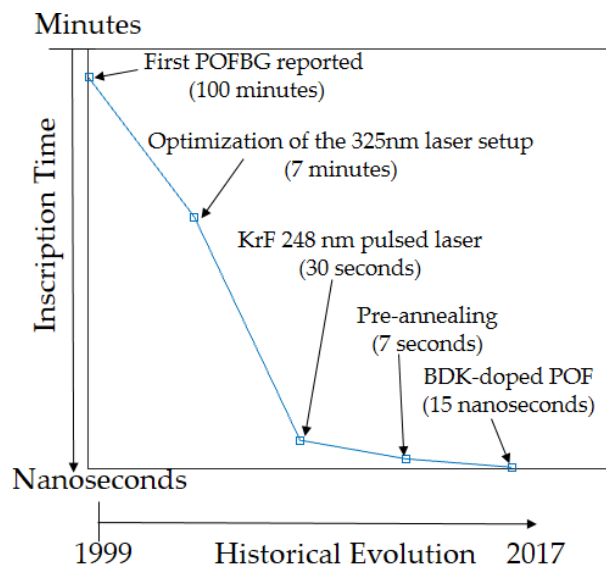


Figure 2-8 Historical evaluation of the inscription times using UV laser (CW and nanosecond pulsed).

It is noteworthy that FBGs are inscribed in other materials, such as TOPAS, Zeonex, PC and CYTOPs. Table 2-1 summarizes the latest developments for He-Cd and nanosecond pulsed lasers (KrF and Nd:YAG) for each material. While PMMA is used as the benchmark for polymer inscription, TOPAS, Zeonex and PC have all been inscribed using both laser types, with their inscription times broadly following the wake of PMMA. However, inscription in CYTOP is more difficult than for other polymers. Indeed, no CYTOP FBG has been reported to date using a He-Cd laser. The first FBG in CYTOP in the telecoms region was reported by Koerdt

*et al.* using a KrF laser [126]. However, due to their own nature with an end functional group ( $-\text{CF}_3$ ), CYTOPs have UV resistance, which hinder the POFBG inscription in such fibers using lasers in this wavelength region. Actually, the inscription time of POFBGs in CYTOP using a KrF nanosecond laser (centered at 248 nm) can be as long as 60 minutes [127].

Table 2-1 POFBG inscription times with different materials.

POF material	HeCd CW laser - Inscription time	Nanosecond pulsed laser - Inscription time
BDK-doped PMMA	4 minutes [124]	8 nanoseconds [125]
TS-doped PMMA	1 second [123]	0.4 seconds [128]
PC	6 minutes [88]	14 seconds [70]
Zeonex 480R	5 minutes [90]	15 seconds [70]
TOPAS 5013	4 minutes [79]	20 seconds [70]
TOPAS 8007	58 minutes [80]	25 seconds [70]
CYTOP	Not reported	<60 minutes [127]

Concurrently with the foregoing developments on UV lasers for grating inscription in POFs, ultrafast lasers (light pulses shorter than tens of picoseconds) have been researched, leading to the popularization of fs lasers as commercial solutions for micromachining in transparent materials[129]. In fs lasers, the FBG inscription occurs mainly by multi-photon absorption, where the carriers are excited by the absorption of photons and the energy transfer occurs from the electron to the lattice due the electron-lattice scattering [130]. This inscription mechanism results in a precise energy deposition, since the interaction between the light and matter occurs only near the focal volume of the laser beam, which results in a selective modification of the material properties, i.e., only a small volume of the material is modified [131]. In addition, the annealing of the lattice that occurs with pulse duration of nanoseconds, does not occur in ultrafast laser pulses [131]. Thus, on the fs laser FBG inscription, the thermal diffusion is suppressed as well as melting and resolidification effects, which can induce additional (and undesired) structural modifications on the material [130].

Aiming at the advantages of fs lasers in micromachining of transparent materials, Theodosiou *et al.* [74] presented a major breakthrough regarding the FBG inscription in CYTOPs using a direct write, plane-by-plane inscription method with optimized parameters, which enabled the FBG inscription in CYTOP fibers within a few minutes. In addition, the proposed technique also enables the control of the mode excitation by means of limiting the inscription to a predefined part of the fiber core, which results in a single peak FBGs, even in multimode fibers as the CYTOP [74]. This advantageous feature also enables the inscription of long FBG arrays in CYTOP fibers [69].

### 2.2.2.2. FBG-based sensors applications

In FBG-based sensors, the shift of the reflected wavelength as a function of the monitored parameter is evaluated. The FBG is intrinsically sensitive to temperature and strain, following Eq. 2.6 [132]:

$$\frac{\Delta\lambda_B}{\lambda_B} = (1 - P_e)\varepsilon + (\alpha_T + \zeta)\Delta T \quad (2.6)$$

where  $\Delta\lambda$  is the Bragg wavelength shift,  $\lambda_B$  is the Bragg wavelength,  $P_e$  is the photoelastic constant,  $\alpha_T$  is the thermal expansion coefficient of the fiber,  $\zeta$  is the thermo-optic coefficient,  $\Delta T$  is the temperature variation and  $\Delta\varepsilon$  is the strain variation. Thus, historically, the typical applications of POFBGs were generic and based on the fundamental parameters of strain and temperature. However, FBGs can be embedded in different structures to sense other parameters besides strain and temperature as discussed below.

In terms of FBG applications, Stefani *et al.* proposed an accelerometer in a PMMA mPOFBG for SHM, displaying higher sensitivity than a silica counterpart [72]. Theodosiou *et al.* demonstrated mode shape capturing using an array of CYTOP FBGs embedded in a metal beam [133]. When compared to a silica counterpart, the authors demonstrated that the POFBG array had a sensitivity up to 6 times greater. A similar application was presented by the same group for a rear helicopter rotor blade, measuring imbalance on the cantilever [44]. The sensors were used to measure the vibration due to imbalances created by loadings positioned at different regions of the cantilever.

POFBGs have also been embedded into patches produced using 3D printing, which is highly relevant for plug-and-play devices [134]. POFBGs embedded within a silicone diaphragm were also used for liquid level measurement, showing a system delivering multi-level measurement [135]. A comparable silica sensor had a

sensitivity 5 times lower than the POF sensor. Then, the sensor was used to compensate some issues associated with conventionally employed sensors, including fuel density sensitivity, temperature and g-force variations [136]. This work could lead towards similar applications in the oil and gas industry where liquid level, temperature, pressure and flow are important monitoring parameters [137]. The pressure response of POFBGs inscribed in CYTOP fibers was demonstrated in [138], where again POF outperformed silica fibers in terms of sensitivity.

Curvature sensors have been proposed by Chen *et al.* [139], who demonstrated angle measurements using an FBG in eccentric core PMMA fiber. This type of sensor can be suitable for gait measurements, where both the angular range and frequencies are within the range for the lower limbs. In addition, gait and movement analysis has been extensively considered in recent years, with another viable example in [50]. In this instance, an array of 5 FBGs were embedded in an insole for plantar pressure monitoring and subjected to static and dynamic testing. The response was in good agreement with the calibration system and the expected behavior during use.

Humidity sensing has been much more explored, as an inherent property of some polymers as characterized in [140]. For POFBGs, the water affinity of the fiber introduces a significant Bragg wavelength shift and, as a result, the wavelength-encoded response is immune to fluctuations in light source and transmission loss. POFBGs do not need any coating or corrugation for humidity sensing and are robust, compact and cost-effective. However, water absorption is very slow and response time remains a key issue for practical applications. It has been shown that etching the fiber (i.e. reducing its diameter) with acetone lowers the response time below the 7-minute threshold [141], where the lowest response time reported is below 10 seconds [48].

A final example of an interesting application is given by Bonefacino *et al.* [142], who presented a POFBG sensor for breathing rate and heartbeat that is worn on the chest of the subject. The methodology in question was shown to be 20-30 times more sensitive than a silica version of the sensor. It is important to mention that FBGs in POFs was also investigated in ultrasonic detection [143] and in radioactive environments [144]. Figure 2-9 summarizes the application fields for optical fiber sensors using POFBGs.

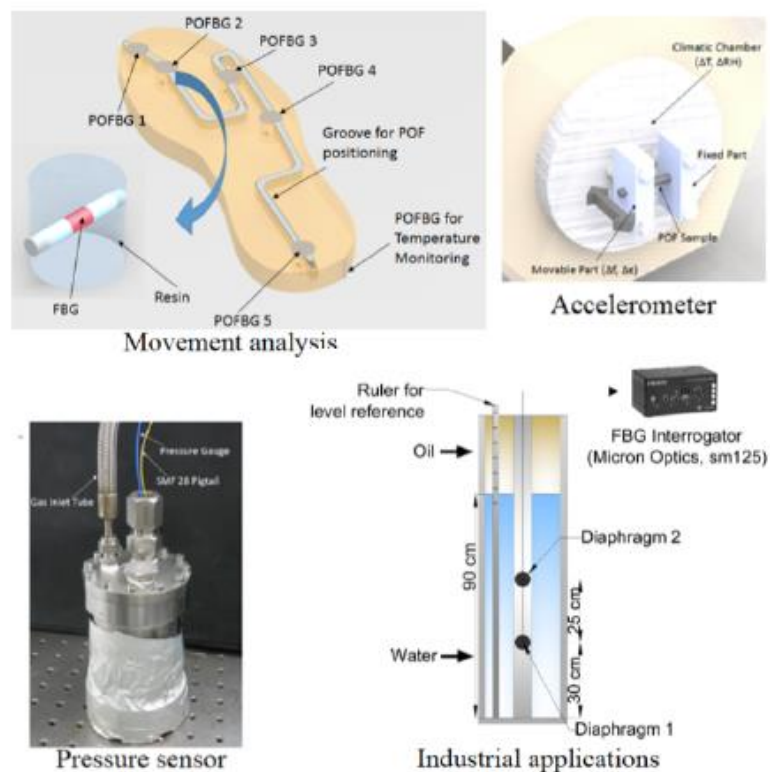


Figure 2-9 Application fields using FBGs inscribed in POFs.

## Chapter 3. Mechanical Characterization of Different POFs

### 3.1.Introduction

In this chapter, the dynamic characterization is performed on PMMA and CYTOP fibers used on the development of the intensity variation- and FBG-based sensors, respectively. The results show the material mechanical properties dependency with parameters such as temperature, frequency of strain cycles and humidity. Furthermore, the creep response at different loadings indicate the possibility of applying viscoelastic models for the POF modeling, where the hysteresis on stress-strain cycles is also demonstrated. Since the CYTOP fiber is used on the FBG inscription, its characterizations are made in two different regions of the same fiber: one without the FBG and the other in the region where the FBG was inscribed to investigate the influence of the FBG inscription (via fs laser) on the POF mechanical properties.

### 3.2.Dynamic Mechanical Analysis

In order to characterize the mechanical properties and polymers viscoelastic response, dynamic characterization tests are performed. The dynamic characterization tests are widely employed for polymers in biological applications [145], automotive [146], aircraft [147], industrial [148], among others. Dynamic tests on polymers can be made by means of nano-indentation techniques [149] and dynamic mechanical analysis (DMA) [150]. Nano-indentation techniques are more suitable for the evaluation of thin films and microstructures. Moreover, it is also applicable to the assessment of local properties of the polymer [149]. Therefore, the DMA technique is a suitable technique due to the fiber dimensions on the order of millimeters. DMA applies an oscillatory load on the polymer with specific temperature and frequency ranges. It is a well-established method to evaluate the polymer glass transition, storage modulus, loss modulus, and stress relaxation [150], which are sufficient parameters to characterize the POF viscoelastic response.

These parameters include the storage modulus ( $E'$ ), loss modulus ( $E''$ ) and relaxation time ( $\tau$ ), which are sufficient to determine the viscoelastic behavior of the material [59]. The combination of the storage and loss modulus is the dynamic Young's modulus ( $E^*$ ) of the polymer (see Eq. 3.1).

$$E^* = E' + iE'' \quad (3.1)$$

The ratio between the storage and loss modulus is the loss factor ( $\tan(\delta)$ ) defined in Eq. 3.2. This is a ratio between the dissipated energy and the storage energy per cycle of applied load.

$$\tan(\delta) = \frac{E''}{E'} \quad (3.2)$$

The analysis of the loss factor  $\tan(\delta)$  presents some advantages over the analysis of the loss modulus. The Young's modulus is divided into the loss and storage modulus due to the duality of a viscoelastic response, which is the combination of the elastic and viscous responses of the polymer. The loss modulus refers to the energy loss due to the viscous effect, whereas the storage modulus refers to the energy storage due to the elastic effect. Therefore, the loss modulus may be understood as the relationship between the viscous and elastic components of the polymer response. For this reason, the loss factor of an elastic material is zero ( $\tan(\delta)=0$ ) and the Young's Modulus is referred as a static Young's Modulus ( $E_0$ ).

If there is no phase transition and the material is in the linear viscoelastic regime for a given temperature range, it is possible to apply the time-temperature superposition (TTS) principle to estimate the material viscoelastic parameters in a range higher than the DMA equipment operation limits [151]. Following the TTS principle, the superposition of frequency and temperature curves are made using a horizontal shift parameter ( $a_T$ ), which is estimated through the Williams-Landel-Ferry equation (Eq. 3.3):

$$\log(a_T) = \frac{-C_1(T - T_r)}{C_2 + (T - T_r)}, \quad (3.3)$$

where the empirical constants  $C_1$  and  $C_2$  are adjusted to fit the  $a_T$  values, whereas  $T$  is the temperature and  $T_r$  is a reference temperature.

The dynamic mechanical analyzer employed on the tests of this Chapter is the DMA 8000 (Perkin Elmer, USA), where the tests for Young's modulus estimation were made following ISO 527-1:2012, which is the standard recommended for Young's modulus estimation in polymers [152]. In addition, the dynamic characterizations were made following ASTM D4065 standard for DMA testing in polymers [153]. The length and width of the DMA's clamps (see Figure 3-1) are about 22 mm and 5 mm, whereas mass of the clamps is about 6 g. The sample length on the tests is about 20 mm. The analyzer also has a climatic chamber with a heater to isothermal tests and tests with temperature increase. The software of the analyzer saves the results on .xls format that is further processed and analyzed in a Matlab tool. The fiber fixation is shown in Figure 3-1.

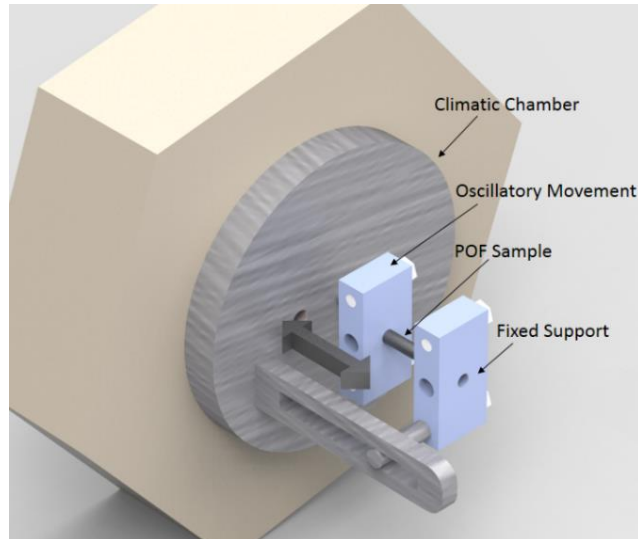


Figure 3-1 Schematic view of the POF sample positioning in the DMA.

### 3.3. DMA on PMMA Solid Core POF

The experimental analysis of this Section includes the temperature scan from 0 to 130°C to evaluate the changes of the polymer properties with this parameter and the glass transition of the fiber. In addition, a frequency scan is made on different temperatures (25°C to 45°C with steps of 5°C), where it is possible to obtain the variation of the viscoelastic properties on the polymer with the frequency and the temperature through the TTS principle [154]. Finally, creep recovery experiments are made on the fiber in order to obtain the POF relaxation time and the dependency of the viscoelastic parameters with the stress rate. After characterizing the POF properties, the strain tests are made to obtain its stress response, which shows a hysteretic response giving guidelines for the dynamic compensation technique for POF sensors developed in the next chapters (see Chapter 4 and Chapter 5).

Three temperature sweeps are made with different samples, the range of these tests are between 0°C and 130°C. The lower limit is chosen not only to start the test with the materials of the POF below its glass transition temperature, but also to present a broader view of the material behavior in lower temperatures. The upper limit is close to the fusion point of the fiber and higher than the fiber  $T_g$ . The employed frequency is 1 Hz and a constant displacement amplitude of 0.05 mm (in order to guarantee the stress-strain curve in the linear region) is applied to obtain a constant strain rate. Figure 3-2 shows storage modulus and the loss factor with respect to the temperature for the PMMA solid core POF. This experiment shows a  $T_g$  of the PMMA on a temperature higher than 100°C, where the storage modulus is low (below the analyzer resolution) and the loss factor is high (above 1.9).

Although the POF manufacturer established an operation range between -40°C and 85°C, an operation limit between 24°C and 60°C is suitable for dynamic sensors applications as it coincides with the two transitions of the fiber, i.e.,  $\alpha$ -transition (about 20°C) and  $\beta$ -transition at 65°C. Since  $\tan(\delta)$  is the ratio between the storage and loss modules, as presented in Eq. 3.2, the storage modulus is almost ten times higher than the loss modulus on temperatures between 5°C and 25°C (see Figure 3-2). Such difference is caused by the lower movement of the polymer molecules, leading to the decrease of friction between them that causes the increase of the storage energy [59], which in this case is almost ten times higher than the dissipated energy. For this reason, the POF curvature sensor presents an elastic behavior even in temperatures below 25°C, which enables its application in dynamic measurements in temperatures below the glass transition presented.

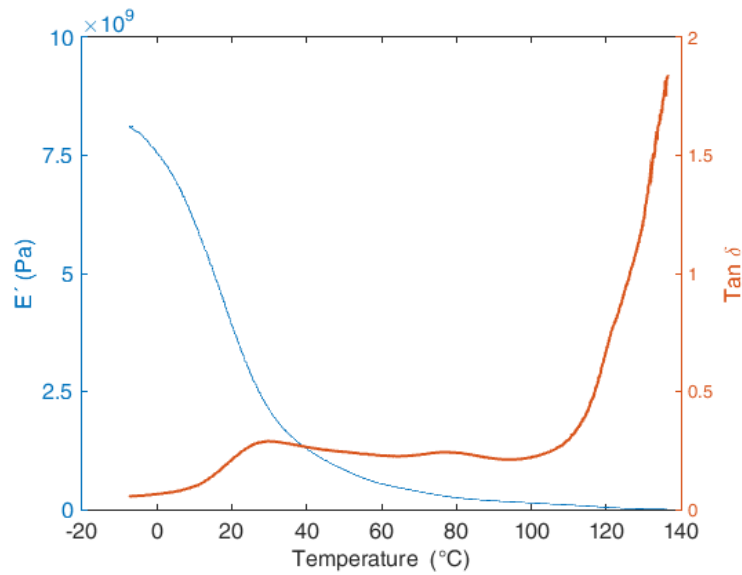


Figure 3-2 Temperature sweep on the solid-core PMMA fiber.

After the determination of the temperature effect over the viscoelastic parameters, the frequency is also evaluated by performing a frequency sweep on the fiber. The frequency range is between 0.01 Hz and 21 Hz and each sweep is performed at a constant temperature. The lower bound of the test (0.01 Hz) is limited by the analyzer resolution, whereas the upper bound of 21 Hz is sufficiently large to cover the frequency of movement for applications of wearable sensors in human joints [155]. The employed temperatures were 25°C to 45°C on steps of 5°C, which is the range of temperatures within the human skin thermal comfort [6]. The combined analysis of the temperature and frequency effects enable the application of the TTS principle. According to this principle, there is an interchangeability between the variation of the temperature and frequency over the viscoelastic parameters [151]. Figure 3-3 shows the results of the frequency scan test for the storage modulus. There are five curves, one for each temperature. Since there is only an offset with the temperature raise, the materials of the analyzed POF are thermo rheological simple [59] and it is possible to apply the TTS principle (see Section 3.2).

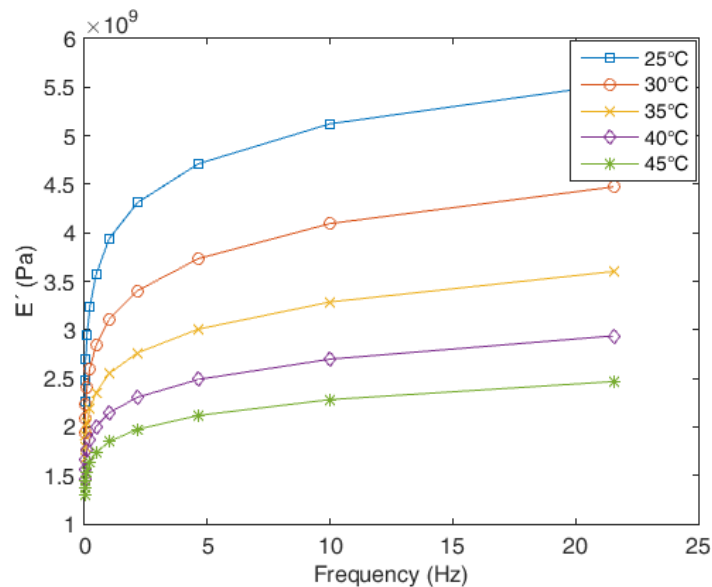


Figure 3-3 Storage modulus for frequencies between 0.01 Hz and 21 Hz with different temperatures.

The next step on the fiber characterization is the creep recovery test, which comprises of applying a constant stress on the fiber with constant frequency and temperature. This test is employed to obtain the polymer relaxation time. In order to evaluate the relaxation time dependency with the stress or strain rate, the creep recovery test is made with different load conditions. In this case, four tests are made with loads of 0.5 N through 2 N on steps of 0.5 N. The frequency of this test is 1 Hz and the test is made at room temperature.

In order to enable the analysis of the relaxation, the input and output are normalized with respect to its mean value. Hence, it is possible to obtain the POF relaxation time for each test. The difference between the curves obtained for each load is its amplitude on strain response. The difference between the maximum and minimum of the normalized strain measured on the test with 0.5 N is 0.058. This difference increases as the force applied on the test increases until it reaches 0.17 on the test with 2 N load. Figure 3-4 shows the results for the test with different loads, where the error bars are related to the precision of the DMA sensors. Similar results are found on the literature [156].

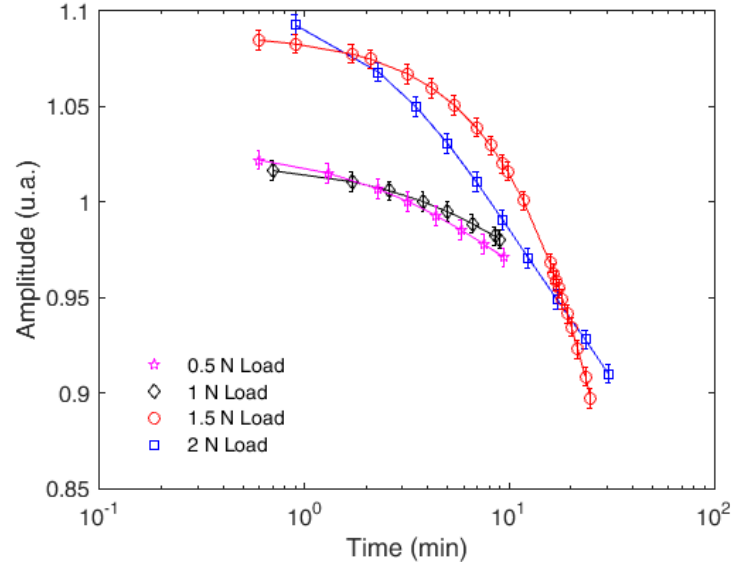


Figure 3-4 POF creep recovery tests with loads of 0.5 N to 2 N.

As presented in Figure 3-4, an exponential fit is made on each curve of the creep recovery tests and the POF relaxation time is the time constant obtained on these exponential approximations. Since there are two different materials, polyethylene and PMMA, the performed exponential regression is a sum on two exponentials, one may be related to the PMMA relaxation and the other to the polyethylene, as presented in Eq. 3.4:

$$\varepsilon = y_1 e^{(\tau_1 t)} + y_2 e^{(\tau_2 t)}, \quad (3.4)$$

where  $\varepsilon$  is the strain,  $t$  is the time,  $\tau_1$  and  $\tau_2$  are time constants.  $y_1$  and  $y_2$  are the weights of each exponential. This approach is similar to the Prony series, which is employed for the estimation of the polymer relaxation [59].

The first relaxation time ( $\tau_1$ ) obtained is  $4.89 \pm 1.61$  seconds, whereas, the second relaxation time ( $\tau_2$ ) is  $273.46 \pm 202.54$  seconds. Since it is closer to the one obtained in the literature, the first relaxation time may be related to the PMMA [156] and the second to the polyethylene (jacket of the PMMA POF). However, the relaxation time is not constant either. For this reason, the viscoelastic material does not have a unique relaxation time, it has a range of relaxation times [156]. This behavior of the polymer also can be a source of its hysteresis. The polyethylene presents higher relaxation time than the PMMA and will also present a range of relaxation times proportionally higher, which can explain the higher variation of the polyethylene relaxation time. In addition, the temperature also influences the relaxation time of some polymers [59], which can be the case of the polyethylene, since there is a variation of about  $0.5^\circ\text{C}$  on the tests with 0.5 N and 1.5 N.

The material hysteresis is shown in the strain scan tests that were carried out. The test comprises of applying cycles of strain on the fiber with constant temperature and frequency. The strain cycle is defined as displacements of the movable part of the analyzer, which are related to the strains of 0.1% to 1%. The lower bound of the test is due to the analyzer resolution, whereas, on strains higher than 1%, the PMMA starts to present a highly nonlinear behavior [41], since Young's modulus analysis requires that the material is on its linear region of the stress-strain curve [154]. The employed frequency is 1 Hz and the temperature is about  $29^\circ\text{C}$  (room temperature). The relation between stress and strain and the viscoelastic parameters is analyzed. Figure 3-5 shows the stress response for two strain cycles. The hysteretic behavior of the fiber is clear on the two cycles. Both cycles present similar hysteresis and the obtained hysteresis is similar to the one presented for viscoelastic materials reported in [151]. Similar hysteresis is found on the analysis of the storage modulus

and loss factor. For this reason, one way to model this hysteretic behavior of the polymer is based on the differences between the loss factor and relaxation time in loading and unloading curves, which will be explored in Chapter 4 and Chapter 5.

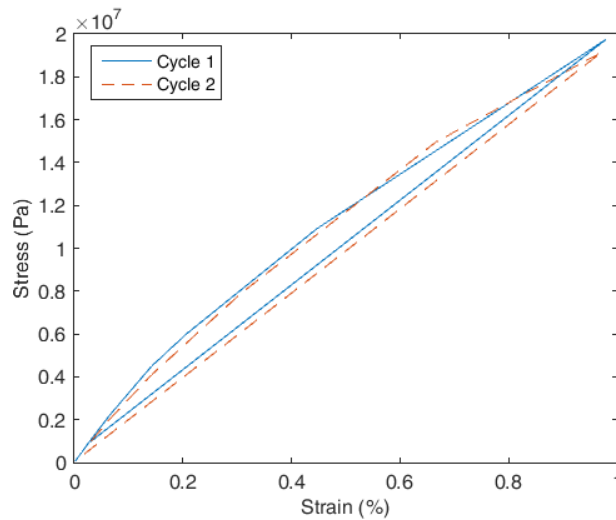


Figure 3-5 POF curvature sensor stress response with two strain cycles.

The last set of tests made with the PMMA POF samples is the humidity tests. These tests present some operational limitations, since the humidity needs to be kept constant for some minutes in order to enable the polymer moisture absorption, where the humidity is kept constant by setting a constant value for the humidity controller for the desired amount of time. The relative humidity (RH) range of the test is from about 65% to 95%, where the lower bound of the test is maintained constant for about 30 minutes to enable the polymer water absorption. Figure 3-6 presents the Young’s Modulus variation of each POF with respect to the RH. Regarding the humidity sensitivity, the PMMA mPOF presented the high humidity sensitivity with a Young’s Modulus variation three times higher than the one of the PC POF, whereas the lowest Young’s Modulus variation was found for the TOPAS mPOF and TOPAS-Zeonex step index POF (see [157]). Thus, PMMA POFs are suitable for humidity sensing and, on the other hand, compensation for humidity effects are needed in temperature and force sensors as will be presented in Chapter 4.

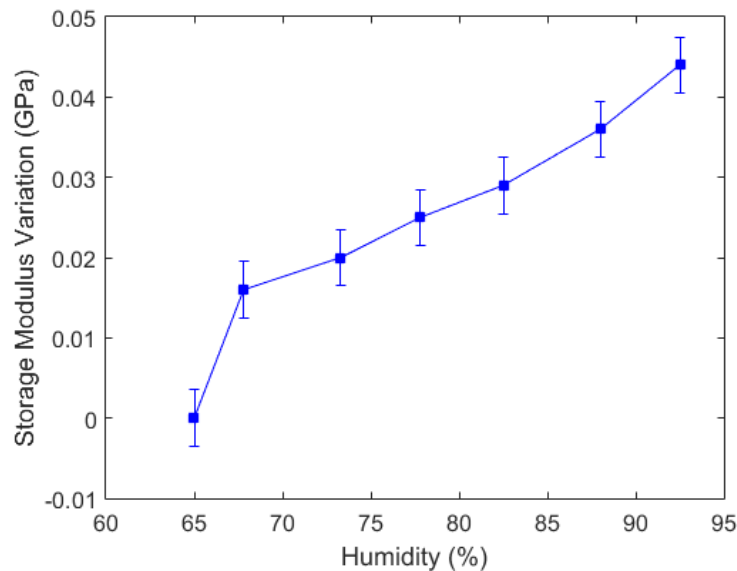


Figure 3-6 POF curvature sensor stress response with two strain cycles.

### 3.4. Dynamic Characterization of CYTOP Fibers

#### 3.4.1. Experimental Analysis

In the CYTOP characterization, the DMA was performed in separate regions of the same CYTOP fiber: one in the region without the FBG and the other in the region where the FBG was inscribed. Each sample has

7 mm length and the tests are made with a maximum displacement of 0.5 mm. For the dynamic characterization of the polymer viscoelasticity, the displacement was about 0.05 mm and, for the temperature characterization of the storage modulus, the temperature varies from 27°C to 125°C at a constant strain cycle frequency was 1 Hz. In contrast, the storage modulus characterizations as a function of the strain cycle frequency are performed at constant temperatures, where the cycle frequency varies from 0.01 Hz to 100 Hz. The frequency characterization was performed at four different temperatures, namely 30°C, 40°C, 50°C and 60°C.

In order to verify the Young's modulus of each sample, stress-strain cycles were applied on the samples with and without FBGs. First, a stress-strain cycles with strain up to 6% is applied on the CYTOP (without FBG) in order to evaluate its response with larger strains. Then, stress-strain cycles are applied on both samples (with and without FBG) with strains up to 0.25%, since this region (0-0.25%) is the one recommended by ISO 527-1:2012 standard for Young's modulus estimation in polymers [152], where the Young's modulus is estimated through the slope of the stress-strain curve.

### 3.4.2. Results and Discussion

The stress-strain test with higher range for the CYTOP sample without FBG is presented in Figure 3-7(a), whereas the tests with smaller range for Young's modulus estimation of both regions of the CYTOP are shown in Figure 3-7(b). The stress-strain curve of Figure 3-7(a) shows a linear response until about 2.5% strain with a yield stress of 70 MPa for the CYTOP fiber (without FBG) and the strain region for the Young's modulus evaluation are also presented. In the evaluation of the Young's modulus, depicted in Figure 3-7(b), it is possible to see a linear stress-strain relation in which there is an increase of the stress-strain curve slope for the sample with FBG inscribed (using direct-write plane-by-plane fs laser). Thus, the sample with FBG has a higher Young's modulus than the one without FBGs. However, the difference between both samples is about 0.22 GPa, which represents a relative Young's modulus variation higher than 10%. It is noteworthy that this relative variation is higher than the standard deviation between the three performed tests. In addition, it is also higher than the measurement uncertainties (due to the equipment resolution), such difference in the POF material properties must be considered in the following evaluations of the POFBG, since the proposed sensor applications are based on the applications of stress, strain and displacements on the POFBGs (see Chapter 5). For this reason, the tests for the POF material evaluation under different conditions are made where the FBG was inscribed.

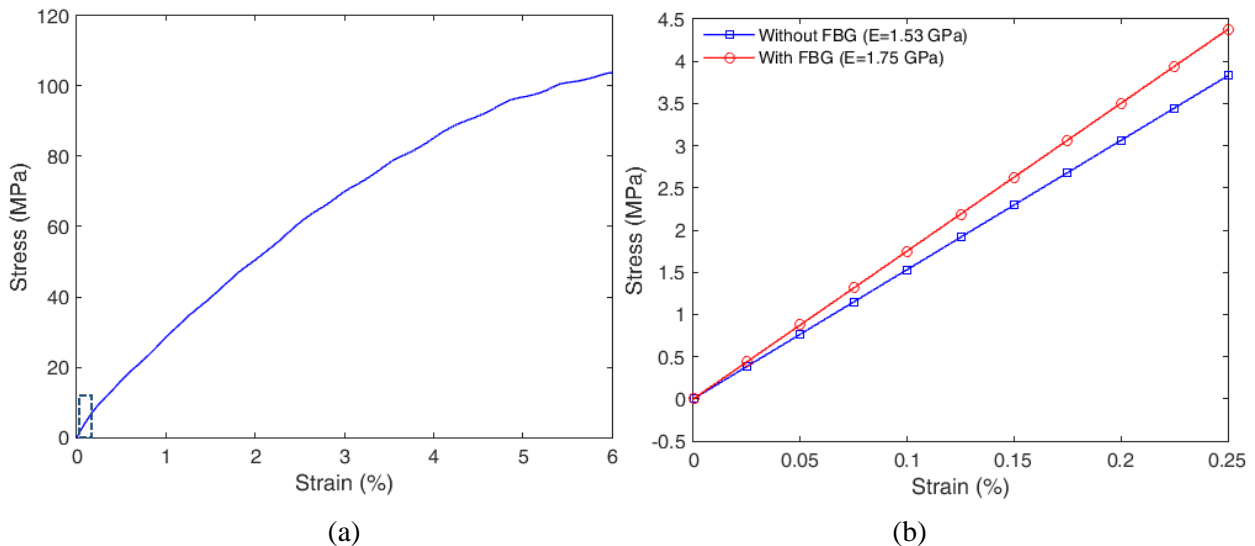


Figure 3-7 (a) Stress-strain curve for the CYTOP without FBGs in a strain range of 0-6%. (b) Stress-strain curves for Young's modulus calculation for CYTOPs with and without FBGs.

The CYTOP (with the inscribed FBGs) material properties is also evaluated under different temperature and frequency of oscillatory movements. In order to estimate the CYTOP moduli at higher frequency range, the TTS principle is applied, which enables the creation of master curves for estimation of the material viscoelastic properties within ranges higher than the ones of the DMA equipment [151]. As the principle requires a linear viscoelastic regime [151], Figure 3-8(a) shows the storage modulus of the sample as a function of the temperature, where Figure 3-8(b) depicts the frequency response of the material within the temperature range 30°C-60°C.

In the analyzed range, the temperature leads to a linear shift ( $a_T$ ) on the storage modulus – frequency curves, which is in agreement with the first requirement for the TTS principle and define the material as thermorheological simple in this temperature range [151]. The second requirement is that there is no physical changes or phase transition on the material on the considered temperature range [151]. In order to verify this assumption, the loss factor,  $\tan(\delta)$ , of the material is analyzed, as Figure 3-9 depicts. In this case, the  $\tan(\delta)$  peak (at 122°C) is associated with the material glass transition temperature ( $T_g$ ), which limits the TTS principle application of the POFBGs in temperature higher than (or close to) the  $T_g$ . Nevertheless, the results of Figure 3-9 also show that the material does not undergo any phase transition in the analyzed temperature range (30°C to 60°C).

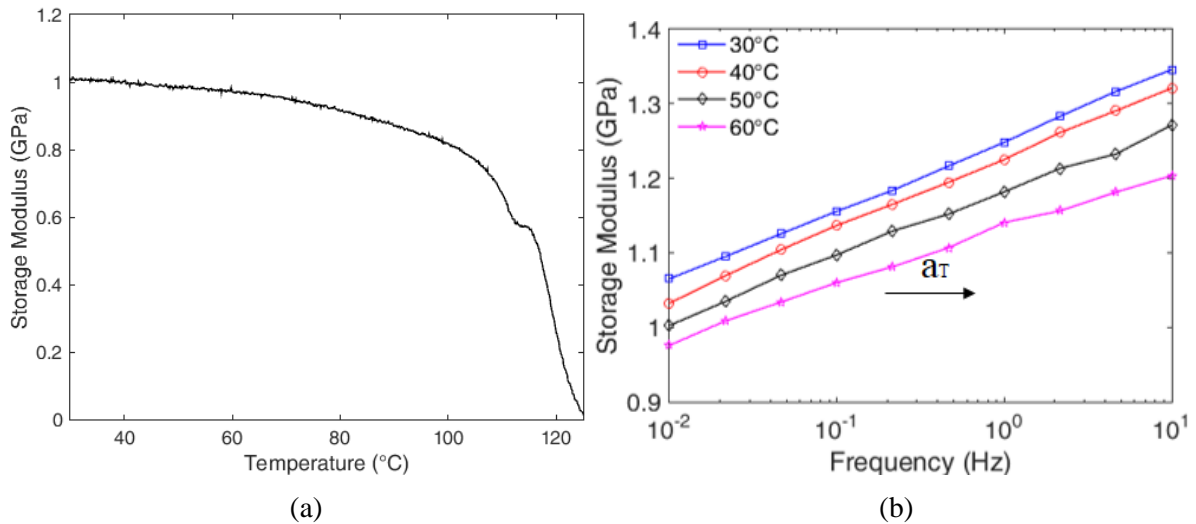


Figure 3-8 (a) CYTOP's storage modulus as a function of the temperature. (b) Frequency response in 4 different temperatures (30°C, 40°C, 50°C and 60°C).

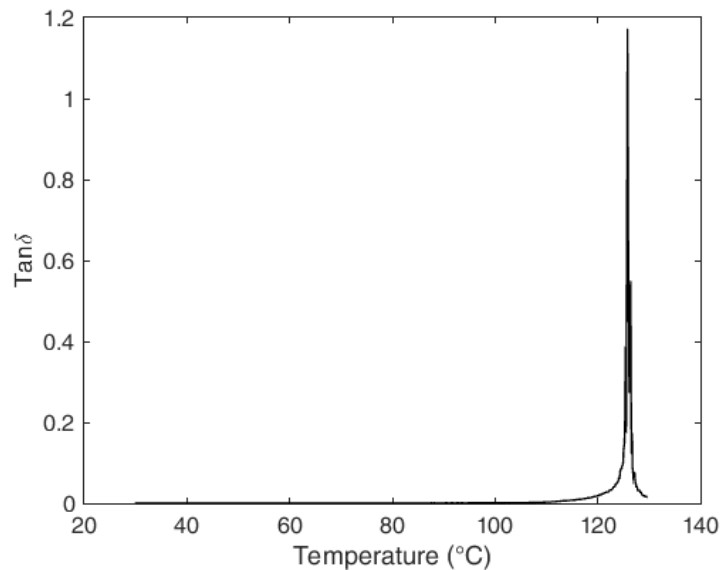


Figure 3-9 Loss factor on the range of 27°C to 130°C.

Hence, Figure 3-8 and Figure 3-9 provide sufficient background to the application of the TTS principle on the frequency and temperature results. In this case, it is possible to extend the estimation of the material viscoelastic properties to a frequency range up to 500 Hz (higher than the DMA operation range) as shown in with a reference temperature of 30°C. The master curve shows an increase of the storage modulus as a function of the frequency, which enables the application of the proposed POFBGs array in such frequencies with the possibility of estimating possible sensitivity variations in such frequencies as will be described in Chapter 5. However, since the proposed applications do not involve frequencies higher than 100 Hz, Figure 3-10 shows the storage modulus variation from 0.01 Hz to 100 Hz.

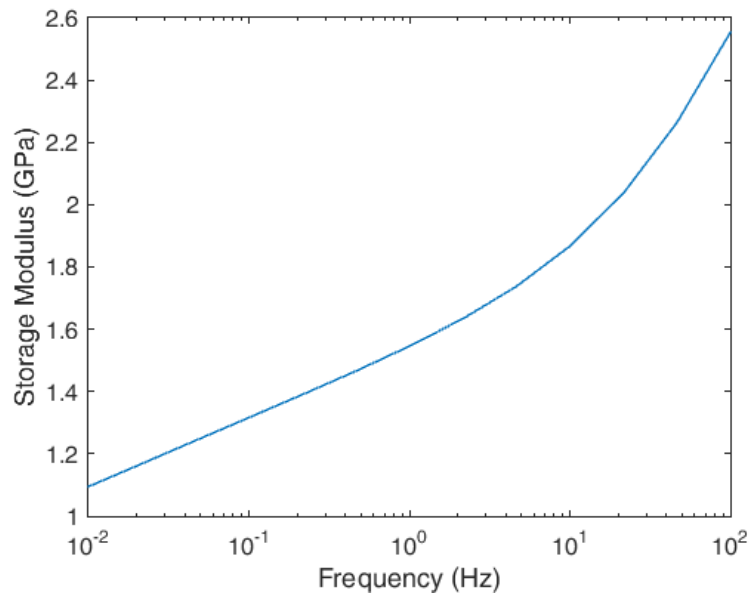


Figure 3-10 Master curve for the FBG inscribed in CYTOP fiber.

### 3.5. Final Remarks

This Chapter presented the dynamic characterization of the POFs that will be applied as intensity variation-based sensors (PMMA) and FBG sensors (CYTOP). First, temperature tests are made to define the variation of the material dynamic Young's modulus, where it can be seen the material transitions ( $T_g$ ,  $\alpha$ - and  $\beta$ -transitions). After defining the influence of the temperature on the POF viscoelastic parameters, the effect of the frequency is analyzed. The variation of the dynamic Young's modulus was evaluated on different temperatures steps on a frequency scan for both materials (PMMA and CYTOP). This analysis enables the application of the TTS principle in order to obtain an equation relating the viscoelastic response and temperature offset, which was applied on the CYTOP fiber. Furthermore, the influence of the FBG inscription using the fs laser was quantitatively assessed in this Chapter, where the sample with inscribed FBG presented a Young's modulus 10% higher when compared with the one without gratings inscribed, leading to higher rigidity of the fiber.

A creep recovery test is made on the PMMA fiber to obtain the variation of the polymer time constant with the load applied on the test. There are two time constants, since the polymer does not have a single time constant and the polymer relaxation can be estimated through a Prony series of order 2 (further explored in Chapter 4 and Chapter 5). In addition, the stress-strain cycles show a hysteresis, which indicate that this undesirable effect can be compensated in POF sensors by analyzing the material features of each fiber. In summary, this Chapter presented fundamental aspects of the polymer behavior, which are the basis for the development of intensity variation-based sensors and on the enhancement of the FBG-based sensors' performances.

## Chapter 4. Intensity Variation-based Sensors

### 4.1. Introduction

This chapter presents developments and applications of intensity variation-based sensors for healthcare devices, particularly, gait assistance and rehabilitation devices. Among different techniques, intensity variation based sensors are the ones that present the lowest cost, highest simplicity in fabrication, since it does not need specialized equipment such as the gratings-based sensors and also have simplicity in the signal processing [158]. Aiming at a low-cost sensor system with the advantages of POFs for sensor applications, the development of different intensity variation-based sensors with multimode POFs is presented. However, intensity variation-based sensors have the disadvantage of errors due to the light source power deviation, which can be reduced by the use of self-referencing techniques [112], [159]. Another important disadvantage is their lack of multiplexing capabilities, which inhibit the application in multipoint [69] or multiparameter [160] measurements. In order to tackle this drawback, a multiplexing technique for intensity variation-based sensors is also proposed and validated.

### 4.2. Curvature Sensor

When the fiber is under curvature, there is a variation of the output signal proportional with the curvature angle. In a concave bending case, there is an increase of the reflections on the convex side of the curvature and a decrease on the concave side. For this reason, if the sensitive zone is on the convex side, there will be more rays escaping when compared with the fiber at the straight position, which leads to the attenuation of the output signal. Furthermore, the angle between the incident ray and the sensitive zone surface increases with the fiber curvature, which leads to a coupling between some higher guided modes and lower guided modes and increase the surface scattering loss, creating an attenuation on a POF with sensitive zone [161] (see Figure 4-1 inset).

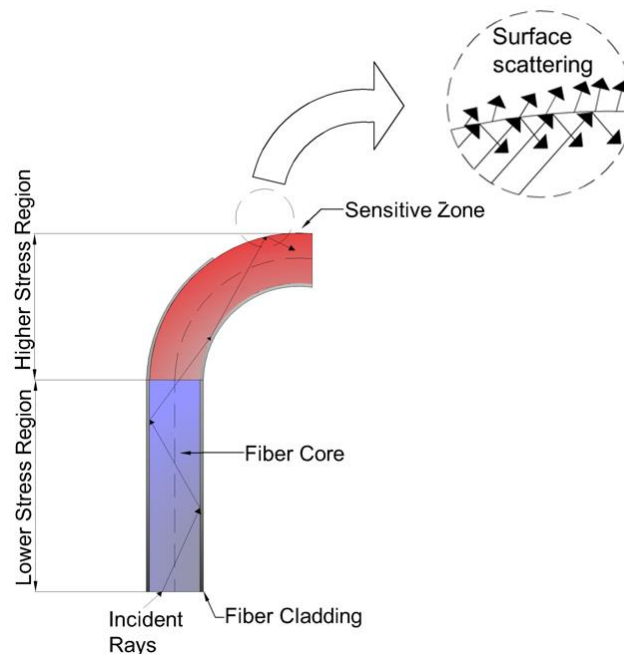


Figure 4-1 Schematic view of the POF sensor under curvature.

Despite the attenuations due to the macrobending and the surface scattering, there is also an output signal attenuation caused by the stress-optical effect. Since the curvature of the fiber also generates a stress on the fiber, the POF refractive index changes and it leads to an attenuation of the POF sensor signal and it is proportional to the stress on the fiber [162]. Figure 4-1 shows the attenuation mechanisms of the POF curvature sensor. In addition, the whole description and analytical model (proposal and validation) for this sensor are depicted in Appendix A. Since the sensitive zone parameters, surface scattering and stress-optic effects can influence the sensor response, the performance of a curvature sensor (with respect to sensitivity, linearity and hysteresis) will be influenced by the sensitive zone length, depth and surface roughness as well as the sensor's curvature radius. These parameters are thoroughly verified in Appendix B, where an optimization of the sensitive zone parameters is presented aiming at the highest sensitivity and linearity with lower hysteresis.

Such optimization resulted in an optimal length of about 14 mm, depth of 0.6 mm in an abrasive removal of material using a sandpaper with 400-grit size.

### 4.2.1. Experimental setup

The POF curvature sensor is positioned on the test prototype presented in Figure 4-2. The test comprises in bending the fiber for flexion and extension in 0-90° range. As the bending occurs, the light attenuation increases due the fiber curvature. The light variation is acquired by a photodiode IF-D91 (Industrial Fiber Optics, USA) with a transimpedance amplifier, where amplifier gain is correlated to the output voltage and, thus, the optical power. The light source is a low cost 3 mW@650 nm laser. A National Instruments USB-6008 board makes the signal acquisition at 1 kHz. Since possible fluctuations in the light source, temperature and humidity can lead to undesired response of the sensor, a reference fiber is applied to compensate such variations [16]. Therefore, the sensor response is normalized with respect to the reference fiber response by means of a subtraction between the sensor and the reference responses. In this compensation technique, the laser provides light for both fibers and these fibers are further split into the reference and transducer fibers through the light coupler IF-562 (Industrial Fiber Optics, USA). The bending angle is acquired by a potentiometer and the motor has a closed loop position controller.

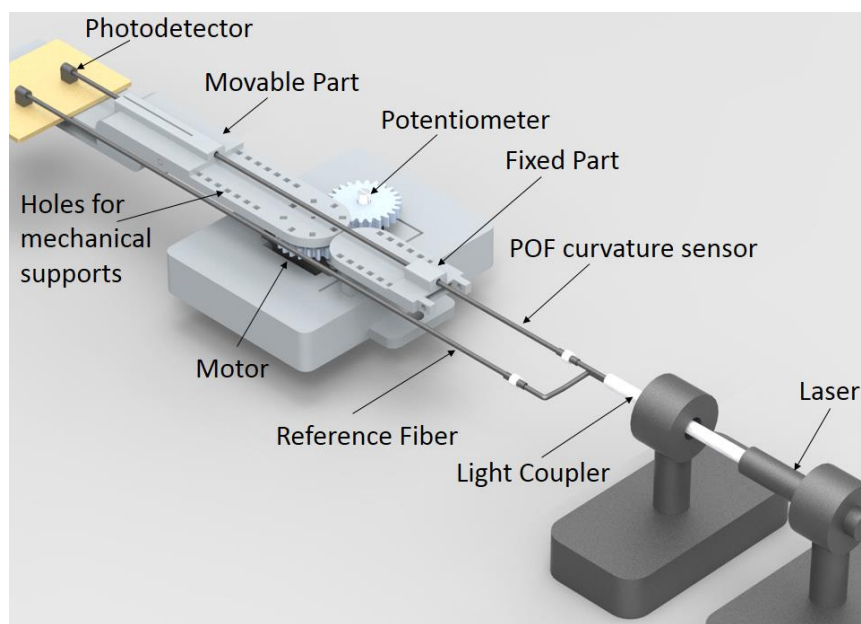


Figure 4-2 Prototype employed on the dynamic tests of the curvature POF sensors.

## 4.2.2. Compensation Technique Based on Viscoelastic Features

### 4.2.2.1. Theoretical Approach and Implementation

The sensor hysteresis compensation depicted in Appendix C is based on a technique that fits the sensor response with the hysteresis presented on each test in different angular velocities. In this case, the goal is to obtain a calibration equation that relates the measured signal and its angular velocity with the measured angle [16]. Even though the technique presented in Appendix C is the first one proposed to deal with the hysteresis in POF curvature sensors, the correlation may be lower in some cases due to the hysteresis variability, which decreases the technique robustness. In addition, this technique requires a high number of tests at each angular velocity, which is a time-consuming and cumbersome method. For these reasons, a compensation technique based on the material intrinsic behavior that results in equations for flexion and extension cycles without the necessity of a high number of calibration cycles can overcome some of the limitations of the previously proposed one. Thus, the compensation technique proposed in this section is based on the application of viscoelastic models (obtained from the PMMA characterization on Section 3.3) on the sensor analytical model for dynamic bending (further discussed in Appendix A). In summary, the model relates the input signal ( $P_i$ ) and sensor response ( $P_o$ ) (considering the bending effects and stress-optic effects thoroughly discussed in Appendix A).

Considering the model presented in Appendix A for the optimized parameters obtained in Appendix B and disregarding the viscoelastic effects on the modeling, the equations of Appendix A can be reduced to the linear equation depicted in Eq. 4.1.

$$\frac{P}{P_0} = -0.00496\alpha + 0.9997 \quad (4.1)$$

Since this equation was obtained without considering the viscoelastic effects, the hysteresis between the flexion and extension cycles is not modelled and cannot be compensated if only Eq. 4.1 is considered. Figure 4-3 shows the sensor response to flexion and the linear regression using Eq. 4.1.

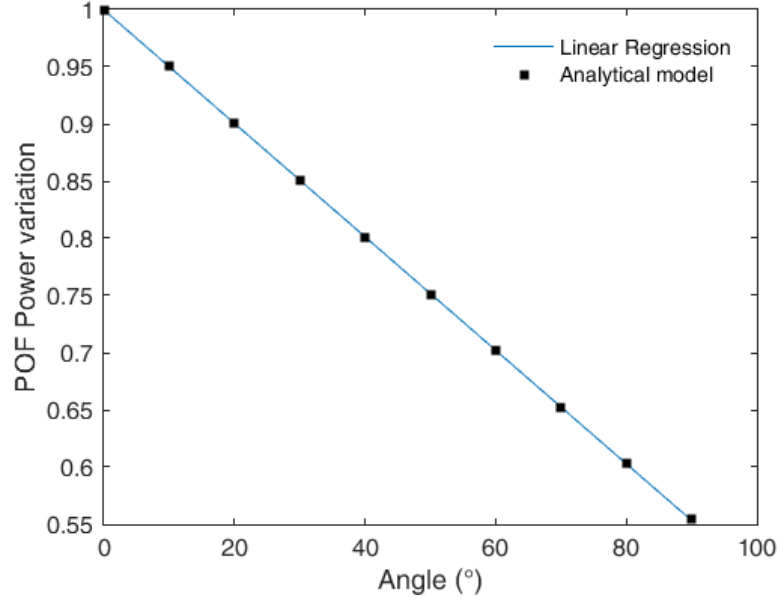


Figure 4-3 POF sensor response estimated by the model and linear regression.

On the analysis of a viscoelastic material, the static Young's Modulus is substituted to a dynamic Young's Modulus, which considers the polymer relaxation and the influence of the movement frequency on the polymer response. An approach for modelling this behavior is by applying the Maxwell model, which considers the viscoelastic response of the polymer as the response of a spring in series with a damper [151]. Solving the differential equations of the spring and dashpot responses, a single exponential is obtained [59]. However, single exponential functions may not provide an accurate behavior of some viscoelastic materials [59]. For this reason, a practical approach to obtain a more accurate response of the polymer is to employ higher order terms on the differential equations for the viscoelastic modelling. Hence, the polymer relaxation function is related with a sum of exponentials of order  $N$ . The exponential sum that results on the polymer relaxation function ( $E(t)$ ) is known as the Prony series [59] and is presented in Eq. 4.2:

$$E(t) = \sum_{n=0}^N y_n \exp\left(\frac{-t}{\tau_n}\right), \quad (4.2)$$

where  $y_n$  is the weight of each exponential,  $\tau_n$  is the time constant of each order of the model and  $t$  is the time. The general disadvantage of the Prony series approach is that it can lead to complicated assemblies of springs and dashpots that cannot be characterized, since there is no identification of these mechanical components as physical features of the material [59]. Nevertheless, for materials that behave as lower order models, the Prony series can lead to more accurate values than the Maxwell model with a single exponential. In this case, the order of the model chosen is 2 (that can be correlated to association with springs and dampers), which is the one obtained in DMA experiments with the same fiber, as presented in Chapter 3.

For the POF curvature sensor, movement frequency is related to the angular velocity on the sensor flexion/extension cycles, whereas the polymer response is the POF sensor response. Assuming that the sensor hysteresis is related to the viscoelastic response, the polymer relaxation leads to the sensor hysteresis and possible variations on its linearity. Therefore, the POF power variation can be substituted on Eq. 4.2. Nevertheless, the response for flexion presented in Figure 4-3 has no hysteresis, which means that the extension

movement presents the same response. Hence, it is the ideal response for the POF curvature sensor. In order to obtain a response close to the ideal one presented in Figure 4-3, the POF responses measured on flexion/extension cycles are compensated with the POF power variation obtained by the analytical model as the reference response. Furthermore, the time presented in Eq. 4.2, is the ratio between the angle and the angular velocity. Thus, the Prony series with order 2 is presented in Eq. 4.3 with respect to the POF power variation:

$$\frac{P}{P_0} = y_1 \exp\left(\frac{-\alpha}{\omega\tau_1}\right) + y_2 \exp\left(\frac{-\alpha}{\omega\tau_2}\right), \quad (4.3)$$

where  $y_1$  and  $y_2$  are the weights of each exponential,  $\tau_1$  and  $\tau_2$  are time constants of the materials and  $\omega$  is the angular velocity. Furthermore, the angle in Eq. 4.3 is substituted by the expression obtained isolating  $\alpha$  in Eq.4.1, where the power ratio is the measured attenuation of the POF sensor on the flexion and extension movement from 0 to 90° with constant angular velocity of 0.34 rad/s. Hence, two equations, one for flexion and one for extension, relating the measured power attenuation and a reference power attenuation, are obtained.

In order to obtain the coefficients  $y_1$ ,  $y_2$ ,  $\tau_1$  and  $\tau_2$ , a regression is made using the least squares method for flexion and extension movements. The equations with the estimated coefficients result in a compensated response of the POF curvature sensor that presents lower errors, hysteresis and higher linearity.

Although the Eq. 4.3 shows that the response depends on the angular velocity that the sensor is submitted, the estimated time constants are related to the material features. Nonetheless, the polymer does not have a constant time response, it has a range of time response, instead. For this reason, the regression made for obtaining the coefficients at an angular velocity of 0.34 rad/s may be suitable for compensating the hysteresis for a wider range of angular velocities. This assumption excludes the necessity of a characterization with different angular velocities as presented in Appendix C, which leads to an easier characterization process and results in a simpler equation. The obtained coefficients are applied in Eq. 4.3, which are substituted in Eq. 4.1. Isolating the angle, Eq. 4.4 and 4.5 are obtained. These equations are the compensated equations for the POF curvature sensor for flexion and extension, respectively, for an angle range of 0 to 90°. These equations are applied on angular velocities between 0.05 rad/s and 1.60 rad/s.

$$\alpha_f = -126.493 \exp\left(0.5983 \left(\frac{P}{P_0}\right)_f\right) + 180.324 \exp\left(-1.858 \left(\frac{P}{P_0}\right)_f\right) + 201.552, \quad (4.4)$$

$$\alpha_e = -128.610 \exp\left(0.5462 \left(\frac{P}{P_0}\right)_e\right) + 242.139 \exp\left(-2.461 \left(\frac{P}{P_0}\right)_e\right) + 201.552, \quad (4.5)$$

where  $\alpha_f$  and  $\alpha_e$  are the angles for flexion and extension, respectively,  $\left(\frac{P}{P_0}\right)_f$  and  $\left(\frac{P}{P_0}\right)_e$  are the POF power attenuation for flexion and extension, respectively. It is worth to mention that such procedure has to be applied for each sensor.

#### 4.2.2.2. Compensation technique validation

To validate the proposed technique, flexion and extension cycles are performed with 9 different constant angular velocities: 0.05 rad/s, 0.09 rad/s, 0.17 rad/s, 0.34 rad/s, 0.43 rad/s, 0.57 rad/s, 0.82 rad/s, 1.04 rad/s and 1.61 rad/s using the experimental setup described in Section 4.2.1. These velocities are within the range of human gait. Three cycles are performed at each angular velocity. The compensated equations, Eqs. 4.47 and 4.48 are applied at each movement cycle. In order to have a comparison between the compensated and uncompensated responses, the results obtained with the application of the compensation technique are compared with the results obtained by applying only a linear regression on the sensor response. Figure 4-4 shows the flexion/extension cycle at 0.34 rad/s for the uncompensated, Figure 4-4(a), and compensated responses, Figure 4-4(b), respectively.

The presented results in Figure 4-4 (with and without the compensation technique) show the improvement that the compensation equation is able to provide. The response without the compensation has a hysteresis of

1.62%, whereas the response applying Eqs. 4.4 and 4.5 presented a decrease of more than 100 times. In this case, the hysteresis of the compensated response is 0.01%. Nevertheless, not only the hysteresis decreases, but also the RMSE shows a high reduction. The RMSE for the uncompensated flexion/extension cycle is  $2.44^\circ$  and the RMSE for the same cycle with the compensation equation is  $0.44^\circ$ , which means an error reduction of more than 5 times. This is a significant reduction, since conventional technologies for joint angles assessment present errors equal or higher than  $2.00^\circ$  [163]. Another advantage of the proposed compensation is the increase of the sensor linearity. In the case shown in Figure 4-5, the linearity of the sensor for the flexion cycle without compensation is 0.9994, which already is a high linearity. However, the linearity of the same cycle with the compensation is 0.9996 showing a slight increase. If the extension cycle is analyzed, the differences are even higher, i.e. the linearity of the extension cycle, which was 0.9965 without compensation, is increased to 0.9999 with the compensation technique based on POF viscoelastic features.

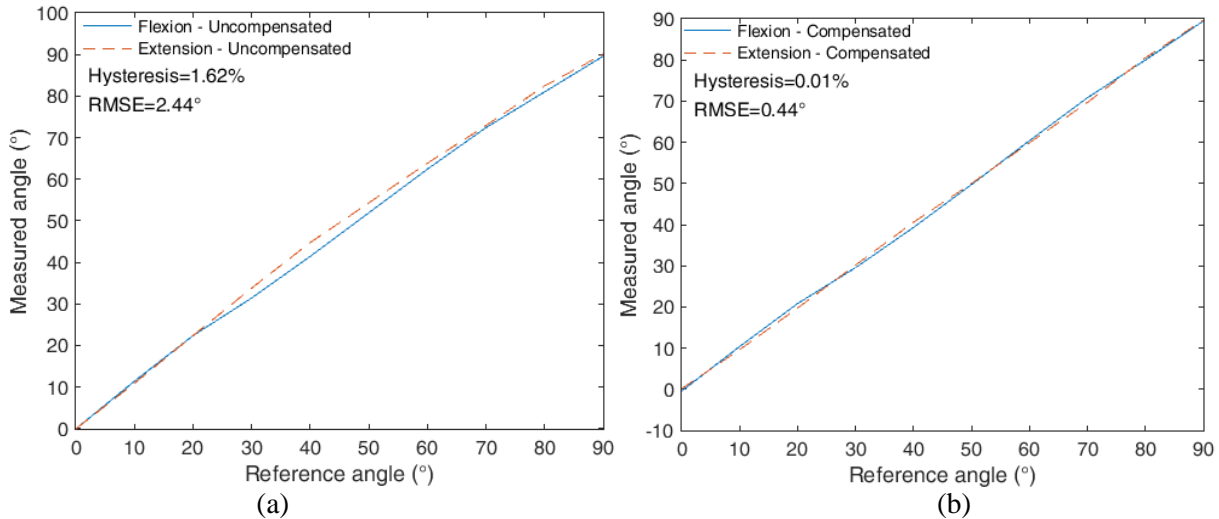


Figure 4-4 (a) POF sensor response without the application of the compensation equation and (b) POF sensor response with the compensation equation.

Since the estimation of the equation parameters presented in Eq. 4.4 was made for the angular velocity of  $0.34 \text{ rad/s}$ , it is expected that the analysis of the sensor response on this angular velocity will lead to a better response of the POF sensor with respect to its linearity, hysteresis and error. Even if different flexion/extension cycles are employed, their responses will present better compensation of the performance parameters mentioned than the ones with different angular velocities. In order to evaluate the response on different angular velocities and explore the limits of the proposed compensation equation, the technique is applied on the nine different angular velocities aforementioned. Figure 4-5(a) shows the comparison of the POF sensor responses with and without the compensation technique with respect to their hysteresis and RMSE. Regarding the hysteresis, the higher reduction of this parameter occurs at the angular velocity of  $0.34 \text{ rad/s}$ , which is the angular velocity employed on the estimation of the parameters from Eqs. 4.4 and 4.5. Furthermore, the proposed compensation technique was able to reduce this parameter in all cycles, except the one at  $0.80 \text{ rad/s}$ .

However, in this cycle the hysteresis was already very low, since the uncompensated hysteresis for this cycle is about 0.22%. Nevertheless, the hysteresis obtained with the application of the compensation technique was 0.50%, which is lower than the ones obtained in [111] and on the results showed in [164]. The lower reduction of the hysteresis was obtained on the angular velocity of  $0.43 \text{ rad/s}$  and can be related to the variation of the viscoelastic properties on this specific cycle. Besides the angular velocity of  $0.34 \text{ rad/s}$ , which was employed for the parameters' estimation, the angular velocity of  $0.43 \text{ rad/s}$  presented the highest reduction of the RMSE.

Although the hysteresis presented a little increase on the cycles at the angular velocity of  $0.80 \text{ rad/s}$ , the RMSE of the uncompensated response at this angular velocity is  $2.32^\circ$ , whereas after applying the compensation equations, the RMSE on the same cycle is reduced to  $0.86^\circ$ . The same behavior occurs in all angular velocities tested, where the compensation technique was able to reduce the RMSE in all tested cases. Furthermore, the compensation technique provides a RMSE below  $1.00^\circ$  for the angular velocities between  $0.09 \text{ rad/s}$  and  $1.04 \text{ rad/s}$ , where the lowest RMSE was obtained at the angular velocity of  $0.34 \text{ rad/s}$ . The average reduction of the RMSE is about  $1.60^\circ$ .

The compensation technique based on the polymer viscoelasticity is also able to enhance the linearity of the POF curvature sensor on both flexion and extension cycles. The linearity of the sensor at each angular

velocity on flexion and extension cycles is presented in Figure 4-5(b). The proposed compensation equations were a suitable solution to increase the sensor linearity on both flexion and extension cycles in all cases tested. The lowest increase, among the ones tested for flexion movement, occurs at the angular velocity of 0.05 rad/s, whereas for the extension movement, there is a substantial increase of the linearity in all cases. The reason for the higher increase of the linearity on the extension movement is that the linearity of the flexion movement without the compensation technique is already high with a mean value of 0.9990. Hence, it has a smaller range for improvement if it is compared with the extension movement, which has a mean linearity of 0.9966. This difference on the linearity of the flexion and extension cycles is a source of errors of the POF curvature sensor and it is related to the polymer viscoelastic response. As presented in Figure 4-5(b), the linearity of the flexion cycle is close to the extension cycle case when the compensation technique is applied.

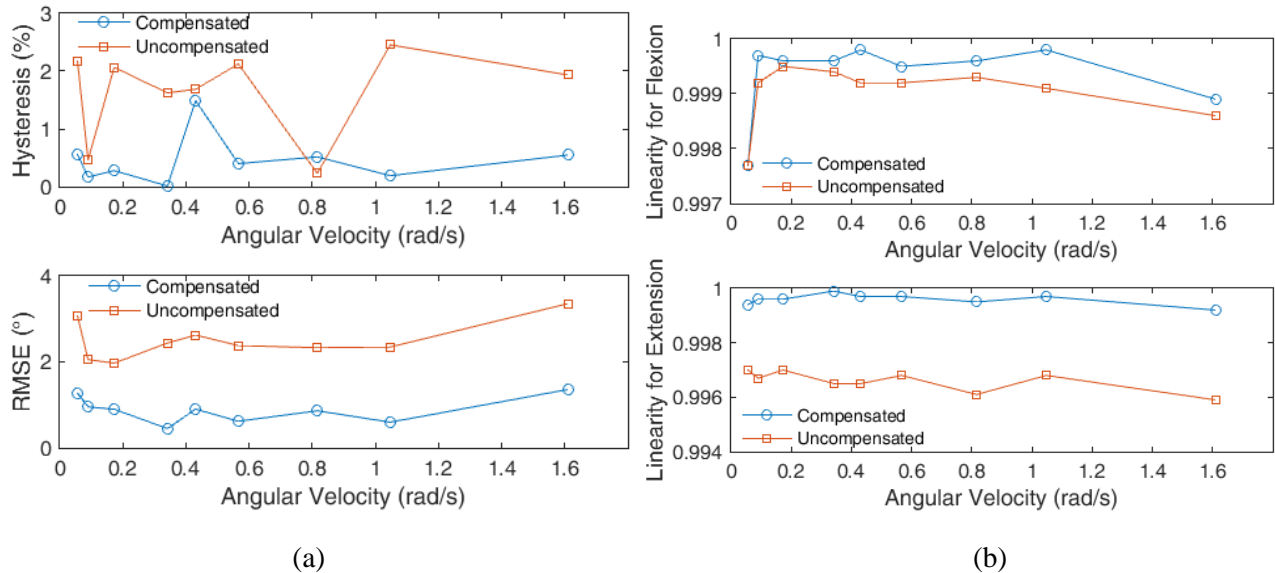


Figure 4-5 (a) Comparison of the measured hysteresis and RMSE with and without the compensation technique. (b) Comparison of the linearity at the flexion and extension movements with and without the compensation technique.

Figure 4-5 shows that there is an interval of angular velocities that provides hysteresis lower than 0.50%, RMSE lower than  $0.80^\circ$  and linearity for flexion and extension close to 1. This interval is between 0.15 rad/s and 1.00 rad/s and it can be considered as the optimum interval of angular velocities when the coefficients of Eqs. 4.5 and 4.6 are obtained from the angular velocity of 0.34 rad/s. If the angular velocity changes, the optimal interval also changes. Therefore, if a wider range of angular velocity is needed for a certain application, it may be necessary to obtain different sets of coefficients for pre-defined intervals. Nevertheless, the same procedure for obtaining compensated equations can be applied to any interval of angular movement. Furthermore, the obtained results with the proposed compensation technique lead to a sensor with lower errors and lower hysteresis than the ones presented in [110], [111], [165]. Moreover, the developed technique presents a better performance with respect to the increase of linearity, reduction of hysteresis and RMSE than the hysteresis compensation technique based on linear regressions presented in [166] (Appendix C), with the additional advantage of requiring less calibration cycles.

### 4.3. Temperature and Humidity Sensors

In order to overcome some of humidity sensors' limitations and to achieve a system capable of measuring the climate parameters discussed in Chapter 1, this section presents the development of a low-cost system for measurements of temperature and humidity with POF intensity variation-based sensors. The sensor is based on the variation of the fiber's mechanical properties due to temperature and humidity variations (as characterized in Chapter 3). If the fiber is submitted to a predefined torsional stress, the variation of its mechanical properties leads to a variation of the fiber's output power due to the stress-optic effect. Such effect is the variation of the fiber's refractive index when it is submitted to a stress discussed in Section 4.2 and modelled in Appendix A. Furthermore, as presented in [141], the stress applied on the fiber can reduce the response time of the sensor. Moreover, a fiber etching is made on the sensor to further reduce its response time as demonstrated in [167].

### 4.3.1. POF Microclimate Sensors Operation Principle

The variation of the refractive index leads to a variation of the POF's output power. In addition, PMMA POFs show variation of their shear and Young's moduli when the temperature is changed. Besides the variation of the mechanical properties of the fiber, the variation of the RH leads to refractive index variation due to water absorption-induced swelling on the PMMA POF [141]. Since the material is affected by the influence of both temperature and humidity, a humidity sensor based on this principle will suffer from temperature cross-sensitivity and vice-versa. For this reason, two POFs under torsion stress were employed. Each sensor's response will be a sum of the contribution of the temperature and RH variations. Therefore, a system with two variables and two equations is obtained. In order to separate the RH and temperature responses, a direct difference between the sensor's equations (considering their sensitivities with respect to temperature and humidity) is applied, as presented in Eq. 4.6. This principle is widely applied to reduce the temperature cross-sensitivity on FBG-based sensors, interferometers or POF intensity variation-based sensors [168]–[170].

$$\begin{bmatrix} \Delta RH \\ \Delta T \end{bmatrix} = \begin{bmatrix} K_{1,RH} & K_{1,T} \\ K_{2,RH} & K_{2,T} \end{bmatrix}^{-1} \left( \begin{bmatrix} P_1 \\ P_2 \end{bmatrix} - \begin{bmatrix} P_{1,0} \\ P_{2,0} \end{bmatrix} \right), \quad (4.6)$$

where  $\Delta RH$  and  $\Delta T$  are the RH and temperature variations, respectively.  $K_{1,RH}$  is the sensitivity of the sensor 1 to the RH variation, whereas  $K_{1,T}$  is the sensitivity of the sensor 1 to temperature variation. The parameters  $K_{2,RH}$  and  $K_{2,T}$  are the sensitivities of the sensor 2 to RH and temperature, respectively.  $P_1$  and  $P_2$  are the measured power of sensor 1 and 2, respectively.  $P_{1,0}$  is the initial power of sensor 1 and  $P_{2,0}$  is the analogous parameter for the sensor 2. In addition, if Sensors 1 and 2 are connected to the same light source, the effects of the power fluctuation from the light source will be compensated by the subtraction between both sensors responses through the application of Eq. 4.6, as discussed in [170]. It is noteworthy that the torque characterization on the POFs used in this work is depicted in Appendix D.

### 4.3.2. Experimental Setup

The tests are made with the experimental setup presented in Figure 4-6. It consists of an acrylic box with an inlet on its top for the injection of steam through an air humidifier. The box also has two holes on its left and right sides for the POF sensors, which are submitted to a constant torque through the four supports presented in Figure 4-6. Each support has a degree of freedom for rotation around the z-plane and a lock mechanism to keep each fiber on the torsion angle applied. The light source is a low-cost laser 3 mW@650 nm, which has its signal divided between both sensors with a 50:50 coupling ratio using a light coupler 1x2 IF 562 (Industrial Fiber Optics, USA). Two photodiodes IF-D91 (Industrial Fiber Optics, USA) make the acquisition of the sensors power variations in volts (V) units. Furthermore, the data acquisition is made with the FRDM-KL25Z board (Freescale, USA) at 200 Hz. For the tests with temperature variation, the experimental setup presented in Figure 4-6 is positioned inside a climatic chamber 400/1ND (Ethik Technology, Brazil) with a closed-loop temperature controller. The reference measurement of temperature and humidity is made with HTU21D (Measurement Specialties, USA) temperature and humidity sensor.

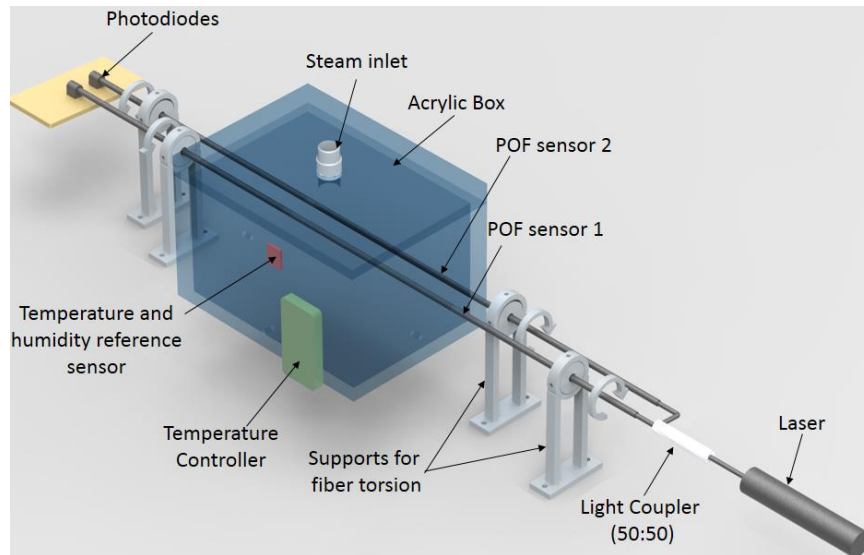


Figure 4-6 Experimental setup for POF humidity and temperature sensors tests.

### 4.3.3. Results and Discussion

#### 4.3.3.1. Relative Humidity (RH) Characterization

After the torque's characterization shown in Appendix D, two POFs with a lateral section are subjected to a humidity characterization. In order to show the influence of the torque's direction in the response of the sensor, the applied torques have different directions. In the Sensor 1, the torque is applied in the counterclockwise direction, whereas in the Sensor 2, the torque is applied in the clockwise direction. A higher torsion angle is applied in the Sensor 2, which will create a higher torque on it. However, Sensor 2 has a lower lateral section depth than the one in Sensor 1. For this reason, the POF's initial output power of Sensor 2 is lower than the one of the Sensor 1. The power variation after the torque's application is higher on the Sensor 2 than on the Sensor 1.

Before the RH characterization tests, silica gel is inserted on the acrylic box through the steam inlet to reduce the RH inside the box (see Figure 4-6). After the reduction of the RH, the output of an air humidifier is positioned on the steam inlet until the RH inside the box reaches values of about 98%. The same process is repeated 3 times and the results obtained for both sensors are presented in Figure 4-7, in which the blue line and the red dashed line represent linear fit of the Sensor 1 and Sensor 2 responses, respectively. Although the test is made until reaching higher RH values, the characterization is limited to the interval of 10% to 70%. The reason for the analysis on this interval is the lower variation of temperature in that range, which provides the characterization with the lowest influence of temperature. The temperature in this characterization is  $23.64 \pm 0.01^\circ\text{C}$ .

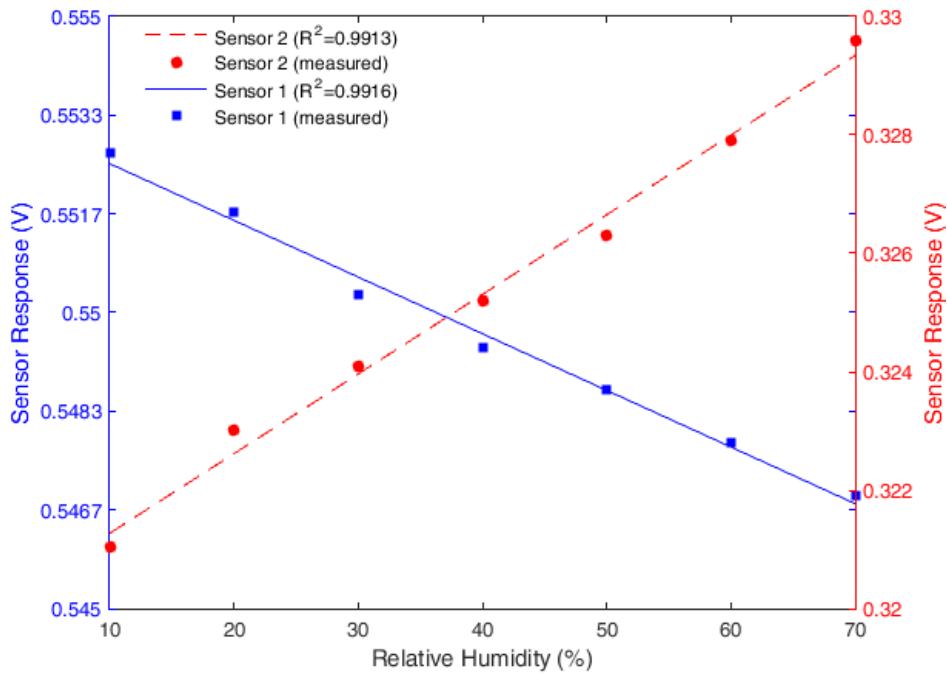


Figure 4-7 RH characterization of POF sensors.

As presented in Figure 4-7, the torque's direction leads to a variation of the sensor polarity. For the counterclockwise torque, the power attenuates when the RH increases. As for the torque on the clockwise direction, the opposite effect occurs. The reason for this behavior is related to the change of the direction of each tensor's component presented in Eq. D.1.

#### 4.3.3.2. Temperature Characterization

The temperature characterization is made by means of positioning the setup presented in Figure 4-6 in a climatic chamber with closed loop control. The test consists of increasing the temperature from 24°C to 44°C. The reason for this temperature interval is the possibility of a thermal expansion on the POF when the temperature is higher. If this effect occurs, it changes the fiber torsion angle, which leads to a variation of the sensor's behavior. Furthermore, if the fiber is submitted to higher thermal expansion, it is possible that it does not return to its original shape. Nevertheless, the temperature range applied is within the limits of the comfort regions for microclimate sensing applications [6], in which such higher thermal expansion may not occur.

With the temperature test in the range of 24°C to 44°C done, the result of the characterization for both POF sensors and the linear regression of their responses are presented in Figure 4-8. Since the used heater does not have RH control, the humidity changes throughout the test. However, the sensor response with respect to the RH are already characterized. Therefore, for the temperature characterization without the RH cross-sensitivity, the RH measured by the reference sensor is applied to the characterization equation obtained in the humidity tests and is subtracted from the response of each sensor in the temperature characterization tests.

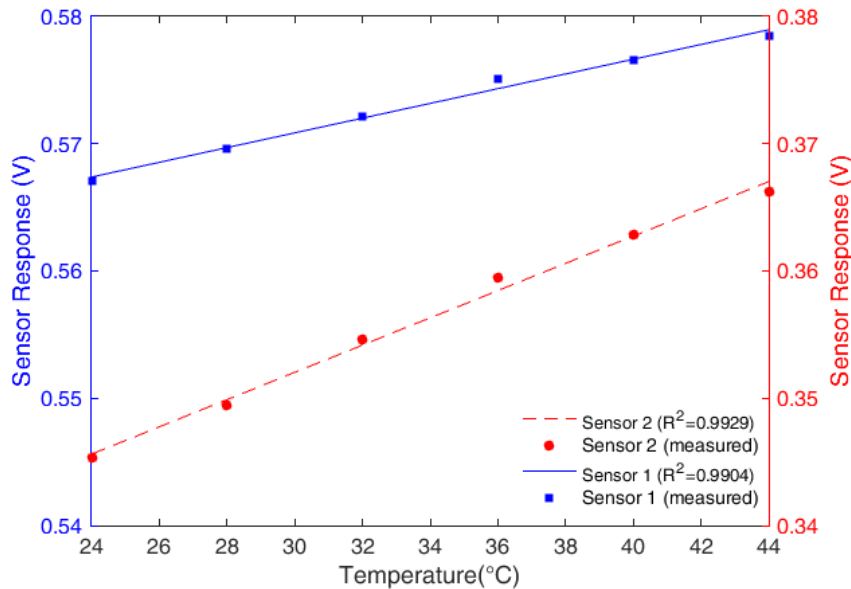


Figure 4-8 Temperature characterization of POF sensors.

In the case of temperature variation, both sensors present the same behavior, i.e. when the temperature increases, the power also increases. This difference in the behavior with temperature and RH may be due to the difference of these parameters in the POF materials, which is related to minor differences between Sensors 1 and 2 torsion angles. In addition, the POF's anisotropy and deviations on the manufacturing parameters such as pulling force and temperature of the fibers can lead to differences in the sensor's behavior. The variation of the humidity may have different effect in the material's mechanical properties, what also can explain the higher sensitivity of the Sensor 2 compared with Sensor 1 (see Figure 4-8). The sensitivity of Sensor 2 with respect to the humidity variations is about 70% higher than the one for the Sensor 1, whereas the sensitivity for temperature variations is 54% higher than the one presented by Sensor 1.

The higher sensitivity of Sensor 2 with respect to the temperature can be related to its higher lateral section depth, which leads to an increase of the stress-optic effect variation due to the temperature effects in the POF's material properties. Since the difference of the sensitivity between Sensors 1 and 2 is higher in the RH analysis, the effect of the RH on both polyethylene and PMMA can lead to an increase of the modulus of one material and a decrease of the modulus in the other. This can explain the difference of 16% of the ratio between the sensitivities of Sensors 1 and 2 with respect to the humidity when compared with the same ratio with respect to the temperature.

#### 4.3.3.3. Simultaneous measurement of temperature and RH

The test is performed with the setup positioned inside the heater and with the air humidifier output positioned on the steam's inlet. In this test, the humidity is increased from 5% to 97% without changing the temperature due to operational limitations. However, the simultaneous variation of humidity and temperature is obtained on the second part of the test, in which the temperature increases from 24°C to 38°C and the humidity drops to almost 25%. Then, the temperature is increased to about 46°C and reduced again to about 41°C, while the humidity had a variation lower than 5%. Figure 4-9 shows the results obtained with the POF sensors in the described test. The response is obtained by applying Eq. 4.6, in which the coefficients of the equation were obtained from the temperature and RH characterization, which are presented in Table 4-1.

The blue dashed lines in Figure 4-9 represent the points or intervals at which the RH of the reference sensor was acquired. The point 'RH1' is the response of the reference sensor in the beginning of the test, and the point 'RH2' is the one of the reference sensor's response when the humidity reaches its maximum value. 'RH3' relates to the interval of the second part of the test, during which the temperature is increased. Since the response time is defined in [171] as the time that the sensor takes to reach the 90% final humidity value (97%), the response time of the proposed sensor is about 5 minutes (measured between RH1 and RH2 without considering the response time of the climate chamber step), which is a response time lower than the ones presented in [141], [171] with the additional advantage of a lower cost. The red dashed lines refer to the intervals of the reference sensor's response with respect to the temperature. 'T1' is the temperature in the beginning of the test; 'T2' refers to the reduction of the temperature during the first part of the test; 'T3' is the

temperature measured after the increase of RH - which rises as long as the humidity reduces - and 'T4' is the maximum temperature obtained during the test. Finally, 'T5' is the temperature measured in the end of the test. It is noteworthy that there is a sharp decrease on the RH at about 8 minutes due to the combined effect of increasing the temperature and turning of the steam inlet.

Table 4-1 Parameters applied on the simultaneous measurement of temperature and relative humidity.

Symbol	Parameter description	Value
$K_{1,RH}$	Relative humidity sensitivity of Sensor 1	$-9.57 \times 10^{-5}$
$K_{1,T}$	Temperature sensitivity of Sensor 1	$-5.78 \times 10^{-4}$
$K_{2,RH}$	Relative humidity sensitivity of Sensor 2	$1.34 \times 10^{-4}$
$K_{2,T}$	Relative humidity sensitivity of Sensor 2	$1.07 \times 10^{-3}$
$P_{1,0}$	Initial power of sensor 1	0.5535
$P_{2,0}$	Initial power of sensor 2	0.3199

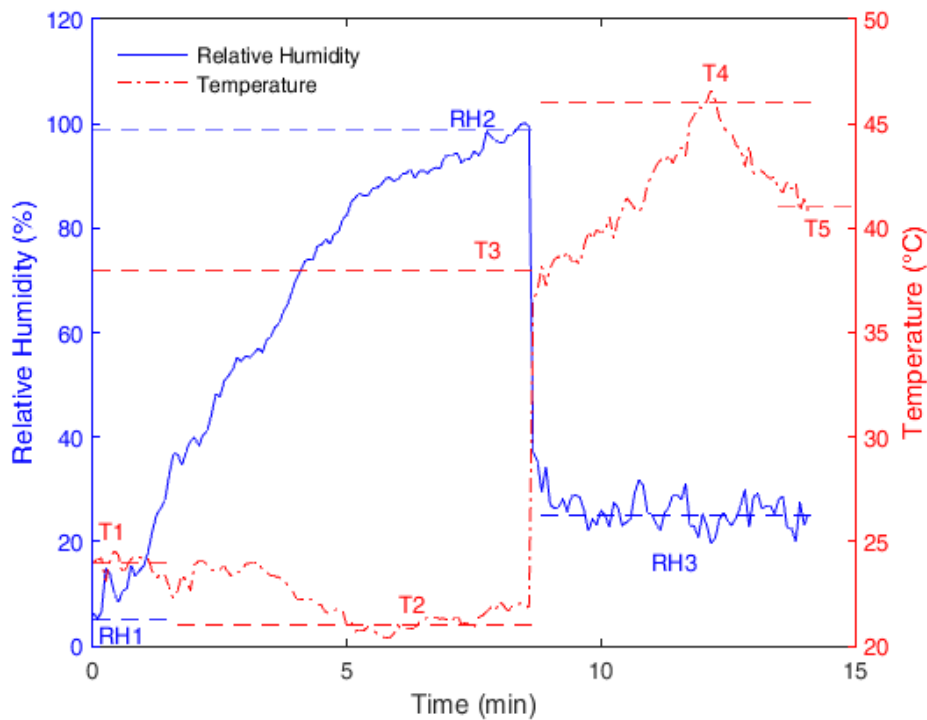


Figure 4-9 POF sensor's response for temperature and humidity tests.

The proposed POF sensors are capable of tracking the humidity and temperature variations. Comparing the measured points of the reference sensor with the POF sensor's responses, the proposed optical fiber sensors showed (with respect to the reference sensor) a RMSE of  $1.12^{\circ}\text{C}$  for temperature and  $1.36\%$  for RH. A limitation of these sensors is that higher changes of the sensor's torque leads to variation of the sensor's behavior. However, it can be reduced if the sensing region of the fibers are protected with a metal coating or some other material (such as 3D-printed materials discussed in the applications of Chapter 6) that prevents the higher variation of the torque in the fiber if it is submitted to an impact or additional strain.

#### 4.3.3.4. Polymer optical fiber etching to reduce humidity sensor response time

Although the proposed sensor is a low-cost solution that is able to measure RH with a response time lower than the ones presented in [141], [171], it still has a response time higher than the one of the etched POFBG presented in [48]. The fiber etching can reduce the polymer Young's modulus and reduce the sensor response time by means of the diameter reduction. In this way, the increase of the POF stress due to fiber diameter reduction improves the humidity sensor's response time [141]. To reduce the response time of the sensor, an

etching was made on the sensor's sensitive zone, such zone was placed inside a container filled with pure acetone for 4 minutes. This chemical treatment leads to a diameter reduction of the POF sensitive zone of about 20% (0.76 mm). Since the solvent absorption leads to a molecular chain relaxation, causing the reduction of the Young's modulus as characterized in [172], the effect of the etching in the fiber results in the response time reduction due to two effects. The first one is the increase of the stress on the fiber due to the Young's modulus and diameter reduction, which improves the sensor's response time as reported in [141]. The other effect is the increase of the rate of water absorption of the PMMA when its diameter is reduced, as reported in [167].

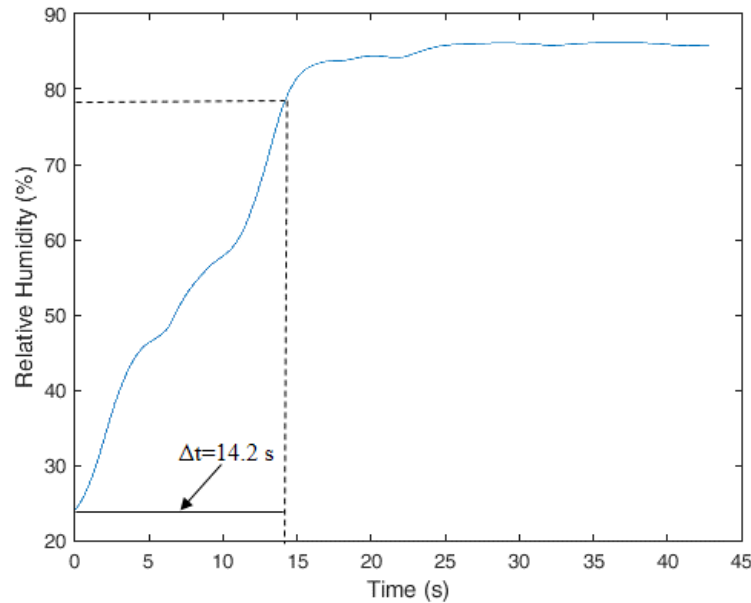


Figure 4-10 Improved response time with the etching on the POF humidity sensor based on induced stress-optic effect.

The response time improvement of the proposed sensor is demonstrated in the tests with the experimental setup presented in Figure 4-6, in which the RH is increased from 25% to about 85%. The obtained results are presented in Figure 4-10, where the sensor presented a response time of 14.2 seconds on the entire range of the test, meaning that for 10% of RH variation, there is a response time lower than 2.0 seconds. Such response time is close to the one presented in [48] since a 4.5 seconds response for a 30% RH variation was reported, meaning a response time for 10% variation of about 1.5 seconds. In addition, the proposed sensor has a lower cost and a higher fiber diameter that makes the POF more robust and easier to handle. However, the etching reduces the sensor's reproducibility and its easiness of its fabrication, creating a tradeoff between the sensor's easiness of fabrication and response time. In applications that response times higher than 2 seconds are not an issue, it may be preferable to use a humidity sensor without etching treatment, such as the one presented in Section 4.3.3.3.

#### 4.4. Multiplexing Technique for Quasi-distributed Sensors Arrays in Polymer Optical Fiber Intensity Variation-based Sensors

The techniques for distributed sensors include optical time-domain reflectometry (OTDR) and optical frequency-domain reflectometry (OFDR), which are commonly employed [173]. However, such techniques have issues related to their spatial resolution of some meters. Although a resolution of centimeter level can be achieved with distributed sensors based on Brillouin analysis, these interrogation techniques generally present much higher cost. In addition, OFDR generally requires bulk hardware that includes components like swept-laser interferometer and microwave photonics circuit. Furthermore, quasi-distributed sensors system based on FBG arrays can have higher resolution, since it is only limited by the physical separation between FBGs. However, these arrays still have aforementioned disadvantages of high interrogation cost and, for FBGs, there is also the necessity of specialized equipment for the grating inscription [68]. A cost-effective sensor quasi-distributed sensor system for liquid leakage detection is presented in [174], where a flexible lamp belt with LEDs is side-coupled to POF with lateral sections. Each end facet of the fiber is connected to a power meter and the forward and backward optical power are compared. However, the system was applied only on the discrete detection of water, i.e., it only shows if there is water or air on each of the detection points [174].

In order to tackle the limitations of the previously proposed distributed and quasi-distributed techniques for optical fiber sensors, this Section presents a multiplexing technique for intensity variation-based sensors. The technique is based on the side-coupling of the light source in a POF sensors with lateral section similar to the one presented in [174]. However, in this case, a control system acquires the signal of each photodetector when each LED is active, which results in a matrix with  $P \times D$  vectors, where  $D$  is the number of LEDs and  $P$  the number of photodetectors. In this way, it is possible to decouple the effects of different parameters in each lateral section of the fiber. The sensor is experimentally validated for 3 degree of freedom (DOF) applications in the simultaneous measurement of temperature, force and angle. The experimental validation also includes two different scenarios: the response of three sensors for the same parameter and with similar sensitivity; and different sensors for different parameters (temperature, force and angle). Since the lack of multiplexing capabilities is regarded as an important issue in intensity variation-based sensors, the technique proposed in this Section enables the advancement of both quasi-distributed sensor techniques and intensity variation sensors. Furthermore, comparing with the conventional technologies for distributed (or quasi-distributed) sensing architectures such as OFDR, backscatter reflectometry, microwave photonics, FBG, the proposed multiplexing technique presents much lower cost and simplicity on the signal processing. In addition, it presents potentially higher spatial resolution than OFDR and OTDR techniques, since the resolution in the proposed technique is limited to the physical distance between the fiber's lateral sections.

#### 4.4.1. Operation Principle and Experimental Setup

The schematic representation of the proposed technique is presented in Figure 4-11. Two photodetectors are positioned on each end facet of the fiber. In addition, each lateral section on the fiber presented in Figure 4-11 is one sensor, where each sensor has a side-coupled LED. A microcontroller is responsible for the activation of the LED array, which are activated with a predefined sequence and frequency in a way that each LED is activated at a time, i.e., there is not the simultaneous activation of two or more light sources. Furthermore, a microcontroller is also responsible for the signal acquisition of both photodetectors when each LED is activated. Thus, a matrix is obtained in which each column represents the POF power acquired by one photodetector when a predefined LED is activated. This matrix is presented in Figure 4-11, where the number of columns is  $2n$  (two photodetectors with  $n$  LEDs) and the number of lines is the number of signal acquisitions. By analyzing and comparing each vector of the matrix, it is possible to obtain the response of  $n$  sensors without the influence of light source deviations.

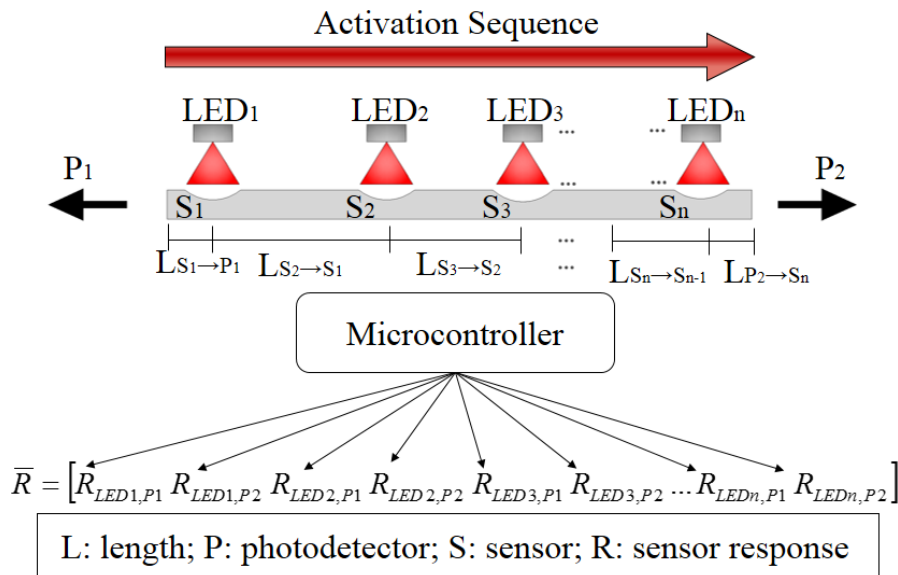


Figure 4-11 Schematic representation of the proposed multiplexing technique for intensity variation-based sensors.

One limitation of the technique is the maximum number of sensors that can be multiplexed. Since there is a power attenuation at each sensor's lateral section, if the fiber presents a high number of sensors, the output power may be too low to be detected. In addition, the sensors sensitivities also lead to a power reduction, which need to be considered in the design of the sensor arrays. However, the initial power attenuation due to lateral section and sensor sensitivity depends on the lateral section parameters (length and depth) of each optical fiber sensor [45], [175]. In order to verify the maximum number of sensors that can be multiplexed, an analytical approach based on the model presented in [176] is performed. Since the sensors work with the power

attenuation principle, the sensors sensitivities and dynamic range also are considered in the POF output power estimation. Taking these parameters into account, the power attenuation with respect to all aforementioned effects is estimated as follows:

$$\frac{P_0}{P_{in}} = \frac{(S_c - NS_0)}{S_c} - \alpha_p L - \sum sens_i r_i. \quad (4.7)$$

Referring to Eq. 4.7,  $N$  is the number of sensors,  $L$  is the fiber's length,  $\alpha_p$  is the fiber attenuation coefficient,  $sens_i$  and  $r_i$  are the sensitivity and dynamic range of each sensor, respectively. After the investigation of the number of sensors and their sensitivities, the next analysis is made to estimate each sensor response of the array. In this case, we consider a fiber with 3 sensors in two scenarios: (i) sensors with the same sensitivity and dynamic range; (ii) sensors with different sensitivities and dynamic ranges. Since the fiber attenuation coefficient and the loss due to the lateral section only lead to an offset in the sensor response, only the last term on the right-hand side of Eq. 4.7 is considered. Thus, the equation for the sensors' simulation is:

$$\left( \frac{P_0}{P_{in}} \right)_{i,j} = \sum_{i=1}^n sens_{i,j} r_{i,j}, \quad (4.8)$$

where  $i$  is the sensor ( $i=1, 2, 3$  in this case) and  $j$  is the photodetector ( $j=1, 2$ ). Equation 4.8 shows that the response of each sensor is comprised of the sum of the other sensors, i.e., the power of Sensor 3 is the sum of the responses of Sensors 1, 2 and 3, whereas Sensor 2 is the sum of 1 and 2. Therefore, in order to obtain the response of a single sensor without the influence of other sensors, it is necessary to compensate the response of the other sensors. In this case, Eq. 4.8 is rewritten as:

$$r_i = \frac{\left( \frac{P_0}{P_{in}} \right)_{i,j} - \left( \frac{P_0}{P_{in}} \right)_{i-1,j}}{sens_i}. \quad (4.9)$$

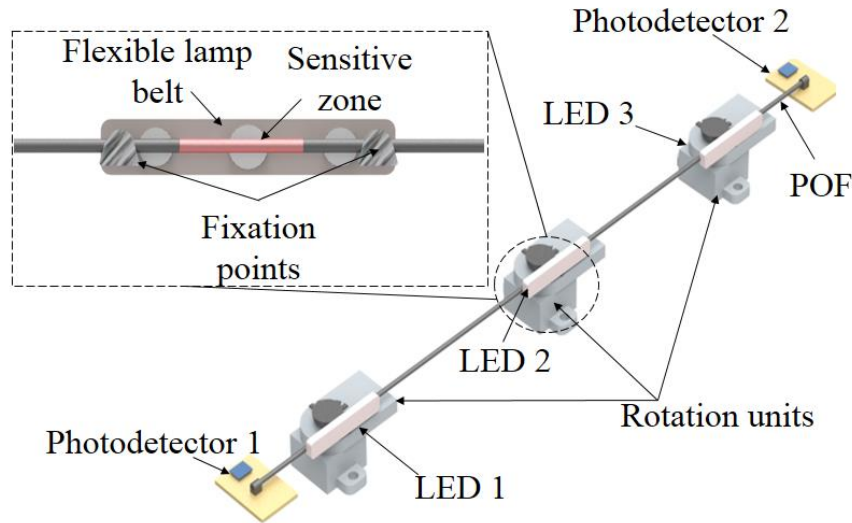
In this way, Eq. 4.9 shows the necessity of characterizing each sensor individually, prior to their applications for simultaneous measurements.

In order to validate the proposed technique for intensity variation-based sensors multiplexing, the same two scenarios are applied. Thus, three lateral sections are made in a multimode POF made of PMMA (HFBR-EUS100Z, Broadcom Limited). In addition, a flexible lamp belt with an array of 3 LEDs each is fixed at each lateral section for the light coupling. The LEDs of the flexible lamp belt emit white light and have about 3 mm diameter each. The POF power is acquired by two phototransistors IF-D92 (Industrial Fiber Optics, USA). The activation of the LED array as well as the control of the signal acquisition are made with a FRDM-KL25Z board (Freescale, Austin, TX, USA), where both the LED activation and signal acquisition frequencies are 10 Hz.

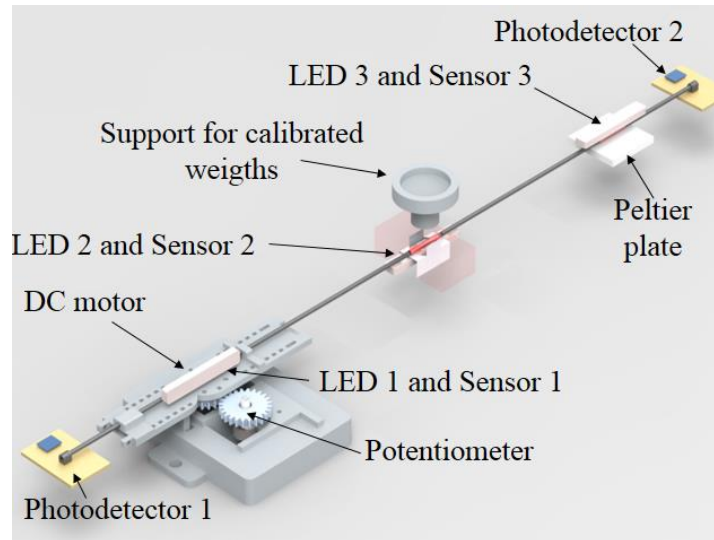
The first set of tests is made with the experimental setup presented in Figure 4-12(a), where there are three rotation units with a goniometer embedded. First, each sensor is individually characterized with relation to the other sensors at  $0^\circ$ , where the maximum range of the sensor characterization is between  $0^\circ$  to  $80^\circ$  in  $20^\circ$  steps. Then, tests with simultaneous movements of all three sensors are performed to show the capability of the system of tracking the response of each sensor. Thereafter, we employ another experimental setup to evaluate the sensor performance for multi-parameter sensing. Thus, the fiber with three lateral sections is positioned on the setup of Figure 4-12(b), where there is the angle variation through a DC motor with a closed loop position control. The angular range for the angle characterization is 0 to  $90^\circ$  with constant angular velocity of 0.1 rad/s. Furthermore, there is a setup for transverse force assessment, in which different calibrated weights are applied on the fiber lateral section, resulting in transverse forces of 0 to 50 N.

Finally, the last lateral section of the fiber is positioned in a thermoelectric Peltier plate (TEC1-12706, Hebei IT) with a temperature controller (TED 200C, Thorlabs). The temperature in this characterization was varied from  $25^\circ\text{C}$  to  $55^\circ\text{C}$  in  $10^\circ\text{C}$  steps. After the characterization, the multi-parameter sensing capabilities of the proposed multiplexing technique is evaluated through the simultaneous variation of all three parameters within the range each sensor was characterized. The fiber used in the tests has about 50 cm length. Moreover,

the distances between the photodetector 1 and the Sensors 1, 2 and 3 (LP1→S1, LP1→S2, and LP1→S3) are 1.6 cm, 7.6 cm and 12.7 cm, respectively. It is worth to mention that all the performed tests were made at controlled humidity conditions of  $64\% \pm 2\%$ , since the humidity can affect the sensor response [141].



(a)



(b)

Figure 4-12 Experimental setup for (a) multiplexing technique validation with the array of 3 curvature sensors. (b) Validation for a multi-parameter application.

## 4.4.2. Results and Discussion

### 4.4.2.1. Angle measurement with 3-DOF

As the first step in the multiplexing technique application, all three sensors are individually characterized, i.e., when one sensor is under curvature the others are at straight position (without curvature). Figure 4-13(a) shows the signal acquired by photodetectors 1 and 2 during a test, where each sensor is individually activated. From the results of Figure 4-13(a) it is possible to observe the interesting feature of the proposed technique, when one sensor is active, the highest response in the photodetector is the one acquired when the corresponding sensor is illuminated by its respective LED, i.e., when Sensor 1 is active, the highest signal variation occurs in vectors RLED1, P1 and RLED1, P2. Similarly, the highest variation for the Sensor 2 was acquired in photodetector 1 (RLED2, P1), which is the one closest to the Sensor 2, where similar feature also happens with Sensor 3. In addition, the characterization of each sensor in different intervals is depicted in Figure 4-13(b), where a linear regression was made for each sensor to obtain the sensitivities and initial offset in the curves. Furthermore, Sensors 1, 2 and 3 are characterized with the angular ranges of  $60^\circ$ ,  $40^\circ$  and  $80^\circ$ , respectively due to experimental limitations of the setup presented in Figure 4-12(a). In this case, the movement of one

sensor is limited, especially for Sensor 2, when the other sensors are kept at the straight position. Moreover, Sensor 3 is the one with more freedom of movement when the other sensors are positioned without bending.

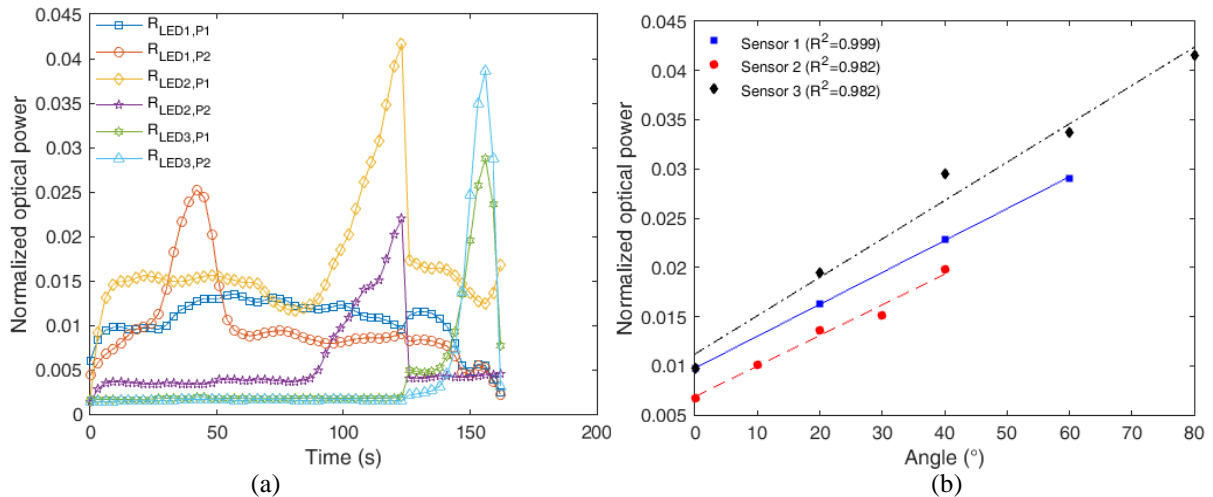


Figure 4-13 POF sensor array characterization for 3-DOF angle measurement (a) signal acquired by the photodetectors when each LED is active and (b) linear regression for the angle characterization with each sensor.

Regarding Figure 4-13(a), it is worth to mention that, besides photodetector 1 for Sensor 1, the sensors responses are acquired by both photodetectors. The reason for the low signal variation in photodetector 1 is related to the distance between Sensor 1 and photodetector 1; and the coupling between the lateral section of this sensor and its respective LED. Nevertheless, Figure 4-13(b) shows almost the same sensitivity ( $3.41 \times 10^{-4} \pm 4.24 \times 10^{-5} (^{\circ})^{-1}$ ) for all three sensors.

The next step is the application of the sensor array in angle measurement with 3-DOF. In this case, the sensors are placed on the desired positions and the signals are acquired by the photodetectors. The test is made by placing the sensors in 10 different positions as presented in Figure 4-14 (as the reference signals for Sensors 1, 2 and 3) with the comparison between each sensor position estimation and the actual position obtained from the goniometer position. The results presented in Figure 4-14 show the capability of each sensor of tracking the angle of each rotation unit (see Figure 4-12(a)). Therefore, the sensor array with the proposed multiplexing technique is an interesting alternative to measure multi-DOF angles, which is a condition commonly observed in lower limb exoskeletons, where there are 3-DOFs, one for the hip joint and the others for knee and ankle joints [18]. Regarding the estimated errors, the RMSE between Sensor 1 and the reference is  $2.76^{\circ}$ , whereas the RMSE for sensors 2 and 3 are  $3.22^{\circ}$  and  $2.44^{\circ}$ , respectively. Comparing to the characterization condition, where the mean of each sensor RMSE is  $2.01^{\circ}$  for the three sensors, the difference between the RMSE in the simultaneous measurement condition is similar to the one when each sensor is activated without the influence of the others. These results also show the feasibility of the proposed technique. The obtained errors may be related to the low signal amplitude obtained from photodiode 1 when Sensor 1 is active and due to influence of modal distribution in the fiber under curvature in different points. Nevertheless, these effects do not lead to high errors in the measurement, since the mean RMSE difference between the 1-DOF (condition used in the characterization) and 3-DOF is about  $0.80^{\circ}$ .

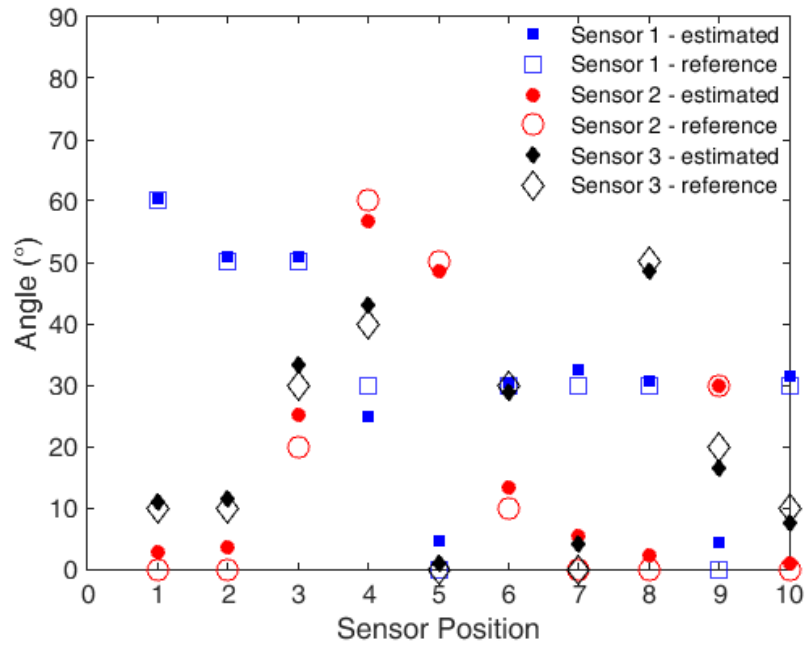


Figure 4-14 Sensor response in the 3-DOF validation test.

#### 4.4.2.2. Multi-parameter application with 3 POF sensors

In order to validate the sensor array for multi-parameter applications, the fiber is positioned in the experimental setup of Figure 4-12(b) and the analysis is made in two steps: sensor characterization and simultaneous measurement of angle, transverse force and temperature. Thus, the first set of tests is performed with the variation of a single parameter, while the others are kept constant. The characterization of each sensor is presented in Figure 4-15, where the sensitivities for angle, force and temperature are, respectively,  $2.08 \times 10^{-4} (\text{°})^{-1}$ ,  $6.41 \times 10^{-5} \text{N}^{-1}$  and  $-1.745 \times 10^{-5} (\text{°C})^{-1}$ .

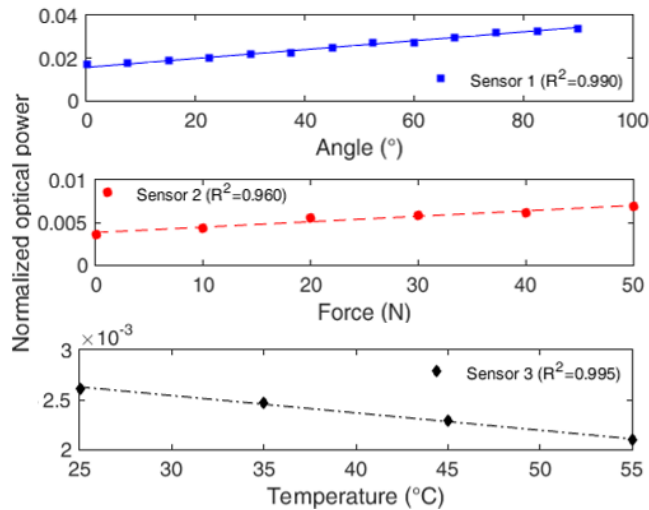


Figure 4-15 Experimental characterization of each sensor for multi-parameter application.

After characterizing the three sensors, simultaneous variations of angle, transverse force and temperature are performed, where the signals acquired for Sensors 1, 2 and 3 with the photodetector 1 are presented in Figure 4-16(a). As also observed in the response of Figure 4-13(a), the signal acquired when each LED is illuminating its respective sensor has the response of the active sensor. Thus, the response of Sensor 1 (employed for angle measurements) presents similar pattern that the one applied by the DC motor, whereas Sensor 2 shows the signal variation when the transverse force is applied. Similarly, the temperature sensor (Sensor 3) shows the signal variation according to the applied temperature variation. However, since its sensitivity is lower than the other sensors, the power variation of the Sensor 3 is lower than the one observed to the other sensors.

Figure 4-16(b) shows the estimated angle, force and temperature with Sensors 1, 2 and 3, respectively. The responses are obtained with the linear regression coefficients of the sensors characterization (from Figure 4-15) for the estimation of each parameter. The presented results show that the proposed multiplexing technique for the POF sensor array is capable of tracking simultaneous variation of different parameters (angle, force and temperature) in sensors with different sensitivities.

Regarding the errors in the multi-parameter application, the RMSE for the angle measurement is about  $2.87^\circ$ , which results in a relative error of 3.18% when the whole angular range is considered (about  $100^\circ$ ). In the force measurement, the RMSE is 3.47 N with a relative error of 5.78% if the whole force range is considered, which is relatively higher than the one for the angle measurement. The reason for this behavior is the nonlinearities of the transverse force measurement, which presents the lowest linearity among the analyzed parameters. Such nonlinearities can be related to the nonlinear behavior of the stress-strain curves in polymers. Thus, the stress transversely applied in the fiber can result in a nonlinear variation of the fiber curvature. In addition, these nonlinearities lead to higher errors when a linear regression is made to obtain the sensor response.

Regarding the errors in the temperature measurement, a RMSE of  $0.75^\circ\text{C}$  was obtained in the temperature range of  $55^\circ\text{C}$  to about  $25^\circ\text{C}$ , which results in a relative error of 2.50%. This relative error is the lowest among the tested parameters. Such lower error can be related to the fact that the fiber fixed in both ends of the Peltier plate, keeping the fiber always in the straight position and without movement, which reduces the influence of modal distribution in the sensor response. In addition, temperature characterization has shown the highest linearity among the ones tested. It also contributes to lower errors in the linear regression of the sensor response for temperature estimation.

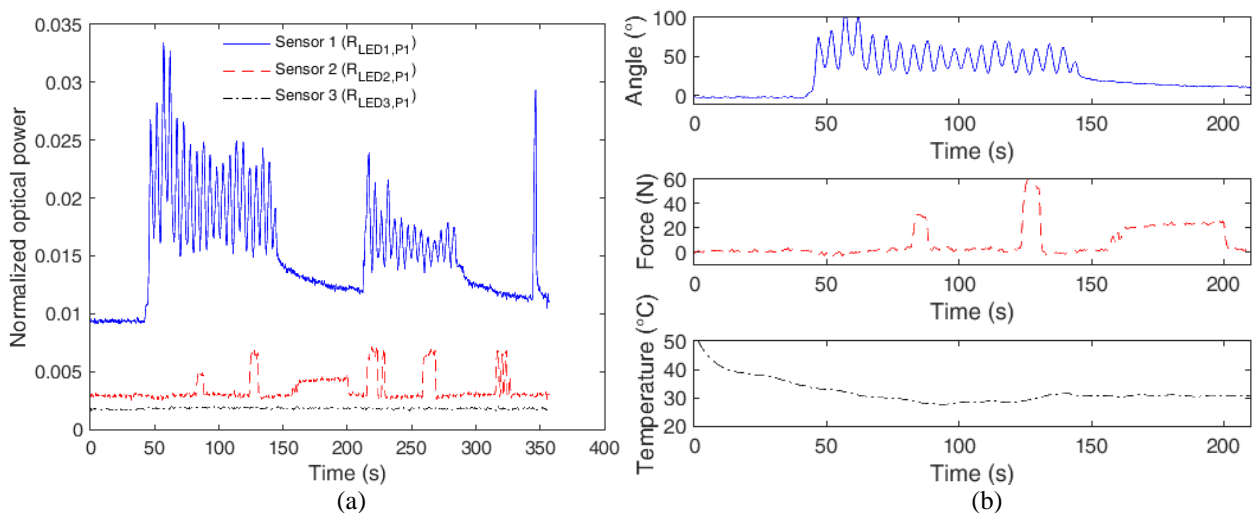


Figure 4-16 (a) Responses of the three sensors acquired by the photodetector 1. (b) Angle, force and temperature measurements using the proposed multiplexing technique acquired for 210 seconds.

In summary, the results presented in this section validate the multiplexing technique in different experimental conditions. In this way, a quasi-distributed sensor system is obtained, where the sensor array presents much lower cost than quasi-distributed sensor arrays based on FBGs [135]. Moreover, the sensor spatial resolution is only limited by the LEDs irradiance, since each lateral section needs to be illuminated by only one LED. For this reason, one can assume that the spatial resolution, i.e., the minimum distance between two sensors can be similar to the ones of sensor arrays based on FBGs.

## 4.5. Final Remarks

Aiming at the advantageous features of low cost, ease of implementation and simplicity on the data analysis and acquisition, in this Chapter, the development and applications of intensity variation-based sensors were presented. The development and performance enhancement of the presented different POF sensors were possible after using the knowledge of the PMMA POF material features acquired in Section 3.3 in conjunction with the operation principle of the intensity variation-based sensors discussed (and modelled in Appendix A). With this background, novel POF-based sensors for microclimate assessment using the stress-optic effect as well as a torque sensor can be proposed and applied in wearable devices. In addition, using the concepts of

polymer viscoelasticity, different compensation techniques for the POF sensors nonlinearities, hysteresis and creep response were proposed and validated.

The sensors proposed in this Chapter enable a plethora of applications in healthcare devices as shown in Chapter 6, which cover from instrumented insoles through SW's instrumentation with many applications in robotic exoskeletons, orthosis and even in FES systems (see Appendix E for FES application). Therefore, the sensor systems proposed in this Chapter can be used in healthcare and can provide sensors feedback in cloud health services. Additionally, it also opens the possibility of novel control strategies in robotic devices for gait assistance. As the advances in polymer processing and characterization occur combined with increasing demands on instrumentation systems, even more applications for those sensors will be proposed in near future. Thus, the results presented in this Chapter can pave the way for optical fiber sensors applications in healthcare devices of different types and purposes.

## Chapter 5. Fiber Bragg Gratings-based Sensors

### 5.1.Introduction

Among different techniques for optical fiber sensing, FBGs attract significant attention due to their multiplexing capabilities, which make it possible to inscribe long arrays with increasing number of sensors in the same fiber [69]. FBGs are periodic modulations of the fiber core's refractive index and different gratings can be inscribed in the same fiber by just modifying the period of this refractive index modulation. In this way, each grating acting as a wavelength selective filter, reflecting light at a discrete wavelength that is directly proportional to the inscribed period. Changes to the period as a result of external perturbations are recovered as wavelength-encoded data. This offers a huge advantage as the data is an absolute quantity and may be recovered even if the signal is temporarily interrupted. For these reasons, this Chapter presents the development of FBG-based sensors for assistive devices. The FBGs were inscribed in commercially available CYTOP fibers using the plane-by-plane direct write inscription method with an fs laser. The sensor development is performed using the background acquired in Chapter 3, where the CYTOP fibers were characterized, enabling the development of the compensation techniques proposed in this Chapter.

### 5.2.FBG Inscription Using fs Laser

The FBGs used in this Chapter were inscribed in Cyprus University of Technology (CUT) using a fs laser operating at 517 nm with 220 fs pulse duration (HighQ laser femtoREGEN) in a gradient index multimode CYTOP fiber (Chromis Fiberoptics Inc) with a core diameter of 120  $\mu\text{m}$ , a cladding thickness of 20  $\mu\text{m}$  and a polycarbonate overladding resulting in a total diameter of 490  $\mu\text{m}$  (see Figure 5-1). Regarding the inscription parameters, the repetition rate of 5 kHz and a pulse energy of 80 nJ were used. As shown in Figure 5-1, the laser beam is focused in a 5  $\mu\text{m}$  extent of the fiber core using a  $\times 50$  objective lens carefully positioned in order to guarantee the refractive index modifications in the center of the fiber core. In this way, a single peak spectrum obtained in a multimode POF due to the optimization of the inscription parameters to control the coupling between the grating and the core modes by inscribing the grating only at a part of the core. In addition, the CYTOP fiber is positioned on an air-bearing translation stage that provides two-dimensional motion with a nanometer precision for the direct write, plane-by-plane inscription. Figure 5-1 inset shows the magnified view of the POF with the inscribed FBGs and, for comparison purposes, a magnified view of the POF without the FBGs is also shown.

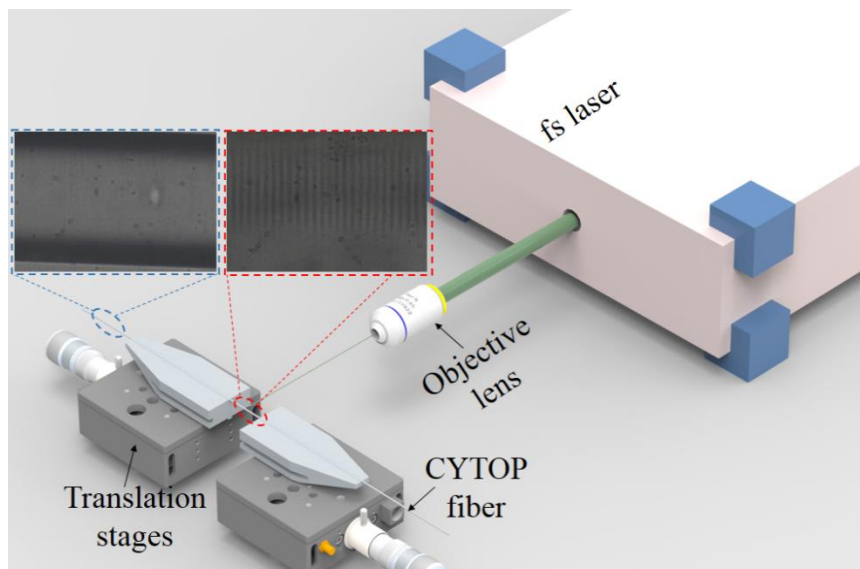


Figure 5-1 Schematic representation of the experimental setup used in the gratings inscription. The insets show a magnified view of the CYTOP with and without FBG.

The FBG interrogators used to inscribe the grating spectra require a connection with a single mode fiber (SMF) to guarantee a stable measurement. This means that we must connect the POF with a silica fiber pigtail and avoid relative movement between fibers to minimize measurement errors. For this reason, the connectorization is made in two steps, first by means of UV gluing (curing) the POFBG with a multimode silica fiber (MMF). Secondly, we fuse splice the silica SMF and the MMF; this ensures a stable connection

between the POFBG and the interrogation system (see Figure 5-2). In addition, for the applications in healthcare devices (see Chapter 6) a 3D-printed structure is positioned on the UV joint in order to increase its robustness and isolate it from mechanical disturbances.

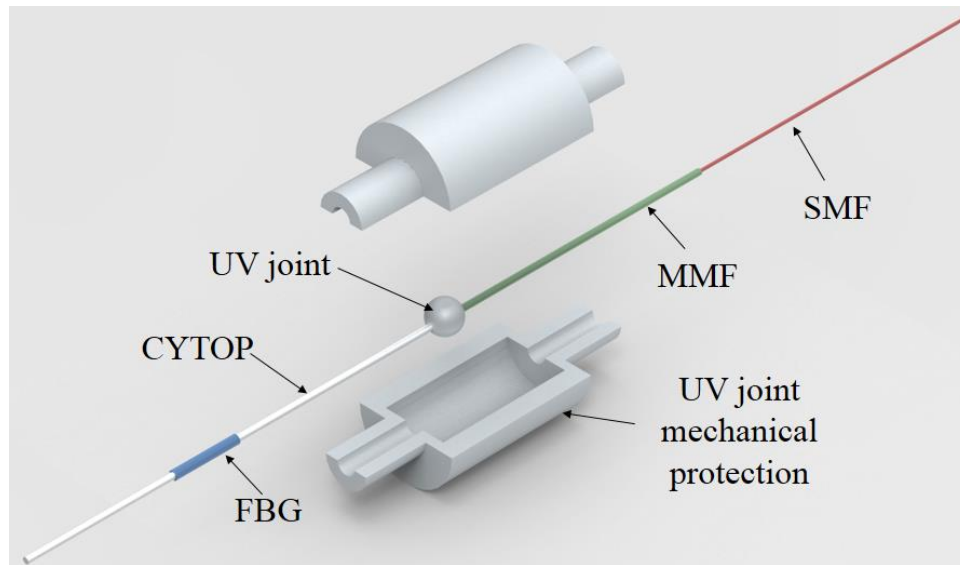


Figure 5-2 Schematic representation of the POF connectorization.

### 5.3. Influence of Thermal Treatments and Compensation Techniques in FBGs Responses

In order to investigate the effects of annealing in POFBGs in CYTOPs, this section presents strain, transverse force and temperature behavior of CYTOP POFBGs before and after annealing for two different conditions, namely annealing at low humidity and a repetition of the same thermal treatment, but under water. In addition, we present a dynamic compensation technique for further improvement of the sensor performance, especially with respect to the reduction of hysteresis.

#### 5.3.1. Experimental Setup

The annealing is a thermal treatment during which the fiber is kept in temperatures close to its glass transition temperature [177]. Such treatment in POFBG sensors can reduce their hysteresis during strain and temperature cycling [178] and increase their sensitivity [179]. In addition, the sensor performance can be improved if the annealing is made under high humidity conditions [60], [180]. For this reason, annealing was made with the sensor under water, for an annealing temperature of 90°C and duration of 24 hours.

The test employs two POFBG samples, where one of them is subjected to annealing at low humidity conditions (RH of about 15%) and the other to annealing under hot water (RH of 100%). The annealing temperature is 90 °C, which is below the CYTOP  $T_g$  (about 108 °C) [181] and the annealing time is 24 h for both low and high humidity cases. The samples are positioned on the setups presented in Figure 5-3(a), (b) and (c) for temperature, strain and transverse force tests, respectively, where there is a comparison of POFs sensitivity, linearity and hysteresis before and after the annealing. In addition, the grating spectra were recorded using an FBG interrogator (sm125, Micron Optics),

In the temperature tests, the climate chamber 1/400 ND (Ethik Technology, Brazil) provides the temperature variation from 30 °C to 60 °C for both increasing and decreasing temperature cycles, where the upper limit of temperature test is below annealing temperature employed to eliminate the effect of additional changes to polymer properties during the temperature test. In addition, strain cycles are made with a translation stage having micrometer accuracy, (Figure 5-3(b)) for a strain range of  $\sim 1000 \mu\epsilon$  ( $\sim 1\%$  strain). Regarding transverse force characterization step, the POFBG is positioned between two plates, as shown in Figure 5-3(c) inset. Then, different calibrated weights are placed on the support that applies a force to the top plate, which is transmitted to the POFBG.

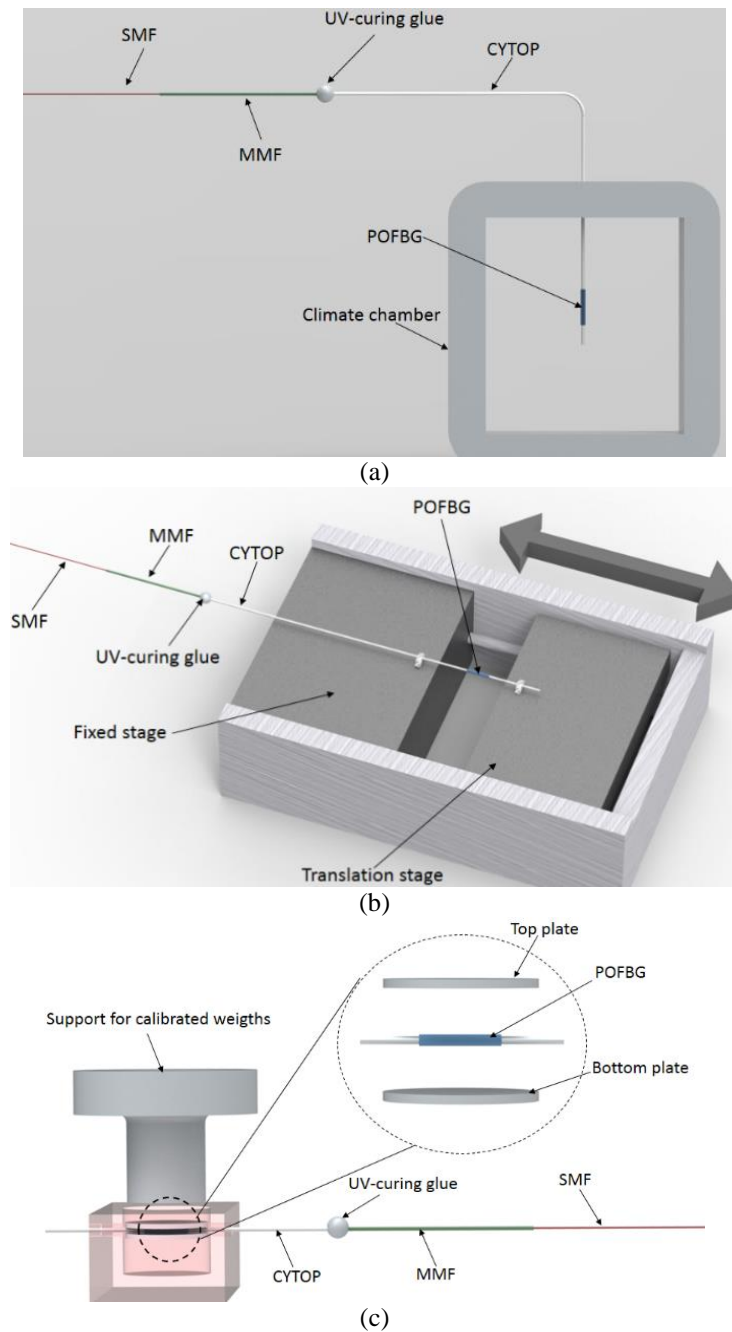


Figure 5-3 Experimental setup employed for (a) temperature characterization, (b) strain characterization and (c) transverse force characterization, the inset shows the assembly of the POFBG between the plates.

The hysteresis compensation technique applied to the sensor requires the characterization of polymer relaxation as further discussed in [182]. In this case, the polymer relaxation is characterized through wavelength shift monitoring at a predefined strain on the fiber and the loading and unloading cases are compared, in which two characterization equations are obtained, one for loading and the other for unloading case. Since there is the same strain rate for all cycles, the compensation technique proposed here is the particular case for which the strain rate is constant.

As a constant load is applied in the fiber, there is relaxation in the polymer chains that can be described as a sum of exponentials, where such sum is known as Prony series [59]. Thus, Prony series is an expression for the polymer relaxation function, which gives a better approach of the polymer response than just applying the Maxwell's model with a single exponential [182]. This analysis is different from the one using Arrhenius fit [183], since it is made with respect to the time, instead of the temperature, as made with the Arrhenius fit. The coefficients of the Prony series are obtained in the polymer relaxation results, where general formulation of the Prony series is as presented in Chapter 4. Prony series considers the sensor response as a sum of exponentials and the hysteresis compensation technique consists of time-dependent terms separation in the

polymer relaxation function. If the POF presents a relaxation function of order 1, the compensated wavelength shift ( $\lambda_0$ ) is given by Eq. 5.1, where  $\lambda(t)$  is the measured wavelength shift.

$$\lambda_0 = \lambda(t) \exp\left(\frac{-t}{\tau_n}\right)^{-1} \quad (5.1)$$

However, for a constant strain rate, the time is the ratio between the strain variation (in  $\mu\epsilon$ ) and strain rate (in  $\mu\epsilon/s$ ), which physically means that there is a direct relation between the applied strain and the polymer relaxation as demonstrated in [78], [184]. In addition, a load dependency was also demonstrated in silica optical fibers operating at high temperatures with regenerated gratings [183]. Thus, it is possible to linearize Eq. 5.1 with respect to the strain rate, since the latter is constant in the performed analysis. Hence, the compensated variation of wavelength shift with a certain parameter can be obtained from a linear equation for loading case; and another one for unloading that considers not only the parameter variation, but also the polymer relaxation variation on loading and unloading cases. Such compensation results in a second order polynomial for the loading cycles.

## 5.3.2. Results and Discussion

### 5.3.2.1. Thermal Treatments

The POF annealing causes a blue shift of the Bragg wavelength proportional to the annealing conditions, namely temperature, time and humidity. Figure 5-4(a) presents the POFBG spectrum before and after the annealing at low humidity, whilst Figure 5-4(b) shows the spectrum before and after the annealing under water.

Although the annealing leads to a blue shift in both cases, the wavelength variation was higher in the case of the annealing under water. The reason for this behavior is the polymer swelling (especially in the polycarbonate coating) and the reaction between the water and the polymer chains of the fiber leads to a refractive index reduction in the fiber core [48]. The blue shift for the low humidity case was about 3.5 nm.

For annealing under hot water, the permanent shift in the Bragg wavelength was 10.8 nm, which corresponds to a fiber shrinkage of  $\sim 0.8\%$ . Through considerations of conservation of mass, we note that as the fiber shrinks it also becomes marginally thicker. In addition, the annealing under water also resulted in an increase of the grating reflectivity, whereas it presented a small reduction for the annealing at low humidity. Nevertheless, CYTOP fibers show a lower blue-shift after the annealing process compared with the results reported for mPOFs [179], [180]. The reason for this behavior is related to the fabrication process of CYTOP fibers that is based on heated extrusion of polymer, and which may introduce lower internal stress in the fiber than the drill-and-draw method for mPOFs fabrication [88]. With lower internal stress, the annealing results in lower fiber shrinkage that leads to a lower blue shift in the Bragg wavelength, for both low and high humidity conditions. The differences between the spectra presented in Figure 5-4(a) and (b) are also related to differences on the fiber connectorization with the UV-curing glue, which is a manually made process and can lead to some inaccuracies or misalignments and lower repeatability than the conventional fusion splice in silica fibers. It is interesting to note that whereas the core diameter is  $120\mu\text{m}$ , the number of core modes that couple to the grating are limited, and we observe just a few strong reflections. This is an advantage of the inscription method.

To evaluate the influence of each thermal treatment on sensors' responses, temperature characterization tests are made for each sensor presented in Figure 5-4. Figure 5-5 shows the temperature results for the non-annealed and annealed POFs. The results are presented with respect to wavelength shift in order to make an intuitive comparison between each sample. It is worth mentioning that the hysteresis standard deviation of non-annealed sample is higher than the annealed ones, since the non-annealed results refer to two POFBGs, one before the annealing at low humidity (see Figure 5-4(a)) and the other before annealing under water (see Figure 5-4(b)).

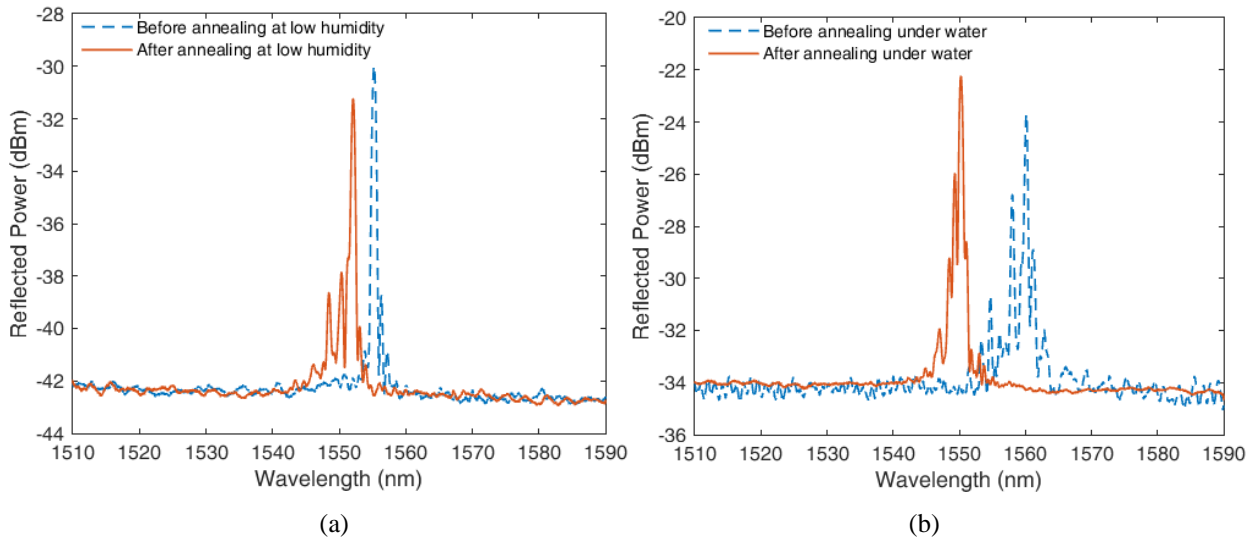


Figure 5-4 Reflection spectra of the POFBGs before and after the annealing (a) at low humidity (b) under hot water.

The sensors that have undergone annealing at low humidity and those without annealing presented similar sensitivities, where the sensitivity of annealed sensor is slightly higher (20.95 pm/°C) than that of the non-annealed (19.75 pm/°C). Also, annealing at low humidity provided a hysteresis reduction of greater than 20% when compared with the non-annealed sensor.

On the other hand, the annealing under hot water resulted in a sensor with lower temperature sensitivity (5.05 pm/°C). However, it also presents the lowest hysteresis among the samples tested (2.28%), which is more than a factor of two lower in comparison with the non-annealed sensor (5.85%). Table 5-1 summarizes the performance parameters obtained for each sensor on the temperature test.

The results presented in Table 5-1 show a tradeoff between all the tested samples, where non-annealed POFBG presented the highest linearity, annealed at low humidity showed the best performance with respect to the sensitivity and the lowest hysteresis was found in the sample annealed under water. Since the linearity of each sample was obtained only as the temperature increases, it does not present a direct relation with sensor hysteresis. For this reason, the non-annealed sample showed higher linearity with the temperature increase, but also presented the highest difference between temperature increase and decrease curves.

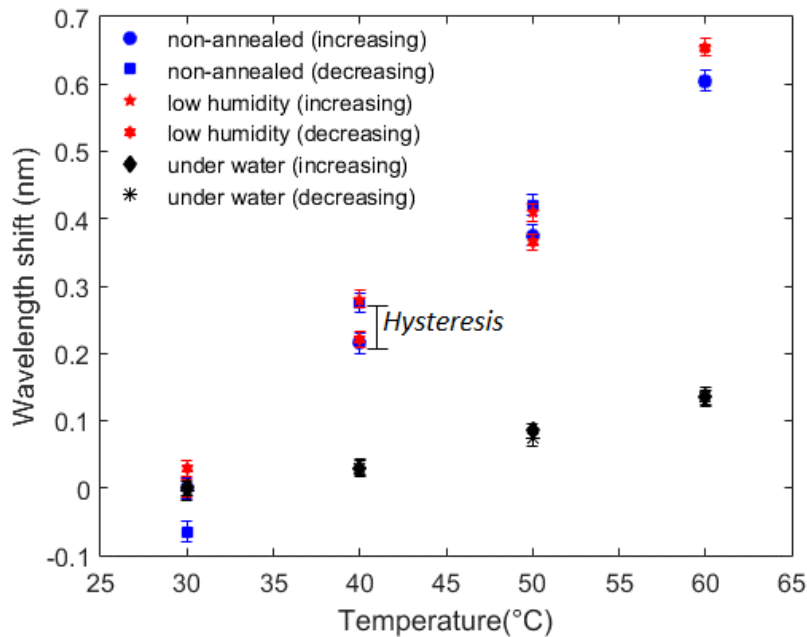


Figure 5-5 Increasing and decreasing temperature response of POFBGs with and without different thermal treatments. The region of high hysteresis is also indicated in the figure.

Table 5-1 POF performance parameters in temperature tests.

Sensor	Sensitivity	Hysteresis	Linearity
Non-annealed	19.75 pm/°C	5.85%	0.996
Low humidity	20.95 pm/°C	4.61%	0.983
Under water	4.50 pm/°C	2.28%	0.986

The comparison between thermal treatments is now performed in the strain response of each sensor. In this case, each sensor is subjected to a maximum strain of 1000  $\mu\epsilon$  in 250  $\mu\epsilon$  steps in loading and unloading cycles. Figure 5-6 presents the results of sensor strain cycles. The results show that there is a hysteresis reduction in the response of annealed fibers, which is indicated by the difference between the wavelength shift in increasing and decreasing cycles, shown in Figure 5-5. In addition, the annealing under water resulted in a sensor with higher sensitivity compared with sensors that were not annealed or annealed at low humidity. Hence, in this case, annealing under water results in a sensor with both lower hysteresis and higher sensitivity. On the other hand, the annealing at low humidity leads to the hysteresis reduction at cost of a small reduction of sensor sensitivity. The comparison of each sensor is summarized in Table 5-2 for the strain performance, where the sensor annealed under water also presented the highest linearity among the ones tested.

Transverse force tests are made with the experimental setup presented in Figure 5-3(c), for which Figure 5-7 shows the sensor response for loading and unloading cycles in the range of 0 to 15 N, in steps of 5 N. Once again, annealing under water leads to the highest reduction of the hysteresis, whereas annealing at low humidity also results in a lower hysteresis when compared with non-annealed POF. Additionally, annealing under water leads to a sensitivity of -341.7 pm/N, which is 48.2% higher compared to the non-annealed fiber (-188.3 pm/N) and 35.5% increase comparing with the sample annealed at low humidity (-225.0 pm/N). This higher sensitivity is related to the reduction of fiber’s Young’s modulus caused by the annealing, which is further reduced when annealing is made under high humidity conditions (100% in this case). The sensor annealed under water also presented the highest linearity among the tested samples. Table 5-3 presents the performance parameters of each sensor under transverse force cycles for comparison purposes.

Table 5-2 POF performance parameters in strain cycles.

Sensor	Sensitivity	Hysteresis	Linearity
Non-annealed	1.13 pm/ $\mu\epsilon$	7.21%	0.980
Low humidity	0.95 pm/ $\mu\epsilon$	4.84%	0.997
Under water	1.69 pm/ $\mu\epsilon$	1.43%	0.998

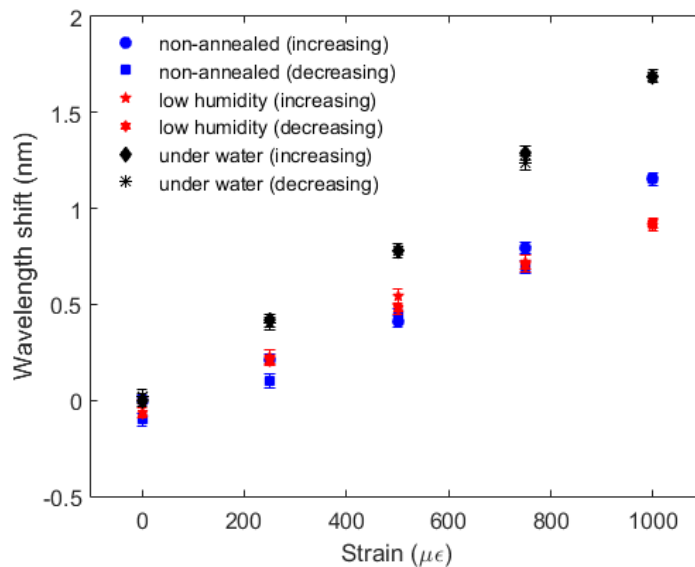


Figure 5-6 Response of POFBGs with and without different thermal treatments for sequential strain cycles.

Table 5-3 POF performance parameters in transverse force cycles.

Sensor	Sensitivity	Hysteresis	Linearity
Non-annealed	-188.3 pm/N	4.62%	0.934
Low humidity	-225.0 pm/N	4.84%	0.995
Under water	-341.7 pm/N	3.12%	0.999

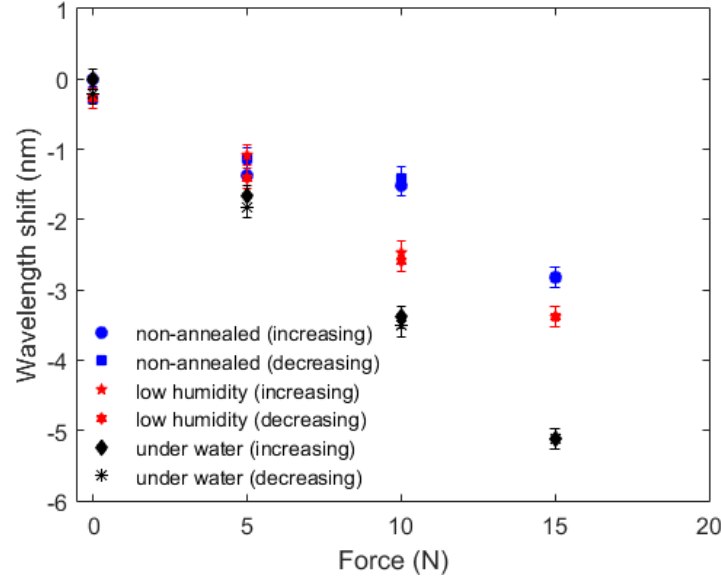


Figure 5-7 Response of POFBGs with and without different thermal treatments for sequential transverse force cycles.

### 5.3.2.2. Dynamic Compensation Technique

The compensation technique discussed in Section 5.3.1 is applied with respect to temperature, strain and force. In addition, a comparison is made for sensors with and without the compensation technique. With the aim of obtaining the sensor with the best performance parameters (among the ones tested), the sample chosen in each case is the one that presents the highest sensitivity, since the technique can improve both linearity and hysteresis, but has no influence on sensor sensitivity [182].

For this reason, the chosen sample for temperature measurement is the one annealed at low humidity, whilst the POFBG annealed under water is the chosen one for strain and transverse force measurement. Thus, the compensation is applied for two sets of samples, the ones after annealing at low humidity and under water. To obtain compensation of the polymer viscoelasticity, we apply three loading and unloading cycles to the fibers, such as the ones presented in previous section, and correlate the responses for loading and unloading, where the same range was used for loading/unloading cycles of each measurement type. Such characterization results in two equations for each sensor, one for loading and the other for unloading cycles. Equations 5.2-5.7 present the compensation for loading and unloading cycles for temperature, strain and transverse force sensing, respectively.

$$\lambda_{l,T} = 0.021T_r - 0.61, \quad (5.2)$$

$$\lambda_{u,T} = -0.027T_r + 1.60, \quad (5.3)$$

$$\lambda_{l,\varepsilon} = 0.0017\varepsilon - 0.077, \quad (5.4)$$

$$\lambda_{u,\varepsilon} = -0.0017\varepsilon + 1.66, \quad (5.5)$$

$$\lambda_{l,F} = -0.342F + 0.018, \quad (5.6)$$

$$\lambda_{u,F} = 0.325F - 5.12, \quad (5.7)$$

where  $T_r$ ,  $\varepsilon$  and  $F$  refer to temperature, strain and force, respectively. In addition, the subscript l is loading, whereas u is for unloading cycles. Regarding the temperature tests, Eq. 5.2 and Eq. 5.3 are applied for increasing and decreasing temperature, respectively. The obtained compensated results are presented in Figure 5-8.

The employed compensation technique leads to a 50% reduction of the hysteresis, which is now  $\sim 2\%$ . Therefore, the combination of thermal treatments and signal processing techniques lead to a sensor with similar hysteresis when compared with the sensor annealed under water, but without adversely affecting the sensitivity, as results from the process of annealing under water. In addition, there was also a slight increase of sensor linearity, it was 0.9883 before the compensation technique application and becomes 0.9890, after the compensation technique.

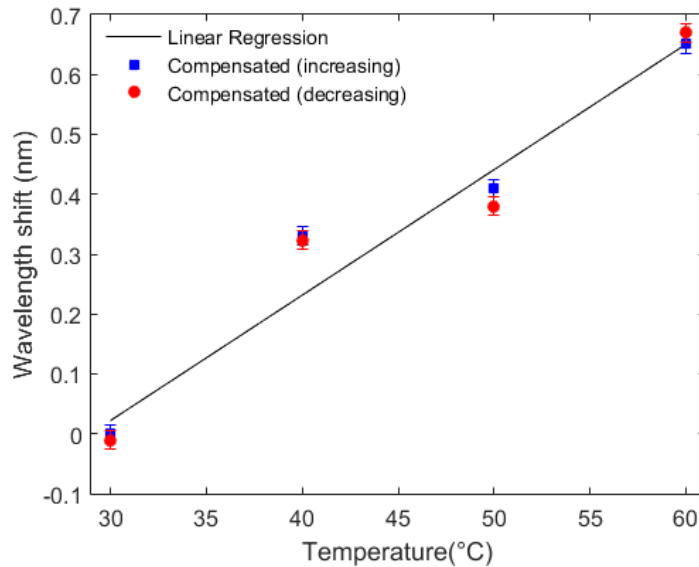


Figure 5-8 Temperature compensated response for the sample annealed at low humidity.

The same methodology is applied on sensor annealed under water for strain and transverse force measurements. Figure 5-9 presents the wavelength shift with respect to strain after the compensation technique application. Once again, the technique was able to reduce the sensor hysteresis. However, the reduction is not as high as in temperature response, since the hysteresis of the sample annealed under water was already low (1.43%). For this reason, for strain sensing applications, the compensation technique will not lead to a major improvement of the sensor response when compared with annealing under water samples. Nevertheless, the compensation technique leads to improved performance when compared with the non-annealed, and annealed at low humidity, sensors.

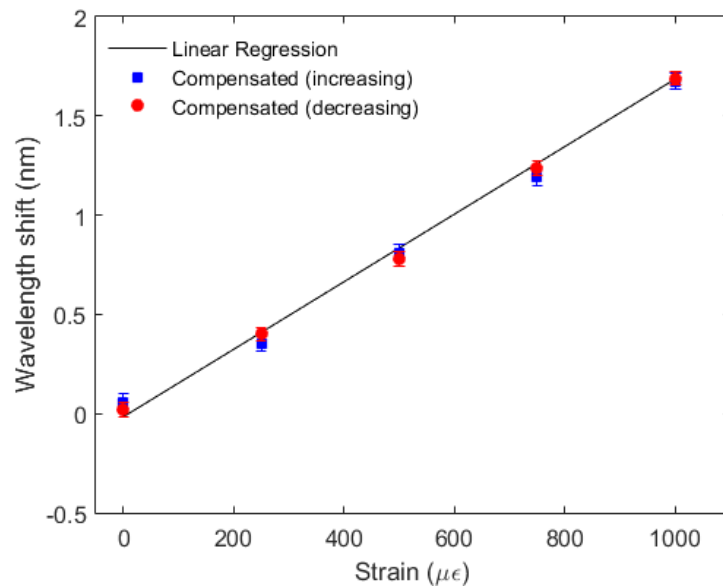


Figure 5-9 Strain compensated response for the sample annealed under water.

Thereafter, same compensation is applied on the annealed under water sensor for transverse force sensing. The obtained results are presented in Figure 5-10, where it can be seen a considerable reduction of the sensor hysteresis. The hysteresis calculated for the compensated response is about 0.74%. Hence, the combination of thermal treatments in the fiber and compensation techniques result in a sensor with high sensitivity, linearity and negligible hysteresis for force sensing applications.

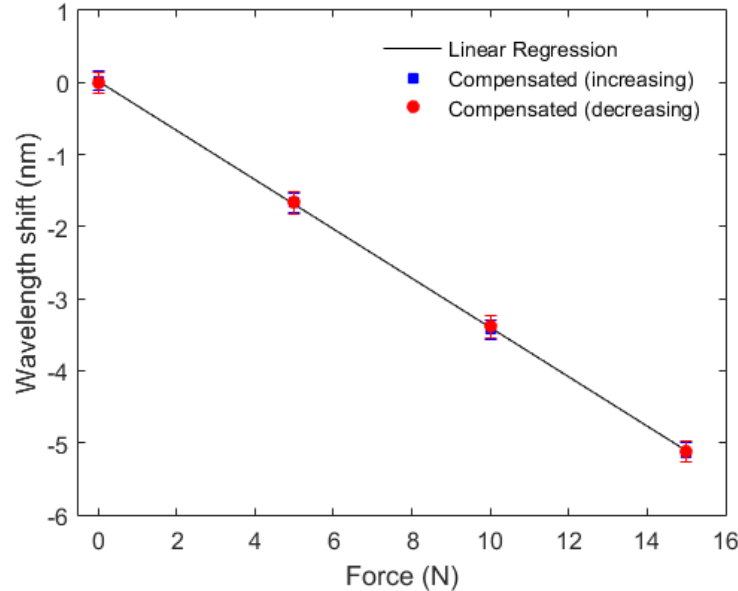


Figure 5-10 Transverse force compensated response for the sample annealed under water.

## 5.4.Compensation Method for Temperature cross-sensitivity in Transverse Force Sensors

Although it offers many advantageous features when compared to silica fibers, the POF material has the disadvantage of being viscoelastic [58], which results in a non-uniform response to stress or strain, and is characterized by creep and relaxation [59]. The role of the viscoelasticity of PMMA gratings-based sensors in strain tests was characterized in [78] and further analyzed in [184] for long term tests. In addition, viscoelastic materials have a variation of their Young's modulus in response to different parameters such as strain cycle frequency, temperature and RH as depicted in Chapter 3. Such characterization was made for PMMA step-index fibers in Section 3.3 and for mPOFs with different materials, namely PMMA, TOPAS grade 5013, Zeonex 480R and PC [157]. Given that a typical behavior of polymers (that was also observed in all these tested fibers) is a reduction of the Young's modulus with increasing temperature, a POFBG will show a variation in its sensitivity to transverse force or pressure with different temperatures. In order to compensate this effect, it is here presented the analysis of the transverse force behavior with different temperatures in POFBGs inscribed in CYTOP fibers.

### 5.4.1.Experimental Setup and Operation Principle

The POFBG monitoring was performed using the FBG interrogator sm125 (Micron Optics, USA). Furthermore, following the thermal treatment and connectorization, the POFBG was positioned in the experimental setup shown in Figure 5-11. The transverse force was applied to the POFBG through calibrated weights for a range of 0 to 6 N with steps of 1 N and the temperature was varied between 30°C to 60°C (10°C steps) inside the climatic chamber 1/400 ND (Ethik Technology, Brazil). The wavelength shift was monitored 5 minutes following the weight placement to ensure both stress and temperature stabilization. Although the CYTOP has a yield stress of about 40 MPa [185], which enables its application with transverse forces higher than 100 N, we limit the transverse force to 6 N to reduce the influence of the polarization and birefringence in the POFBG response, since the polarization dependent loss increases linearly with the increase of the transverse force [186].

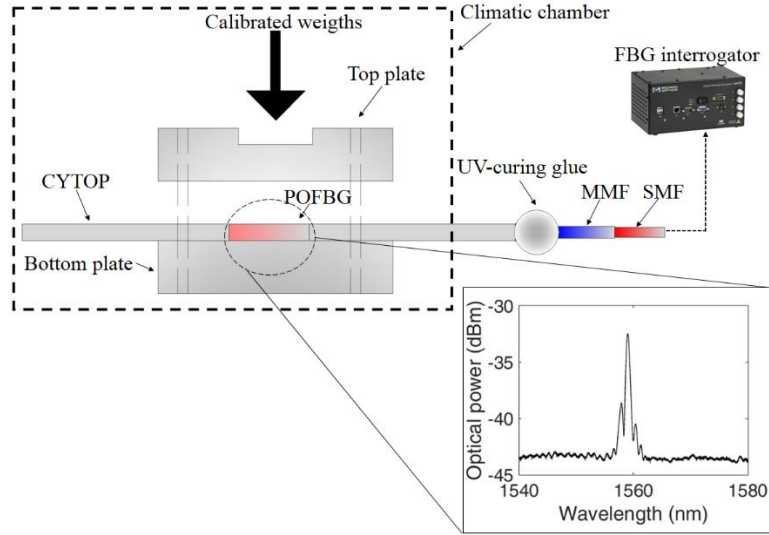


Figure 5-11 Experimental setup employed for transverse force and temperature variations.

The wavelength shift ( $\Delta\lambda_B$ ) of a POFBG for a constant humidity was already defined in Eq. 2.6. If the fiber is under stress, a resultant strain leads to the wavelength shift in POFBGs. The relation between stress and strain is described by Hooke's law in the elastic limit (Eq. 5.9).

$$\sigma = E\varepsilon, \quad (5.9)$$

where  $E$  is the material Young's modulus and  $\sigma$  is the applied stress. However, for polymers, the Young's modulus has a temperature dependency, i.e., when the temperature increases, the Young's modulus decreases [59], and this behavior is described for CYTOP fiber in Section 3.4. By substituting Eq. 5.9 in Eq. 2.6, and considering the Young's modulus temperature dependency we arrive at Eq. 5.10:

$$\Delta\lambda_B = \left[ \frac{(1-P_e)\sigma}{E(T)} + (\alpha + \xi)\Delta T \right] \lambda_B. \quad (5.10)$$

Therefore, in stress tests with different temperatures, the temperature variation causes an offset in the wavelength shift curve as a function of stress and also causes a variation of the sensor stress sensitivity. As shown in Eq. 5.10, the Young's modulus reduction causes an increase in the stress sensitivity. Thus, a higher stress sensitivity is anticipated as the temperature increases. However, Eq. 5.10 shows the wavelength shift with temperature and axial stress, whereas the tests presented here are performed with respect to the transverse force. If a transverse force is applied, the fiber stress and strain depend on the material shear modulus. Nevertheless, this material property has a direct relation with the Young's modulus of the material and the Poisson's ratio (see Eq. 5.11) [187]:

$$G(T) = \frac{E(T)}{2(1+\nu)}, \quad (5.11)$$

where  $G(T)$  is the material shear modulus and  $\nu$  is the Poisson's ratio. It can be seen from Eq. 5.11 that the temperature variation of the shear modulus is similar to that of the Young's modulus [151].

Moreover, Eq. 5.10 can be rewritten for the transverse force case considering the direct relation between the shear and Young's moduli, therefore a relation between stress and transverse force is shown in Eq. 5.12:

$$\Delta\lambda_B = \left[ \frac{(1-P_e)\Delta F}{E(T)(1+\beta)} + (\alpha_T + \xi)\Delta T \right] \lambda_B, \quad (5.12)$$

where  $\Delta F$  is the transverse force variation and  $\beta$  is a constant that summarizes the relation between stress and transverse load, in addition to the relation between shear and Young's moduli.

In order to compensate the temperature effects on the transverse force measurement, the constants presented in Eq. 5.12 need to be characterized. Considering only the right-hand side of Eq. 5.12, the offset in the sensor response caused by the temperature can be obtained with a temperature characterization of the

POFBG without the influence of stress or strain. In this case, the right-hand side of the summation may be rewritten as,

$$s_T = (\alpha_T + \xi)\lambda_B, \quad (5.13)$$

where  $S_T$  is the temperature sensitivity. Similarly, transverse force characterizations at constant temperature conditions are performed to obtain the constants presented in the left-hand side of the summation (Eq. 5.12). But, there are two unknown variables that need to be defined to estimate the temperature effects in the force sensitivity,  $P_e$  and  $\beta$ , since the photoelastic constant of CYTOP is not precisely defined, as yet [188]. For this reason, it is necessary to perform two characterization tests for the force sensitivity with two different temperature conditions. In this way, the constant  $\beta$  can be estimated,

$$\beta = \frac{S_{F,2} - S_{F,1}}{E(T_1) - E(T_2)}. \quad (5.14)$$

With reference to Eq. 5.14,  $S_{F,1}$  is the force sensitivity at one temperature condition ( $T_1$ ),  $S_{F,2}$  is the force sensitivity at the second temperature ( $T_2$ ). In addition,  $E(T_1)$  and  $E(T_2)$  are the Young's moduli at  $T_1$  and  $T_2$ , respectively. Therefore, it is also necessary to characterize the Young's modulus variation to obtain  $\beta$ , which is accomplished through the DMA in CYTOP fibers shown in Section 3.4.

With the theoretical background presented, an equation for temperature compensated transverse force variation,  $\Delta F$ , can be estimated through the combination of Eqs. 5.12 – 5.14, and considering the temperature effect in the force sensitivity:

$$\Delta F = \frac{\Delta\lambda_B - s_T \Delta T}{E(\Delta T)\beta + s_{F,1}}. \quad (5.15)$$

## 5.4.2. Results and Discussion

### 5.4.2.1. Transverse Force and Temperature Characterizations

The first step for the temperature compensation technique is the characterization of the sensor in respect to the temperature and transverse force. For this reason, the POFBG is positioned in the setup shown in Figure 5-11 and transverse forces from 0 to 6 N are applied in steps of 1 N at constant temperatures of 30°C and 40°C. Figure 5-12 shows the wavelength shift of the POFBG at each transverse force and temperature conditions, where the sensor has sensitivities of -158.33 pm/N and -187.50 pm/N for 30°C and 40°C, respectively.

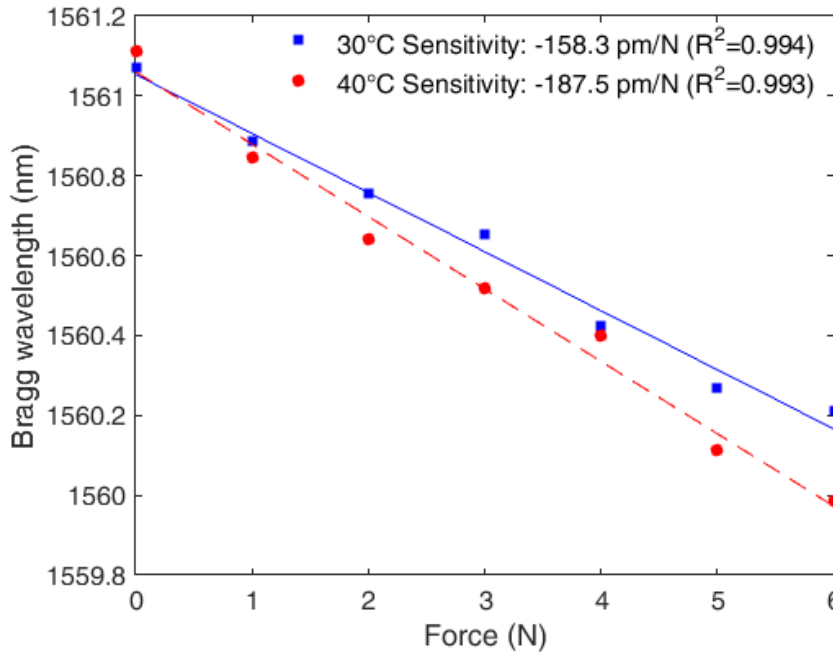


Figure 5-12 POFBG wavelength shift as a function of the transverse force at 30°C and 40°C.

The temperature characterization, shown in Figure 5-13, is performed without transverse force acting on the fiber, for the temperatures of 30°C, 40°C, 50°C and 60°C. In this test, the POFBG temperature sensitivity

of 5.83 pm/°C is obtained, where such low temperature sensitivity is related to the annealing process made with the fiber under water. The annealing leads to fiber shrinkage and relaxation of the polymer chains [118] that can result in a variation of the fiber thermal expansion coefficient, which can be directly related to this low temperature sensitivity. In addition, different of some POFs, such as PMMA, CYTOP fibers present a positive temperature sensitivity, i.e. the temperature increase causes a shift to longer wavelengths (see Figure 5-13), which is a common behavior of this POF, as also reported in [44].

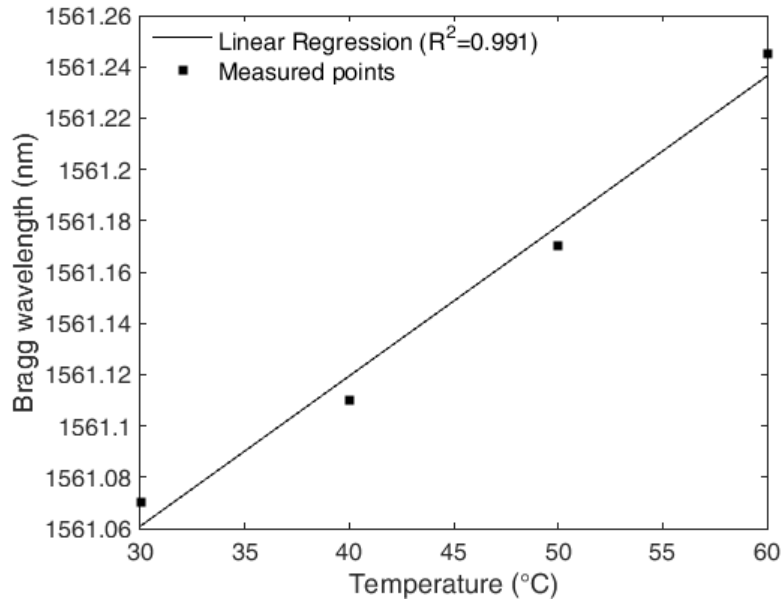


Figure 5-13 POFBG wavelength shift with respect to the temperature increase.

The results presented in Figure 5-13 show the offset caused by the temperature in the sensor response, where the point at zero force will shift with the temperature in the rate shown in Figure 5-13. However, as previously discussed, there is also a sensitivity variation in the POFBG force response at different temperatures, which is related to the CYTOP Young’s modulus variation with temperature. Aiming to characterize this variation, the material characterization is performed using the DMA; results are presented in Figure 5-14, where it is possible to confirm the Young’s modulus reduction with the temperature increase. In addition, the Young’s modulus reduction increases with the temperature increase, over the analyzed temperature range. Therefore, the Young’s modulus reduction does not have a linear variation, and, for this reason, it is expected that the POFBG transverse force sensor also will not show a linear sensitivity response.

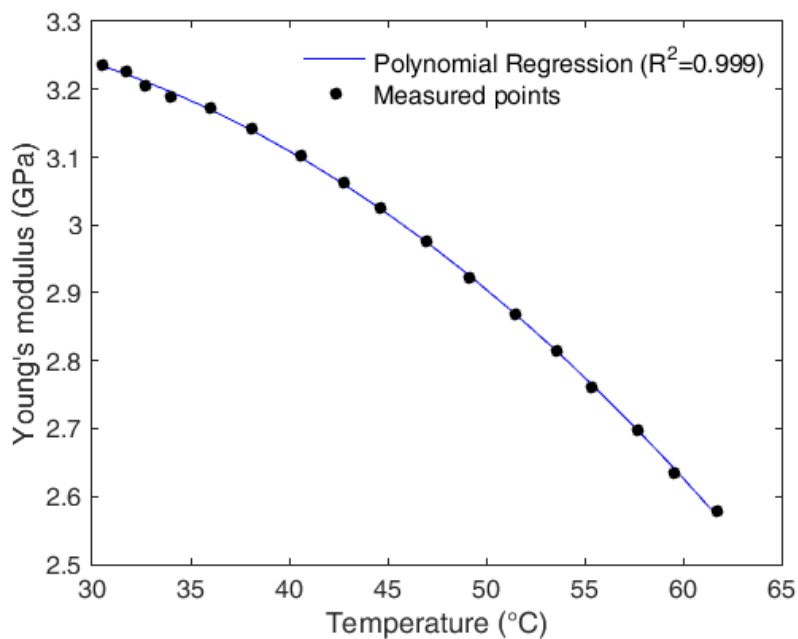


Figure 5-14 CYTOP fiber Young’s modulus variation as a function of temperature.

Based on the polynomial regression (Figure 5-14), the Young's modulus variation (in GPa) with respect to the temperature is given as:

$$E(T) = -3.71 \times 10^{-4} T_r^2 + 1.30 \times 10^{-2} T_r + 3.18. \quad (5.16)$$

In addition, according to the results illustrated in Figure 5-12-Figure 5-14 we can estimate the characterization parameters as  $S_T=5.83$  pm/°C,  $S_{F,T}=-158.33$  pm/N and  $\beta=0.27$ . Thus, the coefficients presented in Eq. 5.15 are characterized and the compensation technique can be applied and validated.

#### 5.4.2.2. Compensation Technique Validation

In order to validate the proposed compensation technique, transversal force tests were undertaken at 4 different temperatures (30°C, 40°C, 50°C and 60°C). Figure 5-15 shows the wavelength shift obtained at each test. The results are presented with respect to the wavelength variation for a clear representation of the sensitivity variation (obtained by the slope of each curve) as a function of the applied temperature. Nevertheless, the Bragg wavelength in each test follows the offset caused by temperature (see Figure 5-13).

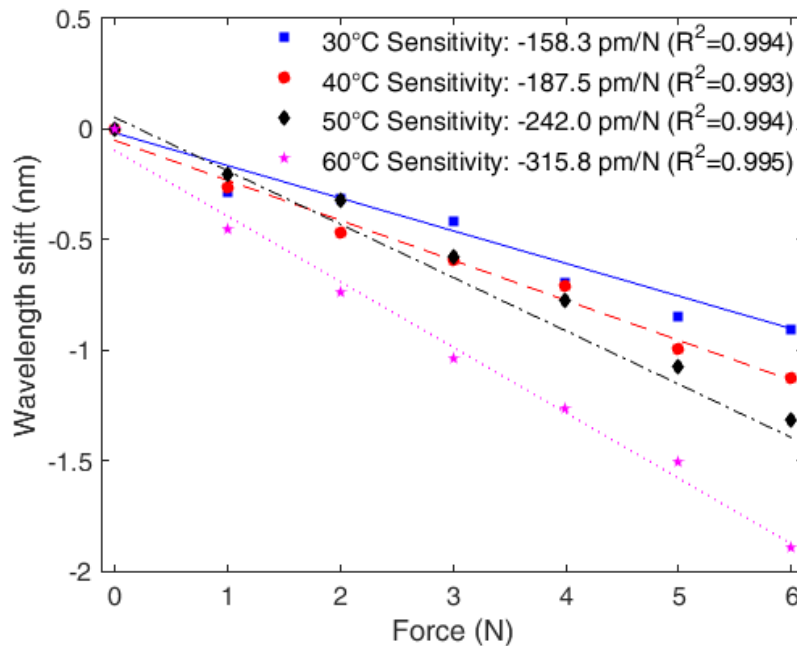


Figure 5-15 POFBG wavelength shift with respect to the transverse force for different temperature conditions.

As expected from the previous results, and more clearly shown in Figure 5-15, the POFBG presents higher sensitivity to transverse force for higher temperatures. More specifically, the highest sensitivity recorded for temperature 60°C and found to be -315.8 pm/N compare to -158.3 pm/N for 30°C. In addition, there is not a significant variation of the sensor  $R^2$  for the linear regression, which indicates the same (or very similar) sensor linearity for the transverse force tests at the different temperatures. Therefore, the sensor sensitivity variation is mainly related to the CYTOP Young's modulus variation at different temperatures, as discussed in the previous section. In order to verify and validate this assumption, Figure 5-16 shows both the Young's modulus and sensitivity variations with respect to temperature. The results show that both curves show the same parallel slope. Thus, Figure 5-16 offers important evidence that the sensitivity variation of the POFBG sensor for transverse force at different temperatures is related to the material Young's modulus variation, and it is proportional to such variation in the material properties.

From the aforementioned theoretical background and the experimental results presented in Figure 5-16, a compensation method for the temperature effects acting on the POFBG transverse force sensor is realized through Eq. 5.15, with due consideration of the characterized parameters. The estimated transverse force after the application of the compensation method is shown in Figure 5-17, for each tested temperature, along with the estimated force without the application of the compensation method.

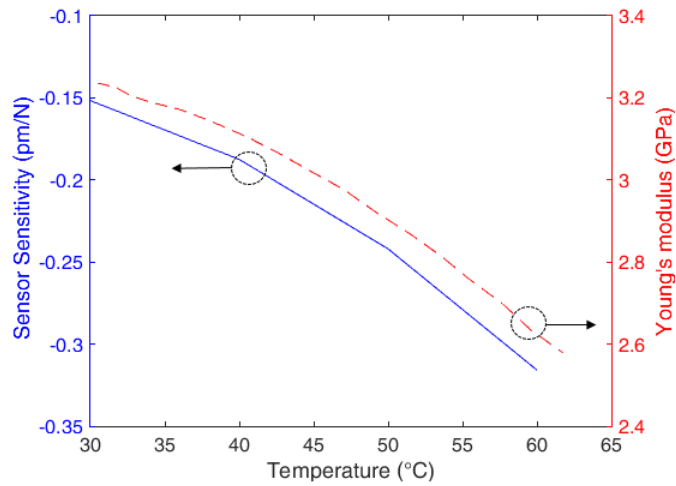


Figure 5-16 Comparison between sensor transverse force sensitivity and CYTOP Young's modulus variations with respect to the temperature variation.

The difference is significant, the compensated results follow a linear regression between the measured and the applied transverse forces at each tested temperature, whereas the uncompensated data shows high errors comparing with the applied force, which increase with temperature. Towards to have a numerical comparison between the errors with and without the proposed compensation technique, Table 5-4 presents RMSE for the sensor response with the applied transverse force, for the compensated and uncompensated cases at each temperature.

The mean and standard deviation (mean  $\pm$  standard deviation) of the RMSE according to the results presented in Table 5-4 found to be  $0.25 \pm 0.03$  N and  $1.68 \pm 1.64$  N, for the compensated and uncompensated responses, respectively. Therefore, there is a mean RMSE reduction of 6.7 times when the compensation method is employed. One should note that the compensated and uncompensated responses share the same RMSE for the characterization and calibration performed at 30°C. For the uncompensated case, the RMSE increases exponentially with temperature in response to the Young's modulus variation. On the other hand, the compensated response shows no significant variation in the RMSE. The largest difference between compensated and uncompensated responses occurs at the highest temperature (60°C) as expected, where the compensated RMSE response is 16 times lower than for the uncompensated case.

Table 5-4 POF performance parameters in transverse force cycles.

Temperature	Compensated RMSE	Uncompensated RMSE
30°C	0.23 N	0.23 N
40°C	0.31 N	1.05 N
50°C	0.26 N	1.41 N
60°C	0.25 N	4.03 N

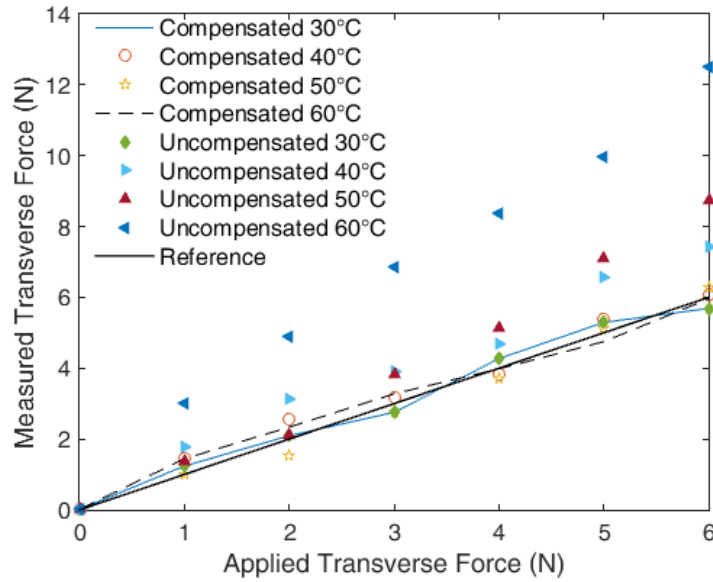


Figure 5-17 Compensated and uncompensated transverse force responses of POFBG sensors at different temperatures.

## 5.5. Development and Dynamic Compensation of FBG-based Curvature Sensors

In order to combine the advantages of POFs and FBGs, in this sub-section, a POFBG curvature sensor is developed with CYTOP fibers, which are commercially available and present lower optical losses at C+L bands than other POFs. Since the material behavior can lead to hysteresis and cross-sensitivity with the movement frequency, the Young's modulus variation with respect to strain cycle frequency was characterized using DMA, an analysis already discussed in Section 3.4. Following the material characterization, a compensation technique to mitigate the effects of hysteresis and frequency cross-sensitivity is proposed and verified for different movement frequencies of the optical sensor. Potential applications of the developed sensor include angle measurements in a robotic exoskeleton [189], as a wearable sensor for joint angle measurements [190] and on the instrumentation of robotic actuators [191].

### 5.5.1. Theoretical Background and Compensation Technique

If the POF is under curvature, the strain in the normal direction (parallel to the fiber length) is defined as [187]:

$$\varepsilon = \frac{1 - \nu^2}{E} \sigma \quad (5.17)$$

where  $E$  is the material Young's modulus,  $\nu$  is the Poisson's ratio and  $\sigma$  is the stress, which is defined in Equation 5.18 for the bending case [187].

$$\sigma = -\frac{Mx}{I_x} \quad (5.18)$$

Regarding Equation (5.18),  $M$  is the bending moment,  $x$  is the displacement in vertical direction and  $I_x$  is the cross-section moment of inertia. Thus, considering the constant temperature and the dependency of the Young's modulus with the oscillatory movement frequency ( $f$ ), the equation for the wavelength shift in FBGs can be rewritten as shown in Eq. 5.19.

$$\Delta\lambda_B = \left[ - (1 - P_e) \frac{1 - \nu^2}{E(f)} \frac{My}{I} \right] \lambda_B \quad (5.19)$$

As can be seen in Eq. 5.19, the Young's modulus variation leads to a variation in the sensor curvature sensitivity. In addition, the polymer viscoelastic response also can show a dependency with the applied strain rate, which explains the relation between hysteresis and angular velocity reported in [166]. Thus, the angular velocity and, consequently, the frequency can influence both the sensor sensitivity and hysteresis, which is defined as the offset between the loading and unloading curves. In the curvature case, the loading curve will

be referred to as the flexion cycle, whereas the unloading as the extension cycle. Figure 5-18 summarizes the effect of the oscillatory movement frequency on the sensor’s response. It is worth noting that Figure 5-18 illustrates the frequency effects that will be experimentally confirmed in the next sections. The frequency influence on the sensor sensitivity is represented by a slope variation, whereas the hysteresis is shown as an offset for the measurements made at the two different frequencies. Referring to Figure 5-18,  $s_1$  and  $s_2$  are the sensitivities for frequency 1 ( $f_1$ ) and 2 ( $f_2$ ), respectively. Additionally,  $h_1$  is the hysteresis at  $f_1$ , whereas  $h_2$  is the one at  $f_2$ . In the case presented in Figure 5-18, frequency 2 is higher than frequency 1.

In order to compensate the effects illustrated in Figure 5-18, the movement frequency needs to be estimated. Since the frequency presents a direct relation with the angular velocity, the movement frequency can be estimated by taking the angle variation rate of the POFBG curvature sensor. In addition, the Young’s modulus with respect to frequency requires characterization and the curvature sensor is tested under different velocities to obtain the relation between the sensor sensitivity and the movement frequency. The hysteresis between flexion and extension cycles is subsequently analyzed at each discrete frequency, which results in an experimental model relating the frequency and hysteresis. This model is applied to the POFBG curvature sensor as the hysteresis compensation. Hence, there are two models: one for the cross-sensitivity mitigation and the other for the hysteresis compensation. Figure 5-19 presents the block diagram of the proposed compensation technique, where the model input is the wavelength shift and the output is the compensated angle.

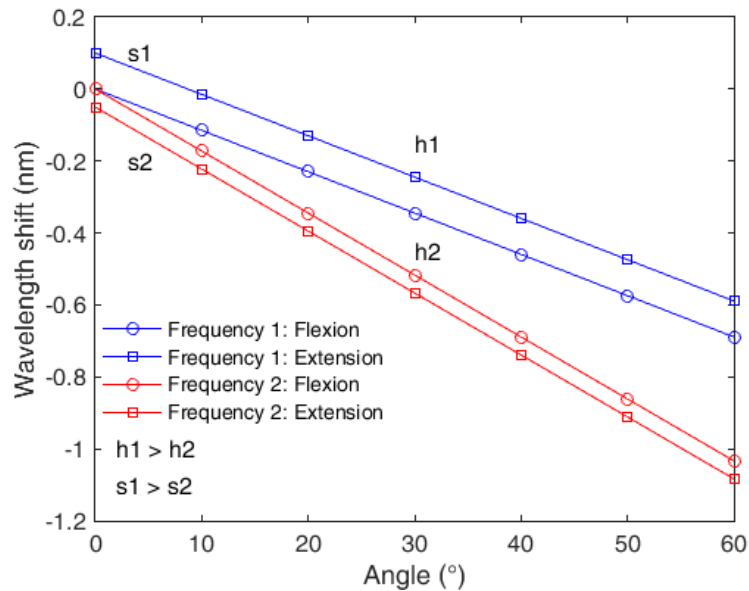


Figure 5-18 Schematic illustration of the frequency effect on the sensor sensitivity and linearity for two different frequencies; where  $h_1$  and  $h_2$  are the hysteresis for the frequencies 1 and 2, respectively. Analogously,  $s_1$  and  $s_2$  are the sensitivities for frequencies 1 and 2, respectively.

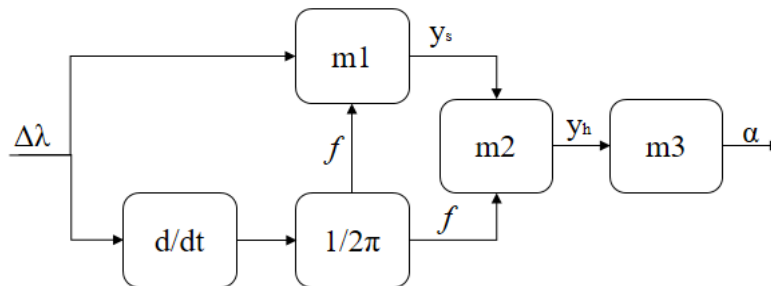


Figure 5-19 Block diagram of the sensitivity compensation (block  $m_1$ ), hysteresis compensation (block  $m_2$ ) and the correlation equation that results in the angle output (block  $m_3$ ).

Regarding Figure 5-19, the block “ $m_1$ ” refers to the sensitivity compensation with respect to frequency, whereas the block “ $m_2$ ” is the hysteresis compensation model. The outputs of models “ $m_1$ ” and “ $m_2$ ” are  $y_s$  and  $y_h$ , respectively. Both models are obtained through the experimental characterization performed in the next sections. Finally, the model “ $m_3$ ” correlates the compensated wavelength shift with the angle ( $\alpha$ ) that results in the compensated angle measurement.

## 5.5.2. Experimental Setup

Following the grating inscription, the sensor is subjected to annealing, which is a thermal treatment in which the POF is kept at temperatures close to its glass transition temperature for extended time periods of several hours [179]. In this case, the annealing is made under water, since the high humidity can further increase its effectiveness [60]. In addition, the thermal treatment is made at a constant temperature of 90°C for 24 hours. The developed POFBG sensor is positioned on the experimental setup as shown in Figure 5-20. The setup comprises of a DC motor with angular position and velocity control, where a potentiometer is connected with the DC motor and a gear (1:1 ratio) to provide the reference angle. The tests are performed over an angular range of 0 to 60°, which is within the knee joint angle interval during gait motion when walking [155]. In addition, two endstop microswitches are employed to prevent system angles exceeding 60°. The CYTOP and MMF are fixed in the 3D translational stage, for the purpose of providing higher stability for the UV-joint during the oscillatory movements. The employed movement frequencies are 0.50 Hz, 0.61 Hz, 1.10 Hz, 1.32 Hz, 1.87 Hz and 4.49 Hz, where these frequencies were selected as they are close to the ones used in the material Young's modulus characterization with respect to the movement frequency.

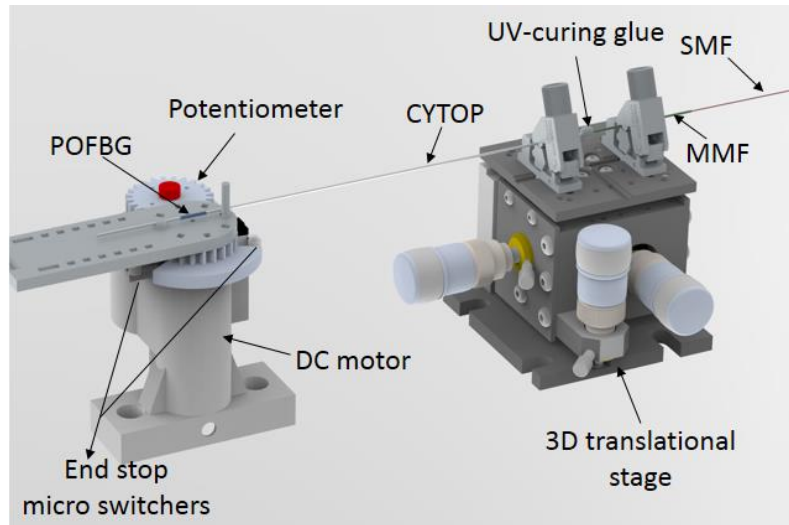


Figure 5-20 Experimental setup for the POFBG curvature sensor characterization.

## 5.5.3. Results and Discussion

### 5.5.3.1. Sensor Characterization

In order to verify the sensitivity reduction with respect to the frequency increase, flexion cycles were performed for different frequencies. Figure 5-21(a) shows the response for three different frequencies, 0.50 Hz, 1.32 Hz and 4.49 Hz. In addition, the direct relation between the sensor sensitivity and the Young's modulus variation with frequency is shown in Figure 5-21(b), where the same linear behavior was obtained for both material and sensor responses. The linear regression between the wavelength shift and the angle is presented in Eq. 5.20 for the test at 0.5 Hz. This test was chosen for the regression due to its higher sensitivity. Equation 5.20 will be referred to as the uncompensated response, since it is the response without the application of any compensation technique.

$$\Delta\lambda = -0.017\alpha - 0.029 \quad (5.20)$$

In addition, the responses presented in Figure 5-21(a) also shows the linear behavior of the sensor at each frequency. Therefore, the model "m3" is a linear regression relating the wavelength shift with sensitivity and hysteresis compensation and the angle. Since the sensor displays a linear response to different frequencies, the model "m1" (see Figure 5-19) can be obtained by determining the linear regression between the sensor sensitivity and the frequency. Equation 5.21 presents the coefficients of this linear regression. Thus, the sensor sensitivity can be estimated at each frequency by applying Eq 5.21.

$$y_s = -0.004f + 0.019 \quad (5.21)$$

A similar analysis is performed for the hysteresis compensation. In this case, the extension cycles are also analyzed, and the hysteresis is calculated as the offset between the flexion and extension curves. Figure 5-22(a) shows the sensor response for 0.5 Hz, whereas Figure 5-22(b) presents the hysteresis with respect to frequency. The relation between the sensor hysteresis and the oscillatory movement frequency follows a second-order exponential regression, which is the same regression found for PMMA POF characterization [58] and in hysteresis compensation based on the material features [182]. Hence, Equation (5.22) may be used to estimate the sensor hysteresis ( $h$ ) based on its movement frequency.

$$h = 168.20 \exp(-17.1f) + 0.06 \exp(-0.14f) \tag{5.22}$$

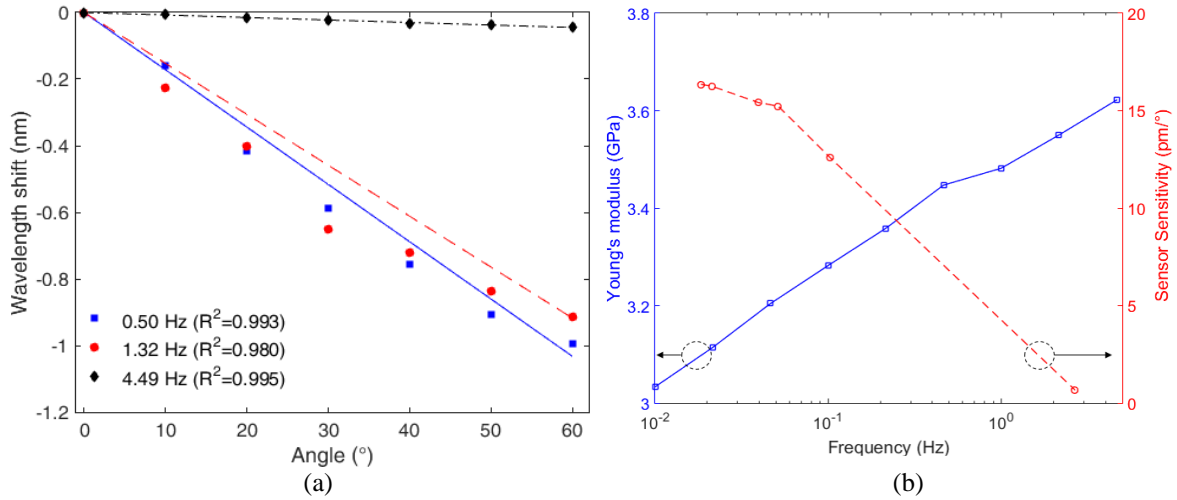
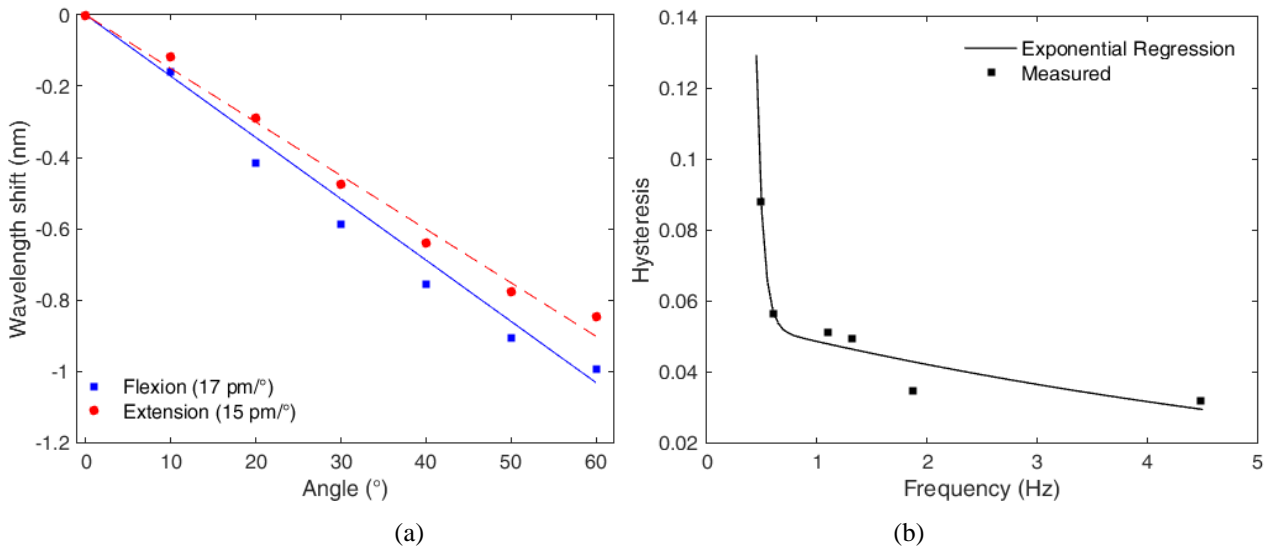


Figure 5-21 (a) POFBG curvature sensor response for three different frequencies (0.50 Hz, 1.32 Hz and 4.49 Hz). (b) Comparison between the sensor sensitivity and Young's modulus variations with respect to frequency.

Additionally, as presented in Figure 5-22(a), there is also a sensitivity variation between flexion and extension cycles, which is a source of hysteresis. Therefore, for the hysteresis compensation, it is necessary not only compensate the offset between the curves, but also the sensitivity variation. For the tested frequencies, the sensitivity of the flexion cycle is greater than the extension cycle. Figure 5-22(c) depicts the sensitivity difference between flexion and extension cycles at each frequency (0.50 Hz, 0.61 Hz, 1.10 Hz, 1.32 Hz, 1.87 Hz and 4.49 Hz), and we observe a hysteresis-related, lower sensitivity for the sensor extension cycles compared to the flexion cycles.



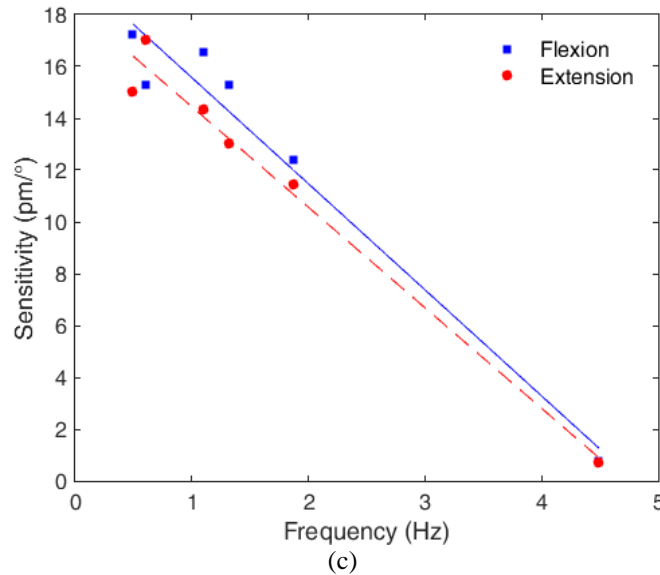


Figure 5-22 (a) Flexion and extension cycles at 0.5 Hz with the sensitivity of each cycle. (b) Hysteresis variation as a function of the frequency. (c) Sensitivity difference between flexion and extension cycles at each frequency.

Equation 5.23 presents the sensitivity with respect to frequency for the extension cycles recovered from Figure 5-22(c).

$$y_{s2} = -0.0038f - 0.0197 \quad (5.23)$$

There will be two equations for hysteresis compensation, one for flexion and the other for extension. The flexion and extension movements can be detected by the direction of the angular velocity obtained after the derivative block in Figure 5-19. The equation for extension is comprised of the sensitivity correction with respect to frequency (Eq. 5.23) and the offset correction as a function of the frequency, shown in Eq. 5.22. The compensated equations for flexion and extension cycles are given by Eq. 5.24 and 5.25, respectively.

$$\Delta\lambda = (-0.004f + 0.019)\alpha \quad (5.24)$$

$$\Delta\lambda = (-0.0038f - 0.0197 + h)\alpha \quad (5.25)$$

### 5.5.3.2. Compensation Technique Verification

The compensation technique presented in the previous sections is applied and verified, where Eq. 5.24 is applied for the flexion movement and Eq. 5.25 for extension. Figure 5-23 shows results of the compensated response for the test at 1.10 Hz, for which was found the highest hysteresis reduction.

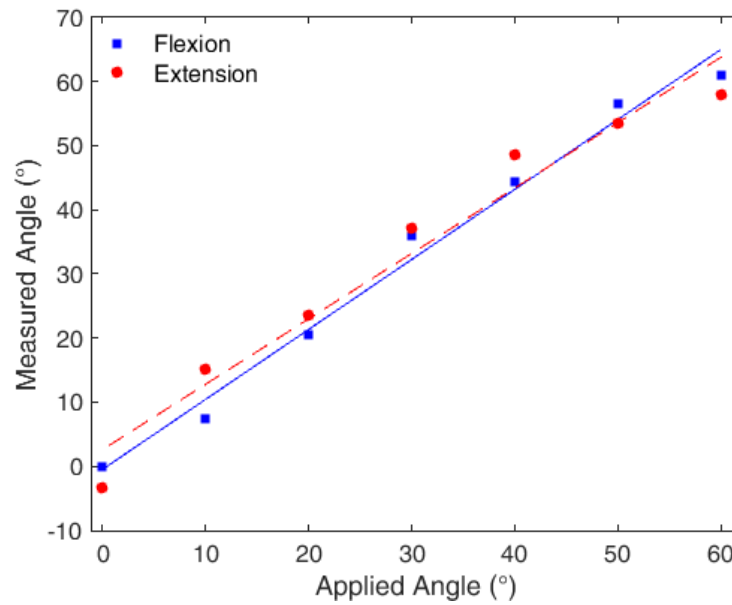


Figure 5-23 Measured angles for flexion and extension cycles after applying the compensation technique.

The comparison between the compensated and uncompensated responses is made with respect to the sensors' hysteresis and RMSE. The uncompensated response is obtained by isolating the angle in Eq. 5.20, whereas the compensated response is obtained by applying Eq. 5.24 and 5.25. The compensation technique verification occurs in two steps: first, validation of the frequency cross-sensitivity compensation is performed, followed by the hysteresis compensation validation. For the cross-sensitivity compensation analysis, the RMSE between the applied and measured angles is compared at each frequency for the compensated and uncompensated cases. Figure 5-24 shows the results obtained, where the RMSE is presented with respect to the frequency. As expected, the results at 0.5 Hz show the same hysteresis, given that Eq. 5.20 (employed for the uncompensated response analysis) is obtained at the 0.5-Hz flexion cycle. As the frequency increases, there is a sharp increase in the error of the uncompensated response, whereas compensated responses are almost constant. In addition, we note that the errors observed in the compensated measurements are related to sensor nonlinearities that lead to a reduction of the correlation coefficient between the sensor response and the linear regression. Nevertheless, the correlation coefficient is higher than 0.98 in all tests.

The compensated and uncompensated responses presented similar RMSEs for all frequencies below 1.5 Hz. The difference between the responses increases when the frequency exceeds 1.5 Hz, as the sensitivity exhibits higher variations at higher frequencies. The mean RMSE of the compensated response is  $4.20^\circ$ , whereas that of the uncompensated response is  $7.45^\circ$ . Therefore, the compensation technique leads to a comparative RMSE reduction of 44%.

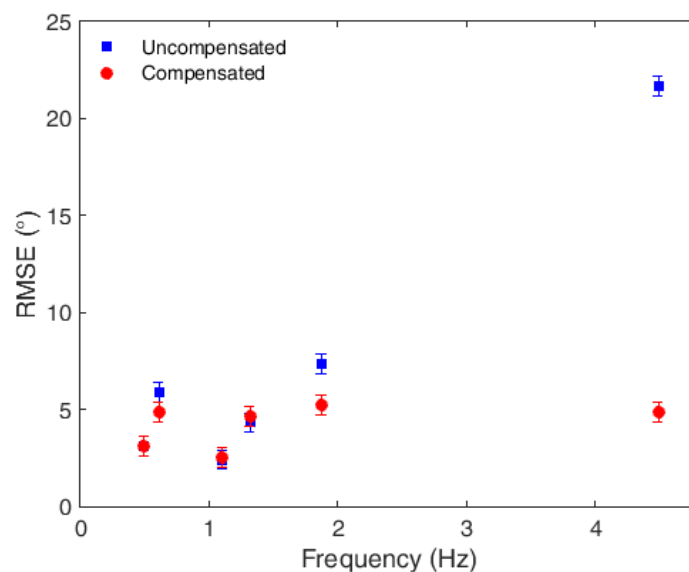


Figure 5-24 RMSE of the compensated and uncompensated responses at each tested frequency.

The verification of the second step of the compensation technique requires a comparison of the sensor hysteresis before and after the compensation, as shown in Figure 5-25. Once again, the results are presented as a function of the movement frequency. In this case, the uncompensated hysteresis showed a downward trend with increasing frequency. Although the hysteresis was reduced for all tested frequencies, it less effective for frequencies  $> 1.5$  Hz. Nevertheless, there is an improvement that is observed across the frequency range. The mean hysteresis before the application of the compensation technique is 0.0403, and 0.022 following compensation; a reduction of 55%.

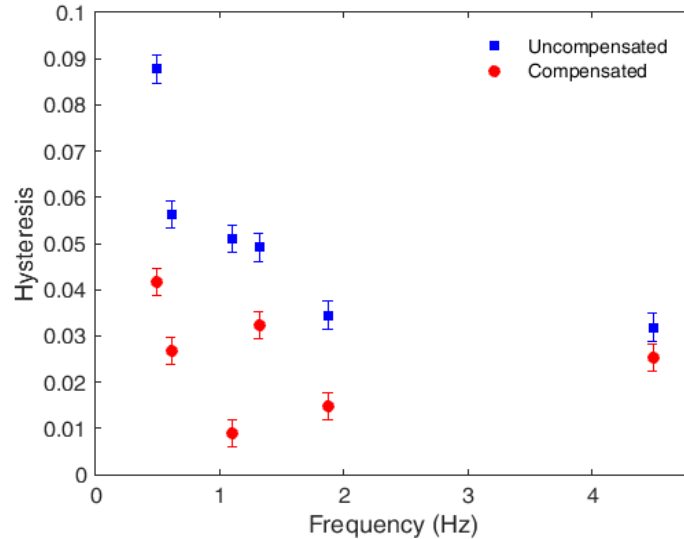


Figure 5-25 Hysteresis of the compensated and uncompensated responses at each tested frequency.

## 5.6. Final Remarks

This Chapter has presented the development of sensors for measuring temperature, strain, force and angle based on FBGs. Using the background provided by the fiber characterization in Chapter 3, compensation techniques for temperature, frequency and creep responses were proposed and a performance enhancement on each sensor was reported. In addition, the investigation of thermal treatment on FBG spectral characteristics and sensor responses was also conducted and shows advantageous features of the annealing at high humidity conditions on the development of highly sensitive sensors with negligible hysteresis.

Even though the cost of FBG interrogation equipment as well as its size and weight are major drawbacks in some applications that require low cost and portable sensors (but is not an issue in many industrial and SHM applications), it is important to mention that many works in low cost and portable interrogators have been proposed [48], [192], where even FBG interrogators on chip have been studied [193]. In addition, there is also commercially available FBG transceivers with higher portability [194]. Therefore, with these advantages on FBG interrogation technologies, it is possible to foresee the application of FBG sensors on the instrumentation of wearable devices for gait assistance outside clinical environment. For these reasons, one can envisage the widespread of FBG technology on the instrumentation of many healthcare devices in multiparameter and quasi-distributed applications as will be further discussed and demonstrated in the next Chapter.

## Chapter 6. POF Sensors Applications in Healthcare Devices

### 6.1. Introduction

In this Chapter, applications of POF sensors in healthcare devices are presented. The sensors development is performed using the background acquired in Chapter 3, where the POFs were characterized, enabling the development of the sensors based on intensity variation principle and FBGs as depicted in Chapter 4 and Chapter 5, respectively.

The proposed sensors were applied in three assistive devices: (i) human-robot interaction forces assessment in a lower limb exoskeleton, (ii) FBG array application in SEA’s spring for angle and torque measurements and (iii) SW for multiparameter assessment. In addition, the multiplexing technique for intensity variation sensors (see Section 4.4) is applied on the development of an instrumented insole for plantar pressure and GRF monitoring. In order to summarize the sensors developed, the devices employed and to clarify the methods used in each application, Figure 6-1 shows an overview of the applications discussed in this Chapter using both sensing technologies (intensity variation and FBG). It is noteworthy that the principles investigated in previous chapters are also used on the development of novel sensors (when compared to the ones presented in Chapter 4 and Chapter 5), such as torque, oximetry, HR and BR sensors.

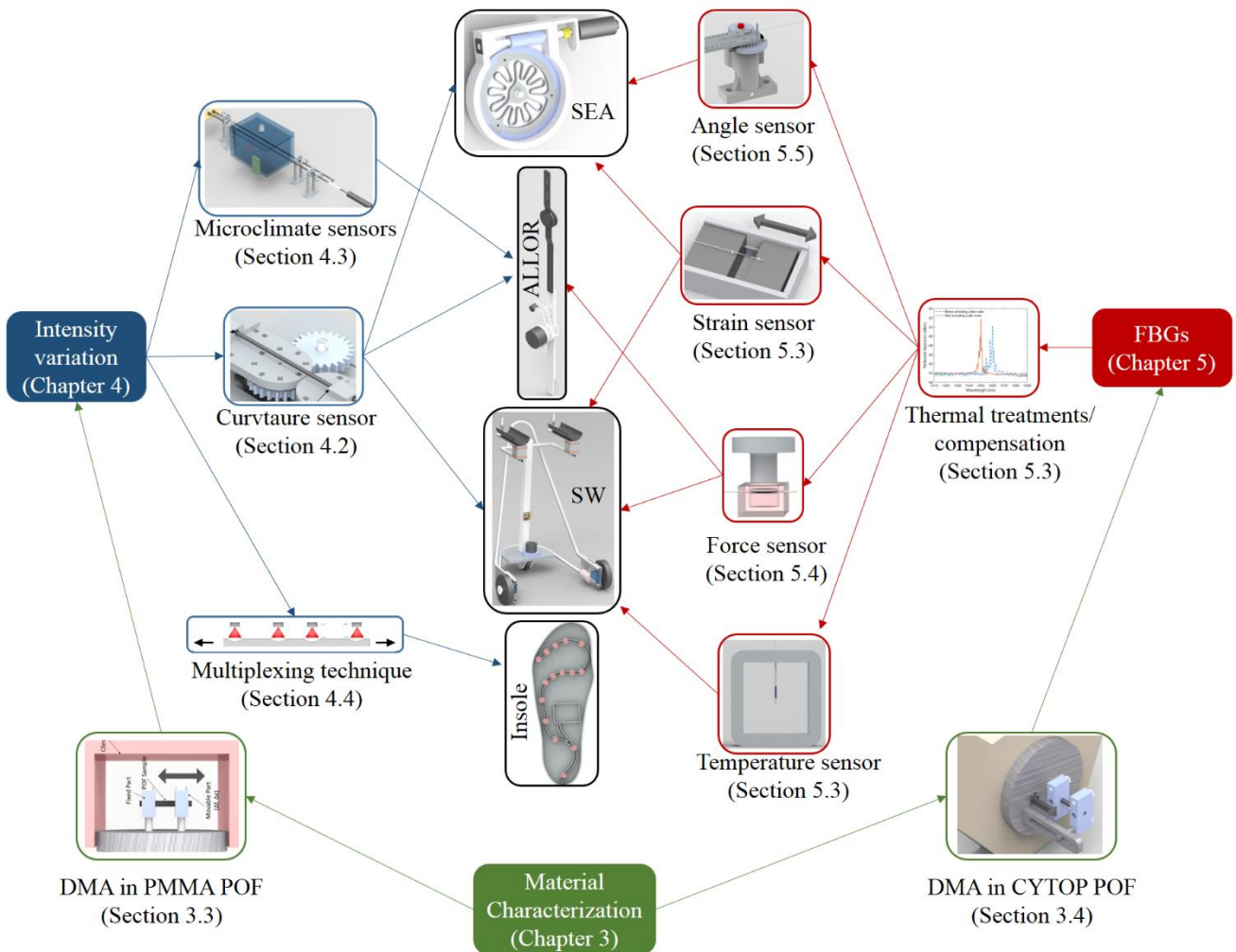


Figure 6-1 Overview of the applications developed in this Chapter and their relation with the developments presented in previous chapters.

## 6.2. Assistive Devices Employed on Sensors Applications

### 6.2.1. Advanced Lower Limb Orthosis for Rehabilitation (ALLOR)

The ALLOR presents an active degree of freedom on the knee, where the motor unit is a direct current (DC) motor (Maxon Motors, Switzerland) and a harmonic drive gear reduction (Harmonic Drive AG, Germany). Such unit provides a range of movement from 0 to 90°. The knee joint angle is acquired with a precision potentiometer of 10 k $\Omega$  and  $\pm 2\%$  of linearity (Vishay, USA) that is connected to a harmonic drive output through a toothed belt. It is worth to mention that the potentiometer signal has to be filtered with a low pass Butterworth filter in order to mitigate the high noise observed in the measurements. In the analyses, the orthosis is positioned on a chair and the user, with the ALLOR attached, makes flexion and extension movements with respect to the knee joint on a predefined angular range. The robotic device provides an assistance on the flexion-extension movement and the degree of this assistance varies from 1, referring to the highest assistance of the ALLOR on the user movement, to 10, which is the lowest assistance of the orthosis. The orthosis positioned on the chair is presented in Figure 6-2.

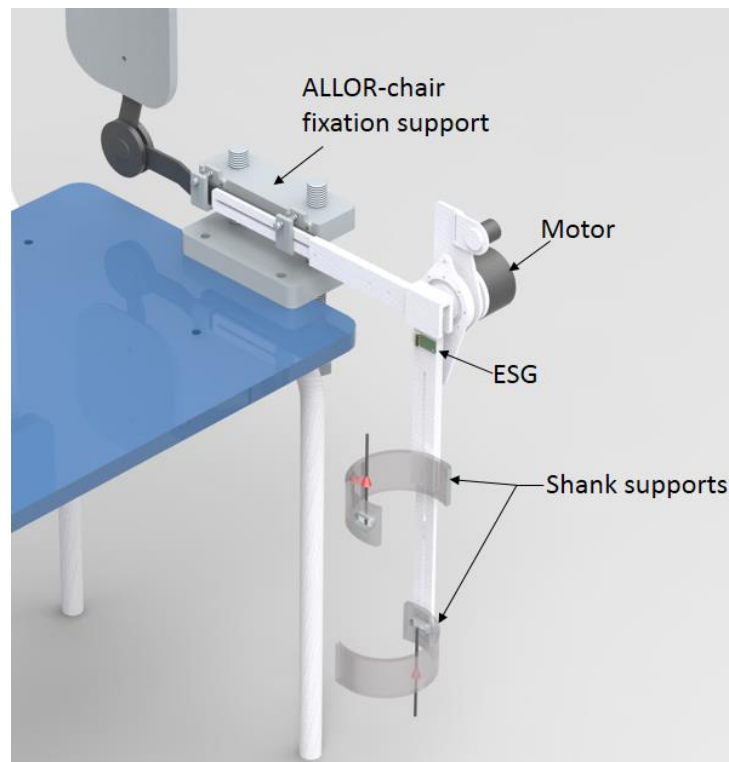


Figure 6-2 ALLOR orthotic device positioned on the chair for flexion/extension cycles.

### 6.2.2. Active Knee Orthosis Driven by a SEA

The employed SEA is shown in Figure 6-3. It comprises of a customized spring, and a DC motor with an encoder. The transmission of movement is made by a worm gear and the alignment and freedom of movement of the motor axis is guaranteed by an angular contact bearing. Another encoder is positioned on the actuator output axis and the spring deflection is estimated by the difference between the motor encoder and the output axis encoder. The orthosis was fabricated at the Engineering School of São Carlos, University of São Paulo, where details of the design and construction of this SEA are presented in [9].

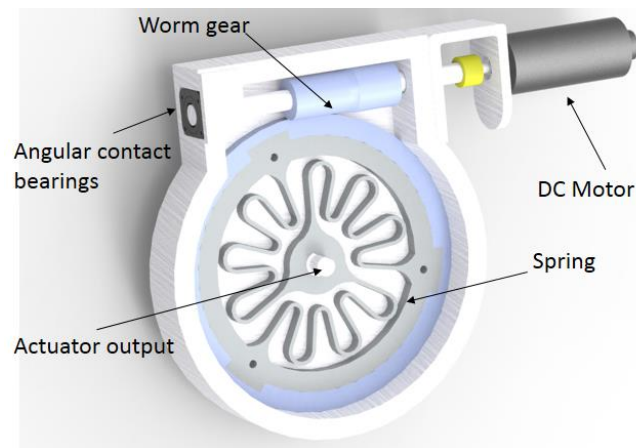


Figure 6-3 Rotary Series Elastic Actuator for an active knee orthosis.

For the validation tests, the spring is fixed in a base, which is positioned on a fixed support to limit the flexion and extension movements to only one plane. Figure 6-4 shows a back view of the spring, where it can be seen the encoder E5 series (US digital, USA) positioned on the output shaft (used for comparison with the POF sensors).

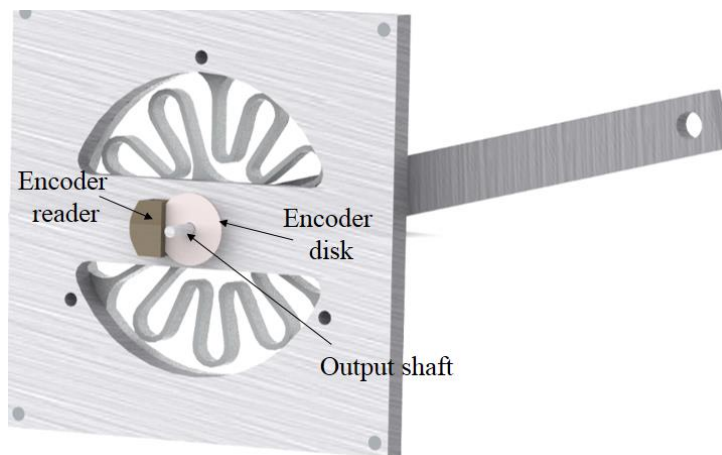


Figure 6-4 Back view of the spring with the encoder used for comparison purposes.

### 6.2.3. Smart Walker

The POF sensors implementation are also on the SW depicted in Figure 6-5, where the motors, mechanical structure and sensors are shown. The SW (UFES Cloud Walker) was conceived and manufactured in Federal University of Esp rito Santo (UFES, Brazil)[195]. The SW has two 3D force sensors (Futek MTA400, USA) for the detection of the user's movement intention as well as two motors (with encoders) (H1 US Digital, USA) for the actuation of the healthcare device. Additionally, there is an IMU (BNO055 Bosch, USA) placed on the SW's center tube to measure its orientation and velocity. Another sensor used for the comparison with the proposed ones is the LRF (Hokuyo URG-04LX, Japan) employed to detect users' legs and, then, estimate gait cadence.

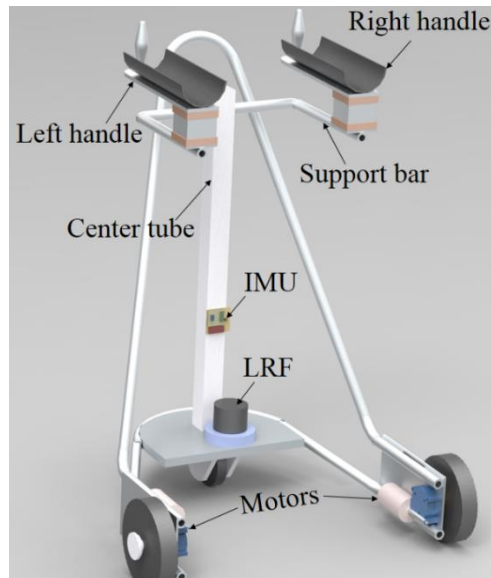


Figure 6-5 Overview of the SW used for the POF sensors implementation – UFES Cloud Walker.

### 6.3. Intensity Variation-based Sensors Applications in Healthcare Devices

#### 6.3.1. Angle Measurements in Lower Limb Exoskeletons

The POF curvature sensor is positioned on the ALLOR as shown in Figure 6-6 and the compensation technique based on angular velocities depicted in Section 4.2 is applied, where flexion and extension cycles are made on the 5 different angular velocities applied on the rehabilitation exercises, which are chosen empirically based on the level of rehabilitation that the patient needs. These angular velocities are presented in Table 6-1 and three cycles were made at each angular velocity. The compensation technique resulted in hysteresis and RMSE reduction at all angular velocities tested. Furthermore, the RMSE and the hysteresis of each cycle are presented in Table 6-1 with a comparison of the response with and without the compensation technique proposed.

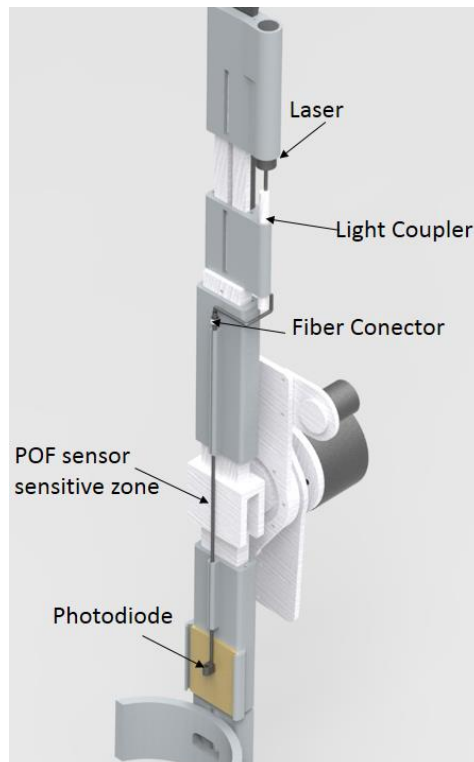


Figure 6-6 POF curvature sensor positioned on the ALLOR through 3D-printed supports.

Table 6-1 RMSE and hysteresis of each cycle with and without the compensation technique.

Cycle	Angular Velocity (rad/s)	Compensated (RMSE)	Uncompensated (RMSE)	Compensated Hysteresis	Uncompensated Hysteresis
1	0.05	1.83	2.78	0.31%	1.68%
2	0.05	2.90	4.50	0.03%	0.84%
3	0.05	2.28	2.96	0.54%	1.57%
4	0.10	2.52	4.00	1.23%	2.07%
5	0.10	2.66	4.01	0.29%	0.68%
6	0.10	2.11	3.30	0.34%	1.70%
7	0.16	1.92	2.10	0.15%	0.57%
8	0.16	2.20	2.50	0.46%	1.18%
9	0.16	1.74	1.92	1.31%	2.02%
10	0.21	2.74	2.96	0.89%	1.02%
11	0.21	2.60	2.87	0.45%	1.55%
12	0.21	2.27	2.30	0.44%	1.32%
13	0.26	1.80	4.23	0.60%	1.65%
14	0.26	1.58	4.56	2.42%	4.77%
15	0.26	2.13	4.40	2.63%	5.10%

Since the compensation technique is already validated on the exoskeleton, a test with a subject is made. The test comprises of 5 flexion/extension cycles on the range of  $10^{\circ}$  to  $80^{\circ}$ . The reason for this range is the patient comfort and the mechanical limits the exoskeleton angles. Moreover, an angle of  $90^{\circ}$  may cause higher vibration of the motor, which is transmitted to the potentiometer response. The patient is comfortably positioned on the chair and the exoskeleton is fixed on his thigh, shank and foot. In case of unexpected behavior of the robotic device, the user may stop the exoskeleton's motion using an emergency button. Figure 6-7 shows the user with the exoskeleton before the experimental validation.

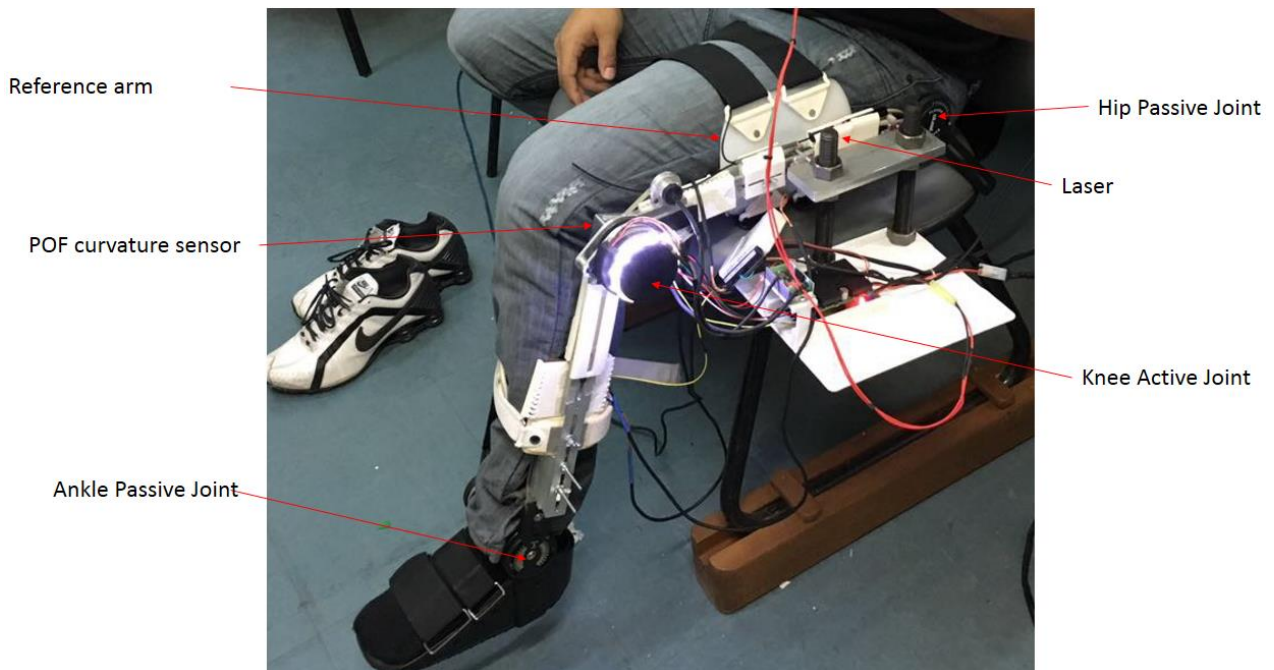


Figure 6-7 Subject with the exoskeleton before the experiment. The hip passive joint as well as the POE curvature sensor and reference arm are not connected at the time of the picture was taken.

Test results are presented in Figure 6-8. The compensation technique was capable of reducing the hysteresis and the error of the flexion/extension movement. Although the compensation technique is capable of reduce the hysteresis of the sensor, it cannot guarantee a constant value of hysteresis, due to the high variation of this parameter. However, it keeps the hysteresis on a range lower than 2.5% in all cycles analyzed. Moreover, it also leads to reduction of the hysteresis in about half of its value when compared with the response without the compensation technique. The flexion/extension cycle shown in Figure 6-8 is the first of the 5 cycles performed. The hysteresis of this cycle is 0.1646% and the RMSE is  $0.9167^{\circ}$ .

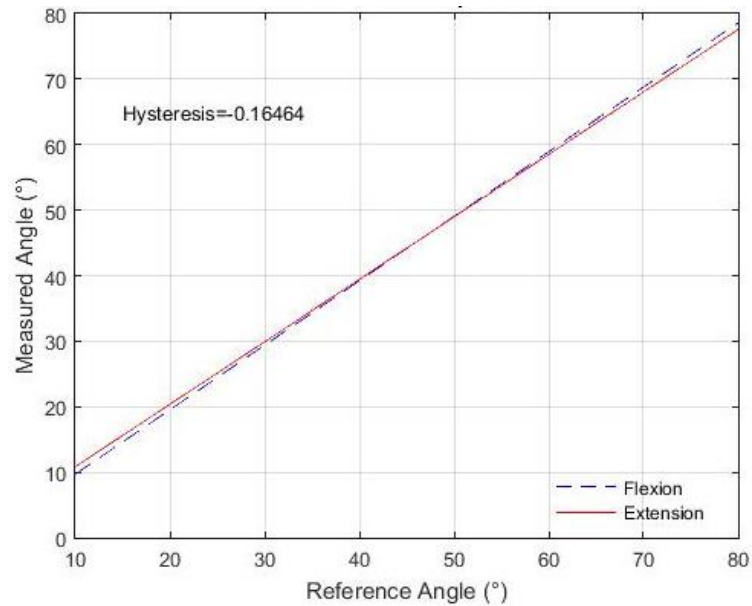


Figure 6-8 POF sensor response (vertical axis) and potentiometer response (horizontal axis) for the first cycle of the rehabilitation exercise.

In Figure 6-8, the flexion and extension responses are shown through a linear equation, since the objective is to show the sensor hysteresis. In order to have a broader visualization of the sensor response at each tested angular velocity, Figure 6-9 shows the POF sensor and the potentiometer response on one cycle at each velocity tested, presented in Table 6-1. Furthermore, Figure 6-9 enables the visualization of the errors at each velocity.

Figure 6-9 shows that the errors tend to be reduced as the angular velocity increases. However, the errors also vary with the angle measured. For this reason, Figure 6-10 shows the error at each angle. The shaded line represents the standard deviation of the error in each velocity at each cycle. Moreover, the maximum error is  $\sim 2.4^\circ$  at about  $47^\circ$ . The region between  $40^\circ$  and  $65^\circ$  has the highest errors, which is expected since the viscoelastic response presents hysteresis on the regions that correspond to the half of the cycle of stress or strain [154]. For this reason, the stress applied on the fiber due to its curvature will provoke higher hysteresis on the regions of the half of the cycle, which leads to errors on the angle measurement on this region.

Nevertheless, the proposed compensation technique reduces this hysteresis as demonstrated above, which means to a reduction of the error on this region, but there still have some remaining hysteresis that lead higher errors on this region when compared with the regions at the beginning or at the end of the movement cycle. However, the mean error of the 5 cycles tested is  $1.2^\circ$ . Furthermore, the standard deviation is less than  $1^\circ$ .

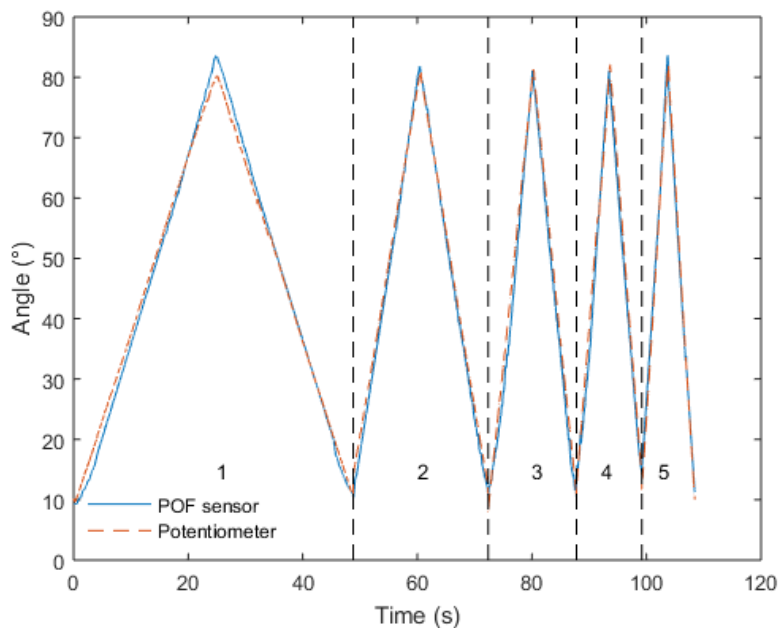


Figure 6-9 POF sensor response and potentiometer response for the 5 different angular velocities tested. Regions 1, 2, 3, 4 and 5 refer to the angular velocities of 0.05 rad/s, 0.10 rad/s, 0.16 rad/s, 0.21 rad/s and 0.26 rad/s respectively.

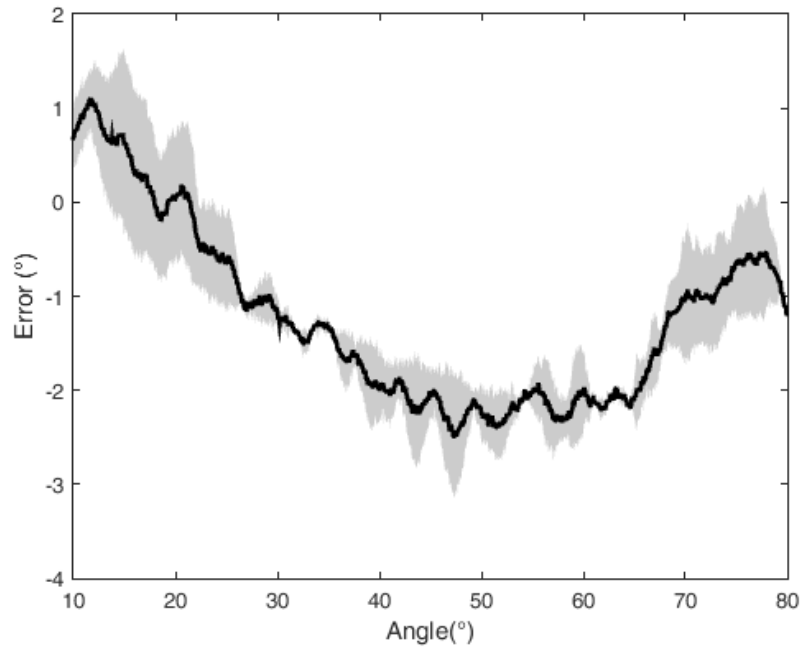


Figure 6-10 Error between the POF sensor and the potentiometer on the vertical axis. The potentiometer angle is presented on the horizontal axis. The shaded part of the error represents the standard deviation of the error in each velocity at each cycle.

### 6.3.2. Angle and Torque Measurements in a SEA Spring

This section presents the application of a POF curvature sensor on the elastic element of a SEA. Since small deflections of the spring have to be measured in an effort to estimate the actuator output torque, the sensor has to be carefully placed to obtain a high sensitivity. Another contribution of this section is a novel torque sensor based on POF stress-optic effect.

#### 6.3.2.1. System's Requirements and Experimental Setup

The spring with its base and a lever to provide the angular deflection are attached to a support that presents two holes: one at  $4^\circ$  with respect to the lever position when the spring is not under deflection and the other at  $10^\circ$  of the same condition. A lever is employed to position the springs on the predefined angles (see Figure 6-11). Furthermore, the encoder E5 series (US digital, USA) is positioned on the spring axis, below the wooden support. This encoder is the reference for the dynamic tests of the POF sensor. Besides its simplicity, this experimental setup also makes the sensor validation easier on both static and dynamic tests.

The positioning of the fiber on the spring is of great importance due to the differences of the movement at each portion of the spring. In order to obtain a higher range of movement for the sensor, an analysis of the spring under a predefined stress is made. In this analysis, the spring is fixed and a torque is applied on the center of the spring to simulate the stress that the lever applies on the spring. Figure 6-12 shows the equivalent strain of the spring when a torque of 15 Nm is applied, which is the maximum torque of the SEA's DC motor when the safety factor is considered [9]. In Figure 6-12, the points *a* and *b* present higher relative movement and low equivalent strain. Therefore, these points are more suitable for the POF sensor position, since there is more range of movement of the sensor and the low equivalent strain, in this region, prevents the fiber rupture and plastic deformation.

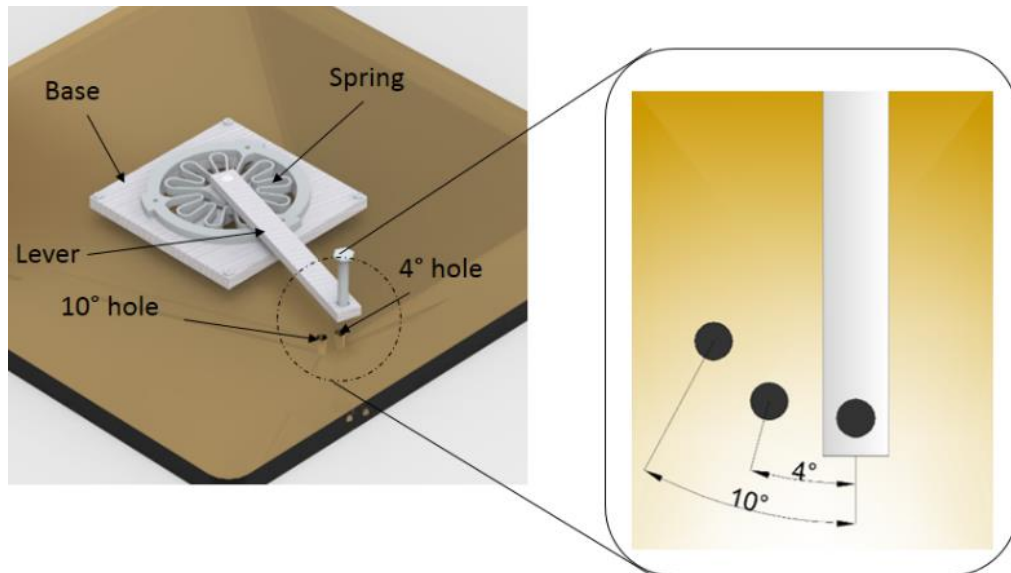


Figure 6-11 Experimental setup for the POF sensor validation.

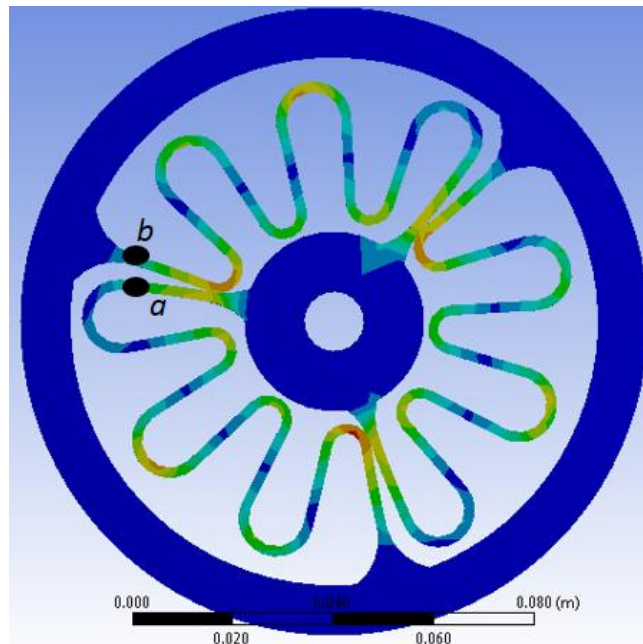


Figure 6-12 Equivalent strain of the spring submitted to a 15 Nm torque. The points a and b are more suitable for the POF sensor positioning.

The POF sensor has to be positioned perpendicular to the face of the spring shown in Figure 6-12. Otherwise, it may interfere on the spring extension movement due to the fiber strain (since a bulk PMMA POF is employed) and can slip on the compression movement. Both in extension and compression of the spring, the effects of the sensor mounted on the spring surface will cause a decrease of the sensor sensitivity. In order to place the sensor perpendicular to the spring surface without inhibit the spring movement, supports for the optical fiber sensor were made. These supports are placed on the points a and b of the spring presented in Figure 6-12. A schematic drawing of the spring with the POF sensor is presented in Figure 6-13(a), whereas, a photograph of the spring with the 3D printed supports and the optical fiber sensor is shown in Figure 6-13(b).

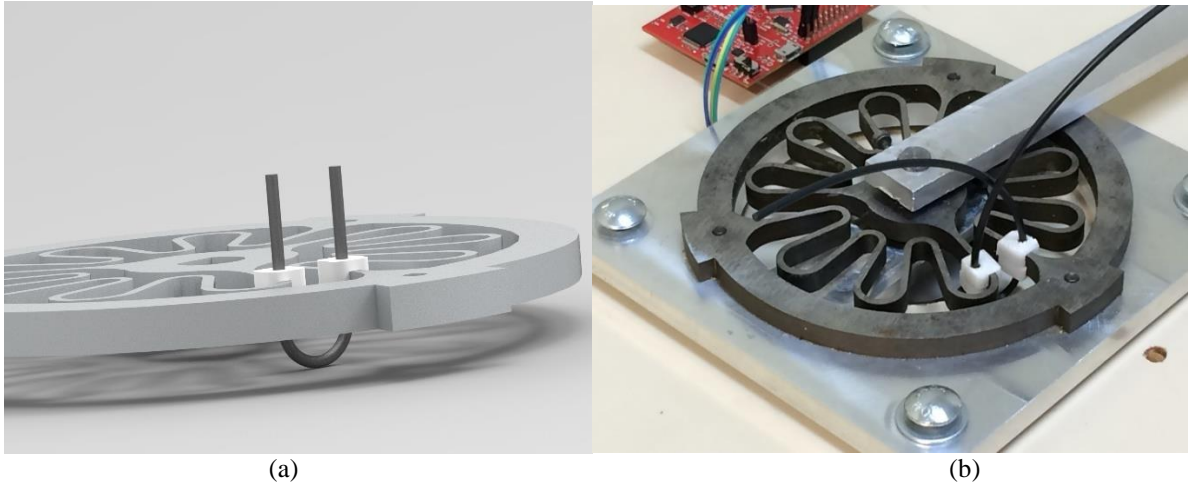


Figure 6-13 (a) Schematic drawing of the POF sensor attached on the spring and (b) Photograph of the spring with the 3D printed supports for the POF sensor positioning.

### 6.3.2.2. Method for Angular Deflection measurement

Applications of POF curvature sensors involve a calibration phase on static or quasi-static conditions prior to the application of the sensor on dynamic measurements. In this case, the first measurements are made on static conditions, which are on  $0^\circ$ ,  $4^\circ$  and  $10^\circ$ . The sensor response at each of these angles are acquired and a calibration curve is obtained. The characterization test comprises of positioning the lever on the holes with  $4^\circ$  and  $10^\circ$  distance of the lever for about 150 seconds at each angle. Since the lever is directly connected to the spring output, a  $10^\circ$  turn represents a  $10^\circ$  deflection of the spring, for example. The lever is connected to the spring output as presented in Figure 6-11. For this reason, the angular movement of the lever is directly transmitted to the spring. Therefore, the characterization of the angular deflection is made by positioning the lever on the holes with an angular displacement with respect to the lever initial position of  $4^\circ$  and  $10^\circ$  (see Figure 6-11) for about 150 seconds at each angle. A laser with 3 mW @650 nm is connected to one end of the fiber, whereas the other end of the fiber is connected to a photodiode with a transimpedance amplifier circuit. The acquisition frequency is 200 Hz. Since the POF sensor can present measurement errors with the variation of temperature and humidity [112], all tests are made without the variation of these parameters. In addition, another POF, connected to the same light source, is positioned close to the spring without any strain applied on it for temperature and humidity monitoring.

The viscoelastic response may be modeled with the Maxwell's viscoelastic model as depicted in previous sections (see also Appendix A). In this model, the viscoelastic response is approximated as a system with a spring and a dashpot connected in series. The spring represents the elastic component of the material response, whereas the dashpot is related to the material viscous response. Applying this principle to the POF curvature sensor response, it is possible to disconnect the time-varying and the static components of the response. By doing so, an equation relating the dynamic response ( $P(t)$ ) and the static response ( $P_0$ ) is obtained by:

$$P(t) = P_0 \exp\left(-\frac{t}{\tau}\right), \quad (6.1)$$

where  $t$  is the time and  $\tau$  is the polymer time constant, which can be obtained by an exponential fit of the creep experiment response. Furthermore, the static response of the sensor can be isolated on Eq. 6.1 to obtain an expression to compensate the viscoelastic effects of the sensor. Figure 6-14 presents the compensated and uncompensated responses for the viscoelastic effect on the sensor response of the static characterization with  $10^\circ$  deflection of the spring. The stress on a fiber generates a variation of the signal. Therefore, it is expected that the optical response of the sensor without the time-varying component will be inverse in modulus when compared to the one obtained in creep recovery.

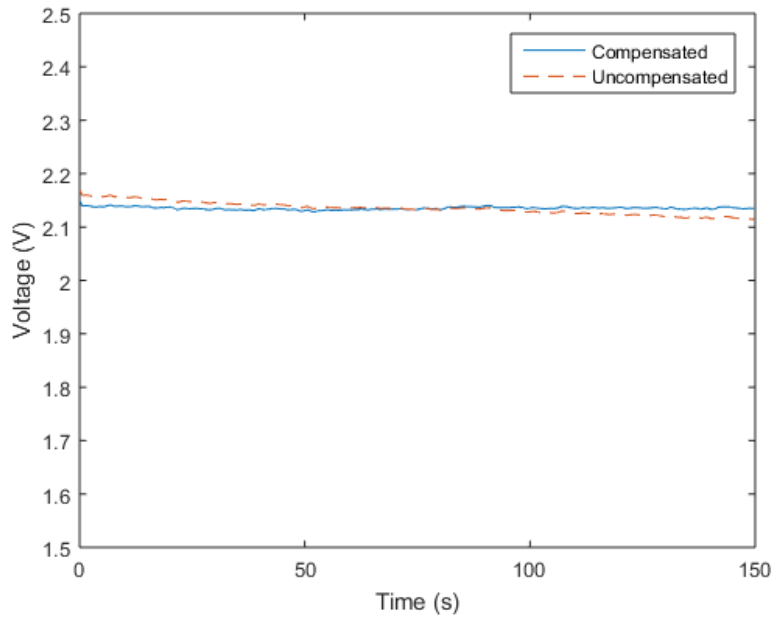


Figure 6-14 Comparison between compensated and uncompensated responses of the POF sensor when the spring is deflected in 10°.

The compensated responses for the 10° and 4° deflections were 2.14 V and 2.01 V, respectively. In addition, the response when no deflection is applied on the spring is 1.92 V. These responses are related to the spring angles through a linear regression. The calibration curve and correlation coefficient are presented in Figure 6-15.

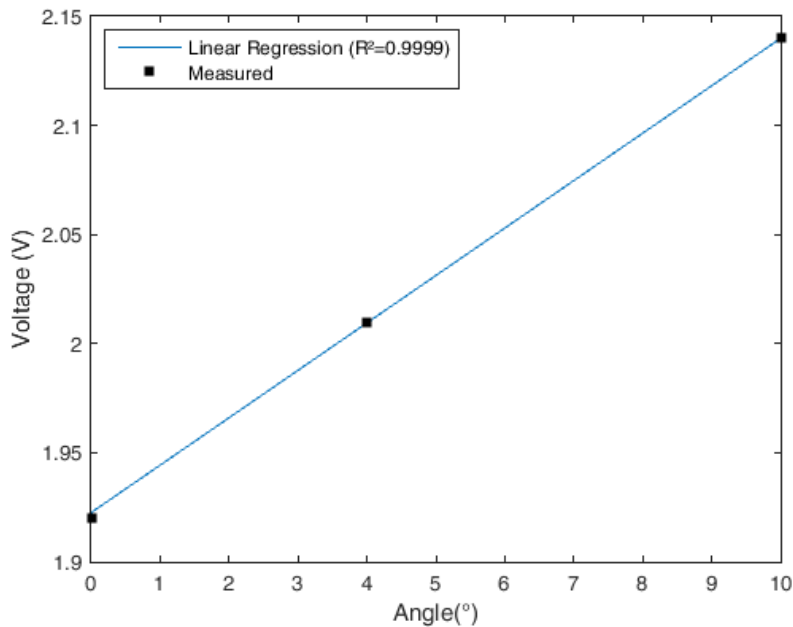


Figure 6-15 Calibration curve of the POF curvature sensor.

The dynamic response of the sensor is evaluated on sequential compression cycles. The tests comprise of loading and unloading the lever for about 3.5 seconds. Figure 6-16 shows the results for the POF sensor and the encoder measurements, which are not continuous for a better visualization of the POF response.

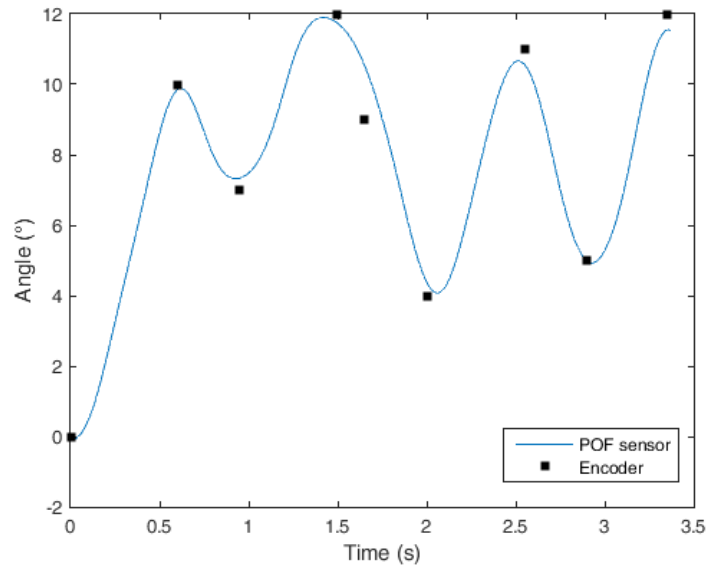


Figure 6-16 POF curvature sensor response for successive loading/unloading cycles and encoder measurements.

For this test, the RMSE (between the POF sensor and the encoder) is about  $0.57^\circ$ . However, it should be noted that both systems present different behaviors on the dynamic tests. The encoder response is in steps of  $0.3^\circ$ , whereas, the POF sensor presents almost continuous response with a resolution of  $0.1^\circ$  when considering the 8-bit ADC. For this reason, it may be an angle that is below the encoder resolution, but it is within the POF sensor resolution that will be detected by the proposed sensor. Although the POF can detect this angle, it is calculated as an error of the POF sensor. Therefore, this RMSE may be lower if a higher resolution system is employed as reference. Nevertheless, the POF sensor presented errors lower than 4% when considering the entire range of the test.

### 6.3.2.3. Proposal and Validation of Novel Technique for Torque Measurement

Despite the good accuracy of the POF curvature sensor, it generally has a saturation trend of its response in angles higher than  $90^\circ$ . However, in this case, the initial position of the sensor is already on a  $180^\circ$  bend (see Figure 6-13(a)) and the sensor shows a linear behavior. One reason for this behavior may be a trade-off between the radiation losses due to the curvature and the attenuation generated by the refractive index variation that the stress-optic effect causes. This assumption is verified, and its suitability is demonstrated in Appendix F as well as the development of the torque sensor POF sensor based on stress-optic effects, where the POF power attenuation is directly related to the applied torque.

Based on the evidences discussed in Appendix F, the assumption for the POF torque sensor is, since the fiber is initially bended in  $180^\circ$ , all the attenuation of the optical power is due to the variation of the refractive index caused by the stress-optical effect. Furthermore, as assumed for the deflection in Section 6.3.2.2, all the torque generated by the spring deflection is directly transmitted to the fiber. For this reason, different refractive indexes are applied on the equation of the sensor attenuation (see Appendix A) to obtain the relation between the output power attenuation and the refractive index variation. The POF sensor properties are presented in Table 6-2. To enhance the signal visualization, the output power signal is normalized with respect to the first signal (when the refractive index variation is 0). Figure 6-17 shows the relation between the sensor output variations with the refractive index variation ( $\Delta n_c$ ).

Table 6-2 POF sensor properties.

Parameter	Value	Unit
$a$	0.49	mm
$p$	0.60	mm
$c$	12.48	mm
$n_c$	1.492	-
$n_{cl}$	1.417	-
$q_{11}$	$10^{-11}$	$m^2/N$

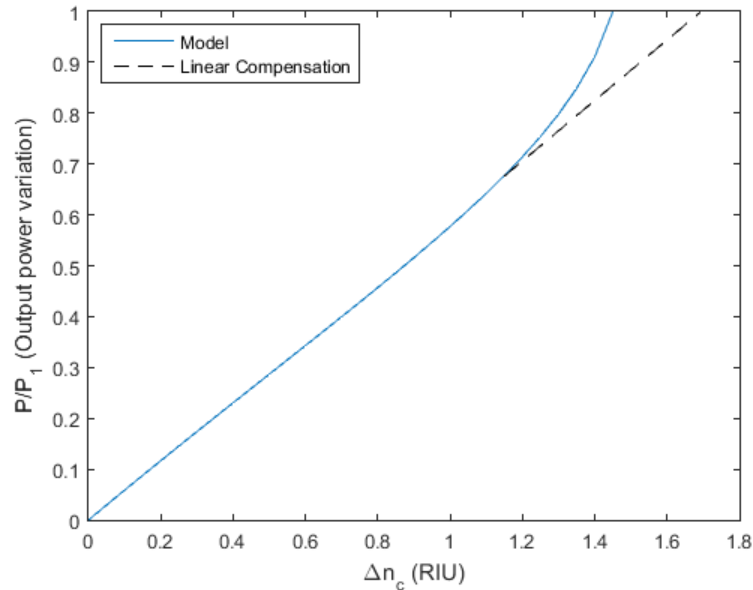


Figure 6-17 POF sensor output power variation with different refractive indexes and the linear compensation for refractive indexes higher than 1.3 RIU.

The output power variation with the refractive index changes is almost linear. However, the relation does not have a linear behavior when the refractive index variation is higher than 1.3. Such relation is obtained under the consideration that all power attenuation is due to the stress-optic effect, and it may lead to errors on the torque measurement. In order to compensate the effect of this nonlinearity on the torque measurement, a linear approximation of the curve relating the refractive index variation and the output power is made for refractive indexes higher than 1.3 (see Figure 6-17).

The variation of the core refractive index due to the stress-optic effect is given in Appendix A. Furthermore, as shown in Section 6.3.2.2, the time-varying component of the sensor viscoelastic response can be isolated from the static component through Eq. 6.1. Since the main assumption here is that all the signal attenuation is due to the stress-optical effect, Eq. 6.1 can be applied for the stress response of the sensor shown in Eq. 6.2. If pure bending stress is considered, the static stress ( $\sigma_0$ ) can be calculated as:

$$\sigma_0 = \frac{Tx}{I}, \quad (6.2)$$

where  $T$  is the torque,  $x$  is the perpendicular distance between the bending axis and the neutral line, and  $I_x$  is the moment of inertia around the neutral axis. Applying the assumption that all the output signal variation is due to the stress-optical effect, Eq. 6.1 can be rewritten with stress terms instead of optical power terms. By taking the compensated response, the torque equation for the POF torque sensor is obtained as:

$$T = \frac{\Delta n_c 2I_x}{n_c^3 q_{11} x}. \quad (6.3)$$

Since the fiber cross sectional area is circular, the moment of inertia depends only on the POF total diameter, which is the 0.98 mm of the core plus the 20  $\mu\text{m}$  thickness of the cladding and the 1.2 mm of the jacket that totalizes the diameter of 2.2 mm of the POF employed. The distance between the bending axis and the neutral line is the length indicated as “higher stress region” in Figure 4-1. The length of this region is about 3.5 mm. Although the value of this distance can change with the bending angle, this variation is not high in this case due to the lower angles of spring deflection, which is lower than  $12^\circ$  (see Figure 6-16) and the lower curvature radius of the fiber in this case. Therefore, the distance between the bending axis and the neutral line  $x$ , is considered constant. In order to get the refractive index variation, the range of variation of this parameter with the output power can be approximated through linear regressions. Equation 6.4 shows the linear regression for the result presented in Figure 6-17. This equation gives the estimated refractive index ( $n_{est}$ ) with a certain output power variation.

$$n_{est} = 1.571 \frac{P}{P_1} + 0.04474 \quad (6.4)$$

The difference between the estimated refractive index when the output power ratio is 1 (1.616, see Eq. 6.4) and the estimated refractive index for a certain output power ratio is the refractive index variation. The torque curve is compared with the measurements made on the spring. Since the spring presented high linearity on both extension and compression movements [9], the torque on the spring under compression is the product between the spring constant for compression, which is 92 Nm/rad, and the spring deflection angle. When the deflection angle is  $4^\circ$ , the spring torque is 6.42 Nm, whereas the torque estimated by the sensor based on POF is 6.78 Nm, this difference represents an error of 5%. However, this error is reduced as the spring deflection angle increases. When the spring angle is  $10^\circ$ , the torque is 16.05 Nm and the POF torque sensor estimates a torque of 16.57 Nm, which is an error of 3.2%.

The POF torque sensor is also validated in dynamic measurements. The test results presented in Section 6.3.2.2 is evaluated with respect to the torque by means of the product between the spring deflection measured by the encoder and the spring constant. Figure 6-18 presents the test results and the torques estimated by the torque sensor. The RMSE is also calculated in this case. The error between the POF sensor and the encoder for the torque estimations is 0.33 Nm. The errors that can be present due to the encoder resolution discussed in Section 4.6.2.2, are also presented in this test. Although the deflection range is low, the assumption of constant moment of inertia and constant perpendicular distance between the bending axis and the neutral line also can lead to minor deviations on the torque estimation. For this reason, the error of the torque sensor is higher than the one of the curvature sensor. The comparison between the RMSE for the torque and the angle is made by calculating the percentage contribution of the RMSE on the total range of the test, which means to calculate a ratio between the RMSE and the test range. In this way, the error percentage contribution of the torque sensor is 5.7%, whereas the percentage contribution of the curvature sensor is 4.7%. The error of the torque sensor may be further reduced if the variation of the distance between the bending axis and the neutral line is considered for the different deflection angles on the spring. Nevertheless, Figure 6-18 also shows the comparison between the proposed technique for torque measurement with POF sensors and the POF curvature sensor with the application of the spring constant to estimate the torque, an alternative manner to determine the torque on a torsional spring. Regarding the sensor resolution, the estimated value for the torque measurement is about 0.15 Nm, which provides a higher resolution than the encoder (about 0.5 Nm). In addition, the sensor errors for the torque measurements is lower than 5%, which indicate high precision of the proposed POF sensor.

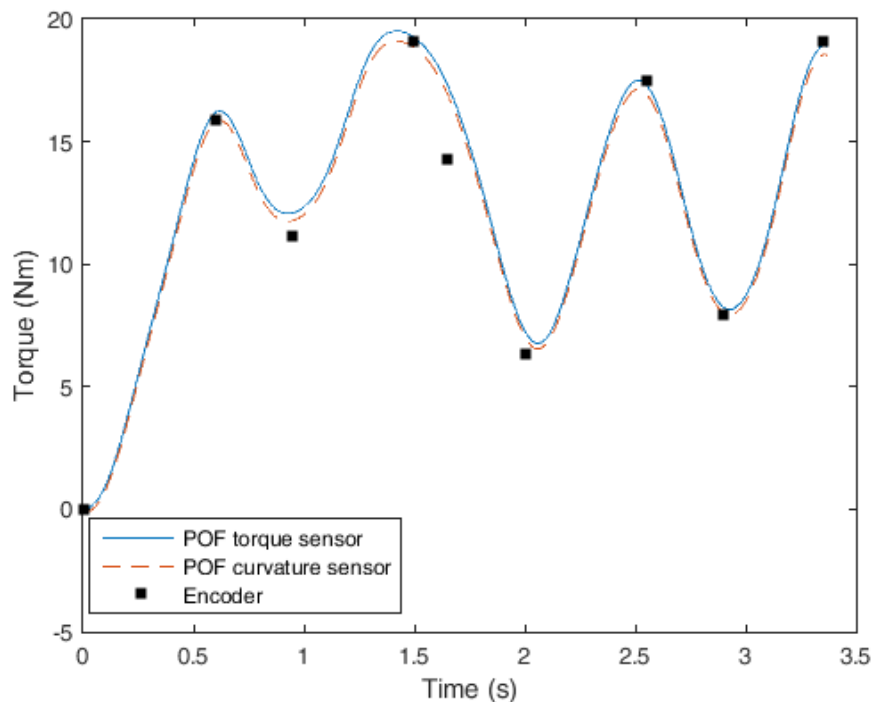


Figure 6-18 Torque estimated by the POF torque sensor for successive loading/unloading cycles and torque estimated by the encoder and POF curvature sensor with the application of the spring constant.

### **6.3.3.POF-Embedded, 3D-printed Support for Microclimate and Human-Robot Interaction Forces Assessment in Wearable Devices**

This section presents the development of a POF sensor system embedded in a 3D-printed exoskeleton's shank support for simultaneous measurement of human-robot interaction forces and the microclimate conditions (humidity and temperature). The presented solution offers flexibility and low-cost that could be used in different wearable devices. The sensors have a modular configuration in which the microclimate sensors are embedded in structures made of rigid materials (ABS) and the force sensors, in flexible materials (TPU). The proposed sensor system is applied in an exoskeleton for knee rehabilitation. In addition, it is also scalable, since their dimensions can be customized for each user. Finally, the rapid prototyping methods employed in conjunction with the low-cost and ease of implementation of POF sensors based on intensity variation result in an instrumented shank support for wearable devices that can be readily employed in large scale production or it can be customized for each user.

#### **6.3.3.1. Sensors Design, Fabrication and Operation Principle**

All the four proposed sensors are based on the light intensity variation and are embedded in 3D-printed structures. Two sensors are positioned for the pressure assessment in flexion and extension cycles of the gait, whereas the other two are used for temperature and humidity assessment. The sensors for temperature and humidity measurement are embedded in rigid structures made of ABS. The reason to employ rigid structures in these sensors is to isolate the sensors from the stress or strain applied in the exoskeleton's shank support. In this way, the intensity variation in these sensors are only due to temperature and humidity. On the other hand, for the sensors employed in the human-robot interaction forces assessment, the stress applied in the support have to be transmitted to the fiber. In order to achieve this, the 3D-printed structure, where the sensor will be embedded is made with TPU due to its higher flexibility.

A schematic representation as well as the picture of the device are presented in Figure 6-19(a)-(c), which also detail the fabrication steps of the proposed instrumented shank support for wearable devices. The POF employed in this study is a multimode PMMA with a core diameter of 980  $\mu\text{m}$  and cladding thickness of 10  $\mu\text{m}$ .

As shown in Figure 6-19(a), the first step in the sensor fabrication is to perform a lateral section on the fiber removing the cladding and part of the core, which creates a sensitive zone with higher sensitivity to curvature and environmental variations. The sensitive zone is created through abrasive removal of material and has 14 mm length and 0.6 mm depth, where such length and depth were chosen as the one with highest sensitivity and linearity according to the analysis presented in previous sections. The lateral sections with aforementioned dimension are made in four pieces of POF, which are applied for the temperature, humidity and pressure sensors.

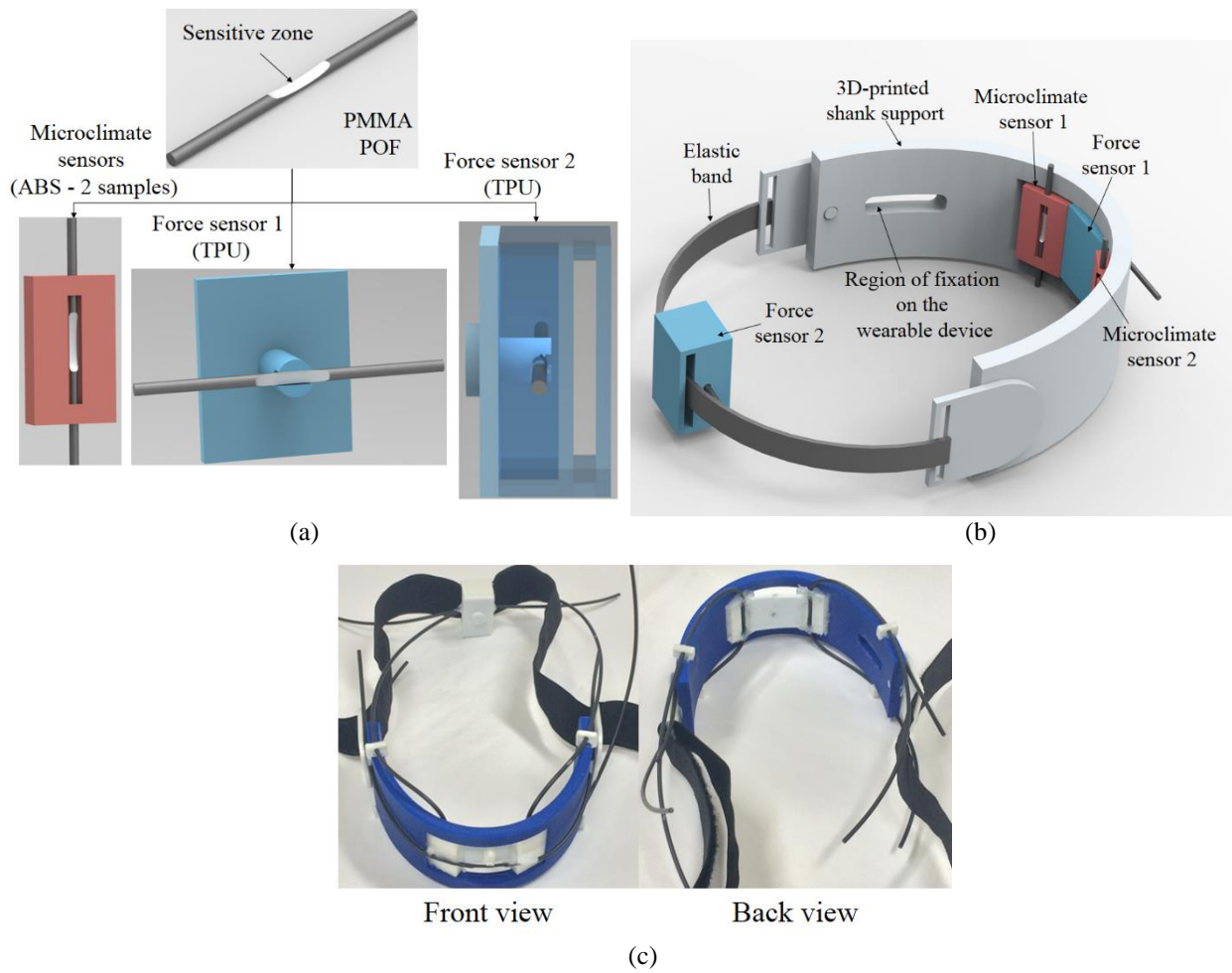


Figure 6-19 (a) POF sensors fabrication. (b) Schematic representation of the instrumented shank support. (c) Pictures of the front and back views of the developed prototype.

After the sensitive zone fabrication, an annealing treatment is performed in the fibers in which they are kept under water. This reduces the internal stress created in the fiber manufacturing process, decreasing the sensors' hysteresis and increasing the transverse force sensitivity [196]. Then, each fiber is embedded in its respective structure manufactured with the 3D printer Sethi3D S3 (Sethi, Brazil). Thus, two pieces of POFs with lateral section are embedded in a 3D-printed ABS structure as shown in Figure 6-19(a). Such structure is rigid, in order to isolate the sensor from the forces applied in the shank support, but it also has an opening to allow the exposure of the fiber lateral section with the environment. In this way, the sensors can be used to measure the temperature and humidity variations with negligible influence of the applied force. It is noteworthy that the stray light has much lower power than the one of the coupled on the end facet of each POF. Thus, it is expected that the side coupling between the stray light and the POF lateral will not lead to significant power fluctuations. The microclimate sensors are close to the subject's skin (distance of about 2 mm), which further reduce the influence of stray light in the sensor response, whereas the force sensor 2 is already embedded in a structure, reducing the stray light coupling. In addition, it is possible to place a 3D-printed housing on the front plane of the instrumented support (see Figure 6-19(c)) to further reduce the stray light influence on force sensor 1.

The operation principle for temperature and humidity assessment is based on the intrinsic feature of polymers, which is the Young's modulus dependency with environmental conditions (temperature and humidity) [59] as thoroughly described in Section 4.3. In order to apply the stress on the fibers, a torsion is made on each fiber that is employed in the ABS rigid structure to guarantee the torsion stress on the fiber as depicted in Section 4.3.

For the force sensors 1 and 2 (see Figure 6-19(a)) the opposite occurs, i.e., the sensors are embedded in flexible structures made of TPU that transmit the applied force to the fiber without being in direct contact with the microclimate variations in the interface between the user's leg and the shank support. When a force is applied to the force sensors, the flexible structure deforms, which leads to a curvature in the fiber, resulting in

a power attenuation. In addition, the force also leads to a stress in the fiber that result in a refractive index variation of the POF due to the stress-optic effect as characterized in [176].

The sensors' positions are presented in Figure 6-19(b) and (c). In this case, the force sensor 1 is positioned in the front of the 3D-printed support, whereas force sensor 2 is positioned in the back of the proposed support (see Figure 6-19(c)). Thus, when extension movements are performed, force sensor 1 is activated and measures the interaction force in this movement. Similarly, when the flexion is made, the force acquisition is performed with force sensor 2. In addition, the sensor assembly is also made with a thermoplastic resin to improve the connection and provide even higher stability to each sensor module. Therefore, the proposed instrumented 3D-printed support presents a modular configuration that enables the variation of each sensor module positions according to the desired application.

### 6.3.3.2. Experimental Setup for Sensors Characterization

The light sources used in the test are two LEDs, one at 660 nm employed in the microclimate sensors characterization (IF-E97 Industrial Fiber Optics, USA) and the other at 870 nm (IF-E91D Industrial Fiber Optics, USA) for the force sensor analysis both LEDs have an output power of about 0.4 mW. The light is coupled from the LEDs to the sensors trough a 1×2 light coupler with 50:50 coupling ratio (IF 540 Industrial Fiber Optics, USA).

In addition, the used photodetectors are the phototransistors IF-D92 (Industrial Fiber Optics, USA). The characterization of the sensors is performed with respect to humidity, temperature and force variations, which is developed in two steps. The first one is the application of those parameters on each sensor module. In this way, each sensor is characterized with respect to each parameter. For the force characterization, a set of calibrated weights are positioned on respective modules, where the range of the test is from 0 to 40 N in 10 N steps. The temperature characterization is made using a thermoelectric Peltier plate (TEC1-12706, Hebei IT) with a temperature controller (TED 200C, Thorlabs) on the range of 25°C to 45°C in steps of 5°C. Finally, the humidity characterization was made with an in-house modified climate chamber 1/400 ND (Ethik Technology, Brazil) with humidity varying from 20% to 90%. The chosen temperature and humidity ranges are within the range of comfort zones defined in [6], whereas the force is within the range of interaction forces obtained in previous works [28].

Since POFs present variation on their Young's modulus with temperature and humidity, the force sensor will present cross-sensitivity with respect to the environmental changes, as demonstrated in [197]. For this reason, the force characterization is also made in different conditions of temperature and humidity. It is expected that the environmental changes will lead not only to an offset in the sensor's force response, but also altering the sensor sensitivity. Therefore, it is necessary to compensate the effects of temperature and humidity on the force sensors' responses. The method employed to achieve this compensation is summarized in the block diagram shown in Figure 6-20. The method is based on the sensor characterization for each specific condition. First, the force sensor is characterized in constant temperature and humidity conditions. Then, the force characterization is repeated in different temperature conditions and humidity conditions, where a correlation is performed between the changes on the offset and sensitivity of the sensor responses as a function of temperature and humidity. In addition, polymers present creep/relation in their stress/strain responses, which is characterized for the PMMA POF used here (see ref. [58]) and their relation in the different sensors responses are presented in [78], [184].

For this reason, creep tests are made in the force sensors, where different forces are applied in the sensors for about 3 minutes and an exponential regression is made on the sensor response. In summary, the general equation for the proposed force sensors is presented in Eq. 6.5, whereas Eq. 6.6 shows the general equation for temperature and humidity as follows:

$$P_{F1,F2} = [a(T, H) \times F + b(T, H)] \times \exp(\tau \times t), \quad (6.5)$$

$$\begin{bmatrix} P_{M1} \\ P_{M2} \end{bmatrix} = \begin{bmatrix} K_{1,H} & K_{1,T} \\ K_{2,H} & K_{2,T} \end{bmatrix} \begin{bmatrix} \Delta H \\ \Delta T \end{bmatrix}, \quad (6.6)$$

where  $P_{F1,F2}$  is the optical power of force sensors 1 and 2,  $a(T,H)$  is the sensor sensitivity as a function of the temperature ( $T$ ) and humidity ( $H$ ), which will be characterized in the following sections. In addition,  $b(T,H)$  is the offset in the sensor response with respect to the environmental changes, also obtained in the sensor characterization stage. Finally, the term  $t$  is the time and  $\tau$  is the sensor time constant characterized in the creep

tests in order to assess the long-term response of the force sensors.  $P_{M1}$  and  $P_{M2}$  are the measured powers for microclimate sensors 1 and 2, respectively. Thus, the  $P_{F1}$  is the force sensor 1, for the interaction force assessment in the flexion cycles, whereas PF2 is the one for the force assessment in the extension cycle (see Figure 6-19(b)). Similarly,  $P_{M1}$  and  $P_{M2}$  are the microclimate sensors positioned next to force sensor 1 as shown in Figure 6-19(b), where the temperature and humidity are estimated using the responses of both sensors after applying Eq. 6.6. These parameters are also presented in the block diagram of Figure 6-20.  $K_{1,H}$  and  $K_{2,H}$  are the humidity sensitivities of the microclimate sensors 1 and 2, respectively. Similarly,  $K_{1,T}$  and  $K_{2,T}$  are the temperature sensitivities of microclimate sensors 1 and 2.

The sensor modules are assembled as presented in Figure 6-19(c) and the second step is made. Such step is the sensor system validation through simultaneous analysis of temperature, humidity and force in all sensors. In this case, there is the application of force in the whole shank support with the positioning of the calibrated weights in a structure that resembles the human shank, which is connected to the front part of the support. Simultaneously, another set of calibrated weights is applied in the back part of the structure in which the force sensor 2 is positioned. In addition, the temperature and humidity are also monitored through microclimate sensors 1 and 2, where the reference sensor for temperature and humidity comparison is the HTU21D (Measurement Specialties, USA). Figure 6-21 shows the schematic representation of the experimental setup used in the sensor validation.

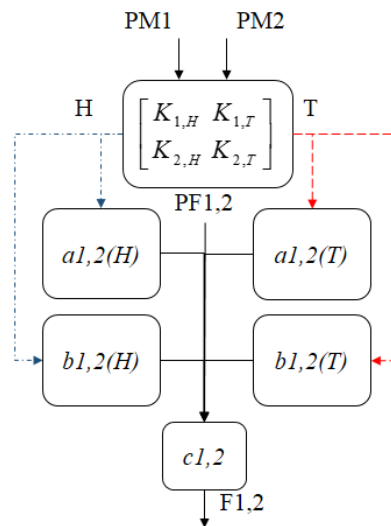


Figure 6-20 Block diagram for the temperature, humidity and force responses of the proposed sensor system.

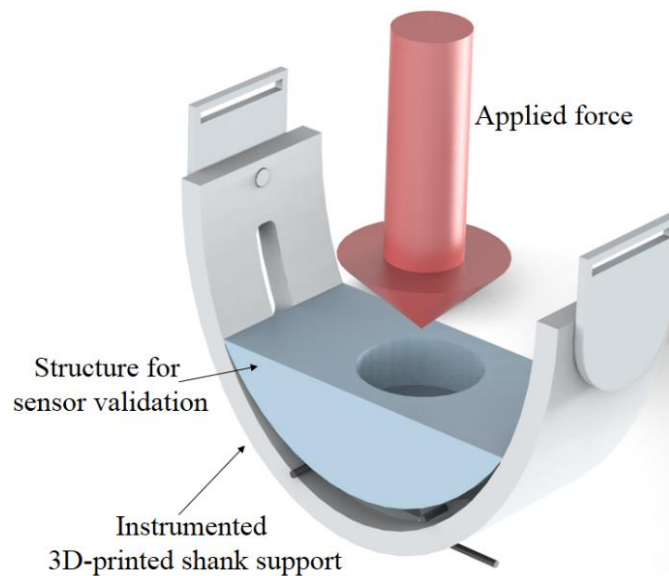


Figure 6-21 Experimental setup for validation of the proposed sensor system.

### 6.3.3.3. Instrumented 3D-printed Shank Support Application in Wearable Devices

After the sensors' characterization and validation, the proposed 3D-printed support is applied in two different wearable devices for gait rehabilitation and assistance. The device is an exoskeleton for knee rehabilitation, which provides different degrees of assistance with an impedance controller [28]. In this case, the proposed 3D-printed support is positioned on the device, whereas another support is positioned on the users' thigh as shown in Figure 6-22.

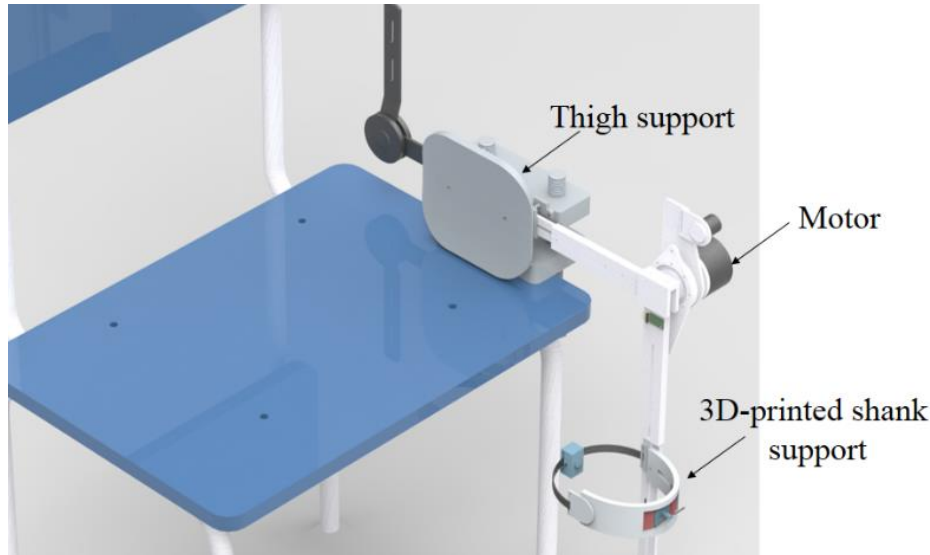


Figure 6-22 Experimental setup for exoskeleton application.

The exoskeleton is positioned on a chair, as shown in Figure 6-22, the user makes flexion and extension cycles and the impedance controller of the exoskeleton provides a certain degree of assistance in the movement (or increase the difficulty of the movement) depending on the user's rehabilitation stage. For the tests with the proposed 3D-printed support, the user is asked to make flexion/extension cycles with the impedance set on the tests is only the one for the gear reduction. Thus, the exoskeleton does not provide any assistance or difficulty in the flexion/extension movements. The exoskeleton is attached on the user through the thigh support and the proposed shank support and the force, temperature and humidity are collected in ten flexion/extension cycles.

### 6.3.3.4. Sensors Characterization Results

The microclimate sensor response and characterization were already demonstrated in Section 4.3. Similarly, the creep response as well as the temperature cross-sensitivity were already depicted in previous Chapters. For these reasons, the characterization results of each sensor are presented in Appendix G, where it is necessary a characterization for each sensor. The results for the sensor validation at these environmental conditions are presented in Figure 6-23(a). In order to test the sensor in different conditions, two sets of tests are presented in Figure 6-23(a): one is a short-term test in which the force variations are performed in a time interval within 30 seconds, whereas the other is a long-term test. In the latter, the force variations are performed for 150 seconds, where it can also be seen the compensation of the creep behavior of the sensors. Furthermore, Figure 6-23(b) shows the sensor validation of the proposed 3D-printed shank support with the experimental setup shown in Figure 6-21 and with the force also applied in Force sensor 2, where the applied force is known (due to the calibration weights). In addition, temperature and humidity sensors are in the same environmental conditions as the proposed POF sensors.

The results of the force sensors validation show a RMSE between the sensor response and the applied force (obtained from the calibrated weights applied on the sensor) for the short-term tests of about 2.8 N for sensor 1 and 2.3 N for sensor 2. Regarding the long-term tests, the obtained RMSEs are 1.9 N and 1.0 N for Force sensors 1 and 2, respectively. The obtained errors are related to nonlinearities of the sensors and deviations in temperature and humidity, since the errors are higher in the short-term tests in which there was lower time for temperature and humidity stabilization. However, considering the whole range of the test, the mean relative error is below 4.5%, which can be regarded as low errors. Thus, the proposed Force sensors are suitable for human-robot interaction forces applications, where, besides short and long-term force variations, there is also the microclimate variation.

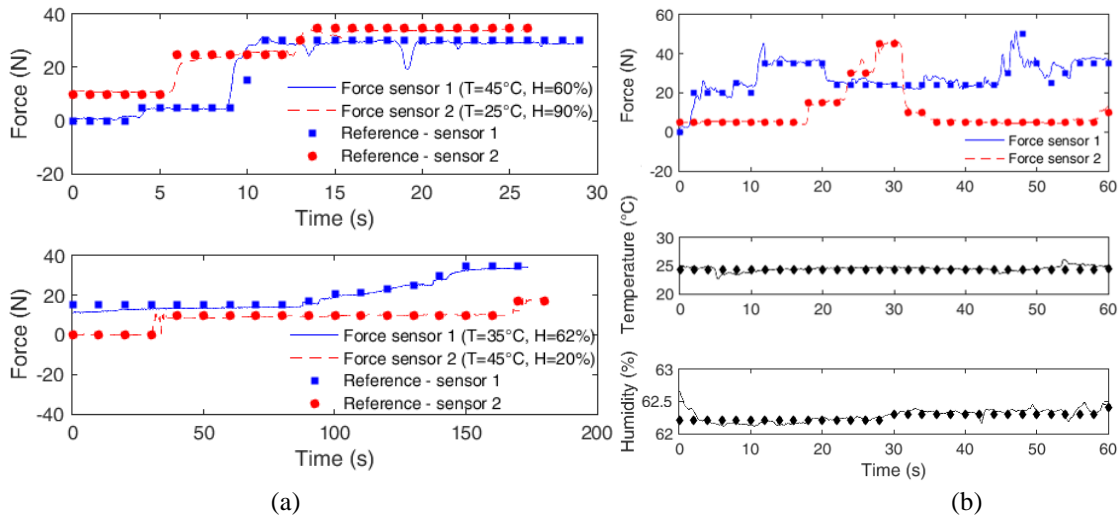


Figure 6-23 (a) Force sensors validation under different temperature and humidity conditions for short (top) and long (bottom) term tests. (b) Validation of the force and microclimate sensors embedded in the 3D-printed shank support.

In the tests presented in Figure 6-23(b), there is an increase of about 10% in the RMSE of the force sensors, where such increase is related to the errors of microclimate sensors 1 and 2. Since the temperature and humidity corrections occur by applying the temperature and humidity responses of the microclimate sensors, the errors of such sensors will be propagated to the force sensor response. Nevertheless, as can be seen in Figure 6-23(a) and (b), the proposed force sensors still present a good agreement with the applied force. In addition, considering both the characterization and validation tests, the RMSE of temperature and humidity sensors are about  $1.1^{\circ}\text{C}$  and 2.5%, respectively.

### 6.3.3.5. Application of the 3D-printed Instrumented Support

After the characterization and validation of the proposed 3D-printed instrumented support, we apply it as a shank support for the ALLOR wearable device discussed in Section 6.2 and presented in Figure 6-22. With the lower limb exoskeleton, the made tests are the flexion and extension of the knee. The results obtained with the proposed 3D-printed instrumented support are shown in Figure 6-24, where the 10 flexion/extension cycles were performed with the exoskeleton. Since Force sensor 1 is activated in the extension cycle and Force sensor 2 in the flexion, the response of Force sensor 2 was inverted in order to provide a better visualization of the results obtained in the exoskeleton application. It can be observed in Figure 6-24 that both sensors respond to the force input in their respective cycles, i.e., sensor 1 in extension and 2 in flexion. Thus, the maximum force of each sensor occurs in distinct instants of the flexion/extension cycle, which is in agreement with what is expected in those cycles and the higher force variation on the extension cycle. Moreover, it is in accordance with the previous works using the same device at the same conditions [28]. In addition, the temperature and humidity responses remain stable during the whole test and within the range of environmental conditions of the room, where the tests were performed.

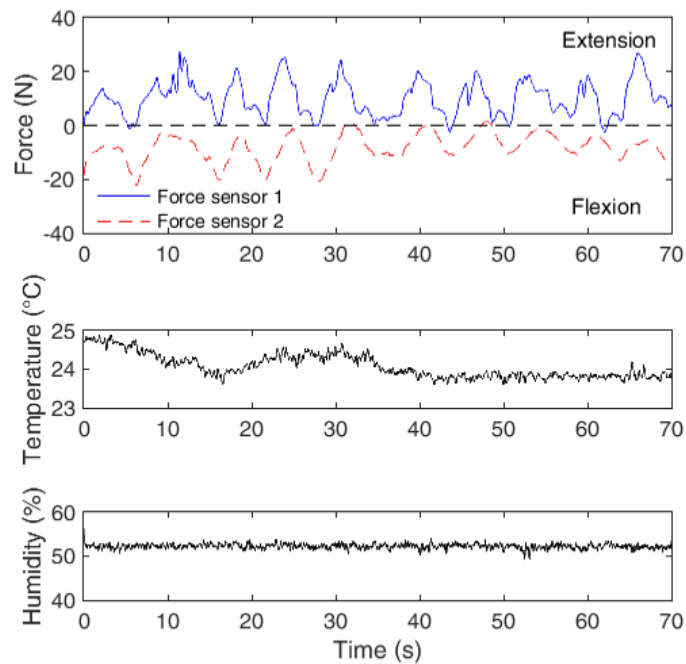


Figure 6-24 Force, temperature and humidity measured in the application of the proposed shank support in an exoskeleton for rehabilitation exercises.

### 6.3.4. Smart Walker Instrumentation and Health Assessment

This Section presents a POF-based smart textile for the assessment of breathing rate (BR) and heart rate (HR) as a tool for monitoring the physiological parameters of individuals. The proposed smart textile is also capable of detecting the cadence of the user, which is applied in human-robot interaction control [33]. Furthermore, we also propose an oximetry sensor that is embedded in the SW structure for the assessment of this parameter while the SW is being used. Thus, the proposed sensor can be readily employed in architectures for remote sensing for e-health applications and in cloud robotics.

#### 6.3.4.1. Experimental Setup

Figure 6-25 presents an overview of the SW with its sensors and motors (already discussed in Section 6.2). In addition, the figure also illustrates the user with the POF-based smart textile positioned in his/her chest. Regarding the reference in the POF-based smart textile analysis, a LRF (Hokuyo URG-04LX, Japan) is employed to detect the users' legs and estimate gait cadence. This sensor presents the advantage of being a non-contact solution, but it also presents some operational requirements. These requirements are related to the user's clothes that cannot be large in order to avoid occlusions and the illumination conditions of the environment.

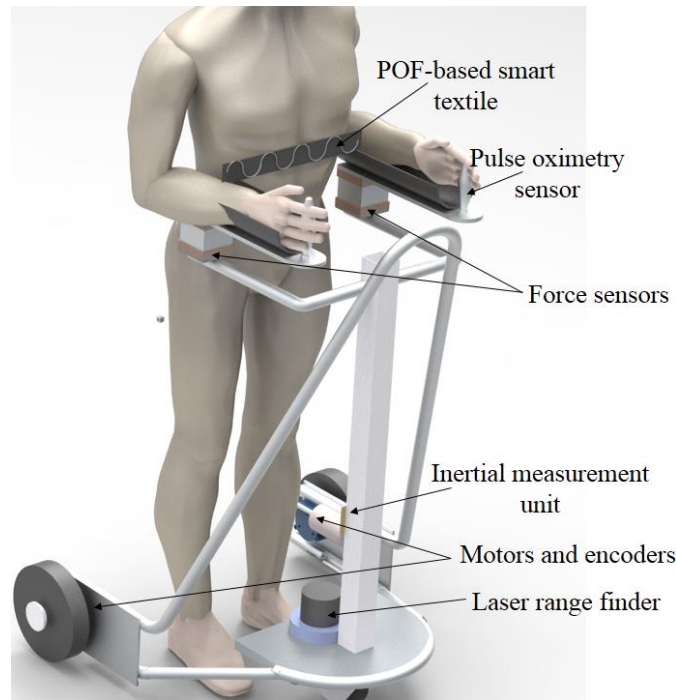


Figure 6-25 Schematic representation of the SW employed and the developed sensors.

As presented in Figure 6-25, the pulse oximetry sensor is embedded in the SW's handles. Thus, when the user starts to walk with the SW, the sensor begins the oxygen saturation measurement, which is an important indicative of the user's health and physical conditions. Simultaneously, the user has a POF-sensor positioned on his/her chest that measures their BR and HR. Additionally, when the person is walking, the POF-based smart textile is also able to track the user's gait cadence. The proposed sensor network offers interesting possibilities for different approaches in SW control schemes. As trends in late technology development, e-health [4] and cloud robotics [198] are regarded as solutions that greatly improve the quality of life of the citizens.

### 6.3.4.2. Polymer Optical Fiber Sensors Development

#### 6.3.4.2.1. Pulse Oximetry Sensor

The percentage of hemoglobin with bound oxygen measured in the pulse, known as  $SpO_2$ , is an important physiological parameter, since an oxygen level below 90% results in hypoxemia, which can be caused by some diseases or intensive physical activities [199]. In general, the pulse oximetry is based on the blood light absorption properties in which there are differences in the absorption of deoxyhemoglobin (Hb) and oxygenated hemoglobin ( $HbO_2$ ) [200]. In this case,  $HbO_2$  has higher absorbance in the near infrared wavelength region than Hb, whereas in the red light (about 660 nm) the absorption of the Hb is higher when compared with  $HbO_2$  [201]. Hence, the oxygen saturation can be estimated (in percentage) as:

$$SpO_2 = \frac{HbO_2}{HbO_2 + Hb} \cdot \quad (6.7)$$

In general,  $SpO_2$  measurements are performed on the ear lobe, finger or toe for an accurate assessment [201]. For this reason, the proposed  $SpO_2$  sensor is embedded in the SW's handles, where it will be in contact to the users' fingers when the SW is being used. In this way, we fabricated a handle for the SW through additive layer manufacturing (ALM) using the 3D printer UP! 3D mini (3D Printing Systems, Australia) with embedded POFs. The POFs used in this work (both in  $SpO_2$  and smart textile) are made of PMMA with a core diameter of 980  $\mu m$  and cladding thickness of 10  $\mu m$ .

Figure 6-26 shows the manufactured handle with the embedded POFs. Since the  $SpO_2$  takes the difference between the absorbance at different wavelength regions, two LEDs were employed, one (IF-E97 Industrial Fiber Optics, USA) with central wavelength at 660 nm and the other (IF-E91D Industrial Fiber Optics, USA) at 870 nm. The optical signal of each light source is transmitted through two POFs in order to increase the region that the sensor is able to measure. In addition, the  $SpO_2$  is estimated through the light reflected by the

person's finger, which is a common approach reported in the literature [52], [201]–[203]. Thus, two 2x2 light couplers with 50:50 coupling ratio (IF 540 Industrial Fiber Optics, USA) are employed with the configuration presented in Figure 6-26. The photodetectors used in this sensor are two phototransistors IF-D92 (Industrial Fiber Optics, USA). It is also worth to mention that the light couplers, LEDs and photodetectors are placed on the SW support (close to the LRF, see Figure 6-25), where the light coupler is fixed to avoid movements that may result in variation of the coupling ratio.

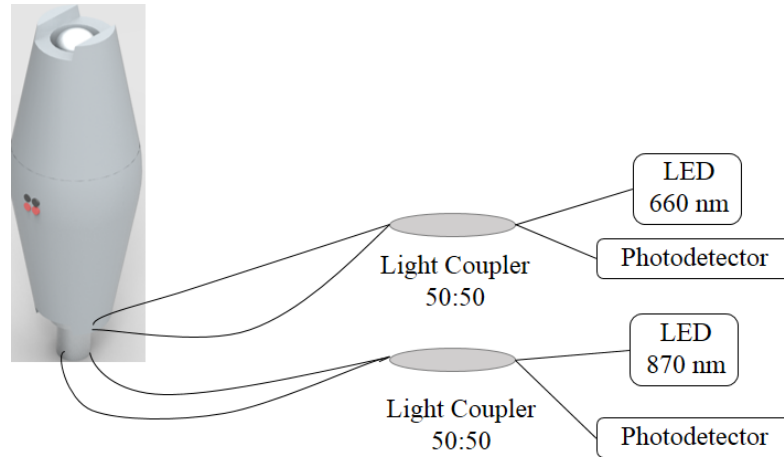


Figure 6-26 Schematic illustration of the proposed SpO<sub>2</sub> sensor.

The light attenuation at each wavelength due to scattering losses can be estimated by means of a modified Beer-Lambert law [53], which is described with details in [204]. Thus, also considering the solution of the modified Beer-Lambert law for 692 nm and 834 nm presented in [52], [203], the equations for Hb and HbO<sub>2</sub>, considering the wavelengths of 660 nm and 870 nm are presented in Eq. 6.8 and 6.9, respectively, as follows:

$$Hb = (-0.17\Delta P_{660nm} + 0.14\Delta P_{870nm}), \quad (6.8)$$

$$HbO_2 = (0.12\Delta P_{660nm} - 0.67\Delta P_{870nm}), \quad (6.9)$$

where  $\Delta P_{660nm}$  is the POF power attenuation at 660 nm and  $\Delta P_{870nm}$  is the power attenuation at 870 nm. In this case, we applied a bandpass filter between 0.6 Hz and 3.5 Hz in order to filter out the movement artifacts and reduce their influence in the SpO<sub>2</sub> estimation. Additionally, by analyzing the signal in the frequency domain, by means of a fast Fourier transform (FFT), the heart rate can also be estimated, as also demonstrated in [52].

#### 6.3.4.2.2. POF-based Smart Textile

The proposed smart textile comprises of an elastic band with an embedded POF, which is positioned on the user's chest (see Figure 6-25). When the person breaths or makes movements, there is a curvature variation in the POF that leads to power attenuation, where the light source is a LED (IF-E97 Industrial Fiber Optics, USA) and the power attenuation is acquired by a photodiode (IF D91 Industrial Fiber Optics, USA). In order to increase the sensor sensitivity, eight lateral sections are made in the fiber with 14 mm length and 0.6 mm depth, which are the optimum parameters found in Appendix B. The positions of each lateral section are presented in Figure 6-27, which also shows the different loadings that the elastic band is subjected when attached to the human chest.

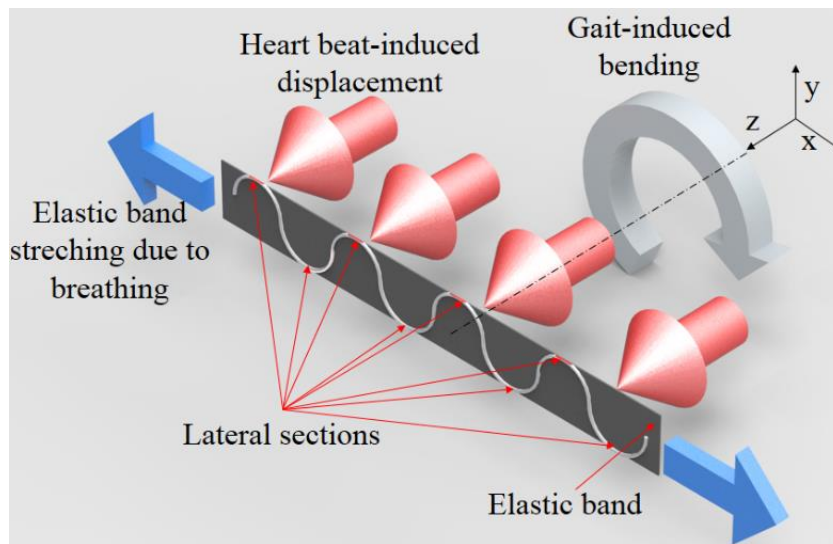


Figure 6-27. Overview of the POF-based smart textile and the loadings acting on it during the gait.

Regarding Figure 6-27, the respiration leads to the stretching of the elastic band, whereas the heartbeat induces a body vibration with low amplitude but can also be detected by the proposed sensor. In addition, there are movements in the frontal plane during the gait that induces a bending in the elastic band. All these aforementioned periodic movements present differences in the frequency or amplitude. The breathing frequency lies between 0.1 to about 0.8 Hz [51]. On the other hand, gait (cadence) and heartbeat present frequency ranges of 1.2 Hz to 3.4 Hz [51] and 0.6 Hz to 3.5 Hz [155], respectively. Although the gait and HR show similar frequency range, the spinal movements during the gait lead to a higher movement amplitude than the one induced by the heartbeat. For this reason, it is possible to separate heart, breathing rate and cadence by analyzing the sensor response in the frequency and time domains.

### 6.3.4.3. Sensors Characterization

#### 6.3.4.3.1. Oximetry Sensor Characterization

The tests for the oximetry sensor characterization and validation were made with four male subjects (mean and standard deviation ages of  $30.5 \pm 5.3$ ). The results are compared with a commercial reference photoplethysmography (PPG) sensor (digiDoc Pulse Oximeter, Norway). Thus, all four volunteers are asked to hold the 3D-printed handle for 30 seconds to 1 minute, where good repeatability was found between measurements with deviations lower than 2%.

Figure 6-28 shows the results obtained with the proposed oximetry sensor. For the  $SpO_2$  estimation, the results obtained at 660 nm and 870 nm are normalized and applied in Eq. 4.8 and 4.9. The results of Eq. 4.8 and 4.9 are substituted in Eq. 4.7 for the  $SpO_2$  assessment, which is presented in Figure 6-28(a). In order to demonstrate the sensor ability of tracking the HR, Figure 6-28(b) shows the sensor response in the frequency domain for each subject, where the peak of each response is the HR, which is also compared with the reference PPG sensor. Since the HR is commonly in the range of 0.6 to about 3.5 Hz, we apply a band-pass Butterworth filter of order 2 in this frequency interval. Then, the peak frequency is multiplied by 60 in order to show the results in beats per minute (bpm).

Regarding the  $SpO_2$  results, the proposed sensor was able to measure this parameter with good agreement with the reference sensor. The RMSE between the proposed and reference sensor is 0.15 %. However, it is worth to note that the proposed sensor has 0.1 % resolution, whereas the one of reference sensor is 1 %. Thus, the RMSE is also influenced by the POF system higher resolution. In addition, the highest difference between both sensors occur in the test with subject 4, which may be related to the user's hand positioning in the SW's handles, since if the fingers do not cover the sensing region, there might be measurement errors. In the HR assessment, there is also a comparison with the reference PPG sensor (digiDoc Pulse Oximeter, Norway), where the RMSE between both sensors is 0.25 bpm. Nevertheless, the HR is defined as the number of heartbeats in a minute interval, which is always an integer number. Thus, this RMSE lower than 1 bpm indicates a good comparison between both sensors.

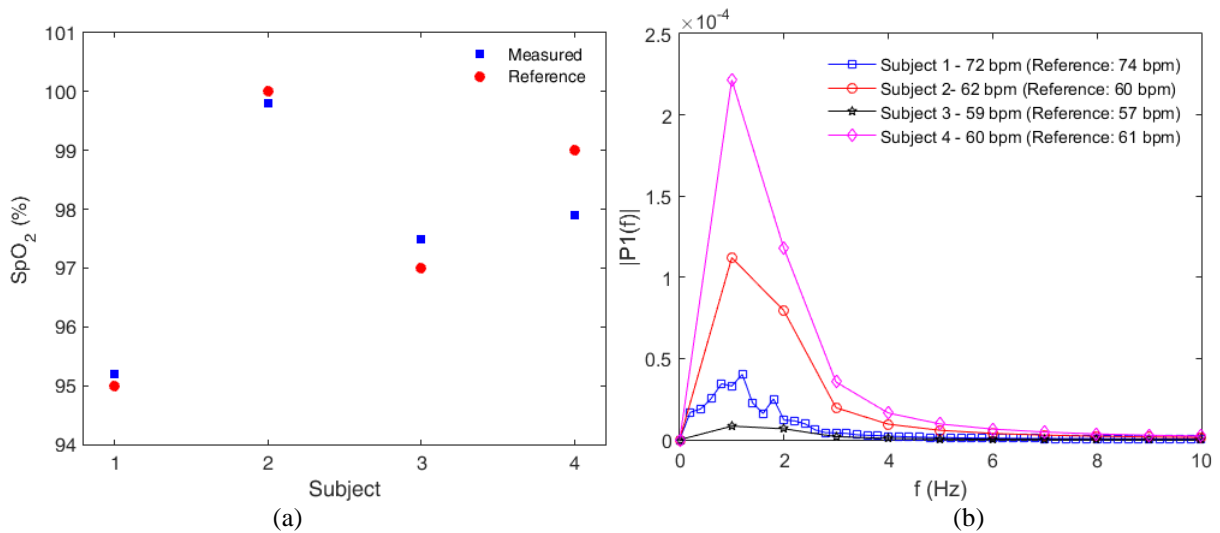


Figure 6-28 SW embedded oximetry sensor response for (a) SpO<sub>2</sub> measurement and (b) HR assessment.

### 6.3.4.3.2. Characterization of the POF-based Smart Textile

The characterization of the proposed smart textile is made in two scenarios: in rest position and during the gait. In this way, it is possible to analyze the sensor in two operation conditions: walking and resting. Conditions that include simultaneous measurement of the BR and gait cadence during the SW use and as a tool for BR and HR assessments when the person is not using the SW.

As mentioned above, the breathing frequency interval is within a different range of HR and gait cadence. Therefore, a straightforward way to separate those parameters in the frequency domain is by filtering the signal in different frequency windows. For this reason, a second-order Butterworth filter is applied in the frequency window of 0.1 Hz to 0.6 Hz for the estimation of the BR. Additionally, the same filter, but in the 0.8 Hz to 3.5 Hz frequency interval is employed for the gait cadence (when the person is walking) and HR (when the person is at rest) assessments. Once again, the proposed sensor is validated with four individuals, where the results for simultaneous assessment of BR and HR are presented in Figure 6-29.

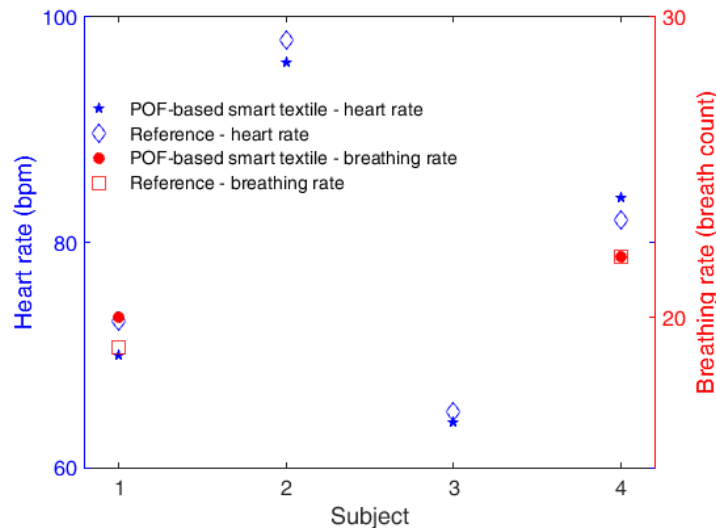


Figure 6-29 Heart and breathing rates measurement with the POF-based smart textile.

Comparison between POF-based smart textile for HR and BR presented a good agreement with the considered reference. The RMSE for HR assessment is 1 bpm, whereas the one for the estimation of breath count is 0.25 breath counts, which show the feasibility of the proposed sensor for measuring HR and BR. The reason for the higher error in the HR measurement is the heartbeat signal amplitude, which is some orders of magnitude lower than the one of breathing. Thereafter, the proposed POF sensor is characterized for simultaneous measurement of gait cadence and BR. In this case, the filter in the first frequency window (0.1 Hz to 0.6 Hz) results in the BR, whereas the one between 0.8 Hz to 3.5 Hz yields in the gait cadence. The reference

of the gait cadence is simply the counting of the user’s steps during the test, which was performed within one minute with one subject. Figure 6-30 shows the POF response in frequency domain after each filter, where the sensor was able to track both BR and gait cadence.

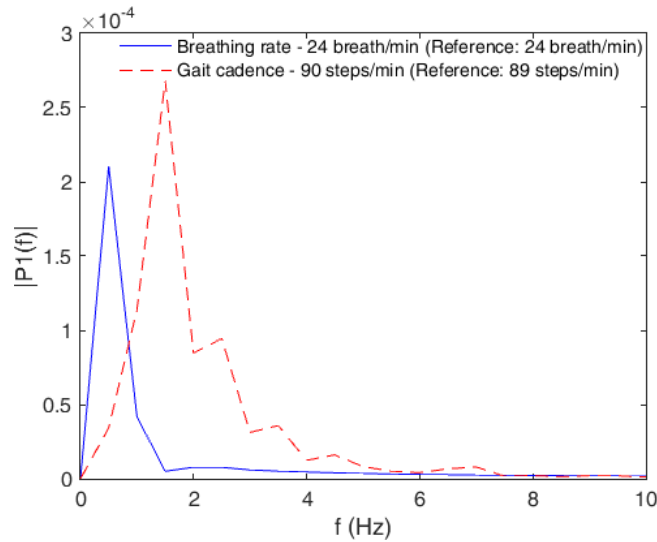


Figure 6-30 POF-based smart textile response for BR and gait cadence.

### 6.3.4.4. POF sensors Implementation in the Smart Walker

After the positive feedback from both oximetry and smart textile sensors, they are applied in the SW with the configuration presented in Figure 6-25. Figure 6-31 shows the block diagram of the sensors implementation in the SW, which is based on the premise that the person needs the SW for locomotion. Thus, if the SW is not active, i.e., is not moving, the person is not walking. Then, the POF-based smart textile makes the acquisition of the HR and BR as presented in Figure 6-30 and the oximetry sensor is not in use. If the SW is active, which can be easily detected by the motor encoders or force sensors (see Figure 6-25), both smart textile and oximetry sensors are being used. In this case, the analysis of the oximetry sensor in the time domain gives the SpO<sub>2</sub>, whereas the HR is obtained in the frequency domain. Since the person is walking, the smart textile acquires both BR and gait cadence, where the latter can be applied in the SW control for human-robot interaction [32].

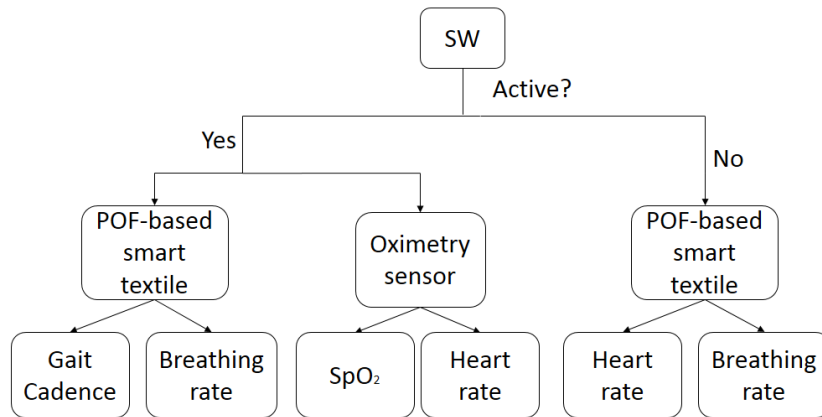


Figure 6-31 Block diagram of the POF sensors implementation in the smart walker.

For the implementation tests, three subjects were asked to walk with the SW in a straight line of about 10 m and the test is repeated five times for each subject. The physiological conditions of the users are compared with the reference PPG sensor, whereas the gait cadence is compared with the SW’s sensors. Although the LRF is responsible for the legs detection and the gait cadence, this sensor presents some limitations in the legs detection related to the user clothing and illumination of the environment. For these reasons, we do not rely only on the LRF to obtain the gait cadence for the comparison with our sensor. Thus, the gait cadence is also obtained by the SW linear velocity estimated from IMUs and encoders and is compared with the one estimated by the proposed POF sensor.

The SpO<sub>2</sub> measurement for each test with the three volunteers is presented in Figure 6-32(a), where it can be seen a slight reduction of the SpO<sub>2</sub> for subjects 1 and 2, which can be related to the users' activity during the use of the SW. Nevertheless, the maximum reduction is lower than 1% and the SpO<sub>2</sub> values are relatively far from the 90% limitation that is related to hypoxemia. Regarding the BR and HR, similar analysis is made in which the results for each subject at each test are presented in Figure 6-32(b) and (c), respectively. In addition, the gait cadences of each user at the five tests are presented in Figure 6-32(d), where the results show the feasibility of the proposed system to estimate all the proposed parameters: SpO<sub>2</sub>, HR and gait cadence.

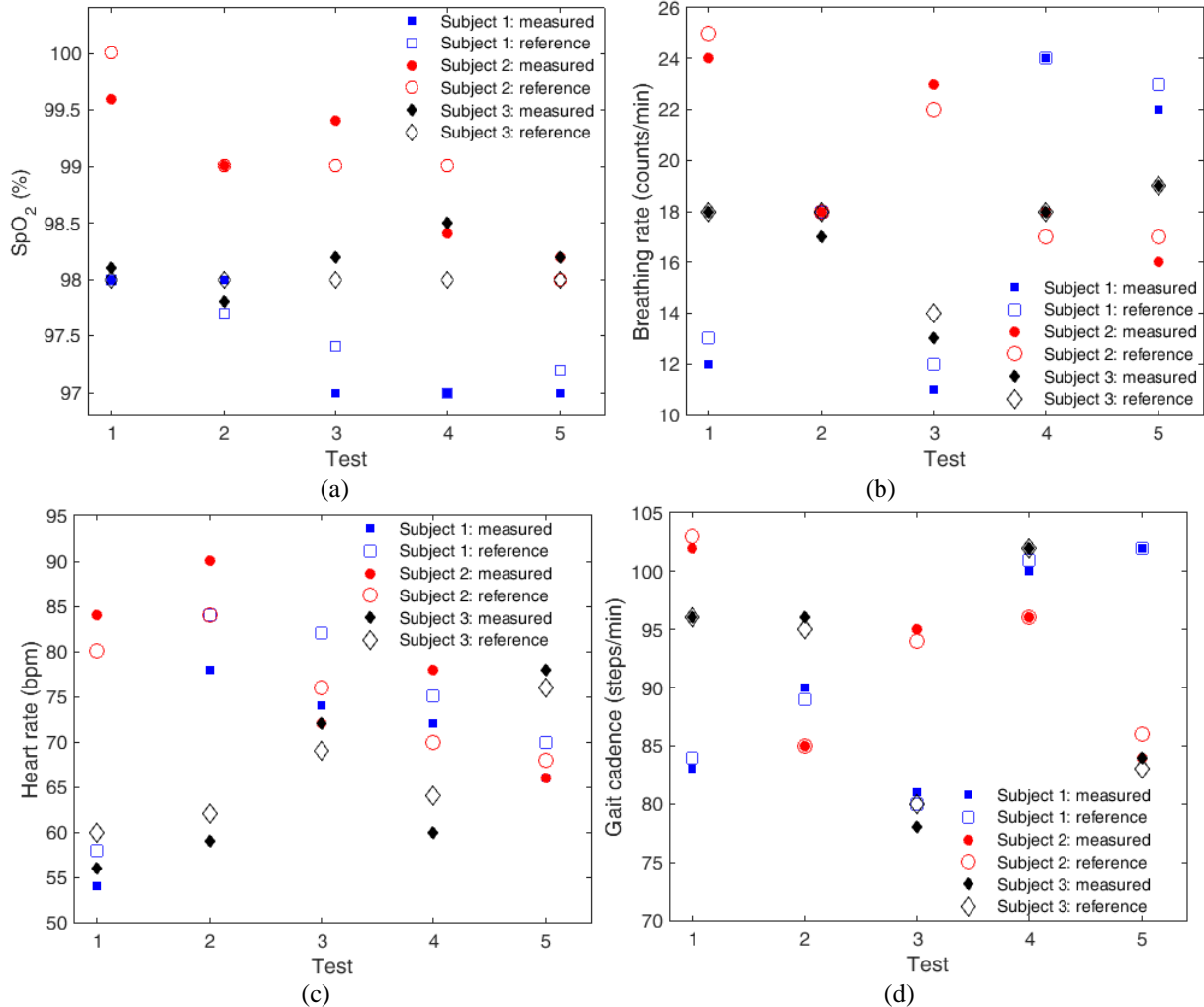


Figure 6-32 (a) SpO<sub>2</sub> measurements in the SW implementation. (b) BR measurement. (c) HR measurement. (d) Gait cadence estimation.

### 6.3.5. 3D-printed POF Insole: Application of Multiplexing Techniques in Low-cost Intensity Variation-based Sensors

This section presents the development of an instrumented insole with intensity variation-based POF sensors. The proposed insole comprises of a single POF with 15 pressure sensors, which cover all pressure points of the foot sole defined in [37], where the response of each sensor is individually obtained using a multiplexing technique for quasi-distributed sensing arrays in intensity variation-based sensors proposed in Section 4.4. Comparing with other optical fiber distributed and quasi-distributed sensors, many distributed sensor technologies may lack on spatial resolution for this particular application. In addition, quasi-distributed technologies based on FBG arrays depend on the type of fiber employed. Even though it is possible to inscribe a 15-FBG array, the fiber brittle nature and material properties lead to a sensor with smaller dynamic range and sensitivity not to mention the complexity of the sensor fabrication due to fiber breakages [50]. These issues can be surpassed by inscribing the array in POFs, however, to date, there is no report of an FBG array with more than 7 sensors [69]. Thus, this is the instrumented insole with the highest number of sensors using optical fiber sensing technology with additional advantage of employing a technique that results in a system with

much lower cost and higher portability. The proposed insole was characterized in static, dynamic and gait conditions, where the results were compared with a commercial force platform.

### 6.3.5.1. Methods

The insole structure was 3D-printed using the Sethi3D S3 (Sethi, Brazil) with two different materials: TPU for the insole base and PLA for the top of the insole, which encapsulates the fiber and sensors. The layer height and material infill density were set to 0.2 mm and 80%, respectively. Regarding the optical part, the commercially available PMMA POF (HFBR-EUS100Z, Broadcom Limited) was used. This fiber has a PMMA core with 980  $\mu\text{m}$  diameter, a cladding of fluorinated polymer with 10  $\mu\text{m}$  thickness. In addition, there is also an overcladding made of polyethylene for mechanical protection of the POF. The light sources used were LEDs (ASMT-BR20-AS000 Broadcom Limited) with a central wavelength of 628 nm and 650 mcd luminous intensity, whereas the employed photodetectors were photodiodes IF-D91 (Industrial Fiber Optics, USA). The signal acquisition and the LED control are performed by the microcontroller FRDM-KL25Z board (Freescale, Austin, TX, USA) and transmitted using the Bluetooth module HC-05 (Logoele Electronics Technology, China). Moreover, all the data were analyzed and processed in MATLAB tool.

As a vital part of the work, all 20 participants of the sensor validation tests are healthy adults with ages between 18 to 36 years without history of gait related pathologies. In addition, the shoe sizes of all participants were between Euro 39 (US 7 for male and 8.5 for female) and Euro 44 (US 10.5 for male and 12 for female), which are within the spatial resolution of the sensors. Participant with higher or lower foot sizes needed to be excluded from the study, since their feet will not cope with the spatial resolution of all sensors. Thus, 10 male and 10 female participants were chosen with the body masses ranging from 46 kg to 97 kg.

The static tests were performed with 4 subjects standing still on the instrumented insole for about 100 seconds and the data of each sensor is recorded. For the validation tests, the force platform (EMG system, Brazil) was employed for the comparison with the proposed insole, where five subjects were asked to perform displacements on their center of pressure (CoP) for about 10 seconds, the test was repeated 3 times. Finally, on the dynamic gait tests, each of the 20 subjects walked in a room for 15 m (in a straight line).

### 6.3.5.2. Instrumented Insole Development

The proposed insole was designed according to general guidelines in instrumented insole for dynamic measurements of plantar pressure. These guidelines include wireless connection, low power consumption, portability, low cost and with sensors distributed along the whole foot pressure points [13]. In order to comply with those design requirements, the sensor comprises of a commercial PMMA POF with 15 lateral sections similar to the ones described in Appendix B, when the pressure is applied on each lateral section, there is an optical power variation, which is acquired by two photodetectors, one at each end of the fiber. In addition, LEDs are positioned on each lateral section. In this way, there is a side coupling of the light at each section of the fiber. Thus, two photodetectors are employed with one serving as a reference to the other, resulting in a self-referencing system to mitigate errors due to the light source power deviations, which is a common issue in intensity variation-based sensors [66]. The position of each sensor was determined by the 15 foot anatomical areas that supports the weight and are responsible for the body balance as presented in [37]. These positions are shown in Figure 6-33, where the foot is divided into hindfoot (sensors 1 to 3), midfoot (sensors 4 and 5), forefoot (sensors 6 to 10) and phalanges (sensors 11 to 15) [205].

The sensing region of the sensors is limited by the fiber diameter, which is 1 mm in this case. Moreover, by having 15 sensors, one at each anatomical area of the foot, the proposed insole complies with the requirement of sensor positioning. After performing the lateral sections, the POF is positioned on a 3D-printed insole made of TPU, which is a flexible material suitable for insole production as shown in Figure 6-34. Thereafter, thermoplastic resin is applied on the POF in the regions close to the lateral section. Thus, the sensor is fixed in two positions (before and after the lateral section) in order to keep the fiber deformation restricted to the sensing region, which inhibits the crosstalk between sensors. This is especially important in the forefoot and phalange regions, where the sensors are close to each other. Then, a 3D-printed structure with 0.1 mm thickness made of PLA is positioned on the top of the TPU structure (as shown in Figure 6-34) and is glued on the TPU structure with a thermoplastic resin. In this structure, there are the housing structures of the LEDs, which are aligned with each lateral section, as also depicted in Figure 6-34. Furthermore, the housing of each LED also has region which is placed in contact to the fiber in a manner that when a pressure is applied to this region, there is a bending of the fiber and an increase of the stress on such region, which also results in power variation. Thus, there are three different attenuation mechanisms on each of the 15 sensors: the macrobending

principle when the pressure is applied, the stress-optic effect due to the stress applied on the fiber that leads to a refractive index variation [162] and the light coupling between the LED and the POF's lateral sections.

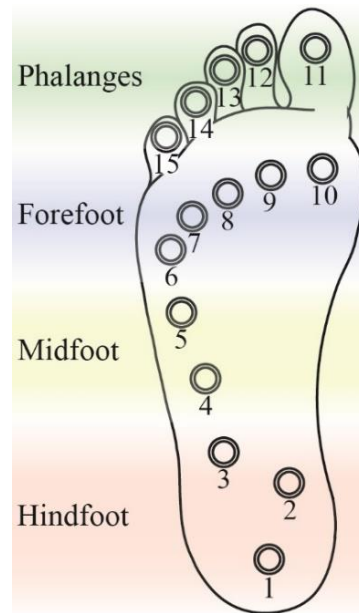


Figure 6-33 Foot anatomical areas and regions of the sensors positioning, where each circle represents the sensor positioning.

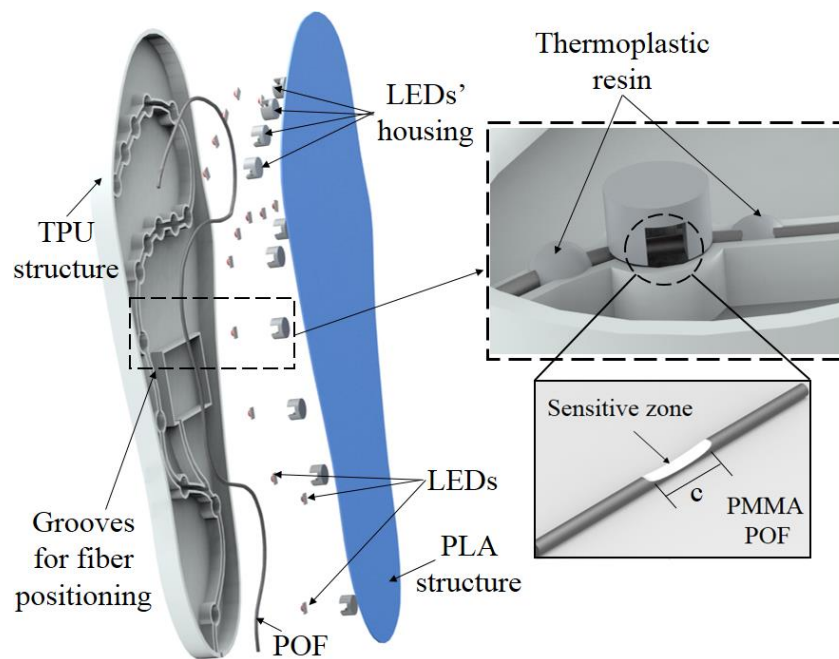


Figure 6-34 Insole components, assembly and POF sensitive zone, where the 'c' is the sensitive zone length.

After the assembly, the 3D-printed, multiplexed POF insole has a total weight of about 150 g, which does not influence the gait natural pattern, since, according to Bamberg et al. [206], an instrumented insole must weigh less than 300 g to not significantly affect the gait pattern. As shown in Figure 6-34, the sensor system comprises of 15 LEDs coupled to 15 lateral sections on the fiber with controlled length and depth creating 15 sensitive zones in which the fiber has higher sensitivity to the applied pressure. The proposed multiplexing technique comprises of the sequential activation of each LED with a predefined frequency and activation sequence. Thus, only one LED is activated at a time, where a microcontroller controls the activation frequency and sequence. The acquisition sequence is from LED 1 to 15 with an activation frequency of 30 Hz, i.e. each LED is activated 30 times per second, due to limitations on the LEDs intensity and operation frequency. In addition, the microcontroller is also responsible for acquiring the optical power measured by each photodetector when each LED is active, which results in two matrices, one for the photodetector 1 and the other for photodetector 2 (P1 and P2 in Figure 6-35(a)), respectively. In this case, each matrix has 15 columns, where each column represents the acquired power one of the predefined LEDs is active, which are represented

by the terms RLED1-15 in Figure 6-35(a). The acquired signals are transmitted to the local processing unit via Bluetooth also using the microcontroller, which also has the possibility of performing all the signal processing. Thus, the proposed insole also complies with the design requirement of wireless connection, where the results can be visualized with a computer or even a smartphone device, as summarized in Figure 6-35(a). In addition, a picture of the device positioned on a subject is shown in Figure 6-35(b).

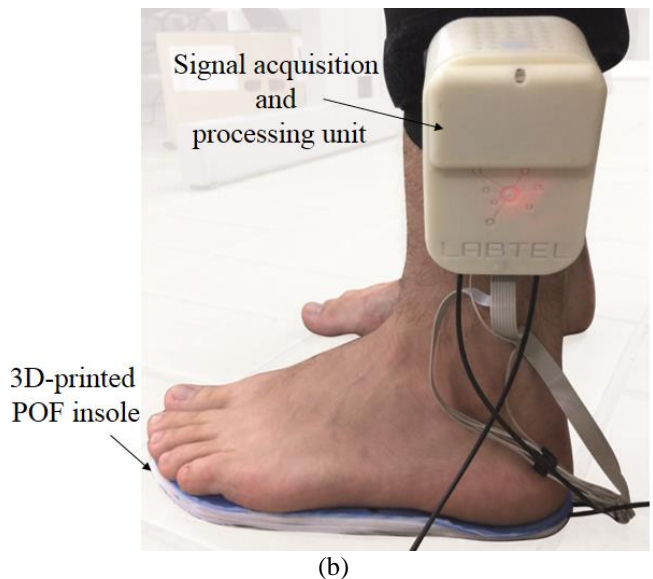
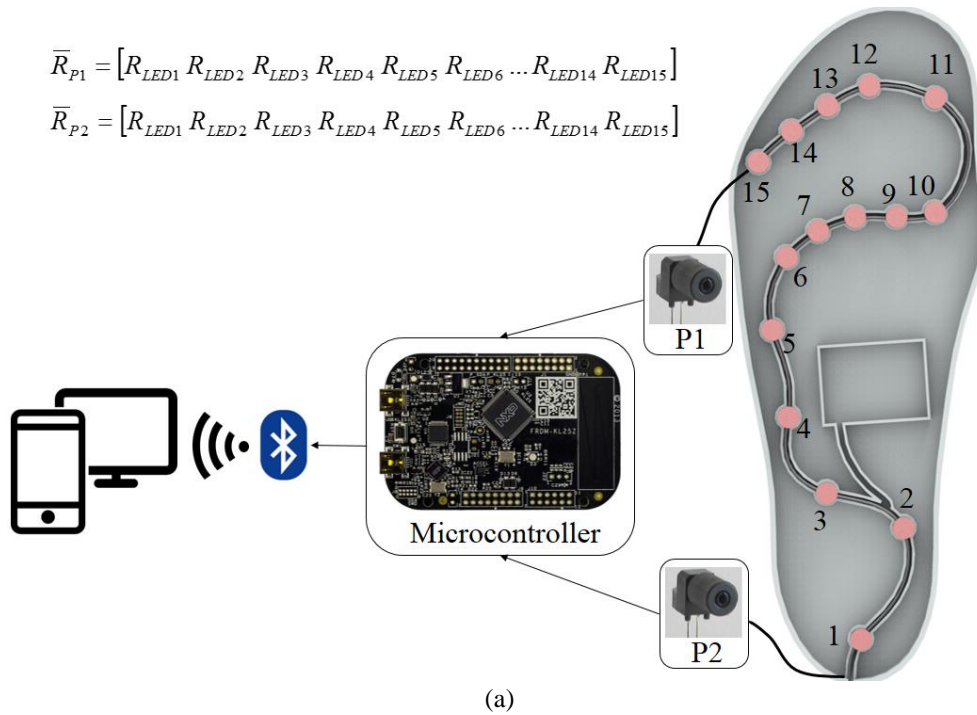


Figure 6-35 (a) Schematic illustration of the insole connection, data acquisition and LEDs numbering. (b) Photograph of the device positioned on a subject.

The matrices  $R_{P1}$  and  $R_{P2}$  shown in Figure 6-35(a) represent the responses acquired by the photodetectors P1 and P2 (see Figure 6-35(a)), where the matrices have the responses when each LED is activated. The signals acquired by each photodetector can have high attenuation depending on the sensor position, e.g, P1 detects a weak signal for the response of sensor 1 (when LED 1 is active) due to the higher distance between P1 and sensor 1, especially when considering the other 14 sensors in which there is optical power attenuation. For this reason, the responses of sensors 1 to 7 are acquired by P2, whereas the responses of sensors 8 to 15 are acquired by P1. In addition, the first step of the proposed multiplexing technique is the characterization of each sensor without the influence of the others, i.e., when pressure (or force) is applied to only one sensor. Then, the response of each sensor can be obtained by Eq. 6.10, where the influence of the other sensors is subtracted. Therefore, by performing both steps (individual characterization of the sensors and subtracting the differences

between them), it was possible to obtain a sensor system with low cross-sensitivity between the parameters and with low relative errors. Furthermore, the proposed technique can also compensate effects of light source power deviations and environmental effects, considering that, when a person is using the insole, the whole fiber will be subjected to temperature and humidity variations, which will be subtracted using Eq. 6.10.

$$R_i = \frac{R_{LEDi} - R_{LEDi-1}}{s_i}, \quad (6.10)$$

where  $R_i$  is the sensor estimated pressure (or force),  $R_{LEDi}$  is the response acquired when  $LED_i$  is active and  $s_i$  is the sensitivity of sensor  $i$  obtained in the sensor characterization step.

Regarding the power consumption, the proposed instrumented insole consumes about 70 mA when all the components are active with the signals transmitted via Bluetooth. Thus, the system can be powered with a 9 V alkaline battery with about 565 mAh, resulting in an autonomy higher than 8 hours. It is worth to mention that more efficient batteries can also be employed on the system, which increases system's autonomy. Nevertheless, such low power consumption is also in accordance with the aforementioned design requirements. In addition, considering the commercially available components used and the low-cost techniques employed both on the sensor interrogation and on the insole manufacture using 3D printers, the proposed instrumented insole can be regarded as a low cost solution, where the cost is also comparable (and lower in some cases) with commercially available insoles based on electronic sensors.

### 6.3.5.3. Results

#### 6.3.5.3.1. Insole Characterization

The pressure sensors in the insole were characterized by the application of a constant pressure on each sensing region. The pressure was applied by means of positioning a calibrated weight over a known area (the contact area for the calibrated weights is equal to the total area of each sensor), where the pressure is obtained through the well-known relation between force and area. The pressures were applied on each sensor at a time in order to characterize the sensitivity of each sensor with reduced influence of the others. The measurements were repeated for each sensor and Figure 6-36(a) shows the linear regressions of sensors 1 to 8 as a function of the applied pressure, whereas Figure 6-36(b) shows the linear regressions for sensors 9 to 15. Furthermore, the response with applied force is also shown, since some analysis are made with respect to the GRF. Figure 6-36(c) depicts the response of sensors 11, 12, 13, 14 and 15 when sequential loadings (F1 and F2, 40 N and 80 N, respectively) are applied on the sensor 13. This case was presented, since it is the worst case concerning the crosstalk and cross sensitivity between sensors due to the proximity between those sensors (see Figure 6-35(a)) and due to the LED activation. As mentioned above, the activation begins on LED 1 and finishes on LED 15, i.e. begins on sensor 1 and finishes on sensor 15. The differences on the sensors' sensitivities depicted in Figure 6-36(a) and (b) are due to the sensor positioning on the insole and are also related to differences on the depth and length of the sensitive zone, which has direct influence on the sensor sensitivity [45]. Differences on the sensor positioning lead to variation on the distance between the sensitive zone and the thermoplastic resins applied to position each sensor as shown in Figure 6-34. Thus, the curvature radius of each sensor has differences when compared to the other ones due to the different positions of each sensor, e.g. sensor 8 is close to sensor 9 and 7, which leads to a lower curvature radius when compared with a sensor distant to the other ones, such as sensor 2. It is also worth to mention that all sensors showed a linear response, where the  $R^2$  between the sensor responses and the linear regression is higher than 0.99 in all cases, which is regarded as high correlation. In addition, the sensor responses depicted in Figure 6-36(c) show a significant difference between the response of sensor 13 (where the pressure was applied) and the responses of the other sensors. Considering the sensitivity of the other sensors (sensors 11, 12, 14 and 15), which are higher than the one of sensor 13, one can assume that the crosstalk between sensors is negligible, especially when Eq. 6.10 is applied.

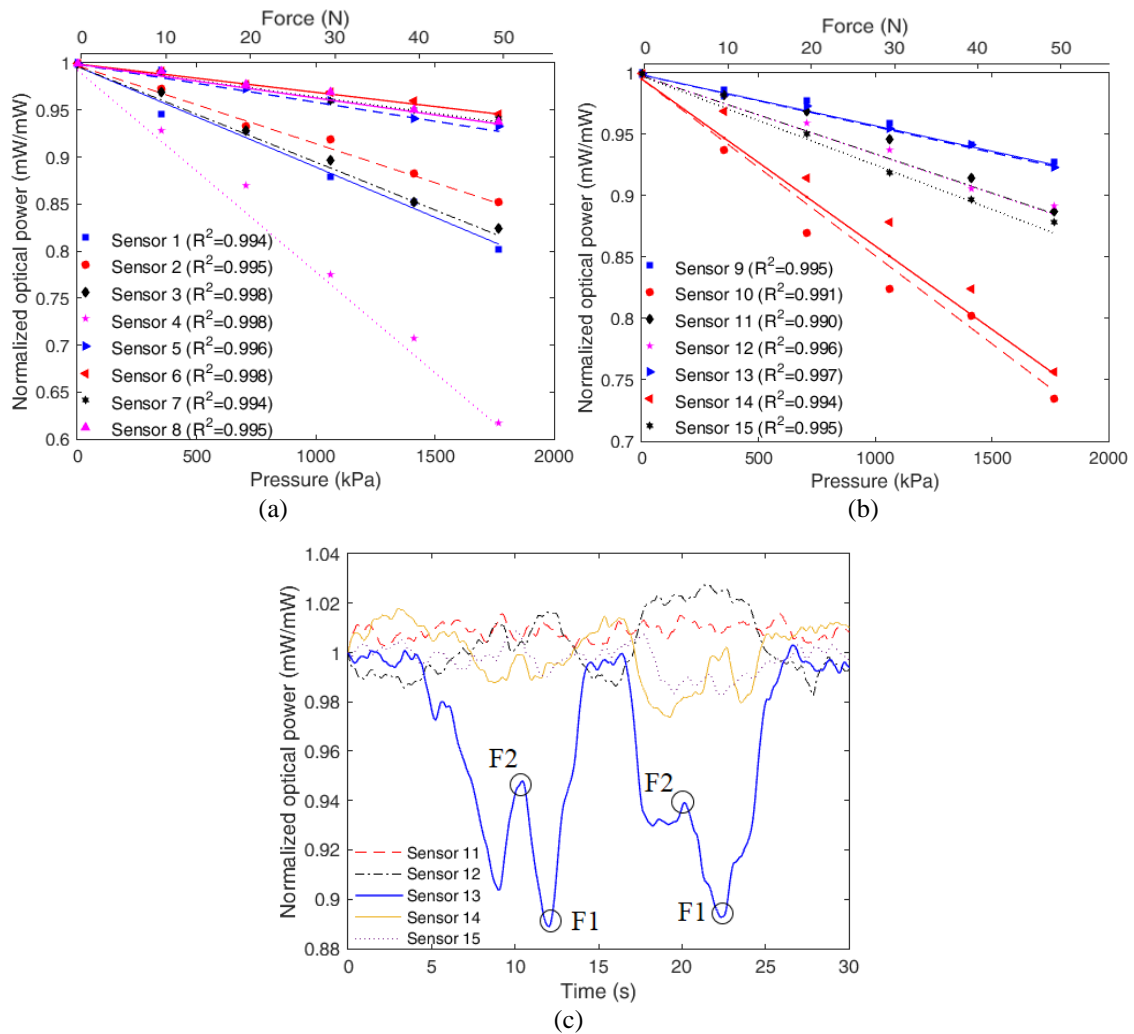


Figure 6-36 (a) Linear regression of sensors 1 to 8 as a function of the applied pressure and force. (b) Linear regression of sensors 9 to 15 with respect to the applied pressure and force. (c) Response as a function of time of sensors 11 to 15 when a loading is applied to sensor 13. F1 and F2 are the applied forces of 40 N and 80 N, respectively.

### 6.3.5.3.2. Insole Validation and Applications

In order to assess the functionalities and performance of the proposed 3D-printed POF insole, three different sets of tests were made. In the first test, four subjects were asked to stand still on the instrumented insole for about 2 minutes. In this way, it is possible to obtain a pressure map of each participant. In addition, it is expected that it is also possible to estimate the weight of each person by the sum of all the pressure points, since the sensing area is known. The weight and height of each participant is shown in Table 6-3 in which the weight estimated by the instrumented insole is also shown. The sensors responses for subject 1 as well as the pressure map obtained on the sensor response for this participant are presented in Figure 6-37.

The pressure maps obtained for the subjects are similar to the ones obtained in reference works on the literature and, thus, similar to the one expected for subjects with foot without abnormalities [155]. In addition, the instrumented insole was capable of measuring the weight of each participant by means of summing the response of all 15 sensors. The errors shown in Table 6-3 have a direct correlation with the height of each subject. Assuming a proportionality between the height and foot size, the results indicate that the error is related to different sizes of the foot of each participant, which can induce errors on the weight estimation. Nevertheless, a RMSE between the participants' weight and the ones estimated by the insole is about 1.9 kg, which represents a relative error of only 2.7%, considering the mean weight of the participants. Furthermore, it shows the ability of the sensor of measuring the plantar pressure on a high range of weights, which in this case were from close to 50 kg to almost 100 kg.

Table 6-3 Body mass estimated by the instrumented insole for each subject.

Subject	Height	Body mass	Estimated body mass	Error
1	183 cm	97.0 kg	96.6 kg	0.4 kg
2	163 cm	53.0 kg	55.7 kg	2.7 kg
3	170 cm	65.0 kg	66.9 kg	1.9 kg
4	168 cm	62.0 kg	59.9 kg	2.1 kg

After the positive feedback from the first set of tests, the proposed 3D-printed insole was validated in a commercial force platform, which can measure the GRF and the two-dimensional CoP displacements. In this case, the insole was positioned on the top of the force platform and five subjects were asked to position their foot on the insole, each test takes about 6 seconds and was repeated 3 times. Then, the subjects were asked to perform on the sagittal and frontal planes as depicted in the arrows of Figure 6-38(a). The comparison between the force platform and instrumented insole on the measurement of the GRF and variations of the CoP on the x and y directions are shown in Figure 6-38(b) for subject 3 on test 2. In addition, the  $R^2$  between the force platform and instrumented insole was compared for all three parameters (GRF, CoP displacements in x and y directions) for all the participants as also shown in Figure 6-38(a).

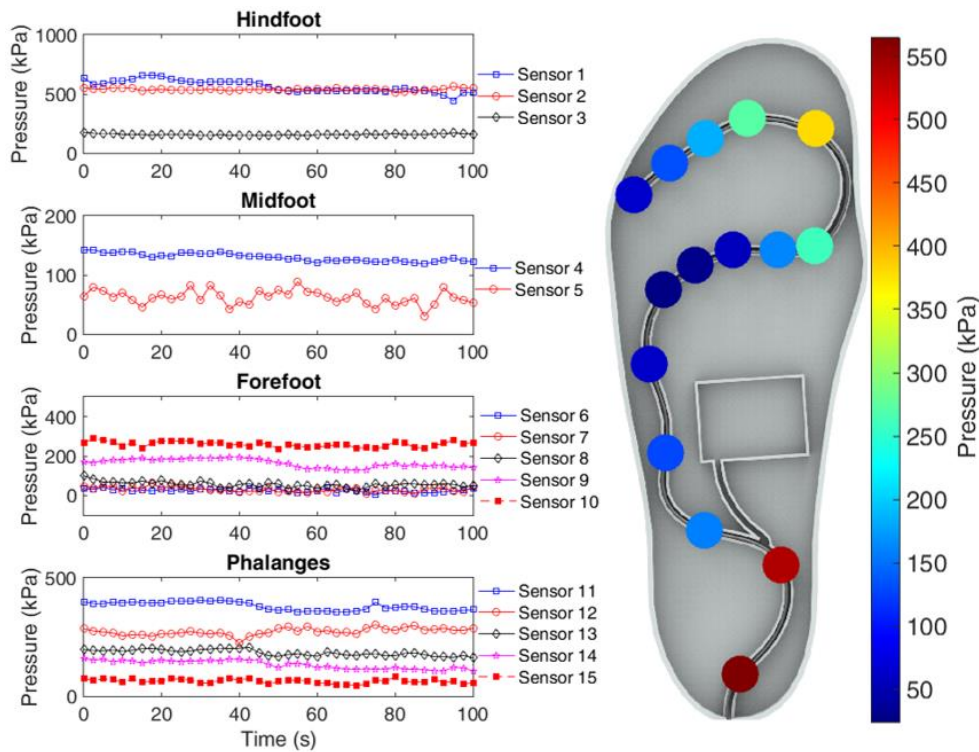
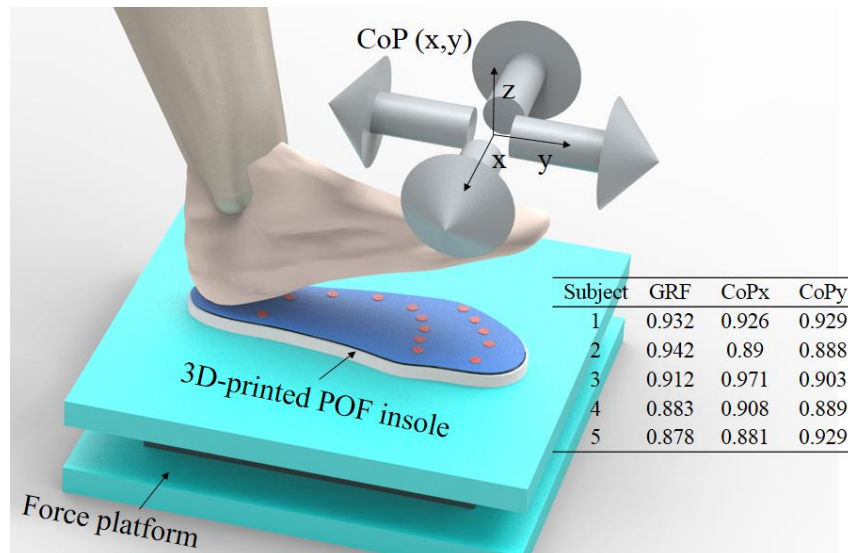
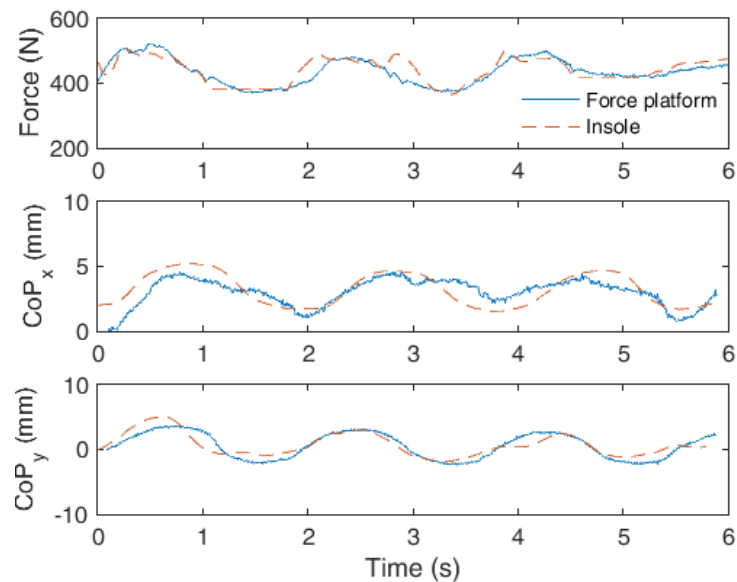


Figure 6-37 Plantar pressure at each part of the foot and pressure map of subject 1.

The correlation coefficients presented in Figure 6-38(a) for all 5 subjects show a high correlation between the force platform and instrumented insole responses, since the lowest one found is for the GRF estimation in subject 5 ( $R^2=0.878$ ). The reason for this higher error is related to errors in the force estimation, which can be due to sensor nonlinearities or differences on the foot of this specific subject that have led to variations in the sensors' responses. Nevertheless, the correlation coefficient is higher than 0.85, which can be considered a high correlation. As the mean weight of the participants is  $67.2 \pm 16.7$ , the responses of participant 3 are shown in Figure 6-38(b), as this participant is the one with weight closer to the mean considering all five subjects. The responses of GRF and CoP for subject 3 shows good agreement between the proposed 3D printed insole and the commercial force platform. It is worth to mention that the CoP measurements were normalized, since the CoP center for the platform (CoP(0,0)) is in the center of the platform, which can have differences with the CoP of the insole if the CoP center of the insole is not precisely positioned on the center of the platform. Thus, in order to reduce this influence on the comparison, both estimated CoPs (from the platform and insole) were normalized.



(a)



(b)

Figure 6-38 (a) Insole positioning on the force platform, direction of the movements and R2 obtained for each subject on the estimation of GRF, CoPx and CoPy. (b) Comparison between the responses of force platform and instrumented insole for test 2 of subject 3.

After the insole characterization and the comparison with a commercial force platform, the last set of tests is the evaluation of the proposed 3D-printed POF insole on gait analysis. In this analysis, 20 participants (10 males and 10 females) were asked to walk in a straight line for about 15 m and the plantar pressure as well as the GRF were monitored using the insole. In order to show the capability of the insole of measuring GRF and plantar pressure for different subjects, the results obtained with the subject with the lowest body mass (46 kg) is shown in Figure 6-39(a). The GRF obtained from the sum of the force response of all 15 sensors is depicted in the blue curve (on the left of Figure 6-39(a)), where the solid line is the mean GRF from all cycles and the shaded curve is the standard deviation between cycles. The GRF results are normalized with respect to the stance phase and show the possibility of identifying gait events on the stance phase. Among many subdivisions reported for the gait cycle, we used the five phases subdivision depicted in Taborri et al. [16], where the stance phase is subdivided into heel strike (HS) when the heel makes contact with the ground (right after the initial contact), flat foot (FF) when the foot is parallel to the ground. Furthermore, there is also the heel off (HO) phase and toe off (TO), where the former is when the heel loses contact with the ground and the latter is in the vicinity of the swing phase when the toe is not in contact with the ground. In this analysis, we also considered a maximum weight acceptance (MA) phase when there is a local peak of the GRF, which resulted in the well-defined M-shape of the GRF during the gait [155]. The plantar pressure distribution on each gait phase is also

shown, where the presented values are the mean of the pressure response of each cycle. Similarly, Figure 6-39(b) shows the response of all 20 subjects. In order to present a better comparison between the participants, the response is not only normalized with respect to the stance phase percentage, but also with respect to the weight of each participant.

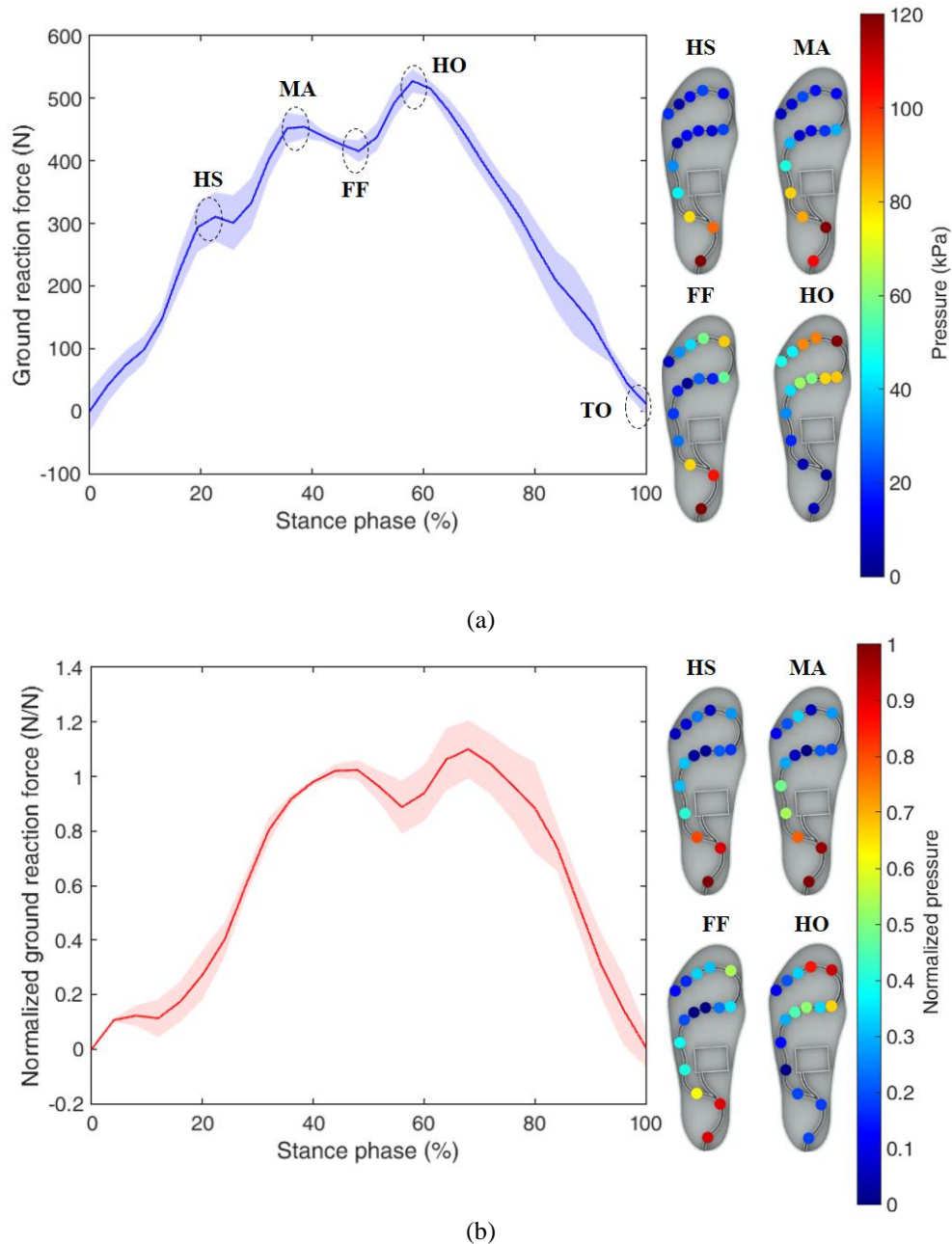


Figure 6-39 (a) GRF and plantar pressure for female subject with 46 kg body mass. Solid line represents the mean GRF and shaded curve represents the standard deviation of 5 cycles. (b) Normalized GRF and plantar pressure measurements for all 20 participants. Solid line represents the mean GRF and shaded curve represents the standard deviation.

The GRF results depicted in Figure 6-39(a) shows a low variation of the GRF, which is within the variation of this parameter in tests with a single subject. The highest variation occurs on the HS region, where there is the impact of the heel on the ground, which can present high variation during the normal gait. In addition, these differences between cycles can also be related to the gait speed, since it also influences the GRF response [207]. As expected, the normalized responses considering all 20 subjects present a higher standard deviation. However, this deviation is similar to the ones previously reported in the literature with similar number of participant [208]. Thus, it is possible to assume that these deviations are due to the gait inherent variability between different participants, instead of a repeatability issue of the instrumented insole. It is interesting to note that a higher variability occurs in the HS region as also obtained in Figure 6-39(a), which can confirm the variability of the gait cycle in this region. In addition, the region with highest variation in Figure 6-39(b) is

HO region, which is also related to the gait velocity variation of each participant. Furthermore, the plantar pressure distribution at each gait phase is in accordance with the well-known plantar pressure distribution reported in the literature with gold standard measuring devices [155]. This feature, in conjunction with the validation on force platform and the instrumented insole ability of estimating the weight of each participant, indicate the reliability of the proposed 3D-printed POF insole for measuring plantar pressure in different scenarios (static and dynamic tests).

#### 6.3.5.4. Discussion

The development of an instrumented insole based on low-cost POF intensity variation-based sensors with the recently reported multiplexing technique for intensity variation sensors (see Section 4.4) is depicted, where the sensors are based on a lateral section on the fiber with increased sensitivity with respect to pressure and force variations. In this way, it was possible the multiplexing of 15 sensors in the same fiber using only two photodetectors for the signal acquisition resulting system with multiplexing capabilities close to the ones of FBGs, but with a cost some orders of magnitude lower when considering the necessity of high cost interrogation equipment and specialized lasers for FBG sensors fabrication and interrogation. In addition, the insole was fabricated with TPU and PLA flexible materials using a 3D printer, which lead to important advantages regarding the ease of fabrication, possibility of customization and relative low cost of 3D printed structures [209]. Thus, the employed methodology enables not only the large-scale fabrication of the proposed insole, but also the customization of the device for each individual, where the number and positioning of the sensors can be optimized for each user considering the foot size and anatomy. These advantages are well aligned with the state-of-the-art requirements for the development of assistive devices in which the device is optimized for each user, the so-called human-in-the-loop design [31].

The characterization performed on each of the 15 sensors in the insole as a function of the applied force and pressure shows the sensitivity differences due to the sensors positioning on the insole, which results in different curvature radii for the sensors. Nevertheless, the normalized responses of all sensors show the linearity of the sensing regions in which a correlation coefficient higher than 0.99 was obtained in all cases. In addition, the capability of isolating the force/pressure response of each sensor was demonstrated, where there is a much higher variation on the sensor in which the loading is applied even when compared with its closest neighbors. Even though a variation can be detected in the closest sensors, such variation is lower than 2% in the worst case analyzed (shown in Figure 6-36(c)). Considering the sensors sensitivities, such variation limits the sensor resolution to about 5 N in the worst case. For this reason, this sensor can, in principle, detect the GRF and plantar pressure variations in users with lower body mass than the ones tested. Hence, with some modifications on the sensors positioning (related to the foot anatomy of the users), it is possible to employ the proposed insole in the assessment of the gait parameters of children, which is a topic for further investigations.

The proposed 3D-printed instrumented insole performance was evaluated in three different scenarios: (i) static tests with the user standing on the insole, (ii) body CoP displacements with the comparison with a commercial force platform and (iii) dynamic tests for the gait assessment. The static tests show the ability of the proposed insole of measuring the body mass of each user, where the highest error obtained was 3.4% for subject 4, whereas, in the best case, the error was lower than 1%. These results show not only the capability of the instrumented insole of estimating the body mass, but also leads to an important discussion about the number of sensors needed in an instrumented insole. Some works report dozens of pressure sensors, which bring important issues on the characterization of each sensor [13]. Thus, the reported ability of the proposed instrumented insole of estimating the body mass by the sum of the force responses between 15 sensors indicates that if the sensors are correctly positioned on the 15 anatomical areas of the foot [37], only 15 sensors are needed for a reliable estimation of the plantar pressure distribution and GRF. However, an important caveat should be noted, all the subjects considered in the study have normal foot and the 15 anatomical areas defined in [37] also considers a normal foot. Therefore, in the case of studies with subjects that have foot abnormalities (such as flat foot) different sensor positioning should be considered in order to obtain reliable measurements of plantar pressure and GRF, which can be easily accomplished with the methodology proposed in this study, where the insole design and sensor positioning can be optimized for each user or application.

In addition, the comparison between the instrumented insole with the force platform shows a high correlation ( $R^2$  up to 0.97) between both devices on the GRF estimation and CoP variations on x and y directions. Since force platforms can be regarded as the gold standard for GRF and CoP monitoring [210], this high correlation between the proposed insole and the force platform indicates the reliability of the proposed device on the measuring of both parameters with the additional advantages of higher portability and lower cost

than force platforms. Furthermore, it is noteworthy that the proposed insole with the wireless connection used can be an important asset on remote health monitoring applications [4]. The GRF and plantar pressure distribution of each person can be monitored when the users are at home, performing their daily activities and the data can be sent to a clinician through a local gateway, where the data can also be processed offline and sent to a clinician through the cloud.

Then, the insole performance was also evaluated in dynamic tests with 20 subjects performing sequential gait cycles, where the mean and standard deviations are in good agreement with the ones obtained in tests using different instrumented insoles and also in force platforms [155]. In these cases, a well-defined M-shape for the GRF was obtained in which was possible to identify 5 different gait events on the stance phase. These identified events can aid on the control of gait assistance devices and can also aid on the detection of gait related pathologies. Similarly, the plantar pressure distribution at each gait event also follows the pattern widely reported in the literature for healthy individuals during the gait [155], which is another important evidence of the accuracy and reliability of the proposed 3D-printed instrumented insole. This insole can also overcome the issue of low dynamic range reported in commercially available and in some previously reported insoles [13], since it was possible to measure the plantar pressure and GRF of subjects from 46 kg to 97 kg of body mass, which indicates the possibility of using this device for clinical evaluations of subjects with a large span of body masses (more than 51 kg).

In summary, the high degree of customization allied with the verified reliability for both static and dynamic measurements enable a plethora of possibilities with the proposed 3D-printed POF insole. Aiming the aforementioned advantages, one can envisage many applications of the instrumented insole on clinical evaluations, remote health monitoring and even on the instrumentation of wearable devices for gait assistance, where its low cost can provide a widespread of this technology in many clinics and to the general population, which, according to World Health Organization [211], is a major drawback of many assistive technologies as the devices generally have high cost.

## **6.4.FBG-based Sensors Applications in Healthcare Devices**

### **6.4.1.FBG-embedded 3D-printed Support for Human-robot Interaction Forces in a Lower Limb Exoskeleton**

Considering (i) the necessity of novel sensing solutions for flexible structures, (ii) the advantages of 3D printing on the development of flexible structures and sensors' embedment and (iii) the advances in the inscription of long FBG arrays in CYTOP fibers, this section presents the development of flexible support for human-robot interaction force assessment using a FBGs array in CYTOP fibers. Two exoskeleton supports are 3D printed with materials that have different degrees of flexibility, namely ABS and TPU. The structure that is attached to the exoskeleton is made of ABS for higher resistance, whereas each FBG of the 2-FBGs array is embedded in structures made of TPU for higher flexibility. Then, each FBG is characterized with respect to temperature and force. Following the sensor validation, the FBG-embedded 3D printed flexible supports are applied on a lower limb exoskeleton for knee rehabilitation exercises. In this way, the contribution of this section is in the development and characterization of FBG-embedded flexible structures for the next generation of wearable robots for rehabilitation.

#### **6.4.1.1. 3D-printed, FBG-embedded Flexible Supports Design**

For the 3D printed, FBG-embedded flexible support design, the first step is the grating inscription using the methods presented in Section 5.2. The second step for the flexible support design is the fiber annealing in which the POF is positioned inside a climate chamber 1/400 ND (EthikTechnology, Brazil) at a temperature of 70°C for approximately 12 hours. Such heat treatment promotes the relaxation of the polymer molecular alignment, which leads to the reduction of internal stress created in the fiber manufacturing process [118]. Thus, it results in the reduction of the fiber Young's modulus, which leads to the increase of the sensor force sensitivity. In addition, the annealing in CYTOP fibers also results in the reduction of the sensor hysteresis as shown in Section 5.3.

The 3D-printed structures are fabricated using the 3D printer Sethi3D S3 (Sethi, Brazil), where the structures have a predefined infill density, which indicates the amount of employed material to fill the 3D-printed structure. For the ABS section of the support (see Figure 6-40), the infill density is 70% in order to increase the resistance of the structure, since it is attached to the exoskeleton. Two ABS structures are printed for each support, where the elastic bands for the attachment of the support on the user's leg are positioned. In

between the ABS structures, a flexible structure made of TPU is placed and the FBGs are embedded in each TPU structure. The proposed method for the exoskeleton support fabrication provides stability in the interface between the robotic device and the user. At the same time, the flexibility of the support provides a comfortable and compliant support for the user’s leg. Figure 6-40(a) shows the schematic representation and block diagram for the 3D-printed flexible support fabrication, where it is possible to customize the support dimensions for each user. In addition, Figure 6-40(b) shows the schematic representation of the assembled support.

The method shown in Figure 6-40 is used to fabricate each one of the two supports, the support is assembled with the aid of a thermoplastic resin. In order to evaluate the repeatability of this approach, the multiplexing capabilities of the FBGs and to provide higher stability for the user’s leg, an array with two FBGs (the distance between the two FBGs is 37 cm) is inscribed in CYTOP fiber. The FBGs spectra after the annealing are shown in Figure 6-41(a), where the spectrum was acquired using a Micron Optics sm125 FBG interrogator. However, this interrogator has low acquisition frequency (2 Hz), which is unsuitable for the proposed application. For this reason, for the tests with the proposed sensors, the spectrometer I-MON 512 (Ibsen Photonics, Denmark) was used. In this case, the peak detection is made through a Gaussian fit on the spectra and the peaks are identified after setting a threshold. In addition, it is also possible to change the integration time of the device, which can act as a low pass filter for the spectra, reducing the side lobes of the spectra that makes the single peak detection easier. Although there are few distortions on the spectrum when the transverse force is applied due to birefringence and polarization effects, the spectrum moves in unison as shown in Figure 6-41(a) for a transverse force of 40 N on FBG 1. Thus, applying the aforementioned methodology a single peak was detected for each FBG at about 1550 nm for FBG 1 and 1560 nm for FBG 2. The picture of the exoskeleton’s support (that will be positioned on the user’s shank region) following the FBGs array embedment is shown in Figure 6-41(b), where each FBG (FBG 1 and FBG 2) from the array is embedded in each shank support (shank support 1 and 2), respectively.

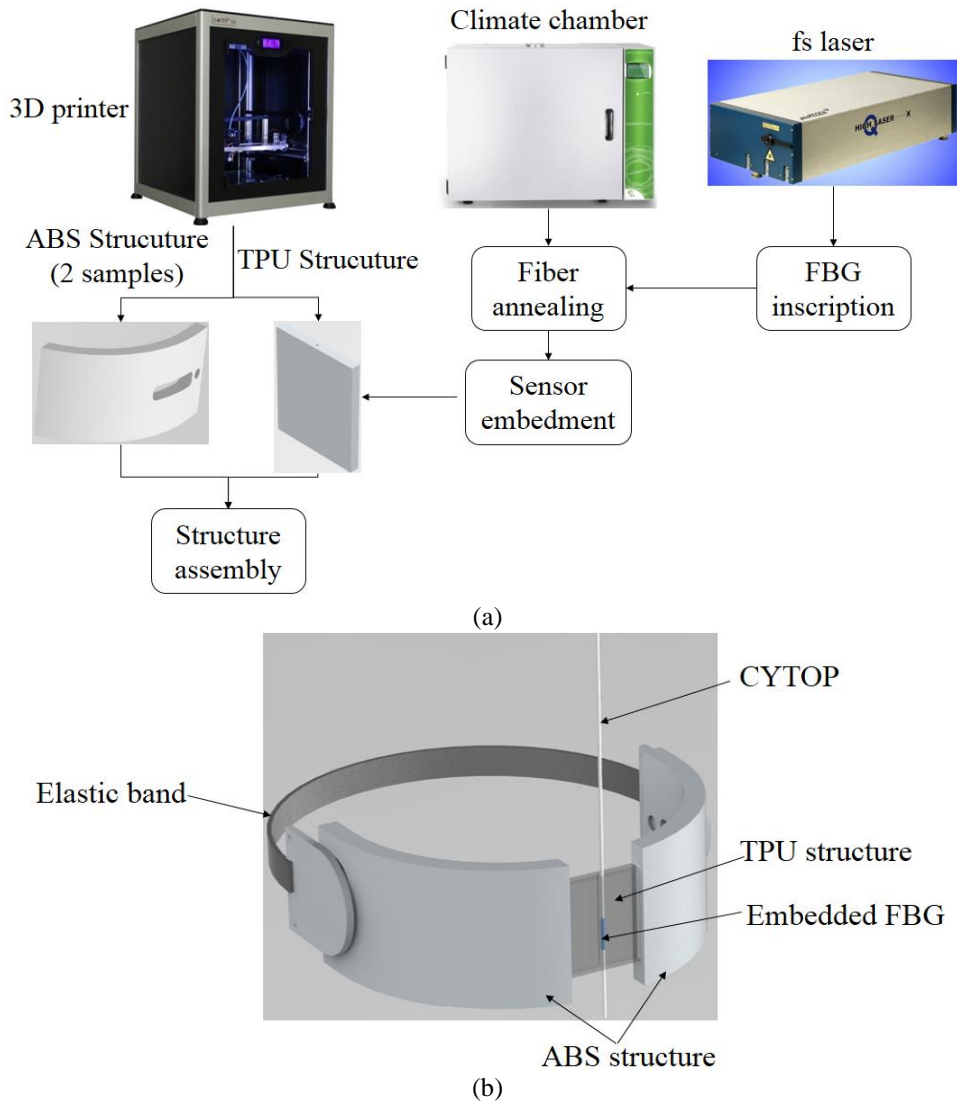


Figure 6-40 (a) Block diagram of the proposed method for 3D-printed, FBG-embedded flexible support fabrication. (b) Schematic representation of the assembled flexible support.

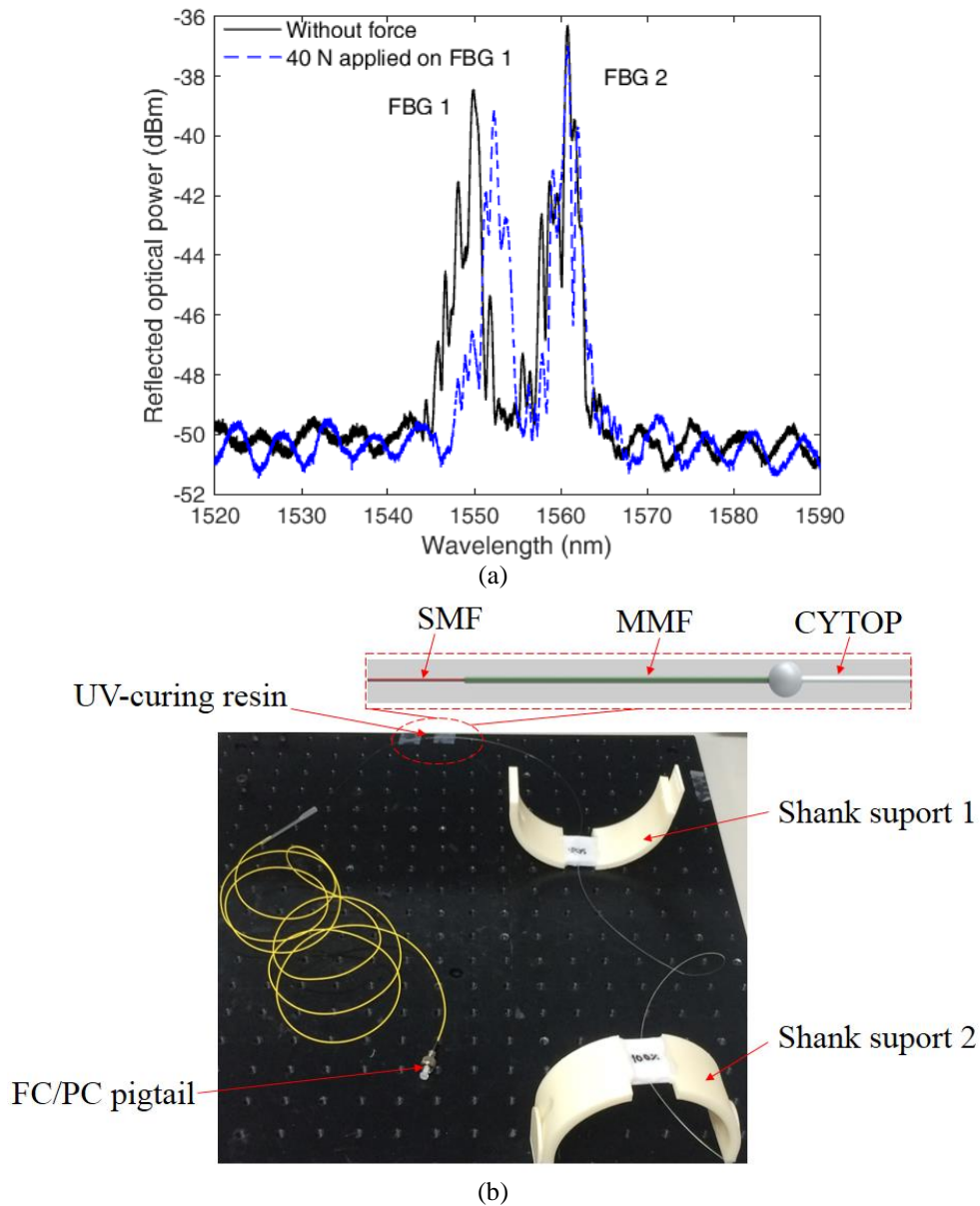


Figure 6-41 (a) Reflected spectrum of the FBG array without applied force and after a transverse force application 40 N. (b) Picture of the fabricated flexible shank supports with embedded FBGs (without the elastic bands). Figure inset shows the schematic representation of the fiber connectorization method (further discussed in Section 5.2).

### 6.4.1.2. Experimental Setup

For a FBG sensor the shift in the Bragg wavelength is correlated with the measured parameter. As well-known, FBGs are inherently sensitive to temperature and strain variations. However, other physical parameters that influence the strain or temperature variations in the fiber also result in the wavelength shift. One of these parameters is the force, which leads to a stress on the fiber that is related to the strain through the well-known Hooke's law as discussed in Section 5.4 and 5.5.

The theoretical background (depicted in previous sections) has led to the development of the characterization methodology for the FBG-embedded force sensors, for which the sensors are characterized with respect to force, temperature and the simultaneous variation of both parameters. One may now evaluate the force sensitivity variation as a function of temperature and enable the compensation of the temperature's influence on the sensor force response. The polymer response under a constant stress or strain is characterized by a creep (or recovery) that is described as a time-dependent viscous deformation when loading is applied [59]. An exponential regression was applied on the creep response, which was compensated by dividing the sensor response to the characterized time constant. It is worth to mention that the transverse force applied on

the FBG also leads to birefringence and polarization effects, which causes a polarization dependent loss that increases linearly with the transverse force. Even though this principle was used on the development of transverse force sensors [186], we considered only the wavelength shift caused by the applied force as shown in previous reported works for pressure [50] and force [212] sensors based on FBGs and described in Sections 5.3 and 5.4.

Following the characterization and validation of each FBG, the 3D-printed, FBG-embedded flexible support (as shown in Figure 6-41(b)) is positioned as the shank supports of a lower limb exoskeleton for knee rehabilitation, as is well shown in Figure 6-42. The supports are positioned such that when the flexion cycle is made, the highest force is applied to shank support 1, whereas, in the extension cycle shank support 2 is subjected to the highest force. In addition, the configuration of the shank supports showed in Figure 6-42 provides higher stability for the user's leg during the rehabilitation exercise. Moreover, the support flexibility provides comfort for the user. Regarding the exoskeleton structure, it is placed on a chair as shown in Figure 6-42, where a DC motor with a harmonic drive is responsible for the control of the flexion/extension movements. A thigh support is used to position and align the user's thigh and the robot structure, whereas the proposed 3D-printed flexible supports are placed on the user's shank. For the tests with the exoskeleton, sequential flexion/extension cycles are performed and the response of each FBG is acquired by the FBG spectrometer I-MON 512 (Ibsen Photonics, Denmark) for a 10-kHz acquisition frequency. Furthermore, the exoskeleton provides three sets of rehabilitation exercises: active assisted, active resistant and passive movements. In the active assisted movement, the exoskeleton motor helps the user on the flexion/extension movements' task, whereas the opposite occurs in the active resistant mode, i.e. the impedance of the robot increases the difficulty in movement. The last, passive operation mode (and the one used in the validation tests) may be regarded as an intermediate operation mode, where the motor does not provide any assistance or difficulty for movement. Thus, the impedance in the flexion/extension cycles are due to friction and back-drivability of the wearable robot.

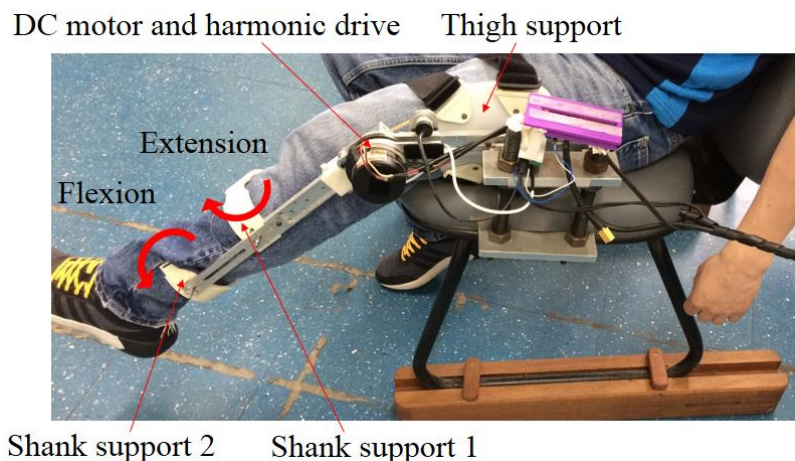


Figure 6-42 Exoskeleton for knee rehabilitation exercises with the 3d-printed flexible supports positioned on the shank region.

### 6.4.1.3. Results and Discussion

A block diagram with the approach for obtaining the calibration equation of each sensor as well as the equation for the estimation of the compensated force (for each FBG) is depicted in Figure 6-43, where  $\tau_1$  and  $\tau_2$  are the time constants for FBG 1 and 2, respectively. The results obtained in the characterization are presented and discussed in Appendix H, since the methods and experiments performed are similar to the ones already presented in 0.

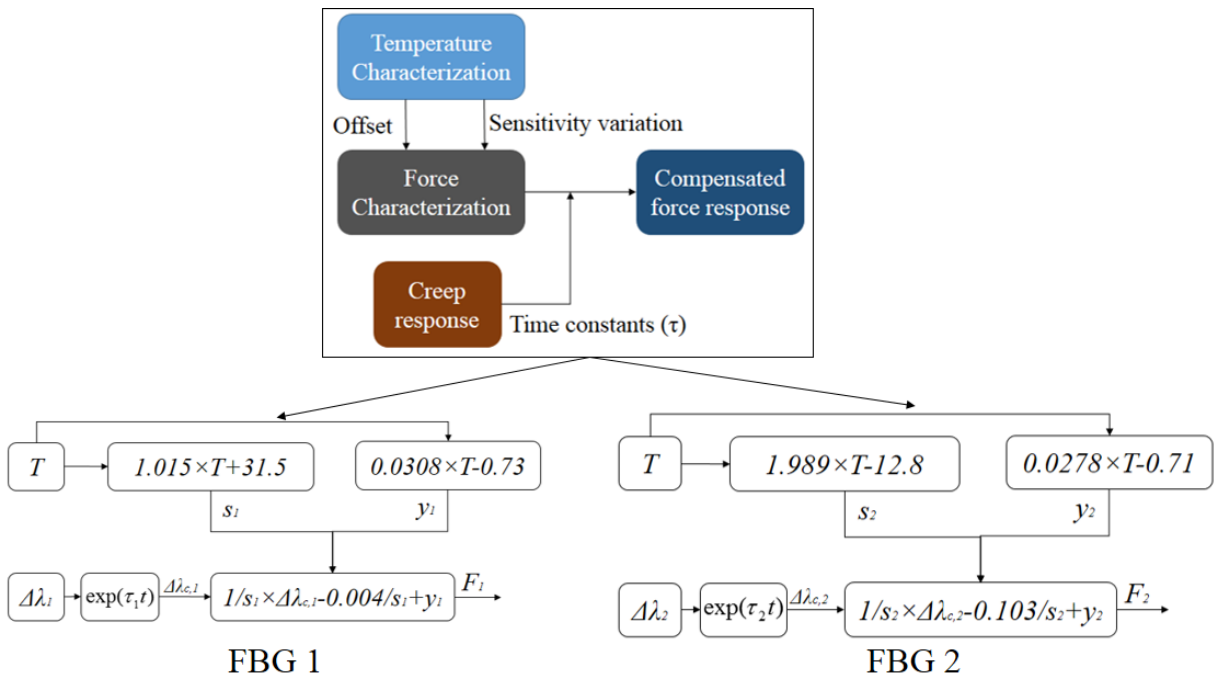


Figure 6-43 Block diagram of the force estimation for FBGs 1 and 2 with compensation of creep and temperature effects.

In order to validate the sensor, additional tests were made under different temperatures and applied forces on both FBGs 1 and 2 as is shown in Figure 6-44. In this validation, 7 tests were made with different forces and temperatures, where tests 1 to 3 were made at room temperature (25°C). The temperature was increased to 35°C and tests 4 and 5 were performed, whereas the tests 6 and 7 were made at 45°C. The forces applied for each test are shown in Figure 6-44 as the ‘reference’ for each test, which are compared with the responses of FBGs 1 and 2. The comparison shows a RMSE of ~ 0.50 N for FBG 1 and ~2.29 N for FBG 2. The reason for the higher RMSE for FBG 2 is the lower sensor linearity, as presented in the characterization tests, which leads to higher errors in the force estimation when the linear regression is made. Nevertheless, the relative error for FBG 2 (considering the whole force range of the test) is 4.5%, which is within the accuracy range of some conventional technologies for exoskeleton instrumentation [6], but with the additional advantages of electromagnetic fields immunity, compactness, flexibility and multiplexing capabilities. In the case of FBG 1, the errors are even lower, since a relative error of 1.0% was obtained, where such low error shows the possibility of achieving POF sensors with greater accuracy than the conventional technologies for robotic instrumentation. It is worth to mention that such low errors are obtained by the combination of the different characterization tests performed, which results in an equation that compensates different aspects of the sensor response, i.e. temperature cross-sensitivities and creep response are obtained. Thus, it is expected that the results presented in Figure 6-44 with the compensation equations will present lower errors than the ones obtained in the characterization tests, where none of the compensation equations were applied.

Following the sensors’ characterization and validation, they are positioned on the exoskeleton (see Figure 6-42) for the application as sensors for human-robot interaction forces, where the user is positioned on the chair with the thigh and shank supports attached. The user is asked to perform flexion and extension cycles. The results for 5 flexion/extension cycles are presented in Figure 6-45, where Figure 6-45(a) shows the response of FBGs 1 and 2 and Figure 6-45(b) presents the estimated force using the equations presented on the block diagram of Figure 6-43. The response of FBG 2 is inverted, aiming to clarify the phase difference between both sensors, where the FBG 1 (shank support 1) is activated at extension movements, whereas FBG 2 (shank support 2) shows wavelength shift when the flexion cycle occurs. Regarding the force estimation presented in Figure 6-45(b), the extension cycles present similar behavior with the measured forces between 10 N and 15 N, which is similar to results previously obtained with electronic and optical fiber sensors [28].

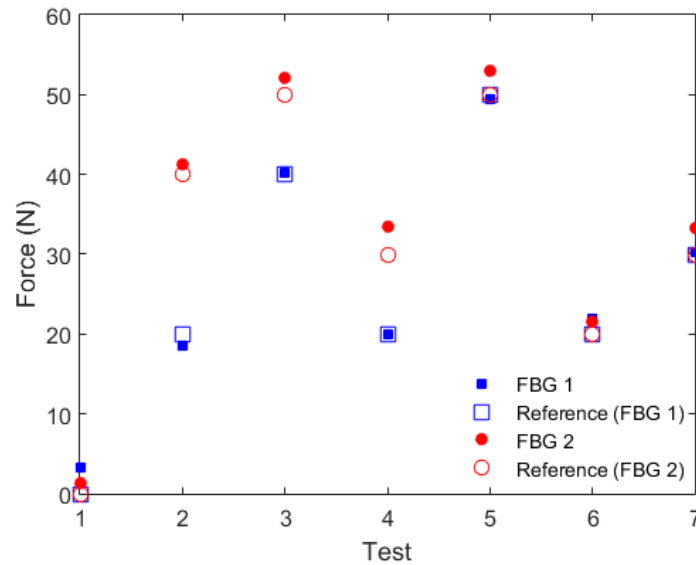


Figure 6-44 Validation tests for FBGs 1 and 2 at different forces and temperatures, where tests 1-3 were made at 25°C, 4 and 5 at 35°C and the remainder (6 and 7) at 45°C.

Additionally, the human-robot interaction forces in flexion cycles have higher variation, where the user applies more force in the exoskeleton, as the test progressed. This behavior is related to variations of the user interaction with the exoskeleton that generally varies between different users. Nevertheless, such increase, in the interaction forces as the test occurs, was also verified in previous work [28]. Thus, the tests with the FBG-embedded shank supports attached to the exoskeleton have showed the feasibility of the proposed approach on the human-robot interaction forces assessment. For this reason, the 3D-printed FBG-embedded supports can be regarded as a viable option not only for the monitoring and validation of control techniques for the minimization of human-robot interaction forces [213], but also in the instrumentation of soft robotics wearable devices [30].

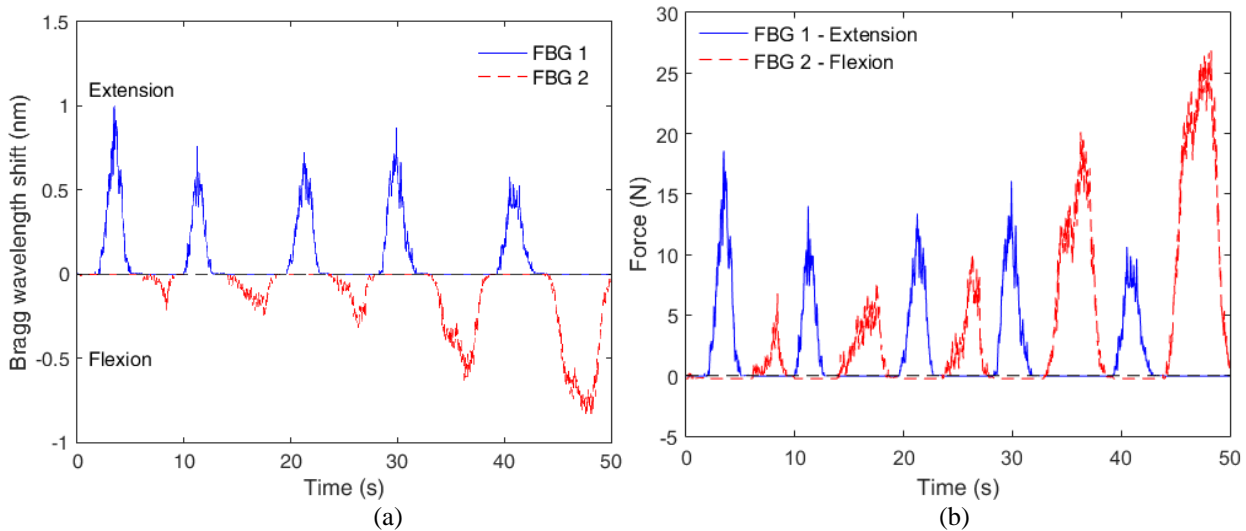


Figure 6-45 (a) Responses of the FBGs embedded in shank support 1 and 2 for extension (FBG 1) and flexion (FBG 2) cycles. (b) Human-robot interaction force measurement with the FBG-embedded, 3D-printed flexible supports.

### 6.4.2. FBG Array Application in a SEA's Spring

Considering the advantages of POF sensors in conjunction with the possibility of inscribing long arrays in commercially available POFs, this section presents the instrumentation of the SEA's spring designed in [9] with two FBG arrays in CYTOP fibers, where each sensor array has 4 FBGs. Thus, 8 FBGs are distributed on the spring, enabling a multi-point strain measurement on the spring. This configuration results in three advantageous features there will be further explored: (i) shape reconstruction of the spring under deformation, (ii) more accurate torque estimation using sensor fusion algorithms such as Kalman filters and (iii) identification and rejection of mechanical disturbances caused by arbitrary external loadings. The sensor

operation and the spring deflection under different loadings are estimated through a numerical analysis using the finite element method (FEM) and confirmed in an experimental analysis.

#### 6.4.2.1. Experimental Setup and Methods

The FBGs were positioned on the spring as is shown in Figure 6-46, where a lever is positioned in the spring output shaft for the application of predefined displacements and torques. The fiber is fixed on the spring by means of 3D-printed supports placed between the FBGs and thermoplastic glue. The spring is fixed in a base, which is positioned on a fixed support to limit the flexion and extension movements to only one plane (as depicted in Section 6.2). The spring has a linear behavior in torques lower than 30 Nm with stiffness constant of 92 Nm/rad for flexion and 96 Nm/rad for extension, as characterized in [9], which enables the torque estimation through the spring angular deflection.

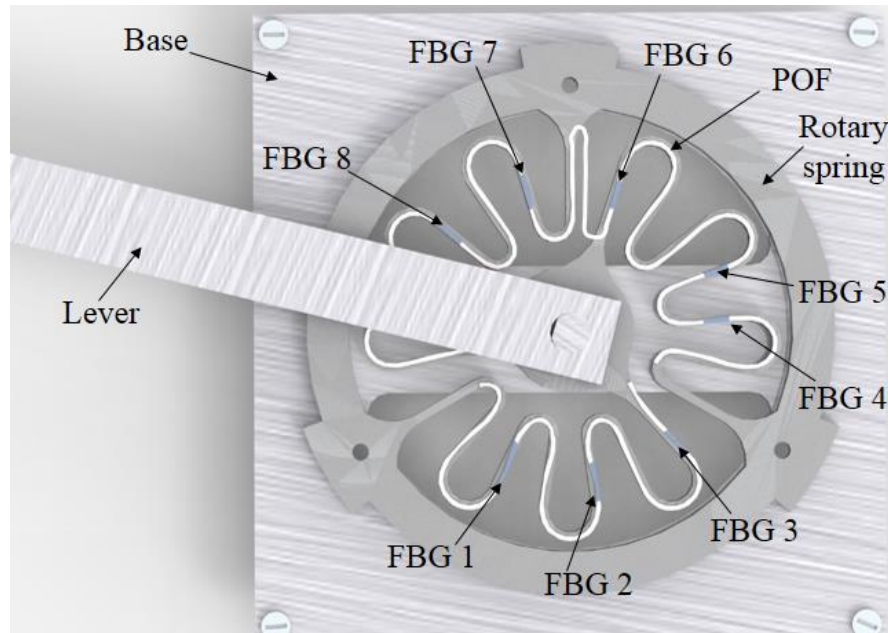


Figure 6-46 Front view of the spring with the FBG sensors positions.

A numerical analysis is made as shown in Appendix I on the spring to evaluate its deflection with different torques and the strain distribution when a transverse force is applied on arbitrary points of the spring. Then, experimental evaluation is performed in which three different flexion and extension displacements are applied on the spring using the lever connected to the spring shaft (see Figure 6-46). In addition, transverse forces are applied on the spring to evaluate the FBG sensors of identifying these forces and discriminate it from the flexion and extension displacements. In order to obtain a reliable measurement of the flexion and extension on the spring, the Kalman filter is applied on the response of the FBGs array using the known displacements applied on the spring as a reference for the filter estimation.

The Kalman filter is a recursive filter that estimates the state of a system from a series of measurements. In this way, the measurements of each sensor and the reference are used to generate an estimate of the measurements of the system. This estimate has a lower error than the measurement of each sensor analyzed separately [214]. The filter uses a procedure that can be compared to a definition of weights of the sensors. The sensor that presents lower errors have higher weight in the estimation of the state than sensor with higher uncertainty. The defined weights are, in fact, the covariance of each sensor. The lower the covariance the higher the weight of the result obtained by the sensor in the final estimation [215]. Kalman filter is employed in sensor fusion due its simplicity and ease of implementation and optimization [215]. Detailed description, modelling and applications of the Kalman filter can be found in [216]. If the system is in state space, the prediction is made through Eq. 6.11 and 6.12; and updated through Eq. 6.13, 6.14 and 6.15.

$$\hat{x}_{k|k-1} = A\hat{x}_{k-1|k-1}, \quad (6.11)$$

$$P_{k|k-1} = AP_{k-1|k-1}A', \quad (6.12)$$

$$G = P_{k|k-1}C'(CP_{k|k-1}C'+R), \quad (6.13)$$

$$P_{k|k} = (I - GC)P_{k|k-1}, \quad (6.14)$$

$$\hat{x}_{k|k} = \hat{x}_{k|k-1} + G(z_k - C\hat{x}_{k|k-1}), \quad (6.15)$$

where  $A$  and  $C$  are the transition matrices of state (at time  $k$ ) and observability, respectively, which have unitary values in this case, since, presumably, the sensor does not alter the system dynamics.  $G$  is the Kalman gain,  $P$  is the covariance matrix,  $z_k$  is the measured signal,  $R$  is the sensors covariance,  $I$  is the identity matrix and  $\hat{x}_{k|k}$  is the estimated state at time  $k$  given observations up to and including at time  $k$ .

### 6.4.2.2. Experimental Analysis

The arrays in the CYTOP fiber were inscribed with the direct-write, plane-by-plane method using the fs laser as discussed in Section 5.2 and two arrays with 4 FBGs each were inscribed. In order to characterize the strain response of the FBGs, the sensors were positioned in a linear translation stage and strains on the range of 0 to 2000  $\mu\epsilon$  were applied at each FBG. The mean and standard deviation of the sensors' responses are shown in Figure 6-47, where the mean and standard deviation of sensors sensitivities are  $1.8 \pm 0.2$  pm/ $\mu\epsilon$ .

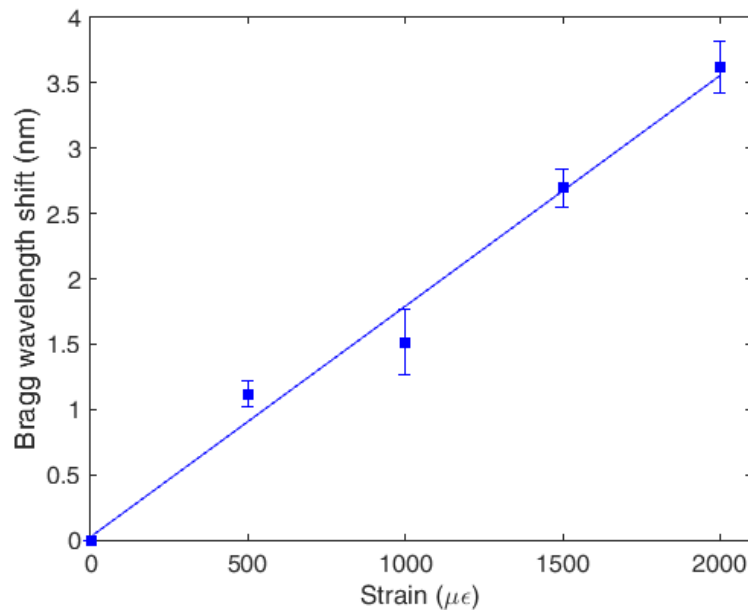


Figure 6-47 Mean and standard deviation of the FBGs responses as a function of the applied strain.

As shown in Appendix I, the deformation at each region of the spring is different. Thus, each FBG will be subjected to different strains. In order to compare the simulated and experimental results, a constant displacement of 0.2 rad is applied on the spring at the clockwise direction (flexion), which results in a torque of about 18.4 Nm considering the spring stiffness of 92 Nm/rad [9].

Figure 6-48 shows the obtained wavelength shift for each FBG at a constant torque, where the experimental results obtained from the FBGs wavelength shift are compared with the strain obtained in the simulations in the region of each FBG (see Appendix I). Since the increase of the strain leads to an increase of the FBGs wavelength shift, the results of Figure 6-48(a) show that the FBGs present similar behavior when compared to the one predicted by the numerical analysis. It also indicates the possibility of using the response of each FBG for the shape reconstruction of the spring under flexion and extension as shown in Figure 6-48(b), where a colormap with the wavelength shift of each respective FBG is placed on the spring at the region where the wavelength shift was measured. As the FBGs have similar strain responses, shown in Appendix I, the spring shape with the deformation at each of the 8 points can be estimated from the wavelength shift of the FBGs.

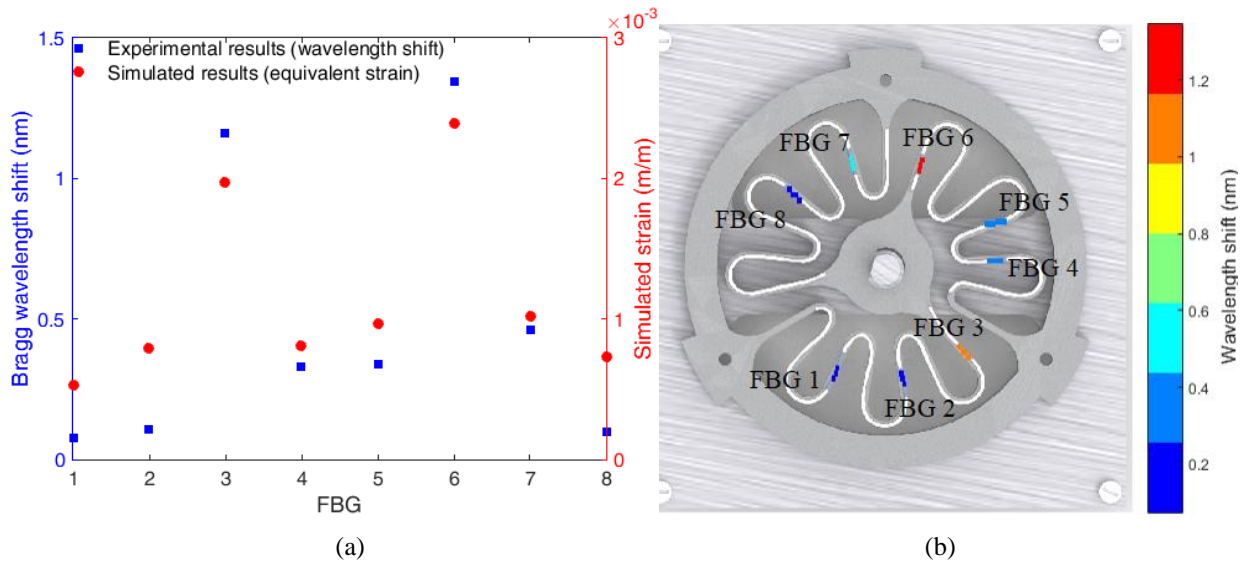


Figure 6-48 (a) Wavelength shift for the 8 FBGs and simulated strain on the region of each FBG. (b) Wavelength shift at each region of the spring as a tool for shape reconstruction of the device under deformation.

The behavior of each FBG inscribed in POF is evaluated under different flexion and extension torques, where extension torques are negative and the flexion ones have the positive signal. Figure 6-49 shows the response of the 8 FBGs, individually, where each sensor has similar behavior when compared to both the simulated and experimental results shown in Figure 6-48(a) at about 18 Nm. Thus, the FBG 6 shows the highest variation, followed by FBG 3, whereas FBGs 1, 2 and 8 presented the lowest wavelength shift, which is strictly related to their positioning on the rotary spring.

In addition, Figure 6-49 shows a linear relation between each FBG and the applied torque, where each FBG has its own linear regression equation depending on its position on the rotary spring. The linear regression terms (a and b) of FBGs 1 to 8 as a function of the torque is presented in Table 6-4. It is worth to mention that each equation has the type shown in Eq. 6.16, where  $T$  is the torque and  $\Delta\lambda$  is the wavelength shift. Furthermore, by isolating the  $T$  term in Eq. 6.16, it is possible to obtain the torque estimated by each FBG sensor. In this way, the estimated responses of the FBGs are compared with the applied torque and the RMSE between the estimated and applied torques are also shown in Table 6-4 for each FBG.

$$\Delta\lambda = aT + b. \quad (6.16)$$

The RMSEs shown in Table 6-4 are related to nonlinearities on the linear regression of each FBG. As depicted in Figure 6-49, FBG 3 shows the lowest  $R^2$  with the linear regression due to nonlinearities on the sensor behavior. Thus, FBG 3 also showed the highest RMSE when the estimated torque is compared to the applied one. In the other FBGs, the RMSE was about 1.0 Nm and the  $R^2$  of these sensors were higher than 0.99 (see Figure 6-49), which can be regarded as low errors if the whole tested torque range is considered. Considering all 8 FBGs, the mean RMSE is  $1.39 \pm 0.73$  Nm, which represents a relative error of about 4.2% when the whole torque range (about 32 Nm) is evaluated.

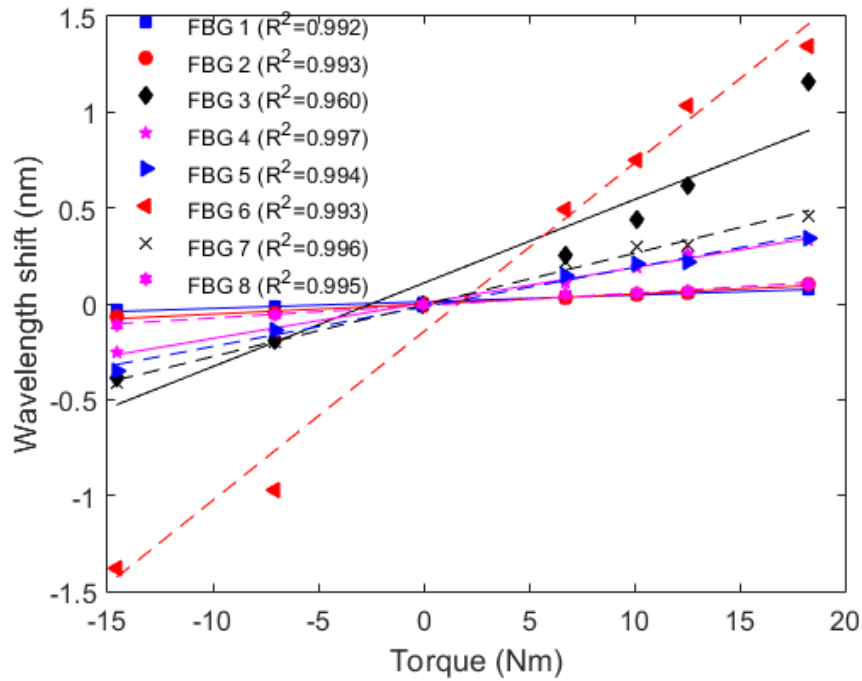


Figure 6-49 FBGs responses as a function of the applied torque on the spring.

Table 6-4 Linear regression and torque response of each FBG.

FBG	$a$ (nm/Nm)	$b$ (nm)	RMSE (Nm)
1	$3.4 \times 10^{-3}$	$1.1 \times 10^{-2}$	1.37
2	$5.0 \times 10^{-3}$	$-1.6 \times 10^{-3}$	1.24
3	$4.3 \times 10^{-2}$	$1.1 \times 10^{-1}$	3.14
4	$1.8 \times 10^{-2}$	$4.0 \times 10^{-3}$	0.87
5	$2.1 \times 10^{-2}$	$-1.7 \times 10^{-2}$	1.16
6	$8.8 \times 10^{-2}$	$-1.5 \times 10^{-1}$	1.29
7	$2.7 \times 10^{-2}$	$-6.0 \times 10^{-3}$	0.89
8	$6.5 \times 10^{-3}$	$-9.3 \times 10^{-3}$	1.10

However, there are 8 sensors providing the same information, i.e., flexion/extension torque on the rotary spring. For this reason, it is possible to apply sensor fusion algorithms in the sensors responses in order to obtain a more accurate measurement. Therefore, the Kalman filter is applied on the sensors' responses. The filter's parameters are estimated recursively by comparing the sensor response after the sensor fusion with the reference torque in order to obtain the lowest possible error for the sensors. In this case, the covariance of each sensor ( $R_{1-8}$ ) is obtained based on the error of each sensor, where the lower errors resulted in lower covariance values as depicted in Figure 6-50. The FBGs torque estimation after the sensor fusion is shown in Figure 6-50, where the applied torque is compared with the estimated one (with the fusion of the 8 FBG sensors).

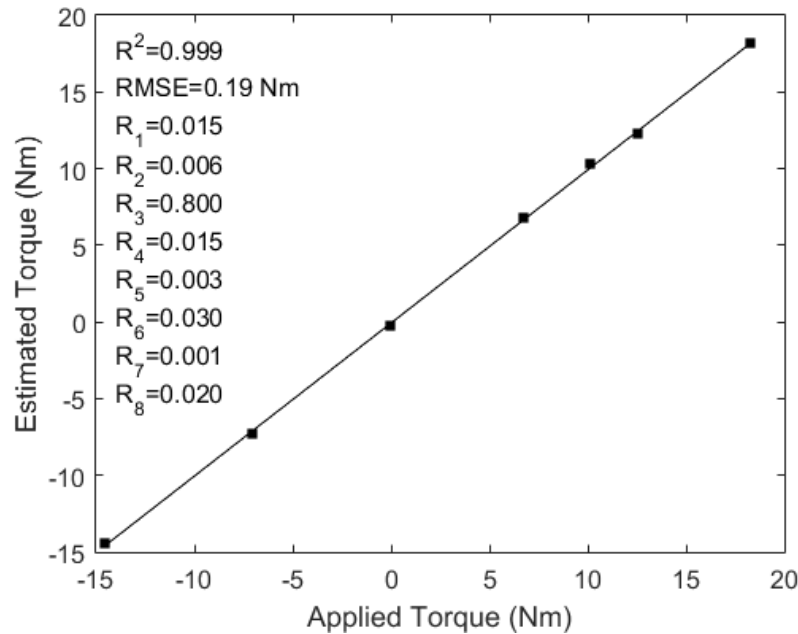


Figure 6-50 Torque estimated after the sensor fusion between 8 FBGs compared with the applied torque. The RMSE and covariance matrix values are also presented.

Regarding the results of Figure 6-50, there is a substantial decrease on the sensor RMSE when compared to the applied torque, which is also related to the increase of the sensor linearity ( $R^2=0.999$ ). Comparing to the results shown in Table 6-4, there is a seven-fold decrease of the sensor's RMSE, which leads to a much more accurate measurement of the torque applied on the spring. In addition, if the whole torque range is considered, the sensor's response after the application of the Kalman filter is only 0.59%. These results show the feasibility of applying a FBGs array in conjunction with sensor fusion techniques on the spring to obtain highly accurate and reliable sensor systems. It is worth to mention that using a higher number of sensors can result in even lower errors on the torque assessment. On the other hand, it is also possible to use a lower number of sensors and obtain acceptable errors on the torque estimation.

However, the quasi-distributed measurements on the spring brings another advantageous feature for the sensor system, which is the possibility of rejecting external mechanical disturbances on the spring. Since it is possible to estimate the strain at each point of the spring, one can estimate if a given deflection on the spring is due to the flexion/extension torques or due to transverse forces on the spring, which are regarded as mechanical disturbances. In order to verify this assumption, arbitrary loads are applied in 5 points of the spring as shown in Figure 6-51(a) and the wavelength shift of each FBG is presented in the tool for spring shape reconstruction for 2 cases. Moreover, all the transverse force conditions and flexion/extension torques are shown in Figure 6-51(b).

In Figure 6-51, all 5 analyzed cases have shown an increase of the wavelength shift on the FBGs close to the point of transverse force application. As expected, the shift was higher on FBGs 3 and 6, since these sensors are positioned on the region of highest strain on the spring, as predicted by the numerical simulation and confirmed in the experimental analysis. As shown in Figure 6-47 and Figure 6-49, the response of each FBG is linear (see Figure 6-49 and Figure 6-50), which means that the response of the sensors follows a well-defined pattern when only flexion and extension are applied on the spring. Hence, a simple and straightforward manner to identify external disturbances on the spring is by comparing the strain distribution (from the wavelength shift of all FBGs) on the spring at a given loading condition with a reference strain condition. The reference condition is obtained when only flexion and extension are applied on the spring.

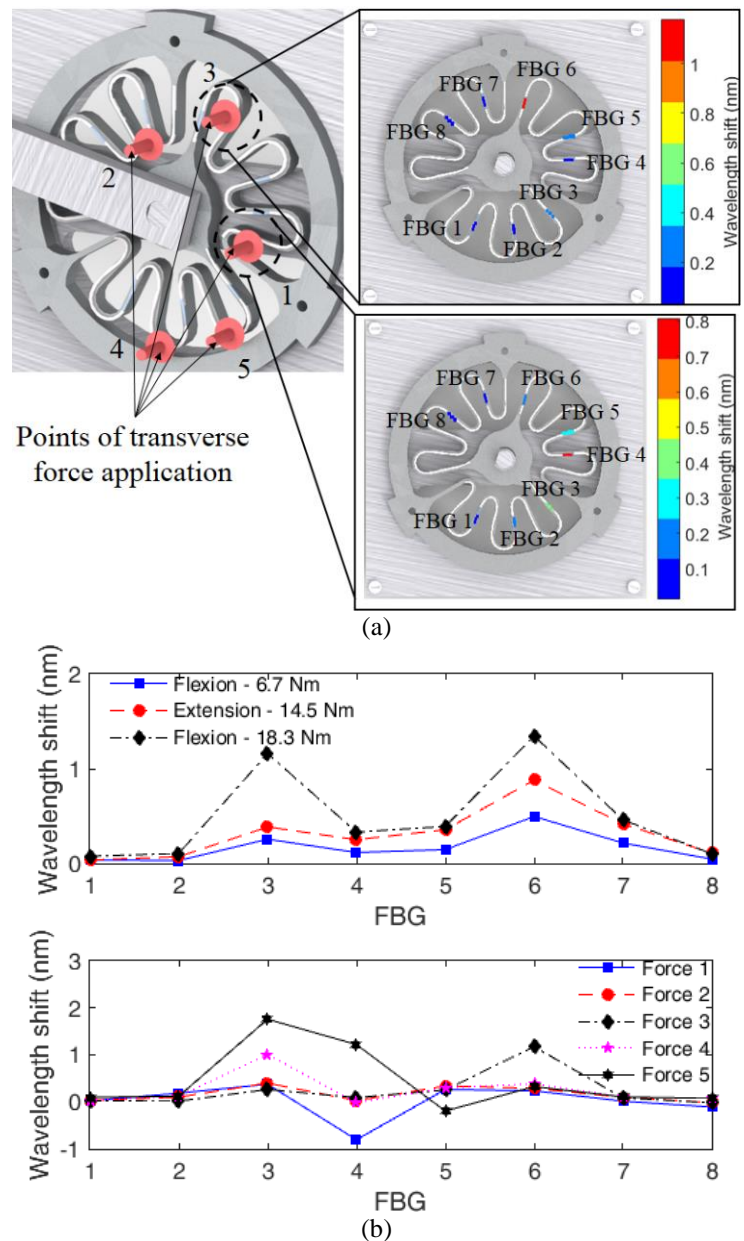


Figure 6-51 (a) Force application points and wavelength shift at each region of the spring at 2 transverse force cases. (b) Wavelength shift of each FBG at flexion/extension torques and transverse force conditions.

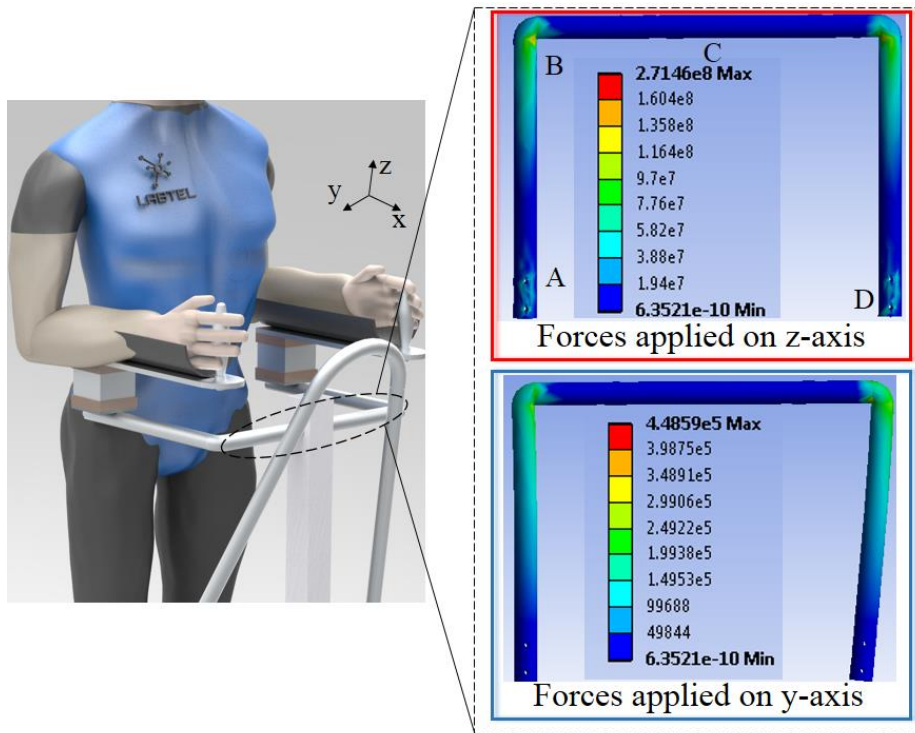
### 6.4.3.FBG Array on Multiparameter Measurements in Smart Walker

The aforementioned advantages of POFs for healthcare devices instrumentation in conjunction with the advantageous optical features of CYTOPs (which not only is widely commercially available, but also enable the application of commercial FBG interrogators and off-the-shelf optical components in the 1550 nm wavelength region) open up new routes on the instrumentation of healthcare devices. Thereby, this section presents the characterization and application of a POFBGs array in CYTOP fibers on the instrumentation of a SW. The application of the POFBG arrays in a SW is evaluated for four different functionalities: (i) SHM of the healthcare device, (ii) detection of the user’s movement intention, (iii) estimation of the user’s gait cadence and (iv) possibility of aid on the mapping of structured environment using the frequency response of the FBGs array.

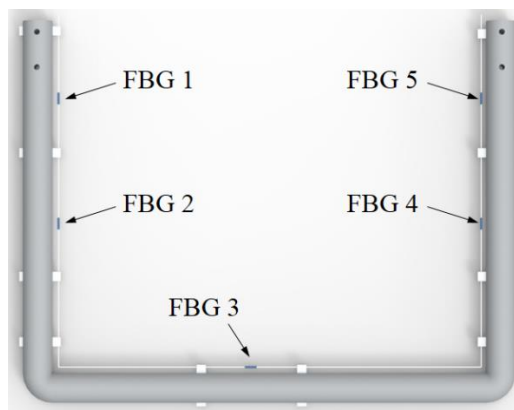
#### 6.4.3.1. FBG Array Characterizations

As a first step on the FBG sensors implementation for the SW instrumentation, a FEM analysis is performed on the SW structure for different loading conditions on the support bar (see Figure 6-52), since it is the element subjected to the highest stress when loadings are applied on the region at which the users’ arms are positioned. Two loading conditions are considered in the simulations, one with constant forces of 1 kN in z-axis (considering the axes shown in Figure 6-52(a)) applied on the support bar in order to simulate the stress on the

structure when the SW is supporting the user’s weight. The other loading condition considers the case where the user is making a turn with the SW. In this case, there is a constant loading in y-axis of 150 N in the right side of the support bar, whereas a 50 N loading (also in y-axis) is applied on the left side of the bar. The stress distribution for both scenarios shows a higher stress in the vertical bars (region A), where there are stress concentrations on the regions in which the support bar is bended (region B). In addition, region C is the one at which the minimum stress occurs, which is expected since this region is fixed to a center bar (see Section 6.2) inhibiting a high strain in this area. If the forces are applied on z-axis, there is the same strain distribution on regions A and D. In contrast, when the force is applied on y-axis, the stress on regions A and D occurs in different directions, where one region will be subjected to compression and the other to extension, depending on the direction of the force. Figure 6-52(b) shows the positions of each FBG sensor in the SW’s support bar. These positions were chosen based on the stress/strain distribution on the SW obtained on the numerical simulation, as shown in Figure 6-52(a). Two FBGs (FBGs 1 and 2) are positioned on region A and two on region D (FBGs 4 and 5), which are the regions with the highest strain variation when a force is applied on the SW structure. Thus, the FBGs in these regions are able to detect the strain and their variations related to the user’s movement intention, which applies different loading conditions on the SW depending on the performed movement (forward, make turns and stop the device). Furthermore, FBG 3 is positioned on region C (due to negligible strain in this area) for the temperature assessment, since FBGs are sensitive to both strain and temperature[132].



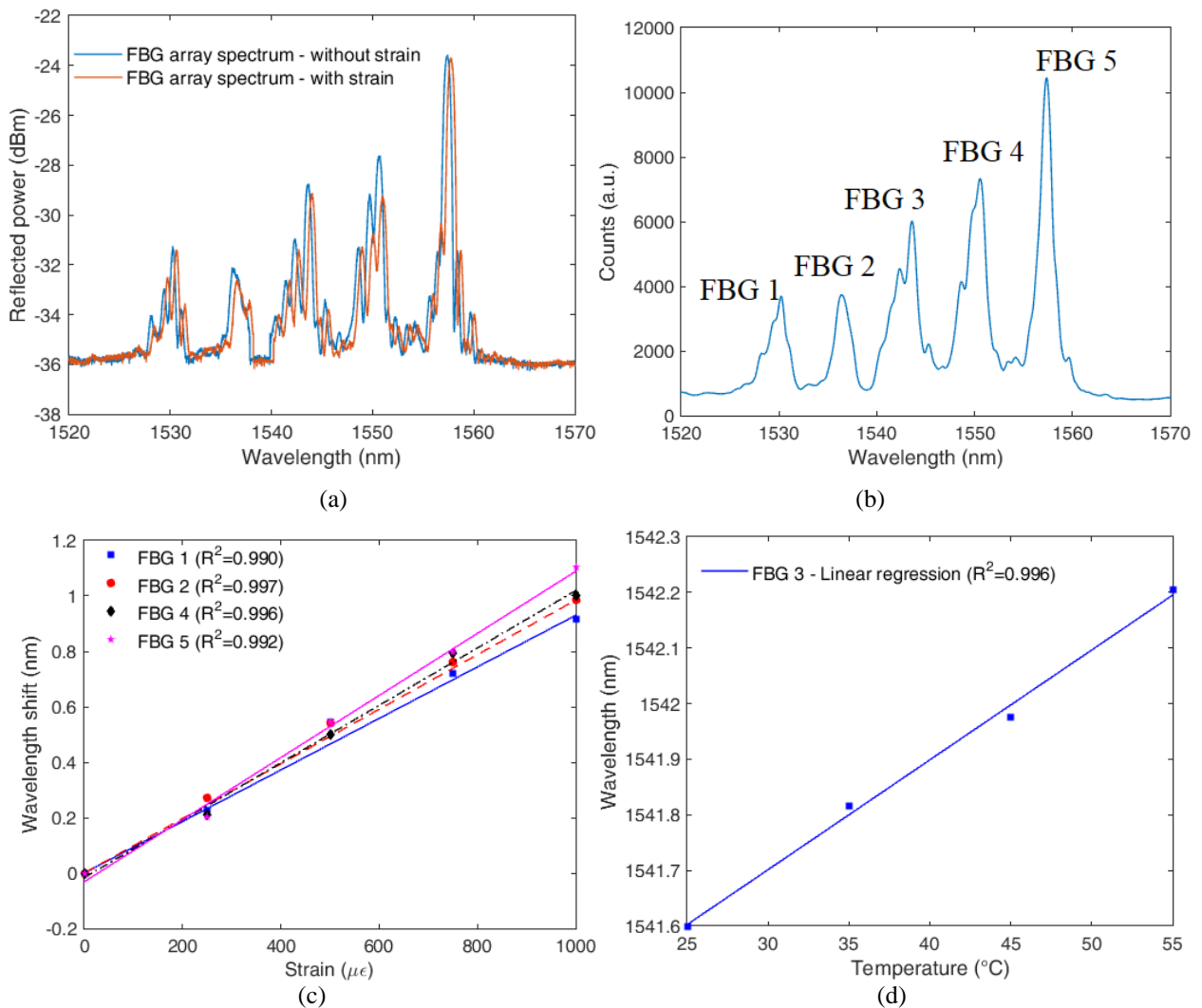
(a)



(b)

Figure 6-52 (a) Finite element analysis on the SW’s support bar for two loading conditions: forces applied only on y-axis and forces applied on z-axis. (b) Positions of the FBGs on the SW structure.

The reflected spectra of the 5-FBG array inscribed in CYTOP fiber is shown in Figure 6-53(a), where the spectrum for the FBGs under axial strain is also presented in order to demonstrate the spectral variations of the array under a strain condition. The spectrum of Figure 6-53(a) was recovered using a sm125 FBG interrogator (Micron Optics, USA) after the connectorization of the CYTOP array in a single mode fiber (SMF). However, this interrogator has low acquisition frequency (2 Hz), which inhibit its application for dynamic measurements (such as the ones proposed on the SW) and the same approach presented in Section 6.4.1 was used. The strain response of the FBGs inscribed in CYTOP is presented in Figure 6-53(c), where all 4 FBGs have similar response to strain (strain sensitivity of  $1.57 \pm 0.15$  pm/ $\mu\epsilon$ ). In addition, the temperature response of FBG 3 is shown in Figure 6-53(d), where a temperature sensitivity of  $20.17$  pm/ $^{\circ}\text{C}$  was obtained. In order to verify the FBGs capabilities of detecting the frequency of an oscillatory movement, dynamic displacements with three different frequencies (three tests at each frequency) –  $f_1$ ,  $f_2$  and  $f_3$ , namely 0.5 Hz, 1.5 Hz and 3.5 Hz, respectively, where similar strain amplitude (about  $750$   $\mu\epsilon$ ) are applied on the POFs in all tests. The wavelength shift for the FBG at each frequency is shown in Figure 6-53(e), where the solid line is the mean from all three tests at a given frequency, whereas the shaded line is the standard deviation (comparing all three tests at each angular velocity). The frequency response of the FBG is depicted in Figure 6-53(f), where the sensors capabilities of detecting different frequencies (within the tested range), with low deviations when comparing with the applied frequencies, are shown.



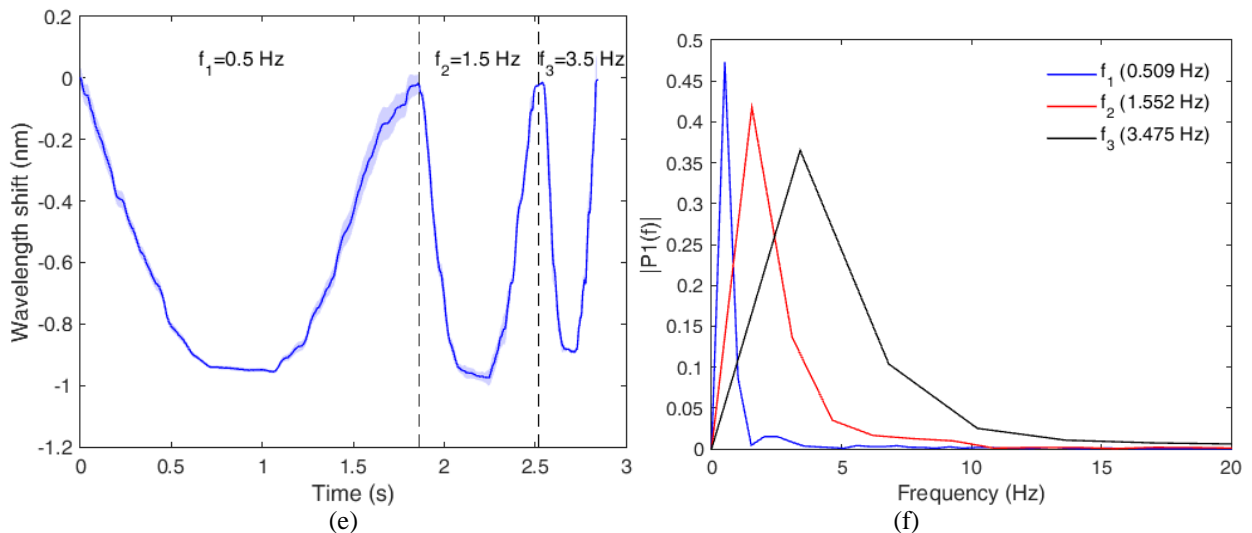
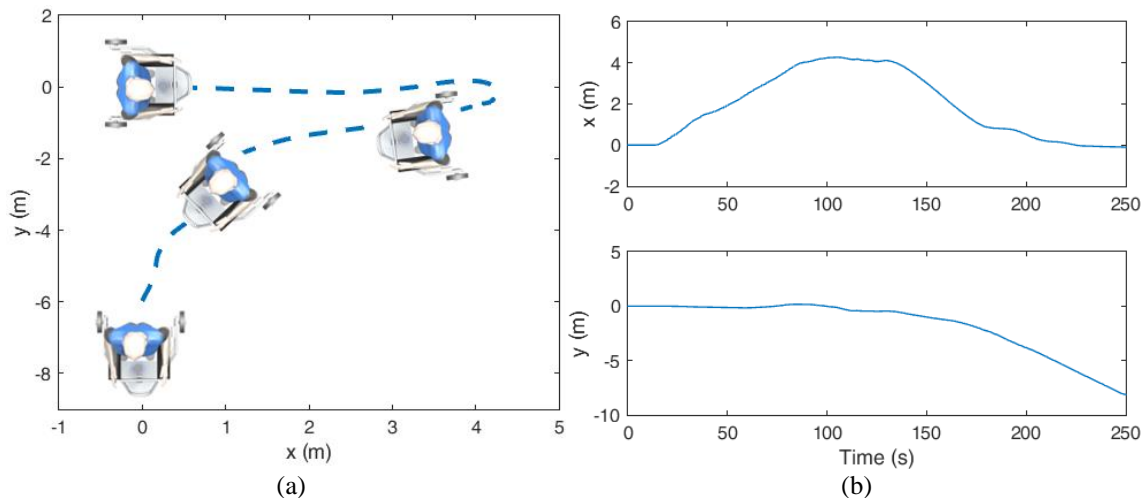


Figure 6-53 (a) FBGs array spectrum recovered in Micron Optics sm 125 FBG interrogator after the POF connectorization and after the application of an axial strain on the fiber. (b) FBGs array spectrum obtained in I-MON 512 spectrometer used on the sensors characterization and implementation on the SW. (c) Wavelength shift as a function of the strain for FBGs 1, 2, 4 and 5. (d) Temperature response for FBG 3. (e) Wavelength shift of FBG 1 under oscillatory loadings at 3 different frequencies (0.5 Hz, 1.5 Hz and 3.5 Hz), where the solid line is the mean and the shaded line is the standard deviation of three tests performed at each frequency. (f) FBG response in the frequency domain for each dynamic test.

### 6.4.3.2. Results

After the characterization of the material properties and sensors' responses, the FBGs array is positioned on the SW (as shown in Figure 6-52(b)). In the first test, the user is asked to make the path presented in Figure 6-54(a), which includes right and left curves as well as commands for forward movement and to stop the healthcare device. The path on  $x$  and  $y$  directions as a function of time is depicted in Figure 6-54(b). Then, the responses of FBGs 1 and 2 are compared with the  $y$ -axis of the force sensor placed on the SW's right handle as shown in Figure 6-54(c). Similarly, FBGs 4 and 5 are compared with the  $y$ -axis of the force sensor on the SW's left handle in Figure 6-54(d), where all tested FBGs showed similar responses when compared with the force sensors used as references for the SW's commands. In addition, Figure 6-54(e) presents the wavelength variations of FBG 3 during the entire test, where it can be seen only minor deviations of the wavelength. In the red curve of Figure 6-54(e), the temperature estimation is presented using the linear regression for temperature response of FBG 3 (see Figure 6-53(d)). It is noteworthy that the temperature estimated by FBG 3 (27.4°C) is similar to the room temperature where the tests were performed (27°C – obtained with commercial thermometers).



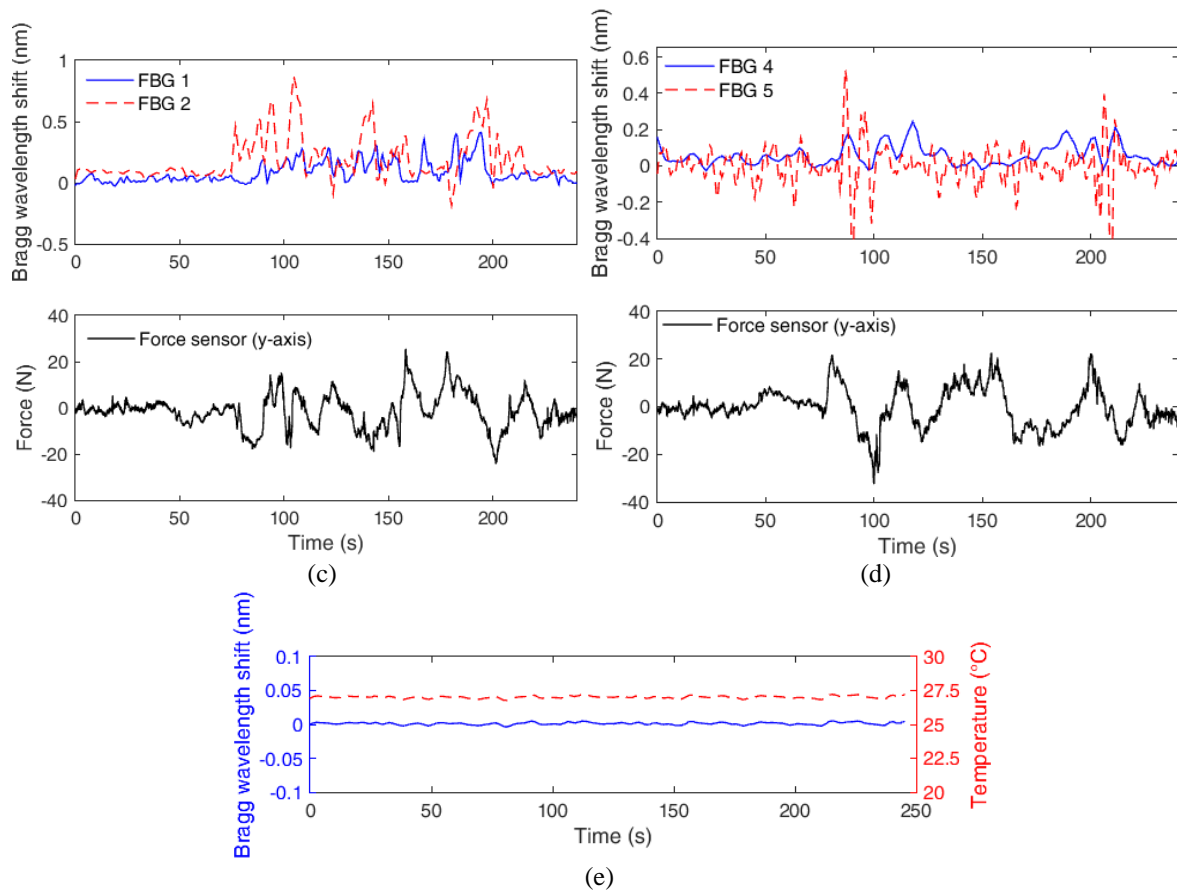


Figure 6-54 (a) Path performed by the user (x and y directions) in the FBGs array implementation tests. (b) Temporal variation of the x and y directions of the path. (c) Comparison between FBGs 1 and 2 with y-axis of the force sensor placed on the SW's right handle. (d) Comparison between FBGs 4 and 5 with y-axis of the force sensor placed on the SW's left handle. (e) Temperature response and wavelength shift of FBG 3 during the test.

In the last set of tests, the user is asked to walk (with the SW) in a straight line at three different floor conditions. In the first condition (Figure 6-55a)), the test is made on a smooth floor, then, the roughness of the terrain at which the tests occur were increased for both floor conditions 2 and 3 shown in Figure 6-55(b) and (c), respectively. In these cases, the sensors' responses are analyzed in the frequency domain where a FFT is applied on each signal. The FBG responses have frequencies' peaks at two regions: a) one at frequencies between 0.5 Hz and 1.5 Hz related to the gait cadence, since the gait is an oscillatory movement with predetermined frequency [155] and the other, b) in frequencies higher than 2 Hz, where the latter is due to the floor-induced vibrations on the SW structure. Thus, the tests performed in a rough terrain e.g. floor condition 3 will present peaks in higher frequencies than the ones made in smoother floor, such as the floor condition 1. Thereby, a second order Butterworth low pass filter (cutoff frequency at 1.8 Hz) is applied to obtain the gait cadence from the FBGs, whereas a high pass filter with cutoff frequency at 2 Hz is employed to estimate the vibration frequency induced by the floor. As depicted in Figure 6-55, the frequencies obtained from the FBGs array are compared to the ones measured by the SW's sensors, where the LRF is commonly employed for the gait cadence estimation [195]. An accelerometer of the IMU placed on the center tube of the SW is employed on the measurements of the floor-induced vibrations.

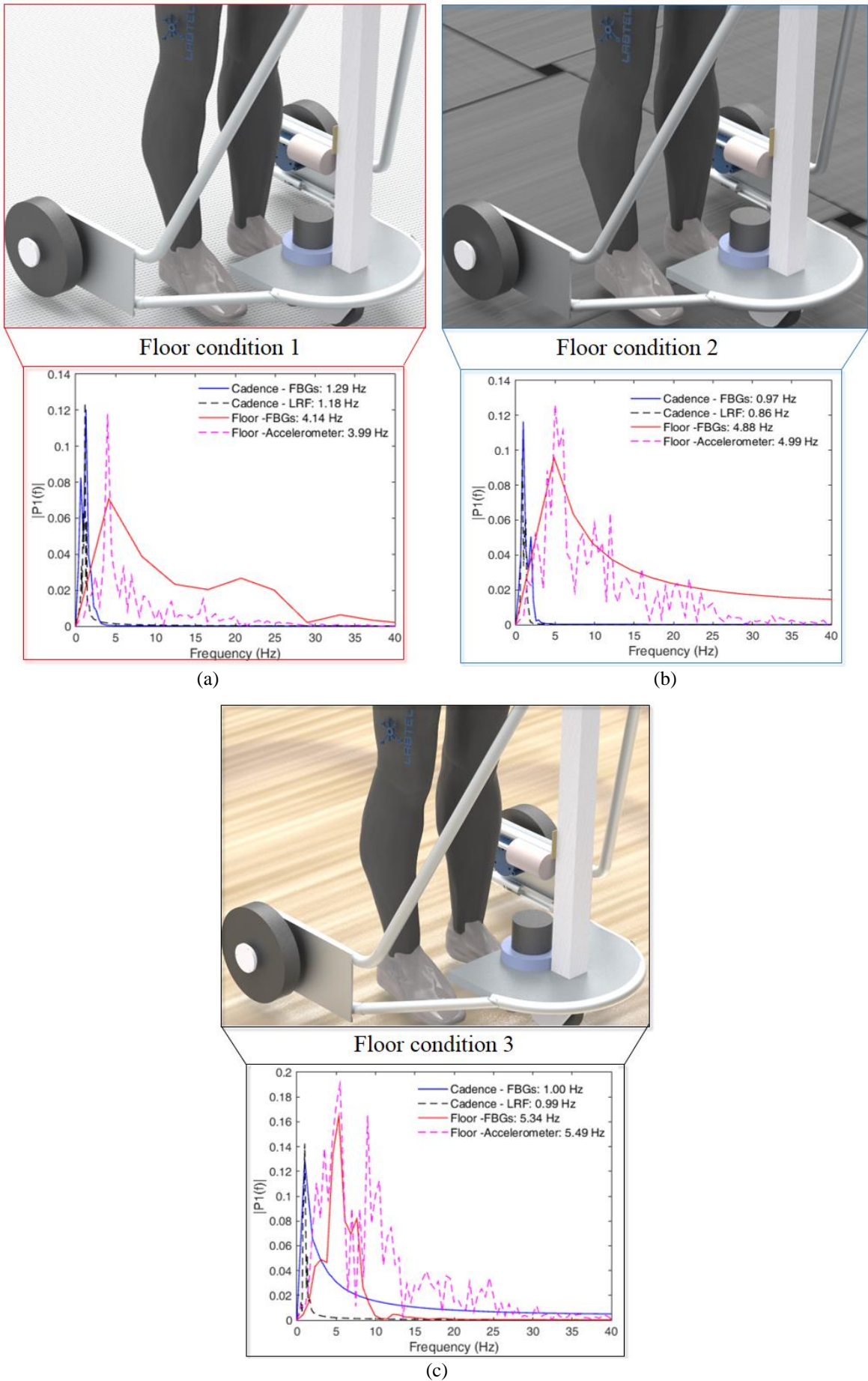


Figure 6-55 (a) FBGs array, LRF and accelerometer responses in the frequency domain for floor condition 1. (b) FBGs array, LRF and accelerometer responses in the frequency domain for floor condition 2. (c) FBGs array, LRF and accelerometer responses in the frequency domain for floor condition 3.

### 6.4.3.3. Discussion

In the continuous quest of developing novel healthcare devices with high battery autonomy, compact and affordable for the general population, this sub-section reported the development, characterization and implementation of FBG-based sensor systems for multiparameter monitoring in a SW. The FBGs were inscribed in a CYTOP fiber using an fs laser through the direct write plane-by-plane inscription method. The CYTOP fiber combines the POF material features desired for sensing mechanical parameters, due to the low Young's modulus and higher strain limits, with the low losses in the 1550 nm wavelength region, which is the region of the majority commercial interrogators. In addition, CYTOPs are widely available commercially and, thus, the sensor system does not need microstructured or specialty doped fibers commonly reported on FBG inscription in POFs [68], [142], [217]. The FBG inscription using an fs laser operating at 517 nm fills a gap on POFBG inscription as the UV lasers commonly employed in gratings inscription are not suitable for FBG inscription in such fibers due to their high UV resistance. As the CYTOP fibers have multimode operation, the direct write plane-by-plane inscription method results in a single-peak FBG even in multimode fibers by controlling the mode excitation, since, due to the mechanisms involved in the grating inscription with the fs laser, it is possible to limit the grating planes inscription to a predefined part of the fiber core.

Thus, a 5-FBG array is inscribed according to the positions in which there are the highest and lowest stresses, obtained through FEM numerical analysis. Thereafter, all FBGs of the array are characterized with respect to strain, temperature and frequency of oscillatory movements. FBG 3 is positioned on a region of SW where there is negligible stress/strain in order to measure the temperature without the influence of mechanical loadings. The temperature assessment is necessary for any sensor application with FBGs, since the Bragg wavelength is temperature-dependent and is particularly important on FBGs inscribed in POFs, since the fiber material properties change with temperature, which need to be assessed and compensated in applications where the temperature variation is critical [197]. Furthermore, the tests with dynamic strain in different frequencies show not only the capability of the FBG on detecting those frequencies (errors of about 1%), but also the high repeatability of the sensor. The deviation between three tests at each frequency shown in the shaded line of Figure 6-53(e) is lower than 0.05 for  $f_1$  and negligible for  $f_2$  and  $f_3$  (as defined in Figure 6-53). Regarding the strain characterization performed with FBGs 1, 2, 4 and 5, all sensors presented linear behavior, where a  $R^2$  higher than 0.99 was obtained in all analyzed cases. The FBGs capability of performing reliable strain measurements show the possibility of applying the FBGs array for SHM in the SW, which is an important parameter on this healthcare device, since the SW generally has to support most of the users' weight when it is in use. Thus, the SHM plays a crucial role in this application, as the possibility of structural collapse of healthcare devices while it is in use is a major concern. In addition, from the best knowledge, none of the SWs have a sensor system for SHM and the absence of structural monitoring can result in major accidents or unwanted risks for the users.

In order to assess additional functionalities of the proposed FBGs array on the SW instrumentation, two sets of tests were made. In the first test, the user follows a predetermined path, which includes left and right turns, stop and forward movements, whilst the responses of FBGs 1, 2, 4 and 5 are compared with the ones of the force sensors in the SW's left and right handles. The data analysis showed a  $R^2$  of about 0.97 when FBGs 1 and 2 are compared with the force sensor in the right handle. Similarly, the  $R^2$  for FBGs 4 and 5 compared with the force sensor in the left handle is about 0.93. In both cases, the calculated  $R^2$  shows good agreement between the force sensors and FBGs array, which proves the feasibility of the second functionality of the FBGs array, i.e., detecting the users movement intention, commonly used in control strategies for human-robot interaction [195]. Then, in the second set of tests, there is the assessment of the FBGs array as a tool for estimating the gait cadence and on the aid of the simultaneous localization and mapping techniques in structured environments (such as the one proposed in Figure 6-56) by means of identifying floor-induced vibrations in different floor conditions. In these tests, the proposed sensor system showed an error of about 5% for the gait cadence estimation and 3.4% for measurement of floor-induced vibrations. Moreover, the determination of floor-induced vibrations and gait cadence can be made using adaptive filtering with additional possibilities of using classifiers or machine learning approaches in order to obtain and classify the sensors responses according to each functionality.

Considering all the functionalities the FBGs array can substitute many of the sensors used on SW instrumentation, including force sensors, LRF (for legs detection) and accelerometers, which result in a much more compact system, since all these sensors are substituted to a single piece a POF. In addition, the substitution of the aforementioned sensors to a POF also reduces the cost of the sensor system, since all the sensors are integrated in the same fiber, which only needs a light source, optical circulator and spectrometer,

instead of two 3D force sensors and LRF that can be very expensive (the cost of a single 3D force sensors is similar to a commercial FBG interrogator). As the sensor system is based on a passive optical component, the use of FBG arrays also results in lower power consumption for the sensor system, where the only elements that require power consumption are the spectrometer and light source (maximum consumption of 400 mA each), whereas the sensor system used for comparison has a consumption of about 1200 mAh. It is worth to mention that the power consumption of 1200 mAh considers the whole system (sensors and CPU board for sensors signals acquisition). Figure 6-56 summarizes the implementation and functionalities of the FBGs array on SW instrumentation. In this case, there is also the sensory information sent cloud for remote health monitoring applications and for cloud robotics, as the control commands for the SW can be received through the cloud using a secured connection [198] considering the data regarding the SHM of the walker, the localization of the healthcare device as well as gait cadence and movement intention of the user. For the many functionalities analyzed and foregoing the advantages of using FBGs arrays on the instrumentation of healthcare devices, one can envisage the widespread of these sensor approaches in novel remote health monitoring and cloud robotics applications.

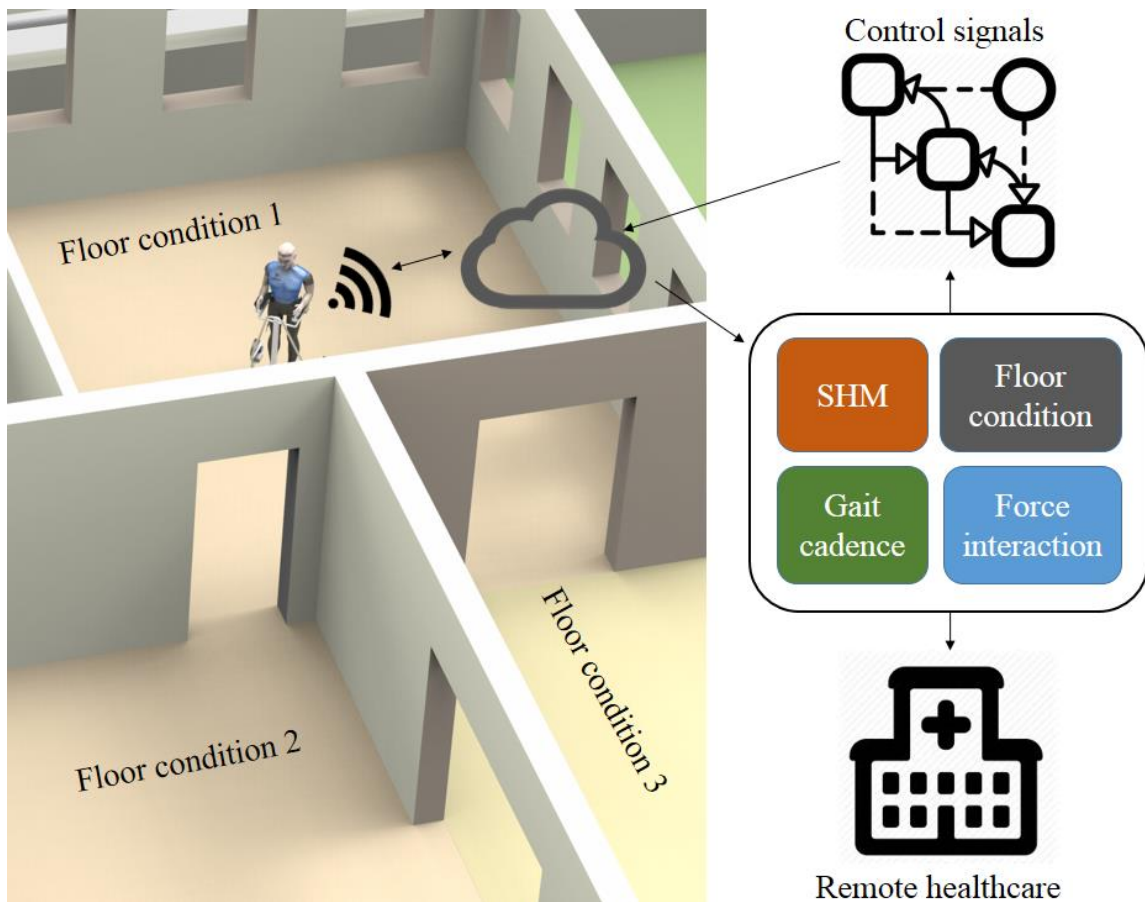


Figure 6-56 Schematic representation of the SW implementation in a structured environment using the proposed FBG array for instrumentation of healthcare devices.

## 6.5. Final Remarks

This Chapter has presented applications of POF sensors (intensity variation- and FBG-based) in healthcare devices, namely a lower limb exoskeleton, a SEA and a smart walker. In addition, an insole for movement analysis was also proposed.

The sensors proposed in Chapter 4 enable the plethora of applications in healthcare devices shown in Section 6.2, which cover from instrumented insoles through SW's instrumentation with many applications in robotic exoskeletons, orthosis and even in FES systems. In addition, the reliable FBG sensors proposed in Chapter 5 were applied on the ALLOR for human-robot interaction force assessment by means of embedding a FBGs array in flexible structures, which shows an advantage of POFs for sensors applications, since it can be easily embedded in different structures using readily available 3D printing techniques. The application of the FBGs array in the SEA's spring shows the complementary advantages of this sensing technology as it was possible to obtain a quasi-distributed measurement on the device using a compact sensor. This application also

enables novel functionalities for the instrumentation system, since it was possible to obtain reliable measurements through the sensor fusion between the 8 FBGs positioned on the spring, shape reconstruction of the actuator under flexion/extension and rejection of mechanical disturbances on the actuator that can harm its control. Finally, the SW instrumentation via FBGs array shows advantageous features, since it can provide a multiparameter sensing using a single piece of CYTOP fiber. In this analysis, it was possible to measure the strain on the SW's mechanical structure, detection of the user's movement intentions, temperature measurements, gait cadence and also was possible to provide a localization and mapping in a structured environment. Thus, a single FBG array was able to obtain the functionalities of almost all sensors in the SW, since, in this device, the gait cadence is estimated with the LRF, the movement intention with two 3D force sensors and the localization can be made with a LIDAR.

## Chapter 7. Conclusions and Future Works

### 7.1. Summary

The goal of this Thesis was to provide novel instrumentation approaches for healthcare devices, especially gait assistance devices, using POF sensors. The motivation of this work (as described in Chapter 1) is some of the limitations of conventional electronic sensors, which include electromagnetic sensitivity, necessity of precise assemblies (increasing the system's complexity and weight) and, in most cases, the inability of being embedded or positioned in flexible structures. These disadvantages are undesirable for the rigid robots used in the sensors validation of this Thesis and specially undesirable for soft robotics, where the robots' structures and actuators are made with flexible materials, which is a trend on wearable systems [31] and assistive devices [54]. Thus, the proposed sensors are compared with the electronic ones in their best operation conditions (precisely assembled and aligned in rigid structures), where the electronic sensors present high accuracy and can be used as a reference for the comparison with the proposed POF sensors. In this way, another contribution of this work is to show that the POF-based sensors present low errors when compared with electronic sensors in their best conditions for operation. Nevertheless, as mentioned above, POF sensors can also be applied in flexible structures in which potentiometers and encoders cannot be employed with the same precision. In this case, intensity variation-based POF sensors were used due to: (i) their low cost (in some cases, even lower than the ones of electronic sensors for the same performance), (ii) ease of implementation, since the sensor system only needs low cost LEDs and photodetectors; and (iii) simplicity on the signal processing, since the only acquired signals are the analog response of the sensors. Furthermore, as the advances of grating inscription in POFs as well as novel portable and low relative cost FBG interrogators occur, FBG sensors were also explored in this Thesis taking advantages of the high multiplexing capabilities and wavelength-encoded data. The later offers a crucial advantage (especially when compared with intensity variation-based sensors) as the data is an absolute quantity and immune to light source power deviations.

In order to achieve the mentioned goals, first, a theoretical background and state of the art review of both intensity variation-based POF sensors and POFBG sensors are presented in Chapter 2. In addition, the fundamentals and overview of optical fibers, particularly POFs, are also depicted in this Chapter. Then, the robotic devices used on the sensors' applications are described. Thus, Chapter 2 provides the knowledge required for the developments proposed in the following chapters.

Then, in Chapter 3, the dynamic characterization of POF materials is presented, where the materials characterized are PMMA (for intensity variation-based sensors) and CYTOP (for FBG sensors). This Chapter is the cornerstone of the works is presented in the remainder of the Thesis, since Chapter 3 presents the foundation of all the compensation techniques for enhancing or even creating the innovative sensors presented in Chapter 4 and Chapter 5. In this case, creep response, temperature and frequency dependency as well as humidity dependency of PMMA complex modulus are thoroughly discussed. Moreover, the assumptions of material-related hysteresis in POF sensors are also confirmed by means of sequential stress-strain cycles. Another contribution of this chapter is on the characterization of the CYTOP fibers with and without FBGs, which not only serves as basis for the development of the FBG sensors in Chapter 5, but also indicates the advantages of the fs laser inscription as the FBG inscription with this method only leads to minor deviations on material properties (unlike the FBG inscription using CW or nanosecond UV lasers [142]).

In Chapter 4, the development of intensity variation-based sensors is presented. Firstly, using the background provided by Chapter 3, compensation techniques for undesirable effects (hysteresis and nonlinearities) of POF sensors are proposed and validated. It is noteworthy that the background and fundamentals provided by Chapter 3 also enables the development of temperature and humidity sensors based on stress-optic effects on the fiber under torsion and similar approach was made to propose a novel torque sensor, which was applied in a SEA's spring. Since one of the drawbacks in intensity variation sensing approaches is the lack of multiplexing capabilities, a cost-effective multiplexing technique was also proposed in this chapter, which was validated at quasi-distributed and multiparameter scenarios.

Chapter 5 presented the development of FBG sensors inscribed in CYTOP fibers through direct write plane-by-plane inscription method using an fs laser (centered at 517 nm). In this case, compensation techniques (based on the results of CYTOP characterization in Chapter 3) as well as thermal treatments for the fiber were made and the performance enhancement using these techniques were verified for strain, temperature and force applications. The temperature effects on force sensing using FBGs were also compensated and the dynamic effects on different frequencies were evaluated and compensated for FBG-based curvature sensors.

Regarding the applications, besides the aforementioned spring, it was also proposed the complete instrumentation of the ALLOR with sensors for human-robot interaction forces assessment and joint angle measurements as depicted in Chapter 6. After the positive feedback of the multiplexing technique proposed in Chapter 4, a 3D-printed insole was proposed with 15 independent sensors. The proposed insole not only is a low-cost and highly customizable device (due to the materials and methods employed), but also is the insole with optical fiber sensing technology with the highest number of sensors, where the number of sensors on the proposed insole is more than two times higher than the ones of the FBG-based insole proposed (6 sensors [218]). Thus, in this specific case, and regarding the multiplexing capabilities, the proposed multiplexing technique outperforms FBGs, where FBGs are regarded as gold standard for spatial resolution and multiplexing capabilities among optical fiber sensors. Nevertheless, the developments and breakthroughs in FBG sensors shown in Chapter 5 have led to the applications of FBG sensors in assistive devices, where the force sensors were embedded in 3D-printed flexible structures for human-robot interaction forces assessment and FBG arrays were applied in SEA's spring and SW. In every proposed application, the multiplexing capabilities of FBGs were considered for multipoint (in the SEA's spring) and multiparameter (in SW) measurements. In all analyzed scenarios, the application of FBG arrays resulted in either higher precision of the sensor system or the increasing of compactness and reduction of the cost per sensor in a healthcare device, with the additional advantage over intensity variation-based sensors regarding the wavelength-encoded data, which is insensitive to light source power fluctuations.

## 7.2. Future Works

This Thesis paved the way for a multitude of applications in healthcare devices as well as novel sensing approaches taking into account the material mechanical properties. For these reasons, many research fields and future works are available on each of the 3 keystones of the Thesis (material characterization, intensity variation-based sensors and FBG sensors), many of these works are already under investigation.

The future works perspectives for the material characterizations shown in Chapter 3 are listed as follows:

- Characterization of POFs with different materials;
- Characterization of novel 3D-printed POFs;
- Development of new polymer optical fibers using environmental-friendly techniques;
- Investigation of POF mechanical properties after the FBG inscription using UV nanosecond pulsed and CW lasers;
- Investigation of the UV radiation influence on the material response of different POFs;
- Analysis of different dopants for POFs and their influence on the material properties under different conditions of UV radiation;
- Analysis of the POF fabrication parameters such as pulling force and extrusion temperature and their influence on POF viscoelastic response;
- Characterization of photoelastic constant and thermo-optic coefficients in different POFs.

The future works involving intensity variation sensors (Chapter 4) are listed below:

- Analysis of intensity variation-based sensors under higher frequency regime;
- Intensity variation-based sensors in acoustic and ultrasound applications;
- Low cost biochemical sensors based on POF material features;
- Novel applications in healthcare devices;
- Applications in soft robotics;
- Investigations of tendon-driven actuators using POFs;
- Development of 3D sensors for movement analysis
- Further applications of the proposed multiplexing technique for POF intensity variation-based sensors.

Finally, regarding perspectives of future works using FBGs inscribed in POFs:

- Application of the compensation approaches in non-uniform gratings;
- Development of novel portable and low cost FBG interrogators;
- Smartphone integration with FBG sensors;
- Applications of the FBG-based curvature sensor in robotics and movement analysis;
- Investigations of the spectral response of FBGs under different loading conditions for innovative sensing solutions;
- Novel cost-effective techniques for grating inscription.

## Appendix A. Analytical Model for Intensity Variation POF Sensors Based on Macrobending

This section presents an analytical model for dynamic bending of a POF, which is based on the geometrical optics approach combined with the stress-optic analysis and viscoelastic models. The validation is performed for the dynamic bending case with two different experimental setups: one using a goniometer for quasi-static tests and another using a servomotor for dynamic measurements. Moreover, the analyzed POF curvature sensors have different lateral section parameters and are analyzed under different angular velocities. The analysis of different POF sensors in different experimental setups and different dynamic conditions prove the robustness of the model.

### Geometric optics Model

A typical macrobending-based POF sensor employs a POF with a lateral section, which creates a sensitive zone to increase the sensor sensitivity and linearity of the signal attenuation when the fiber is bending. As the bending occurs, the incident angle increases and creates a variation on the transmission mode. When the sensitive zone of the fiber is bending, there are more losses due to the absence of the cladding in that region, increasing the radiation losses. Another source of loss is the surface scattering caused by the coupling between higher and lower guided modes [161].

Figure A-1 shows the fiber geometry considered in the POF sensor modelling. This figure is out of scale, since the diameter of fiber core is not much smaller than the cladding part as observed in practical perspective. The sensitive zone along the curvature region is represented by the section length given by  $c$ . The polished side with section depth of removed material on the fiber core is denoted by  $p$ . The optical fiber length in Figure A-1 is given by  $L$ , meanwhile the optical fiber diameter is  $d$ , and the curvature radius is  $R$ . This will compose the sensitive zone for sensing the curvature.

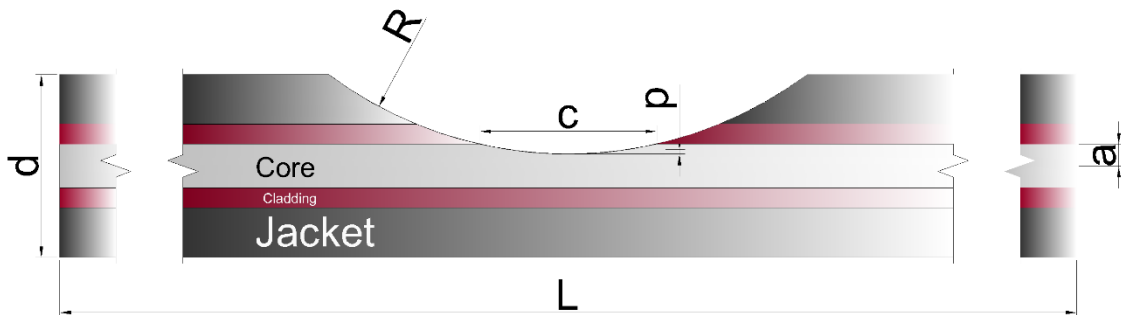


Figure A-1 Section view of the POF sensor analyzed.

The optical power coupled to the POF sensor is modeled under geometrical optics concepts, as considered by [219], and written as:

$$dP = 2\pi L_0 \cos(\theta) \sin(\theta) d\theta dS, \quad (\text{A.1})$$

where  $(dP)$  is an element power radiated into a solid angle  $d\Omega$  subtended by a section  $(dS)$  at an angle  $(d\theta)$ .

$L_0$  is the light source radiance. The integration of Eq. A.1 over the cross-sectional area gives the input power of the model. Equation A.2 presents the result of this integration, where  $a$  is the optical fiber core radius, and  $\theta_c$  is the critical angle.

$$P_{in} = \pi^2 L_0 a \sin^2(\theta_c) \quad (\text{A.2})$$

Assuming uniform mode distribution, where the light source has constant radiance, it can be defined [220] from the parameters of Figure A-1, the difference of the fiber core cross sectional area ( $S_c$ ) and the maximum area of removed material ( $S_o$ ) as in Eq. A.3.

$$S_C - S_o = \frac{\pi a^2}{2} + a^2 \arcsin\left(\frac{a-p}{a}\right) + (a-p)\sqrt{a^2 - (a-p)^2} \quad (\text{A.3})$$

Equation A.3 defines the cross section of the sensitive zone, which is critical for the evaluation of the optical fiber sensitive zone power ( $P_S$ ).  $P_S$  can also be defined as the remaining power when it enters the sensitive zone, i.e.,

$$P_S = \pi L_0 (S_C - S_o) \sin^2(\theta_c). \quad (\text{A.4})$$

Furthermore, a loss of power due to partial transmission can occur when the light meets the side-polished interface [220]. Since this is a dielectric media, the losses are calculated through the Fresnel's equations and the reflection coefficient ( $r_T$ ) for an unpolarized light as presented in Eq. A.5:

$$r_T = \frac{(r_{PP}^2 + r_{PL}^2)}{2}, \quad (\text{A.5})$$

where  $r_{PP}$  is reflection of the perpendicular rays defined in Eq. A.6 and  $r_{PL}$  is the reflection of parallel rays defined in Eq. A.7. Referring to Eq. A.6 and Eq. A.7,  $\theta_p$  is the angle of propagation and  $n_C$  is the POF core refractive index.

$$r_{PP} = \frac{\sin(\theta_p) - \sqrt{\frac{1}{n_C^2} - \cos^2(\theta_p)}}{\sin(\theta_p) + \sqrt{\frac{1}{n_C^2} - \cos^2(\theta_p)}} \quad (\text{A.6})$$

$$r_{PL} = \frac{\frac{1}{n_C^2} \sin(\theta_p) - \sqrt{\frac{1}{n_C^2} - \cos^2(\theta_p)}}{\frac{1}{n_C^2} \sin(\theta_p) + \sqrt{\frac{1}{n_C^2} - \cos^2(\theta_p)}} \quad (\text{A.7})$$

Considering multiple reflections can be observed inside the sensitive zone of the fiber, the number of internal reflections ( $N$ ) is the closest integer number obtained by Eq. A.8.

$$N = \frac{c \tan(\theta_p)}{2(2a - p)} \quad (\text{A.8})$$

The combined effect of the power losses when the rays enter the sensitive zone and the losses due to the reflected rays results in POF sensor output power ( $P_o$ ) defined in Eq. A.9.

$$P_o = \pi L_0 (S_C - S_o) \int_0^{\theta_c} r_T^N \cos(\theta) \sin(\theta) d\theta \quad (\text{A.9})$$

Equation A.9 shows the output power for a fiber without bending. In order to account the bending, the integral upper limit has to be corrected to evaluate the effect of the fiber bending by a certain angle. The fiber has a decrease on its numerical aperture when it is bending and the output signal decreases. The angle corrected by the fiber bending ( $\theta_b$ ) is defined in Eq. A.10 for a concave sensitive zone.

$$\theta_b = \theta_c \sqrt{1 - \frac{2a}{R\theta_c^2}} \quad (\text{A.10})$$

By relating the ratio between the input and output power before and after bending the fiber with respective parameters and characteristics, it is possible to obtain (Eq. A.11):

$$\frac{P_o}{P_i} = \frac{(S_C - S_o) \sin^2(\theta_b)}{S_C \sin^2(\theta_c)}. \quad (\text{A.11})$$

Analyzing Eq. A.11 together with Eq. A.3 and Eq. A.10 it is possible to see that only the curvature radius ( $R$ ) will increase or decrease depending upon the positive or negative bending and the bending angle. Therefore, such expression relies only on the curvature radius, which may not be an adequate approach for dynamic measurement and for a sensor under stress or strain condition due to viscoelastic effects thoroughly discussed in Chapter 3.

### Stress-optic effects modelling

The model does not include any effect of the load on the fiber. When the fiber is bending there is a symmetric second-rank stress tensor with six independent variables acting on it [162]. Moreover, the elements of the tensor are not constant due to the viscoelasticity of the POF material. Viscoelastic material has a relationship between stress and strain varying with time due to its molecular rearrangement, which dissipates part of the accumulated energy leading to a time varying tensor [59]. Therefore, the viscoelastic effect has to be taken into account on the stress-optic analysis. In addition, some assumptions have to be made for the stress-optic analysis. First, the second-order effects due to temperature changes are neglected. Furthermore, the model is valid only for step-index POF, which is also considered transparent, homogenous, and isotropic [162]. Although there are minor differences between the optical behavior along the fiber and perpendicular to it due to the anisotropy induced on the fabrication processes, these differences for a PMMA fiber are not very large and are difficult to measure [221].

The stress-optic effect is described by a second-rank tensor ( $\Delta B_i$ ) to represent the changes of coefficients in optical indicatrix under the action of the bending stress [162]. Equation A.12 defines the stress-optic relation aforementioned.

$$\Delta B_i = q_{i,j} \sigma, \quad (\text{A.12})$$

where  $\sigma$  is the stress,  $q_{i,j}$  is the stress-optical tensor, which is a fourth-rank tensor with 36 components. However, the isotropy assumption reduces the number of independent variables to only two ( $q_{11}$  and  $q_{12}$ ). The values of the elements of the stress-optical tensor depends on the material of the fiber core and it can be measured through the experimental setup presented in [222]. Equation A.13 shows the stress-optic tensor for the symmetry conditions obtained in an isotropic material assumption.

$$q = \begin{bmatrix} q_{11} & q_{12} & q_{12} & 0 & 0 & 0 \\ q_{12} & q_{11} & q_{12} & 0 & 0 & 0 \\ q_{12} & q_{12} & q_{11} & 0 & 0 & 0 \\ 0 & 0 & 0 & q_{11} - q_{12} & 0 & 0 \\ 0 & 0 & 0 & 0 & q_{11} - q_{12} & 0 \\ 0 & 0 & 0 & 0 & 0 & q_{11} - q_{12} \end{bmatrix} \quad (\text{A.13})$$

Although the fiber has a shear stress component, most of the stress acting on it is an axial stress. Therefore, in order to simplify the stress tensor, it is possible to apply a correction on the Young's modulus of the material

to cover the effects of the shear stress [223]. Equation A.14 shows the expression for the corrected Young's modulus for shear stress.

$$E^* = E_a^* \left[ 1 + \frac{6}{5} (2 + \nu^*) \left( \frac{d}{L} \right)^2 \right], \quad (\text{A.14})$$

where  $E^*$  is the corrected dynamic Young's modulus,  $E_a^*$  is the uncorrected Young's modulus,  $\nu^*$  is the material Poisson ratio,  $d$  and  $L$  are defined in Figure A-1 and represent the fiber diameter and length, respectively. However, the fiber length generally is some orders of magnitude higher than the fiber diameter. For this reason, the quadratic term in Eq. A.14 is almost zero. Since the Poisson ratio of the materials typically lie on the range 0.3 to 0.5, the second term of the summation continues to be close to zero. Hence, the corrected Young's modulus is close to the uncorrected one. In addition, the stress tensor depends on the load condition on the fiber. One considers the fiber under a bending stress with the configuration of Figure A-2.

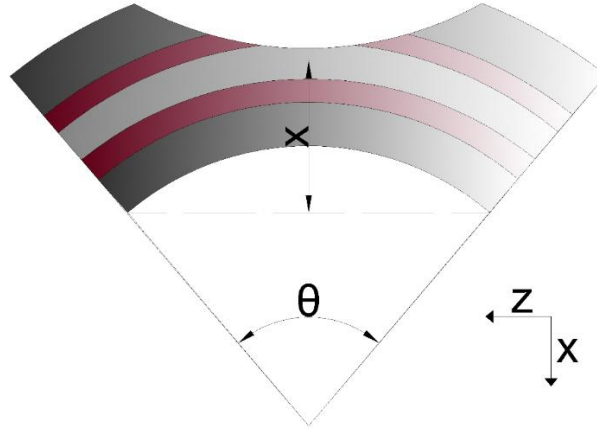


Figure A-2 Polymer optical fiber under the bending stress condition.

Regarding Figure A-2,  $x$  is the distance between the bending part to the neutral line, and  $\theta$  is the bending angle. For this stress condition, the only component of the tensor different from zero is the axial stress on the  $z$  direction. The multiplication of the stress tensor and the stress-optical tensor gives the following results for  $\Delta B_i$  (Eq. A.15-Eq. A.18).

$$\Delta B_1 = q_{12} \sigma(t) \quad (\text{A.15})$$

$$\Delta B_2 = q_{12} \sigma(t) \quad (\text{A.16})$$

$$\Delta B_3 = q_{11} \sigma(t) \quad (\text{A.17})$$

$$\Delta B_4 = \Delta B_5 = \Delta B_6 = 0 \quad (\text{A.18})$$

In this case,  $B$  is defined as Eq. A.19 [162].

$$B = \frac{1}{n_c^2} \quad (\text{A.19})$$

The combination of Eq. A.15-Eq. A.19 result in the variation of the refractive indexes  $\Delta n_x$ ,  $\Delta n_y$ , and  $\Delta n_z$  for the bending condition (Eq. A.20-Eq. A.22).

$$\Delta n_x = \frac{n_c^3 q_{12} \sigma(t)}{2} \quad (\text{A.20})$$

$$\Delta n_y = \frac{n_c^3 q_{12} \sigma(t)}{2} \quad (\text{A.21})$$

$$\Delta n_z = \frac{n_c^3 q_{11} \sigma(t)}{2} \quad (\text{A.22})$$

As discussed in [59], the Maxwell model is the simplest among the differential models. Moreover, it can predict the response of a POF with good degree of approximation [156]. In the Maxwell model, the total strain ( $\varepsilon$ ) is the sum between the strain due to the elastic effects and the one due to viscous effects. Equation A.23 shows the variation of the strain with time.

$$\frac{d\varepsilon}{dt} = \frac{1}{E^*} \frac{d\sigma}{dt} + \frac{\sigma}{\eta}, \quad (\text{A.23})$$

where  $E^*$  is the Young's modulus, and  $\eta$  is the polymer viscosity. However, the strain is kept constant and the polymer viscosity is a multiplication between the Young's modulus and the polymer time constant [156]. Hence, substituting the viscosity term and solving the differential equation (Eq. A.23) for constant strain yields in Eq. A.24 as follows:

$$\sigma(t) = \sigma_0 \exp\left(\frac{-t}{\tau}\right), \quad (\text{A.24})$$

where  $\tau$  is the time constant and  $\sigma_0$  is the initial stress. The time constant can be obtained from an exponential fit of the fiber response. In the pure bending stress case, the initial stress is calculated in Eq. A.25.

$$\sigma_0 = -\frac{E^* x}{R} \quad (\text{A.25})$$

The Young's modulus of a viscoelastic material has two components: elastic or storage component and the loss modulus. The dynamic Young's modulus is the summation of the two components (Eq. A.26).

$$E^* = E_0 \cos(\delta) + iE_0 \sin(\delta), \quad (\text{A.26})$$

where  $E_0$  is the static Young's modulus and  $\delta$  is the phase shift between the input stress or strain and the viscoelastic response.

Substituting Eq. A.26, Eq. A.25 and Eq. A.24 in Eq. A.20-Eq. A.22, it results in the refractive index variation of a POF under a bending stress condition, which can be substituted in Eq. A.10 and Eq. A.11 to provide the attenuation on the optical signal in a fiber during the bending. The jacket of the fiber does not have any influence on the optical part of the model. Moreover, the cladding part also does not have a major importance on the model derived in this section due to its small diameter compared with the core [162].

## Experimental validation

The model presented in previous sections is validated. In order to show the robustness of the model, two different setups for two different tests are made. First, the results for a quasi-static test are shown, and then, the results are presented for a dynamic test.

### Quasi-static tests

The quasi-static test is made by fixing a multimode HFBR-EUS100Z POF (Broadcom Limited, Singapore) step-index PMMA POF on a plastic goniometer through 3D printed supports. The test comprises of bending the fiber on sequential  $10^\circ$  steps for flexion in  $0-90^\circ$  range. The fiber remains on the desired angle for 10 seconds. However, the test bench applied in this case is a goniometer with supports for the fiber. The samples were fabricated with section depth of 0.7 mm and section length varying from 5 mm to 40 mm on 5 mm steps interval. It is important to notice that the fiber lateral section is made taking into account the core, cladding and jacket parts of the fiber. Therefore, the presented section depths are made with respect to the fiber jacket.

Three consecutive tests were made for each sample. In these tests, the best and worst results are discarded. In order to simplify the analysis and avoid the electrical circuit modeling, the output signal of the experiments is normalized with respect to the signal of the fiber in straight position (no bending). The same procedure is made on the calculated values.

The POF sensor output is calculated by substituting the fiber parameters in Eq. A.3, the critical angle is obtained by the well-known Snell's law. Since the refractive index changes with the fiber bending, the core refractive index value is updated in every model iteration. The changes in core refractive index is obtained by the parameters in Eq. A.26, Eq. A.25, and then Eq. A.24 to obtain the stress on the fiber. Furthermore, the resultant stress is substituted in Eq. A.22 to obtain the refractive index of the core in this iteration. After obtained the updated critical angle, this result has to be substituted in Eq. A.10. Finally, the results in Eq. A.10, Eq. A.3, and the fiber parameters are substituted in Eq. A.11 to obtain the sensor output power. Table A-1 shows the fiber parameters applied on the calculation. These parameters are obtained in components datasheet and reference works [162] and [102].

The time constant and the phase shift are calculated in each test. The results showed a variation of the time constant, its minimum value is 0.008 for the fiber with 5 mm lateral section length and its maximum value is 0.013 for the fiber of 40 mm lateral section length. The analysis of the time constant show a linear increase of its value with the increase of the section length. The phase shift analyzed for each sample does not lead significant variations to the dynamic Young's modulus, the cosine of the phase shift of every test was higher than 0.98. Therefore, for this test, the dynamic Young's modulus value can be approximated as the static Young's modulus.

Table A-1 POF sensor parameters

Symbol	Parameter	Value
$a$	Fiber core radius	0.49 mm
$n_c$	Core refractive index	1.492 RIU
$n_{cl}$	Cladding refractive index	1.417 RIU
$p$	Lateral section depth	0.3 mm
$E_0$	Static Young's modulus	3.09 GPa
$q_{11}$	Stress-optical coefficient	$10^{-11} \text{ Pa}^{-1}$

The model obtained good results for each sample analyzed. The correlation coefficient ( $R^2$ ) is  $0.9913 \pm 0.0070$ . The found worst correlation coefficient was 0.9788 for the sample with 40 mm lateral section length. The loss of precision of the model in this case may be due accumulation of errors of the sample sensitive zone manufacture process, which can make the lateral section deviate in its depth and length and errors provided by the test itself. Since the process is made manually, some errors on the goniometer position or in the time that the fiber remains on the position may occur. The best correlation coefficient obtained was 0.998 for the fiber with 25 mm section length (see Figure A-3).

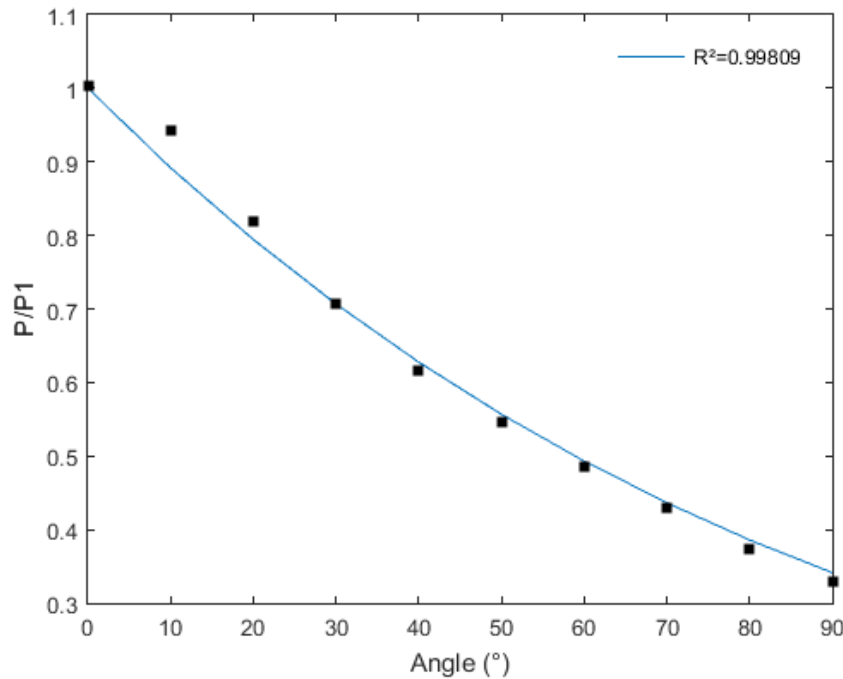


Figure A-3 Results for the quasi-static test of the POF with 25 mm section length.

## Dynamic tests

The test comprises in bending the fiber for flexion and extension in 0-100° range. In this case, USB-6008 board (National Instruments, USA) makes the signal acquisition and the sample rate is 1 kHz. In order to validate the model under different dynamic parameters, the test was made with 11 different angular velocities, which were: 0.034 rad/s, 0.0426 rad/s, 0.0561 rad/s, 0.086 rad/s, 0.1105 rad/s, 0.1656 rad/s, 0.1959 rad/s, 0.262 rad/s, 0.3906 rad/s, 1.5 rad/s, and 2.9 rad/s. It was made three flexion/extension cycles in each velocity. The POF employed in these tests has lateral section of 12.48 mm and depth of 0.66 mm.

A good repeatability of the time constant and the phase shift was found, these parameters remain almost constant when the bending of one cycle is compared with the bending of the other cycle. However, the time constant and the phase shift are not constant in flexion and extension. The variation of these parameters is one of the causes of the hysteresis in flexion/extension analysis. Furthermore, the phase shift on the flexion is small, therefore the cosine of the phase shift is approximately 1 and the sine is about 0, in this case it is a good approximation to define the dynamic Young's modulus equal to the static Young's modulus. However, when the extension movement is occurring this approximation is not valid due to the higher values of the phase lag. Hence, besides the difference between the time constant of flexion and extension, the hysteresis of POF response is also due to the phase lag difference between the flexion and extension movements.

The methodology used to calculate the fiber response is the same as presented in quasi-static tests. The fiber parameters are also the same as presented in Table A-1. Since the test bench provides higher repeatability of the test and almost eliminates the position errors, the correlation coefficient of the dynamic test is higher than the one obtained on quasi-static tests. The obtained correlation coefficient is  $0.9938 \pm 0.0014$ . Furthermore, the standard deviation decreases, which proves the higher repeatability of the method. However, the dynamic tests' results show that the model presents lower hysteresis than the hysteresis measured. This may be due to the oversimplification of the Maxwell's model. Furthermore, the model estimates a lower response for the 100° angle than the one measured. This happens due to the saturation trend of the sensor when the bending angle is higher than 90°, which is not considered by the model. In order to illustrate the dynamic response characteristics aforementioned, a test comprised of five flexion/extension cycles with angular velocity of 1.5 rad/s was made (see Figure A-4).

The analytical models previously presented for POF curvature sensor with sensitive zone are applicable only to static measurements [175], [219], [220]. Furthermore, it presents errors higher than the ones obtained on the analytical model proposed. The error was analyzed only in [220], which presented errors on different sensitive zone length and depth of about 3%, whereas the error of the analytical model for proposed dynamic bending is below 3% on the worst case among the range analyzed (0.034 rad/s). Therefore, besides the possibility of apply this model in dynamic measurements, it also show an error lower when compared to the

analytical model presented in [220]. The model presented in this Section is the basis for the development of the intensity-variation sensors of subsequent Section. In addition, the errors reported on hysteresis estimation also indicate the necessity of using the knowledge and data obtained in the fiber's dynamic characterization (see Chapter 3) for the development of not only the compensation techniques presented in Section 4.2, but also on the microclimate and force sensors developed in Chapter 4.

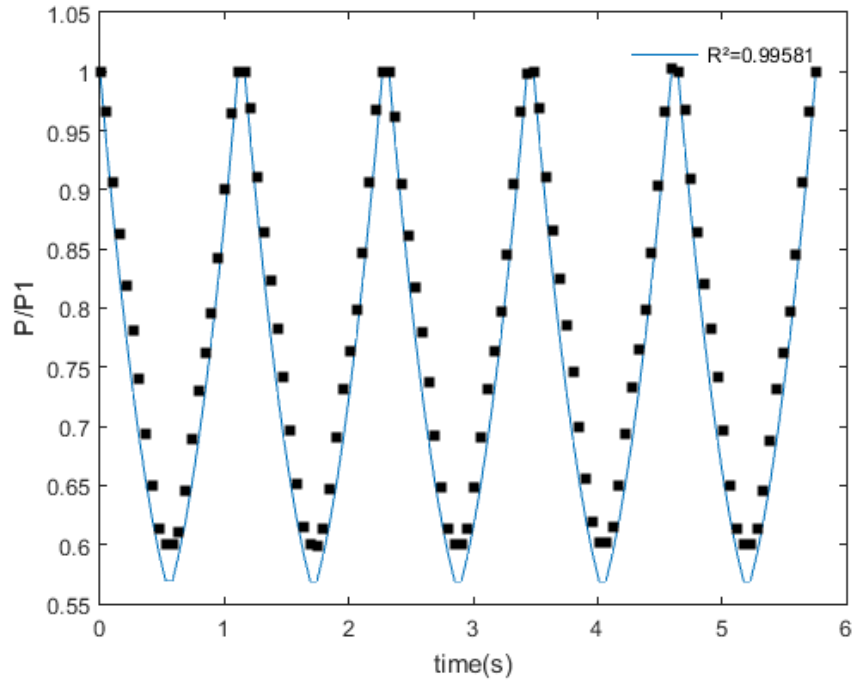


Figure A-4 Calculated and measured values for five cycles of POF flexion and extension with 1.5 rad/s.

## Appendix B. Sensitive Zone Parameters Evaluation

The lateral section parameters influence the sensor performance. Different section length, depth, and surface roughness provide different sensitivity, hysteresis, and linearity on POF sensors. Furthermore, if the fiber is under stress, there is also the stress-optical effect, which causes a variation of the POF refractive index and leads to higher signal attenuation [162]. For this reason, the sensor curvature radius may also have influence on the sensor sensitivity, hysteresis and linearity due to the stress increase and viscoelastic effects. In order to understand each parameter influence, this section presents a thorough study of the lateral section parameters of a POF sensor with continuous sensitive zone. Moreover, analysis of the mechanical supports of the sensor are made by positioning the supports in different distances of the fiber center of curvature shown in Appendix A. The investigation is based on experimental results for POF curvature sensor with different section length, depth, surface roughness, and curvature radii. The sensor is bent dynamically in angles between 0 and 90°. The sensor performance is evaluated with respect to the sensitivity, hysteresis, and linearity. The objective is to introduce guidelines for the choice of lateral section parameters and curvature radius. Furthermore, it presents a sensor response prediction in a POF based curvature sensor with sensitive zone.

The dynamic test is made by fixing a multimode HFBR-EUS100Z POF (Broadcom Limited, Singapore) with step index profile (the same as Appendix A) on the test bed shown in Figure 4-2. The test comprises of bending the fiber for flexion and extension in 0-90° range. The fiber is bent on a constant angular velocity of about 0.095 rad/s. The bending angle is acquired by a potentiometer and the motor has a closed loop position controller. As the bending occurs, the light attenuation increases due the fiber curvature. The light variation is acquired by the photodiode (PD) IF-D91 (Industrial Fiber Optics, USA). The light source is a low cost 3 mW@650 nm laser. A National Instruments USB-6008 board makes the signal acquisition and its sample rate is 1 kHz. Since possible fluctuations in the light source, temperature and humidity can lead to undesired response of the sensor, a reference fiber is applied to compensate such variations. Therefore, the sensor response is normalized with respect to the reference fiber response. In this compensation technique, the laser provides light for both fibers and these fibers are further split into the reference and transducer fibers through the light coupler (LC) IF-562 (Industrial Fiber Optics, USA). Figure B-1 shows block diagram of the experimental setup described.

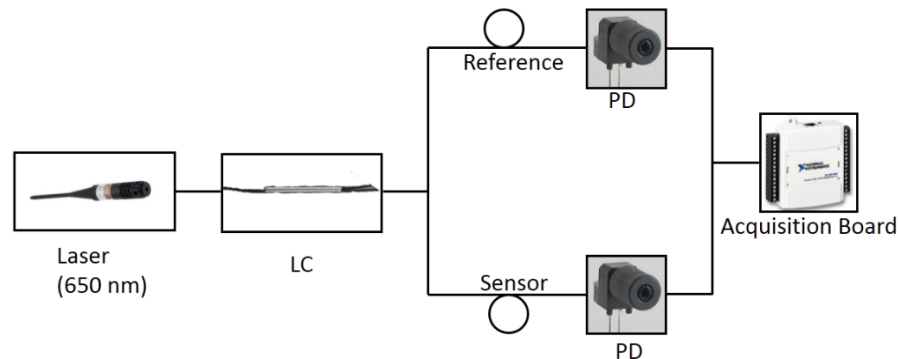


Figure B-1 Experimental setup for dynamic test of the optical fiber curvature sensor.

The fiber sensitive zone is created through abrasive removal of material. In other words, a sandpaper with controlled grain size is connected to a rotary tool, which is used to create the continuous section on the fiber. The process to obtain desired section length and depth comprises of positioning the POF on a fixed support, there is another part over this support, which limits the rotary tool advancement to the desired length and depth of the POF sensor (controlled support). The employed sandpaper grit sizes were 80, 120, 220, 320, 400, 600, and 800. Furthermore, the POF sensitive zone length tested were 3.25 to 31.66 mm. Upper and lower limits are chosen due to the rotary tool limitation and high attenuation on larger sensitive zones, respectively. In addition, the POF sensitive zone depth tested were 0.6 to 1.1 mm in 0.1 mm steps interval. The lower limit of 0.6 mm is because the fiber has a polyethylene jacket and the lowest section depth to achieve the fiber core is 0.6 mm. Since the POF total diameter is 2.2 mm, the upper limit is 1.1 mm because the fiber is very fragile in higher section depths and can break in high bend angle. Figure B-2 shows the equipment employed to create the POF sensor sensitive zone.

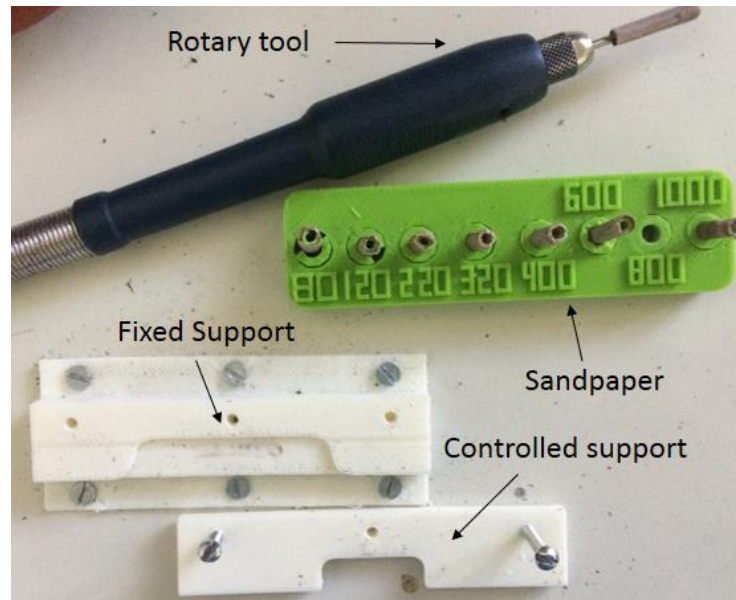


Figure B-2 Equipment to create the POF sensor sensitive zone.

Three sets of samples were created. The first one (sample 1 to 7) has the section depth of about 0.6 mm and section length varying to 3.25 mm to 31.66 mm in approximately 5 mm steps with the sensitive zone created with a sandpaper grit size of 220. The second set of samples (sample 8 to 13) has the section length of about 25 mm and section depth varying to 0.6 mm to 1.09 mm in about 0.1 mm steps with the sensitive zone created with a sandpaper grit size of 220. Finally, the last set of samples (sample 14 to 20) presents a length of about 22 mm and depth close to 0.7 mm. In this case, the sandpaper grit size varies to create samples with different surface roughness. Since the sensitive zone parameters defined above are created with respect to the polyethylene jacket, Table B-1 shows the measured parameters of each sample manufactured with respect to the fiber jacket. The sensitive zone parameters are analyzed with respect to the core due to its influence on the response of the sensor. The analysis of the sensitive zone parameters is made with a constant curvature radius of 60 mm.

As shown in Figure 4-2, the employed prototype has a series of holes to connect different mechanical supports. These supports enable the variation of the curvature radius of the sensor. The tested curvature radii were 60 mm to 25 mm in steps of 5 mm. The upper limit of the tested curvature radii is 60 mm due to the physical limits of the prototype employed, whereas the lower limit is 25 mm because it is the minimum curvature radius recommended by the fiber manufacturer. In order to isolate the effect of the sensitive zone parameters on the sensor response, the same fiber is applied in all tests. This fiber has a sensitive zone of 12.48 mm length and 0.66 mm depth with a sandpaper grit size of 220 (Sample 12 – see Table B-1).

Each sample is tested three times and the analysis are made with respect to the sensor sensitivity, hysteresis and linearity. The sensitivity is defined as the difference between the initial sensor response, when the fiber is at  $0^\circ$ , and the sensor response after the bending, when the fiber is at  $90^\circ$ , divided by the bending limits, which is  $90^\circ$  in this case (see Eq. B.1). Both initial and final sensor response are acquired in Volts (V) and the bending angle in degrees ( $^\circ$ ).

$$Sensitivity(V / ^\circ) = \frac{Po(\theta_f) - Po(\theta_i)}{\theta_u}, \quad (B.1)$$

where  $Po(\theta_i)$  is the sensor response for the lower bound of the interval in volts,  $0^\circ$  in this case, and  $Po(\theta_f)$  is the sensor response for the upper bound of the interval in volts,  $90^\circ$  in this case,  $\theta_f$  is the upper bound angle in degrees, which is also  $90^\circ$ .

Table B-1 POF Sensor sensitive zone characteristics

Sample	Length	Depth	Sandpaper grit size
1	3.25 mm	0.63 mm	220
2	7.36 mm	0.60 mm	220
3	12.48 mm	0.66 mm	220
4	16.25 mm	0.64 mm	220
5	22.13 mm	0.65 mm	220
6	26.19 mm	0.62 mm	220
7	31.66 mm	0.66 mm	220
8	18.63 mm	0.60 mm	220
9	19.80 mm	0.67 mm	220
10	21.62 mm	0.77 mm	220
11	22.41 mm	0.89 mm	220
12	22.13 mm	0.95 mm	220
13	22.06 mm	1.09 mm	220
14	22.58 mm	0.71 mm	80
15	22.23 mm	0.72 mm	120
16	22.13 mm	0.65 mm	220
17	21.33 mm	0.69 mm	320
18	21.29 mm	0.65 mm	400
19	21.82 mm	0.68 mm	600
20	21.67 mm	0.68 mm	800

The sensor hysteresis can be understood as the output signal difference due to the trajectory of the sensor movement [224]. In this case, it is the difference of the sensor response for flexion and extension cycles. For a viscoelastic material, the stress-strain response presents a hysteretic behavior for loading/unloading cycles, where the highest value of hysteresis is presented on the middle of the cycle [59]. Since the POF curvature sensor works with stress and strain applied on the fiber due to its curvature, sensor response is expected to present a similar behavior of the stress-strain curve for viscoelastic material presented in Figure B-3.  $(x_{fm}, y_{mp})$  are the points of maximum hysteresis for the loading cycle and  $(x_{em}, y_{mn})$  are the points of maximum hysteresis for the unloading cycle, which generally occurs at the middle of the cycle. For the fiber curvature case, the loading cycle is the joint flexion movement, whereas the unloading cycle is the joint extension movement.

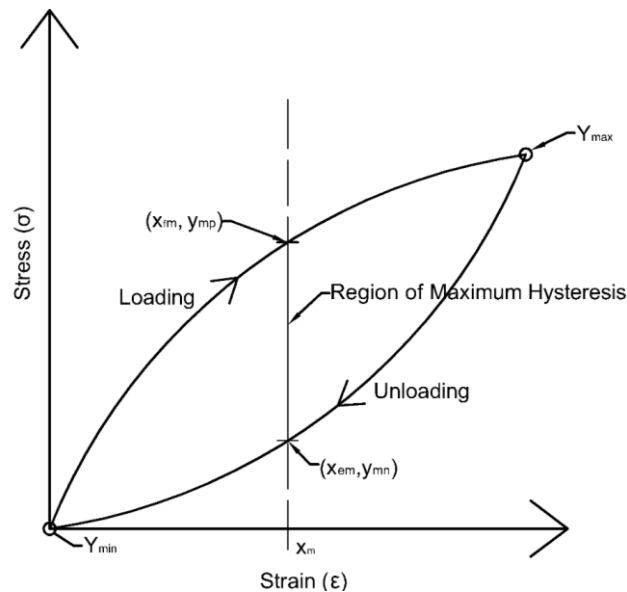


Figure B-3 Typical stress-strain curve for a viscoelastic material.

Since the maximum hysteresis for viscoelastic materials typically occurs on the middle range of the cycle, the maximum hysteresis (see Eq. B.2) is obtained through the ratio between the vertical distance of flexion and extension linear approximations curves [224].  $(y_{mn} - y_{mp})$  is the distance between the flexion and

extension curve on the middle point of the curve and  $(Y_{Max} - Y_{Min})$  is the difference between the maximum and minimum points of the sensor response presented at the stress-strain curve of Figure B-3.

$$Hysteresis(\%) = \left| \frac{(Y_{mn} - Y_{mp})}{(Y_{Max} - Y_{Min})} \right| \times 100\% \quad (B.2)$$

Furthermore, the sensor linearity is estimated as the correlation coefficient between the sensor responses to its corresponding linear regression curve. The closer it gets from one, the higher is the sensor linearity.

The presented analyses are divided in section length, section depth, surface roughness, and curvature radii. The samples 1 through 7 are the ones employed on the section length analysis. The samples 8 through 13 were applied in section depth analysis. Moreover, samples 14 through 20 are employed on the surface roughness analysis. Finally, sample 12 was applied on the curvature radius analysis.

## Sensitive zone length analysis

Three consecutive tests were made with the samples 1 through 7. Good repeatability was found for the sensitivity and linearity parameters. However, the hysteresis exhibits higher fluctuation. Therefore, the best and worst result are discarded (see Figure B-4(a) and (b)). Figure B-4(a) shows the hysteresis and sensitivity for each section length, it is possible to apply a polynomial regression with the well-known least squares method, which results on a second degree polynomial with correlation coefficient ( $R^2$ ) higher than 0.98 for hysteresis and higher than 0.94 for sensitivity.

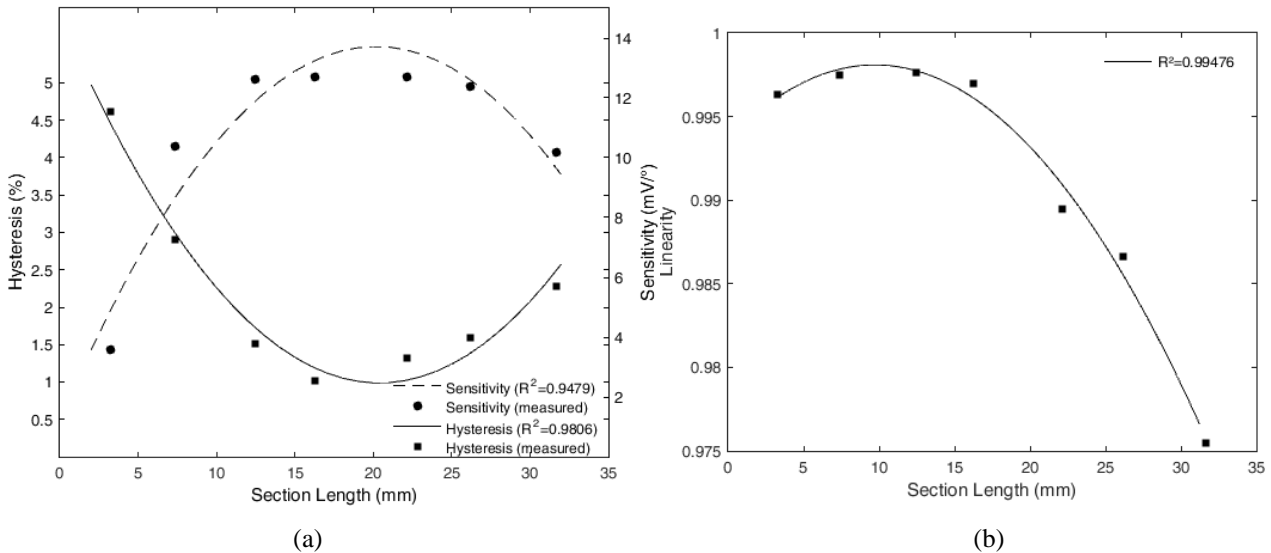


Figure B-4 (a) Hysteresis and sensitivity for sensitive zone length of 3.25 mm through 31.66 mm. (b) Linearity for different POF sensor section length. The correlation coefficient with the second-degree polynomial is 0.9948.

Referring to Figure B-4(a), the sensitive zone with lower hysteresis is 16.25 mm, the hysteresis presents a downward trend until reach its minimum point, after this point starts to increase again. The hysteresis is high with small section length due to the different accommodation of the polymer under flexion and extension, which means that the polymer have a range of relaxation times instead of a single value of relaxation time [156]. There are three different values for the material properties: the one of the core, the properties of the jacket, and the different properties presented by the sensitive region due to the fiber cross sectional area variation caused by the material removal. The relationship between these three different material characteristics can cause different viscoelastic accommodation under dynamic bending tests. Moreover, the hysteresis increases again with section length above 16.25 mm because there is more material removed, which leads to more attenuation of the optical power and more fragility of the sensor. Therefore, with less removed material, the fiber is more resistant for some of the stress tensor components than the fiber with more material removed, which can lead to higher deviations between the flexion and extension response for the fiber with higher section length and increase of the hysteresis. Moreover, these different material properties and stress tensor components also generate the variations of the hysteresis of the same sample under different tests.

A similar behavior of the hysteresis analysis is observed in the sensitivity response. However, on the sensitivity analysis, it has a point of maximum sensitivity on 16.25 mm of section length, after that, it starts to

decrease. After the 12.48 mm of section length, the increase of the sensitivity is very small. The same happens when the sensitivity starts to decrease after the 16.25 mm section length until it reaches the 26.19 mm. After that, it has a considerable decrease again. The minimum sensitivity is found on the minimum section length, this happens due to the lower dimensions of the sensor sensitive zone length. As the sensitive zone length increases, the sensor sensitivity also increases due to the higher surface area of signal attenuation. Nevertheless, it reaches its maximum value and starts to decrease. This can be due the saturation of the output signal due to the high attenuation caused by higher length on the sensitive zone.

The last sensitive zone length analysis is the linearity evaluation. It is of paramount importance that the sensor has linear variation with the measurand, since the sensors with exponential behavior, for example, may present a saturation trend that can limit its dynamic range. The linearity evaluation is made by the analysis of the correlation coefficient of the linear regression for each sample. As observed on the sensitivity analysis, there is a good repeatability of the sensor linearity in each test. The POF sensor linearity behavior can be well approximated by a second-degree polynomial (see Figure B-4(b)). The linearity behavior is similar to the sensitivity. However, the sensor exhibit higher linearity in lower sensitive zone length. The maximum linearity is found on the interval between 7.36 mm and 16.25 mm of section length. In higher sensitive zones, the linearity has a considerable decreasing, which is associated with higher influence of non-principal stress tensor components on the fiber response. Moreover, this negative correlation between sensor linearity and sensitive zone length can be related to a nonlinearity of the signal attenuation due to higher section lengths. Therefore, higher sensitive zone lengths can lead to lower sensor linearity. The sensor sensitive zone length capable of provide the highest sensor sensitivity is on the interval between 12.48 mm and 22.13 mm, whereas the highest linearity is for the lateral section length between 7.36 mm and 16.25 mm. Furthermore, the lowest hysteresis was found on the sample of 16.25 mm of lateral section length.

### **Sensitive zone depth analysis**

Three consecutive tests were made with the samples 8 through 13. Once again, the hysteresis shows more variation than the other sensor performance parameters. Moreover, the hysteresis exhibits the same behavior as presented in the sensitive zone length analysis. Although the hysteresis is lower than the ones of the section length experiment, it also has a downward trend until reach its minimum value, and starts to increase again (shown in Figure B-5(a)). Therefore, it can be approximated by a second-degree polynomial with a correlation coefficient of 0.9703. The minimum hysteresis was found in 0.95 mm section depth, whereas its maximum value is associated with the 0.6 mm section depth, which is the minimum depth that actually increases the sensor sensitivity.

The POF sensor sensitivity has a linear behavior with the increase of section depth and the correlation coefficient obtained was 0.9714, which represents a strong correlation. The maximum sensitivity was found on 0.6 mm section depth. One reason of this behavior can be the higher attenuation caused by higher material removal, which can lead to lower variation between the maximum and minimum signal amplitudes due to the fact that the signal is already too attenuated. For example, the sample 13 has its initial response (when the fiber is not bent) of 0.75 V. When the fiber is bending, it cannot decrease too much, for this reason, the maximum sensitivity for this sample is 8.3 mV/°. However, the signal does not reach the 0 V due to the sensor saturation and the sensitivity obtained is 6.8 mV/°. Therefore, an intuitive assumption that the increase the section depth will always increase the sensor sensitivity is not truth, because higher section depths lead to higher attenuation and, after a certain angle, the signal does not decrease much. This sensor saturation trend at higher angles when the section depth increase also leads to lower sensor linearity.

Figure B-5(b) shows the sensor linearity changes due to the increase of the sensitive zone depth. The linearity reduction can be approximated by a second-degree polynomial, the correlation coefficient is 0.9801, which shows a sharp decrease of the linearity when the section depth is higher than 0.95 mm. As aforementioned, the linearity decrease is associated with the sensor saturation trend in angles higher than 60°. An analysis of the linearity of the POF sensor with section depth higher than 0.95 mm shows a linearity of about 0.9915 on the interval between 0 and 60° and 0.9676 when the interval is 60° to 90°. Therefore, a POF curvature sensor with sensitive zone depth higher than 0.95 mm is only feasible for angles below 60°.

The hysteresis, sensitivity, and linearity analysis show a trade-off of the sensor sensitive zone depth choice. Although a section depth of 0.95 mm shows the lowest hysteresis, the highest sensitivity and linearity among the samples tested occur when the sensitive zone depth is 0.6 mm. Therefore, it is necessary to analyze the desired parameters for each sensor application before choose the sensitive zone parameters.

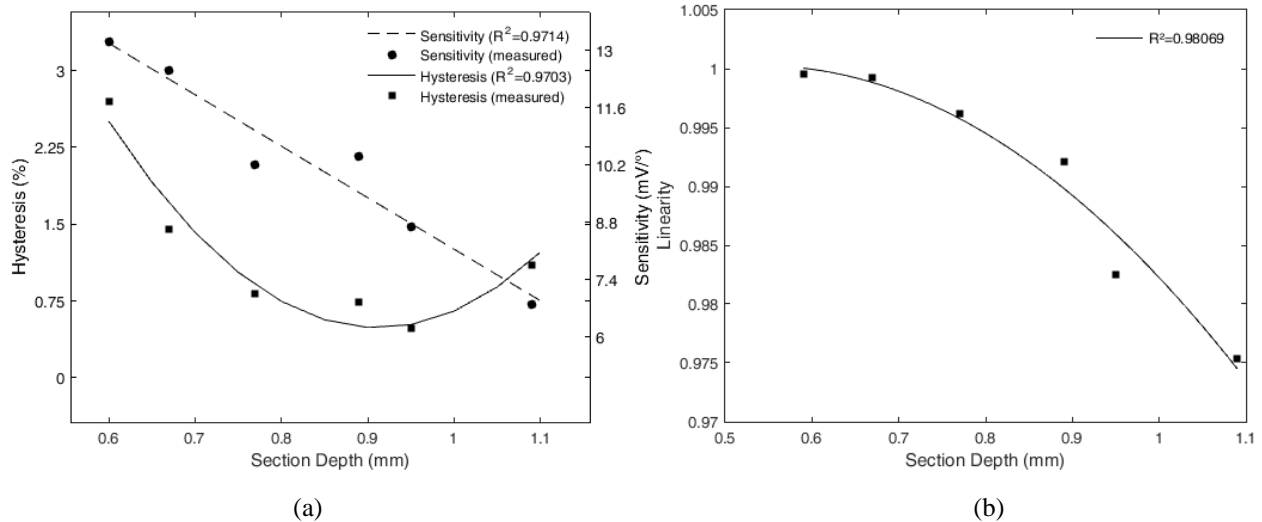


Figure B-5 (a) Hysteresis and sensitivity for sensitive zone depth of 0.6 mm through 1.09 mm. The results can be approximated by a second-degree polynomial. (b) Linearity for different POF sensor section depth. The correlation coefficient with the second-degree polynomial is 0.9806.

If only the lateral section depth is analyzed, the lateral section depth of 0.60 mm provides the highest linearity and sensitivity, at the same time. However, this lateral section depth provides the highest hysteresis among the ones tested. Therefore, there is a trade-off on the decision of the section depth parameter. Applying the same weight for the hysteresis, sensitivity and linearity, the lateral section depth chosen is 0.60 mm.

### Sensitive zone surface roughness analysis

One of the attenuation mechanisms of the POF sensor is the surface scattering on the sensitive zone, and the assumption here is that it depends on the sensitive zone surface characteristics. Therefore, the section surface roughness provides different sensor response. For this reason, the samples 14 through 20 are tested and the sensor hysteresis, sensitivity, and linearity are analyzed. The surface roughness is assessed as the sandpaper grit size employed for the sample manufacturing.

The hysteresis has a negative correlation with the sandpaper grit size until the 600-grit size and a slightly increase on sample 20 (800-grit sandpaper). Although the second-order polynomial is presented in Figure B-6(a) due to its higher correlation coefficient ( $R^2=0.9951$ ), it is also possible to approximate the results as an exponential decay curve. In this case, the correlation coefficient is 0.939. Since the difference between the hysteresis of the samples 19 and 20 is not large, it is possible to say that as the sandpaper grit increases, the hysteresis decreases. This behavior can be explained by the reduction of the surface scattering when the sensitive zone has a smoother pattern. Since the surface scattering can have a non-uniform behavior, a surface with lower roughness presents a similar response under flexion and extension, which provides lower sensor hysteresis. Figure B-6(a) also shows the sensor sensitivity variation with respect to the sandpaper grit size. The sensor sensitivity relation with the surface roughness also can be approximated by a second-degree polynomial. However, there is a point of maximum sensitivity at the 400-grit size, which is about the midpoint of the grit size analysis. Therefore, if the grit size is low, the surface roughness is high. For this reason, the surface scattering increases and the sensor response is attenuated, which leads to lower sensitivity due to the output power saturation. Nevertheless, if the grit size is high, the surface roughness is low and there is a decrease on the surface scattering. Since the surface scattering is one of the attenuation mechanisms of the sensor, its excessive reduction implies on sensor sensitivity decrease.

The POF curvature sensor linearity is evaluated with respect to sandpaper grit size. Figure B-6(b) shows a complementary behavior between hysteresis and linearity, which is a positive correlation between the sensor linearity and the sandpaper grit size until the 600-grit size sandpaper and a slightly decrease on sample 20 (800-grit size), whereas the hysteresis decreases until the sample 19 (600-grit size sandpaper). This behavior also can be explained as the non-uniform behavior of the surface scattering leading to a decrease of the sensor linearity. Another explanation is the high signal attenuation on rough surfaces, which leads to a saturation trend of the POF curvature sensor on angles above  $60^\circ$ .

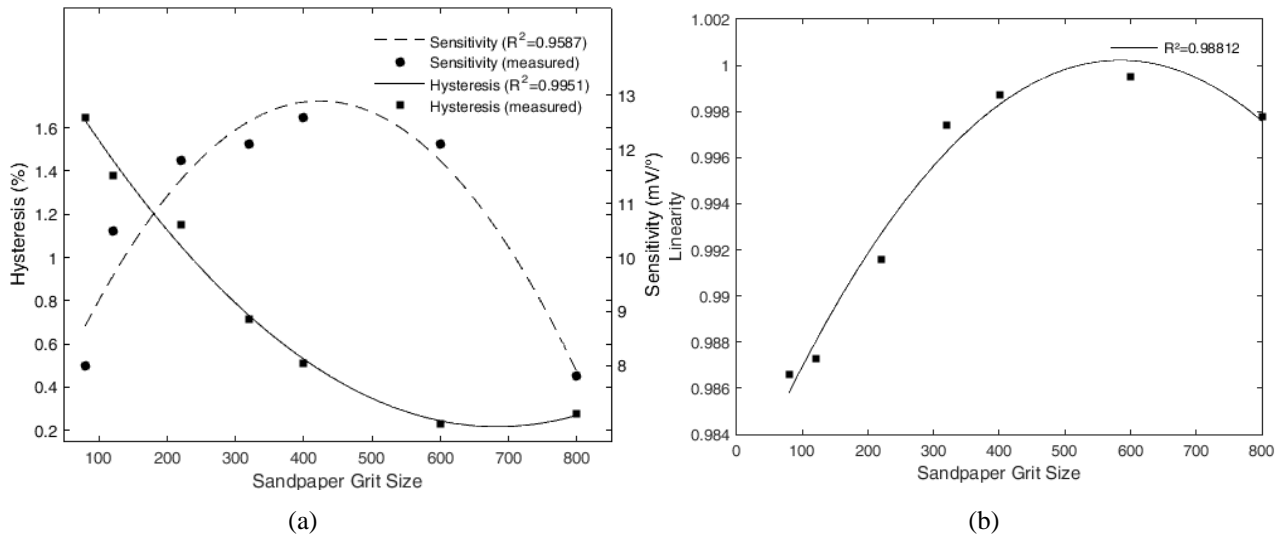


Figure B-6 (a) Hysteresis and sensitivity for different POF sensor sensitive zone roughness (samples 14-20), which is represented as the sandpaper grit size. (b) Linearity for different POF sensor sensitive zone roughness.

The sensitive zone surface roughness analysis shows that sandpaper with higher grit sizes are preferable when the objective is to obtain the lowest hysteresis and highest linearity. However, higher grit sizes do not provide high sensitivity for the sensor. Therefore, there is a trade-off between these parameters, which has to be analyzed prior to the sensor sensitive zone design. In the analysis of surface roughness, the sandpaper grit that achieved the best value of sensitivity was 400 and, for the linearity, the sandpaper grit is 600. Since the parameters of surface roughness that result on the high sensitivity and linearity are close, the choice for this sensitive zone parameter is simple. The values of the linearity between the sandpaper grits of 400 and 600 were close, whereas the value of sensitivity has higher difference between these two sandpaper grits. In addition, the lowest hysteresis was found on the sample made with sandpaper grit of 600. For these reasons, the sandpaper grit size for the sensor manufacture that may provide the best response on the POF curvature sensor is 600.

## POF sensor curvature radius analysis

If the curvature radius is reduced, the stress increases, which leads to higher variation of the fiber refractive index. Therefore, the sensor is more sensitive to curvature with lower curvature radius (as shown in Figure B-7(a)). The effect of the curvature radius variation with the sensor sensitivity can be well approximated with a linear equation through the least squares method. Figure B-7(a) shows the hysteresis for each curvature radius, it is possible to apply a polynomial regression, which results on a second degree polynomial with correlation coefficient ( $R^2$ ) higher than 0.98. Since the hysteresis depends on the viscoelastic response of the material, its correlation with the curvature radius is not direct as the sensitivity. One reason for this behavior is a non-uniformity of the viscoelastic response with the curvature. In other words, the viscoelastic parameters also have variation with the curvature angle applied for each test due to the higher stress rates when the fiber has higher angles and lower curvature radii, which may increase the hysteresis [154]. However, it is possible to see that the hysteresis is high for curvature radii lower than 45 mm and sharply decreased when the curvature radius is higher than 45 mm. The decrease observed on the interval between 45 mm and 60 mm is related to the reduction of the stress on the fiber, which also reduces the viscoelastic response of the POF.

Figure B-7(b) shows the sensor linearity changes due to the increase of the curvature radii. The linearity can be approximated by a second-degree polynomial, being the correlation coefficient of 0.984. Since the viscoelastic response is not linear [148], the linearity of the sensor with lower curvature radius is also lower. However, when the curvature radius is high, the dominant attenuation mechanism is the radiation loss due to the macrobending. Nevertheless, this attenuation mechanism alone may not be as linear as when combined with the stress-optical effect. Therefore, the linearity has a second order behavior and the maximum value of this parameter, among the curvature radii tested, is shown on the middle of the curvature radius range tested.

The curvature radius analysis is not straightforward as the sensitive zone parameters analysis. The curvature radius of 25 mm has highest sensitivity among the curvature radii analyzed, whereas the highest linearity is found on the curvature radius of 45 mm. In addition, the lowest hysteresis was found on the curvature radius of 60 mm. Since there is a large interval of values, a multi-objective genetic algorithm optimization [225] is

applied to obtain a smaller range of curvature radii that provide low hysteresis and, at the same time, high sensitivity and linearity. The results of the optimization were in the range of 28 mm to 42 mm. Therefore, this interval of curvature radii provide the best balance between linearity, sensitivity and hysteresis among the ones tested.

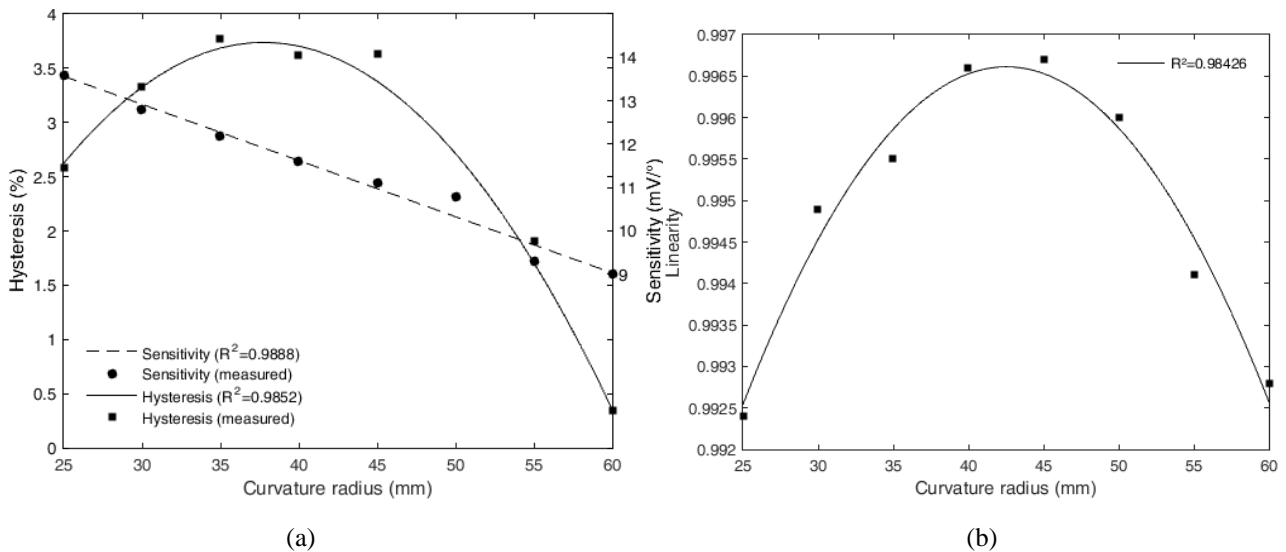


Figure B-7 (a) Hysteresis and sensitivity of the sensor with different curvature radii. The correlation coefficient between the results for the sensitivity analysis is 0.9888 and 0.9852 for the hysteresis analysis. (b) Linearity of the sensor with different curvature radii. The correlation coefficient between the results is 0.9843.

As presented in Figure B-4-Figure B-7, the relation between the sensor performance (hysteresis, sensitivity and linearity) and its sensitive zone parameters and curvature radius can be approximated by a second-order polynomial in all cases except sensitivity variation with respect to sensitive zone depth and curvature radius, Figure B-6(a) and Figure B-7(a), respectively. The similarity between the results presented may be related to the high range of parameters tested, which leads to a saturation of the sensor response that usually results in a decrease of the sensor performance. For this reason, each sensitive zone parameter may present a range of values that leads to lower hysteresis and both high sensitivity and linearity.

In summary, the analysis of the sensitive zone parameters and curvature radius resulted in a POF curvature sensor with sensitive zone length of 15.05 mm, depth of 0.65 mm with the sensor manufactured with a sandpaper grit size of 400. Furthermore, the curvature radius of this sensor is 40 mm, which is in the range of curvature radii aforementioned. Figure B-8 shows the response of the optimized sensor on flexion/extension cycles. In order to present the sensor hysteresis on this cycle, the response is shown with respect to the reference angle measured by the potentiometer.

Analyzing the sensor with these lateral section parameters and curvature radius, it was obtained a sensor with sensitivity of about 20.9 mV/° and linearity of 0.9992. The mean hysteresis of this sensor is below 1%. The results of sensitivity, linearity obtained with the optimized sensor are higher than the ones obtained in reference works [111], [165]. Although not measured on these reference works, the hysteresis obtained on the optimized sensor seems to be lower than the ones of [111], [165].

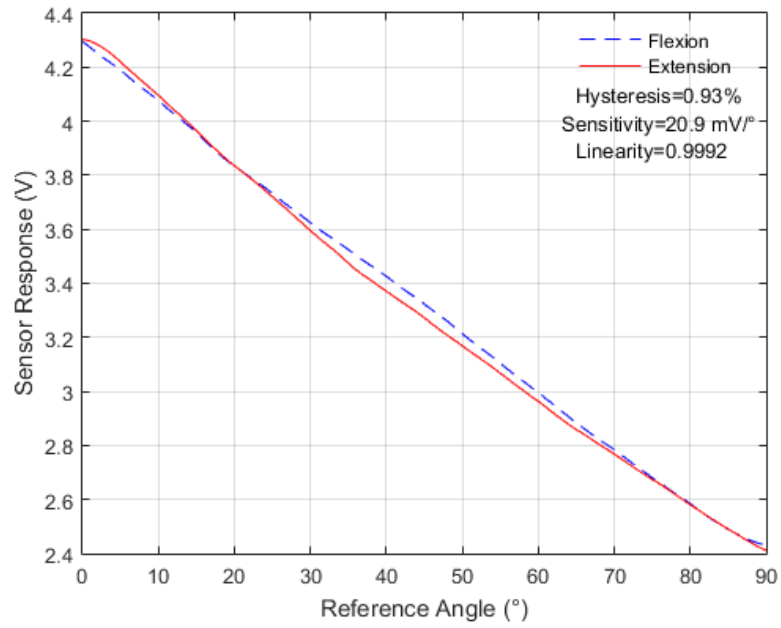


Figure B-8 POE curvature sensor response with optimized sensitive zone parameters and curvature radius

## Appendix C. Compensation Technique Based on Angular Velocity

The hysteresis of POF sensors can be reduced by annealing the fiber [178]. The fiber annealing comprises of keeping the fiber at a temperature close, but below its glass transition temperature for more than 12 hours [180] or it can be made at room temperature with solution-mediated that leads to a reduction of the polymer glass transition temperature as presented in [226]. Furthermore, annealing at high RH (about 90%) can improve the sensor sensitivity and reduce the hysteresis for sensor applications, especially in temperatures higher than 50°C [180]. In order to achieve the hysteresis reduction, the POF employed as curvature sensor was annealed in a climate chamber at 80°C for 24 hours. Although it leads to a mean hysteresis reduction of about 30%, the sensor still presents hysteresis of about 2%. For this reason, it is necessary a dynamic compensation technique for POF curvature sensors based on intensity variation capable of reduce the sensor hysteresis.

The high hysteresis of the POF sensor may be related to the polymer viscoelasticity. This effect causes a phase lag between the excitation and its response and a tendency to relax when it is under stress. Therefore, polymers do not have a constant response to stress or strain with different velocities of movement and this effect is related to the polymer molecular rearrangement [156]. For this reason, it is possible that the hysteresis of POF curvature sensors is associated with the polymer relaxation and the phase lag (see Chapter 3). The polymer viscoelastic response also depends on the time that the stress or strain is applied [184]. This means that the behavior of a POF sensor may be different for long periods of relaxation [184] and, for dynamic tests, the viscoelastic response may be related to the frequency of movement or its angular velocity.

In order to overcome these limitations, this section proposes a dynamic compensation technique for the hysteresis of a POF curvature sensor. The proposed technique comprises of an experimental model relating the sensor angular velocity and its response for angular velocities up to 3.4 rad/s, which results on a calibration equation that can be applied in real-time measurements. The sensor root mean squared error (RMSE) and hysteresis are compared for the sensor response with and without the compensation technique.

### Experimental analysis

The flexion and extension tests were made with a multimode PMMA POF (HFBR-EUS100Z, Broadcom Limited, Singapore) with different angular velocities in the interval of 0 to 90°. In this study, the sensor was designed with a POF with 1 mm of diameter, which does not require high precision tools for connecting with the power source and acquisition electronics. These advantages lead to a system with lower cost and easier to install than the single mode POF sensors [41]. The control of cleaving parameters like temperature, speed and angle are important for good cleaving of POFs [91]. Such control is easier to be made in fiber with larger diameters, where the cleave is made with a razor blade perpendicular to the fiber as presented in [41] with the razor blade IF-FC1 (Industrial Fiber Optics, USA). For the lateral section of the fiber, the sectioned region is polished with a sandpaper with controlled grit size to guarantee a smooth surface as presented in [111]. Since the sensor sensitive zone parameters have influence on the sensor response (see Appendix B), the sensitive zone parameters are kept constant. The sensitive zone length of the sensor is 15.05 mm and the depth is 0.65 mm as experimentally verified in previous sections. The POF sensor curvature radius also influences the hysteresis response as presented in previous sections. In order to minimize this influence, the curvature radius is about 40 mm in all tests (optimized parameters following Appendix B). The experiments done to obtain the dynamic compensation are made with nineteen angular velocities between 0.02 rad/s and 3.4 rad/s. Each test is performed three times for each angular velocity proposed and the mean value is analyzed.

### Dynamic compensation technique

Figure C-1 presents the block diagram of the dynamic compensation technique proposed, which results on calibration equations for flexion and extension relating the sensor angular velocity and measured voltage with the angle. The method for obtaining these equations are divided in two parts: one for the hysteresis compensation and another for the error reduction.

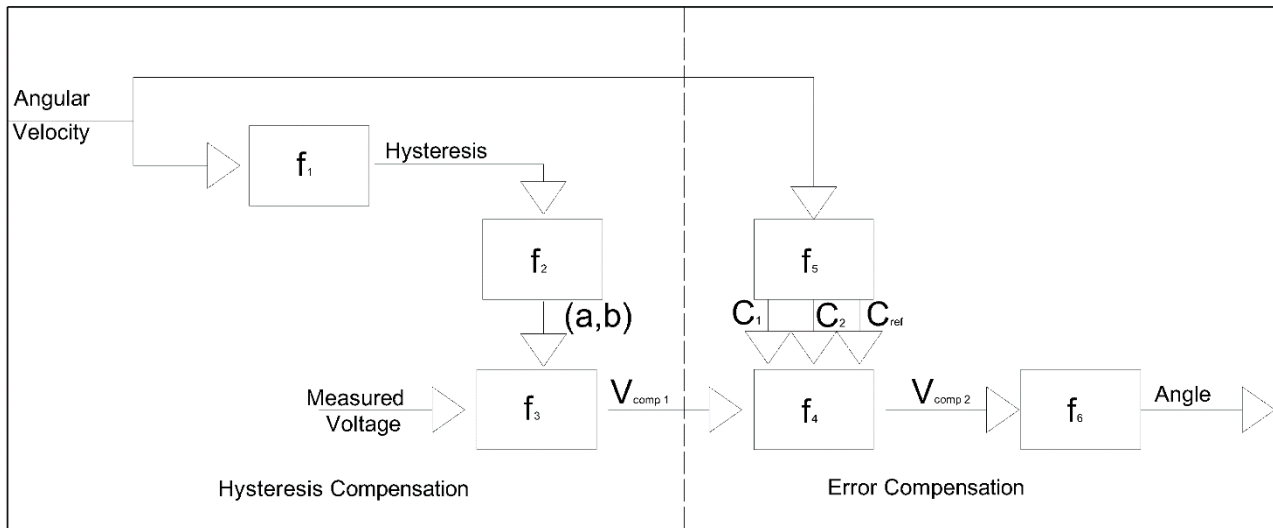


Figure C-1 Dynamic compensation technique block diagram.

The hysteresis compensation may lead to higher errors on the sensor measurement in some cases. For this reason, there is an error compensation phase after the hysteresis compensation. The aim is to reduce both hysteresis and RMSE of the POF curvature sensor when compared with the sensor response without these compensation phases. The parameters shown on the block diagram of Figure C-1 are presented on Table C-1, which describes the parameter and indicates its role on the compensation technique i.e. if it is a result, input or characterization parameter. Each parameter presented in Table C-1 is further discussed and estimated on the next sections.

Table C-1 Parameters employed on the dynamic compensation technique

Symbol	Parameter description	Parameter Role
$V_{meas}$	Measured Voltage	Input
$\omega$	Angular Velocity	Input
$V_{comp1}$	Hysteresis compensated voltage	Characterization
$a$	Linear regression parameter between measured and hysteresis compensated voltage	Characterization
$b$	Linear regression parameter between measured and hysteresis compensated voltage	Characterization
$h$	Estimated hysteresis	Characterization
$V_{comp2}$	Error compensated voltage	Characterization
$C_{ref}$	Reference parameter for error compensation	Characterization
$C_1$	Parameter for error compensation	Characterization
$C_2$	Parameters for error compensation	Characterization
$\alpha$	Dynamic compensated angle	Output

Referring to Figure C-1, the hysteresis compensation phase comprises of the blocks 'f<sub>1</sub>', 'f<sub>2</sub>' and 'f<sub>3</sub>'. The analysis is made considering a reference angle provided by the potentiometer. This reference angle, is converted into reference voltage through the calibration equation obtained on a quasi-static test, which is represented in Figure C-1 as the block 'f<sub>6</sub>'. A model relates the reference voltage, the sensor voltage response, and the estimated fiber angular velocity to obtain a compensated voltage, which is further converted into angle after the error compensation phase. The steps made to obtain the models of the blocks 'f<sub>1</sub>', 'f<sub>2</sub>' and 'f<sub>3</sub>' are discussed as follows.

The first step of the technique is to perform quasi-static tests on the sensor. The quasi-static tests are performed for calibration purposes and allow obtaining a calibration curve with the lowest influence of the sensor angular velocity. In order to do so, the quasi-static characterization is made in angles of 0 to 90° in steps of 5°. The fiber is positioned on the desired angle for a period higher than 5 seconds, which is higher than the

PMMA POF relaxation time and time constants (see Section 3.3). Therefore, it characterizes a quasi-static test. The mean response of the sensor at each angle is obtained and a calibration curve is derived. The calibration equation obtained on quasi-static tests is applied for convert the reference angle into reference voltage, which is compared with the measured voltage to obtain a linear regression relating the measured and the reference voltage. By doing so, the measured voltage ( $V_{meas}$ ) is an input of a model that enable to obtain the hysteresis compensated voltage ( $V_{compl}$ ), which results in two equations, one for flexion (represented by the subscript 'f') and other for extension (represented by the subscript 'e'). These flexion and extension equations compose the block 'f<sub>3</sub>' and are presented in Eq. C.1 and Eq. C.2, respectively.

$$V_{compl,f} = a_f V_{meas,f} + b_f, \quad (C.1)$$

$$V_{compl,e} = a_e V_{meas,e} + b_e. \quad (C.2)$$

However, the coefficients  $a$  and  $b$  of each equation are different at their respectively angular velocity ( $\omega$ ). For this reason, the presented linear regression is made for each angular velocity, among the angular velocities tested. The coefficients obtained for flexion presented high correlation in a linear regression with the sensor angular velocity (correlation coefficient higher than 0.9). Similarly, the coefficients for extension also presented a correlation coefficient higher than 0.9 in a linear regression with the sensor hysteresis ( $h$ ). Eq. C.3-Eq. C.6 represent the block 'f<sub>2</sub>' of Figure C-1 and provide the equations for obtaining the coefficients of the linear regression presented in Eq. 4.29 and Eq. 4.30.

$$a_f = 0.03609\omega + 1.042, \quad (C.3)$$

$$b_f = -0.09913\omega - 0.2655, \quad (C.4)$$

$$a_e = 0.02018h + 1.039, \quad (C.5)$$

$$b_e = -0.06682h - 0.2604. \quad (C.6)$$

Nevertheless, the hysteresis of the sensor response is related to its velocity. Therefore, Eq. C.7 presents the relation between the sensor hysteresis and its angular velocity. This equation is shown in Figure C-1 as the block 'f<sub>1</sub>'.

$$h = 9.104 \times 10^{-5} \omega^{8.17} + 1.252. \quad (C.7)$$

Since the presented hysteresis compensation may increase the errors of the POF sensor, an error compensation phase is proposed. It comprises of the blocks 'f<sub>4</sub>', 'f<sub>5</sub>' and 'f<sub>6</sub>' of Figure C-1. The main equation of this compensation is presented in block 'f<sub>4</sub>'. The input of this model is the hysteresis compensated voltage, which is compared with the reference voltage. However, in this case, it is compared through an equation similar to the Williams-Landel-Ferry (WLF) equation employed on the TTS principle, which is applied to account the shift effects of loads with different frequencies on the polymer response [150] (see Chapter 3). Nevertheless, a different application of this equation is proposed here. In this case, the shift between the reference voltage and the hysteresis compensated voltage is evaluated and it is added to the hysteresis compensated voltage to correct possible drifts of the sensor response caused by the hysteresis compensation or from the POF sensor response. By doing so, two equations for the error compensation of the POF sensor are obtained, once again, one for flexion and another for extension, Eq. C.8 and Eq. C.9, respectively. These equations represent the block 'f<sub>4</sub>' of Figure C-1.

$$V_{comp2,f} = V_{compl,f} + \frac{-C_{1,f}(V_{compl,f} - C_{ref,f})}{C_{2,f} + (V_{compl,f} - C_{ref,f})}, \quad (C.8)$$

$$V_{comp2,e} = V_{compl,e} + \frac{-C_{1,e}(V_{compl,e} - C_{ref,e})}{C_{2,e} + (V_{compl,e} - C_{ref,e})}. \quad (C.9)$$

In order to obtain the material constants  $C_1$  and  $C_2$ , the shift is evaluated at two reference voltages (3.5 V and 2.6 V) to obtain a linear system of two equations to calculate the material constants at each angular velocity of the sensor. Furthermore, a reference constant ( $C_{ref}$ ) is chosen at each analysis. However, the material

constants are different at each velocity. For this reason, a linear regression between the sensor angular velocity and each constant is made, which results in five different equations Eq. C.10-Eq. C.13 and these equations represent the block 'f<sub>5</sub>' of Figure C-1,

$$C_{ref} = 0.7536\omega - 0.01575, \quad (C.10)$$

$$C_{1,f} = 0.6268\omega - 1.900, \quad (C.11)$$

$$C_{2,f} = -19.19\omega + 61.65, \quad (C.12)$$

$$C_{1,e} = -0.1381\omega + 0.4546, \quad (C.12)$$

$$C_{2,e} = 7.275\omega - 22.98. \quad (C.13)$$

Finally, the block 'f<sub>6</sub>' of Figure C-1 is the equation relating the error compensated voltage ( $V_{comp,2}$ ) with the angle ( $\alpha$ ). This equation was obtained through the quasi-static tests, since it results on an equation with the lowest influence of the sensor angular velocity. Eq. C.14 shows the result obtained in this characterization.

$$\alpha = \frac{V_{comp,2} - 4.3508}{-0.02} \quad (C.14)$$

The calibration equation with the proposed compensation technique is obtained for flexion movement by substituting Eq. C.3 and Eq. C.4 on Eq. C.1, which are applied on Eq. C.8 with the parameters obtained in Eq. C.10- Eq. C.12 that is further applied in Eq. C.14. An analogous process is made to obtain the calibration equation for the extension movement. In this case, the angular velocity is substituted on Eq. C.7, which is employed to obtain the parameters of Eq. C.5 and Eq. C.6. These parameters are employed on Eq. C.2 to obtain the hysteresis compensated voltage that is applied on Eq. C.9 with the results of Eq. C.10, Eq. C.12 and Eq. C.13 to estimate the error compensated voltage. Finally, the error compensated voltage is applied on Eq. C.14 to obtain the angle.

### **Comparison between the POF sensor response with and without the compensation technique**

Combining Eq. C.1- Eq. C.14 it is possible to obtain two calibration equations, one for flexion and one for extension case. The POF curvature sensor flexion and extension equations are applied on the sensor response at each angular velocity and at each cycle as well to obtain a compensated response of the sensor. In contrast, only Eq. C.14 is applied on the sensor response at each angular and at each cycle to obtain a response without compensation, which is the commonly employed approach for POF curvature sensor of this type [111], [165].

The proposed dynamic compensation technique was able to reduce hysteresis or RMSE in all angular velocities tested. The hysteresis of the sensor response with the compensation technique is reduced in about 20%, whereas the RMSE with the compensation technique is reduced in about 3 times. Therefore, not only the sensor hysteresis is lower, but the error is reduced with the compensation technique application. Figure C-2(a) shows the sensor response with the compensation technique for the first cycle of the test with constant angular velocity of 0.09 rad/s, whereas Figure C-2(b) shows the sensor response without the compensation technique proposed. The POF sensor with the compensation technique has a hysteresis of about 0.44% and a RMSE of about 1.0°, which is lower than the one presented without the compensation technique (hysteresis of 0.6% and RMSE of 6.8°) and is lower than the ones presented in reference works [111], [165].

Although the hysteresis reduction was not high in the case shown in Figure C-2, the RMSE is greatly reduced. On the one hand, it has some cases that the hysteresis is not decreased but the RMSE is. On the other hand, there are cases with the hysteresis reduction, but with the increase of the RMSE. This may be due to the fact that viscoelastic parameters of a material are not constant, it has a range of values instead [156]. However, in all cases both the increase of the hysteresis or RMSE with the compensation technique is not high. Actually, it is lower than reference works with POF curvature sensors and also lower than the errors obtained with different technologies for angle assessment [163]. Moreover, in most cases both hysteresis and RMSE is reduced. Table C-2 shows the comparison between the POF sensor response with and without the compensation technique with respect to the sensor hysteresis and RMSE for all velocities tested. The angular

velocity that leads to the higher hysteresis and RMSE reduction is 0.82 rad/s (see in bold – Table C-2), which can be related to the best correlation between the predicted hysteresis and angular velocities with the measured hysteresis among the velocities tested, which leads to a better performance of the compensation technique.

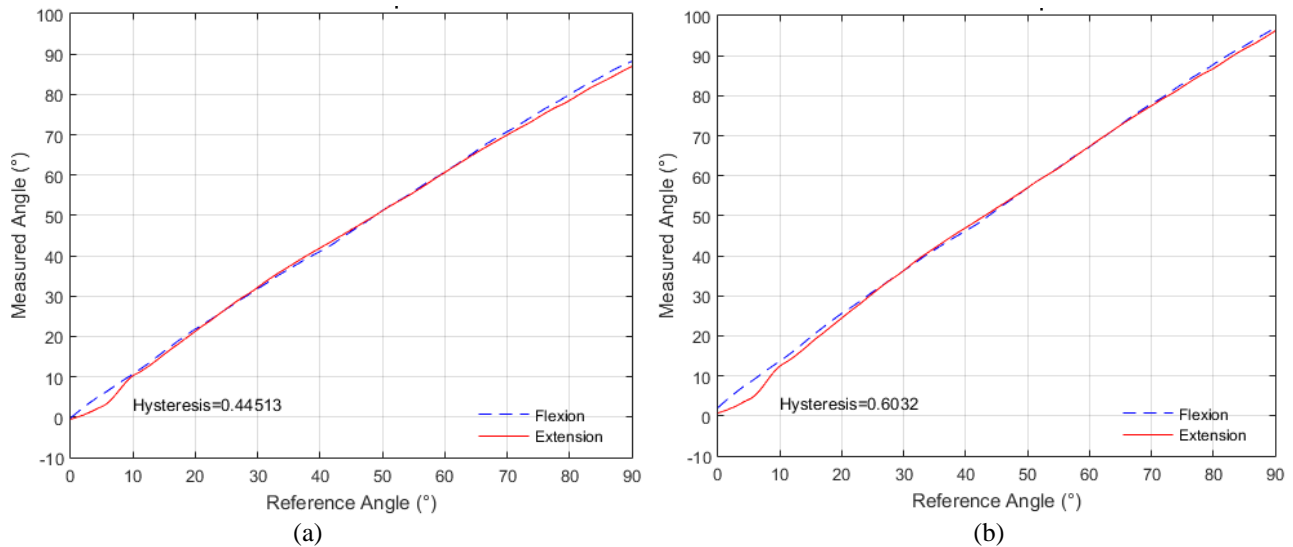


Figure C-2 POF curvature sensor response for constant angular velocity of 0.09 rad/s. (a) Response with the compensation technique. (b) Response without the compensation technique.

Since there is a large interval of angular velocities, from 0.02 rad/s to 3.41 rad/s, it may be difficult to obtain a single calibration equation that reduces both error and hysteresis in the whole interval analyzed. However, the dynamic compensation technique guarantees the reduction of the RMSE or hysteresis in all angular velocities tested. Referring to Table C-2, there are five angular velocities that the compensation technique was not able to reduce the hysteresis, namely 1.05 rad/s, 2.99 rad/s, 3.21 rad/s, 3.24 rad/s and 3.31 rad/s. Viscoelastic parameters have a range of values instead of a single one [156]. Therefore, a possible reason for the hysteresis increase in these angular velocities is related to the variation of the viscoelastic parameters, which can lead to higher variability of the hysteresis. For this reason, it is possible that the hysteresis was out of the range of hysteresis predicted by the compensation technique. However, in these velocities, the RMSE was reduced in half, at least, whereas there are two angular velocities that the RMSE was not reduced with the dynamic compensation technique. Nevertheless, the hysteresis was reduced in these cases. Therefore, the compensation technique proposed is a feasible technique for the compensation of the sensor high hysteresis and the high RMSE presented in high angular velocities.

Table C-2 Comparison between the sensor with compensation and without technique

$\omega$ $\left(\frac{rad}{s}\right)$	No compensated Hysteresis	Compensated Hysteresis	No compensated RMSE (°)	Compensated RMSE (°)
0.02	3.18%	1.06%	2.07	2.32
0.03	2.51%	0.42%	3.45	1.98
0.04	2.01%	0.016%	3.75	1.80
0.06	2.15%	1.56%	9.05	1.64
0.09	0.60%	0.44%	6.79	1.15
0.10	1.57%	0.89%	3.00	4.01
0.17	0.45%	0.092%	6.99	1.91
0.34	0.46%	0.14%	7.06	1.68
0.43	1.69%	1.23%	6.69	1.05
0.57	2.12%	1.89%	7.11	1.03
<b>0.82</b>	<b>0.23%</b>	<b>0.071%</b>	<b>6.61</b>	<b>1.76</b>
1.05	2.09%	3.05%	3.17	1.59
1.61	1.93%	0.25%	8.28	1.69
2.99	0.96%	3.34%	9.16	3.18
3.14	1.47%	0.95%	9.93	2.71
3.21	0.31%	2.95%	7.90	2.81
3.24	0.22%	2.41%	6.55	2.90
3.31	1.18%	1.62%	9.07	2.89
3.41	0.56%	0.17%	6.25	2.79

## Appendix D. Torque Characterization

As discussed in Appendix A, when the fiber is under stress, there is a variation on its refractive index due to the stress-optic effect. This effect is described by a second-rank tensor that represents the changes on the optical indicatrix under a predefined stress as presented in [162]. Such variation of the refractive index leads to a variation of the critical angle and the number of modes in the fiber. For the case of fiber torsion presented in Figure D-1, the stress tensor of the fiber is presented in Eq. D.1:

$$\sigma = \begin{bmatrix} 0 \\ 0 \\ 0 \\ \mu\gamma x \\ -\mu\gamma y \\ 0 \end{bmatrix}, \quad (\text{D.1})$$

where  $\mu$  is the material shear modulus,  $\gamma$  is the torsion angle,  $x$  and  $y$  are the directions of the Cartesian plane defined in Figure D-1.

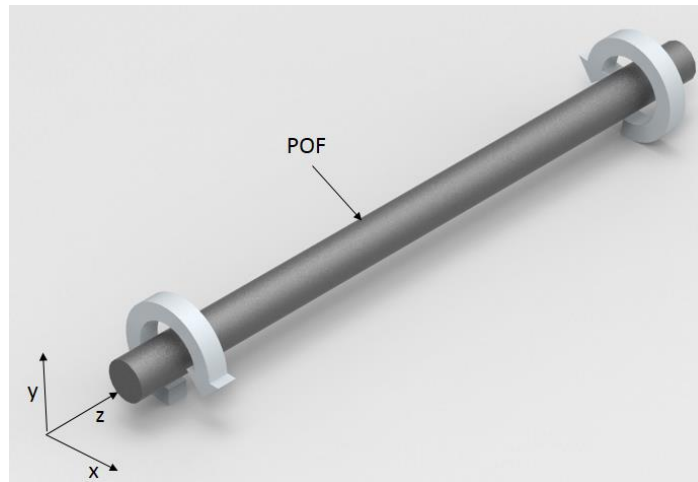


Figure D-1 POF under torsion stress.

The sensor needs a fiber submitted to a constant torque to enhance its sensitivity to temperature and RH variations. For this reason, different torques were applied on the fiber to characterize their influence in the POF output power. The torque is applied by rotating the fiber in a predefined torsion angle in the directions shown in Figure 4-6. Since the refractive index variation is directly proportional to the torsion angle [162], it is possible that a higher angle leads to a sensor with higher sensitivity. Furthermore, if the torque is applied in a different direction, it is expected that the power variation will also occur in a different direction, which demonstrates the sensor polarity, i.e., it can distinguish the increase or decrease of the temperature and humidity. In order to enhance the sensor sensitivity, a lateral section is made on the fiber, which consists of polishing the side of the fiber to remove its cladding and part of the core using the optimized parameters defined in Appendix B.

Four different torques are tested. Two of them are in clockwise direction and the other two are in counterclockwise direction. Figure D-2 shows the results of the torque characterization. The torsion angles indicated as  $\tau_1$  and  $-\tau_1$  are related to approximately the same torsion angle with  $\tau_1$  in the clockwise direction and  $-\tau_1$  in the counterclockwise direction. The same approach is made for  $\tau_2$  and  $-\tau_2$ , in which the torsion angles  $\tau_0$ ,  $\tau_1$  and  $\tau_2$  are  $0^\circ$ ,  $15^\circ$  and  $45^\circ$ , respectively. However, the torque presented on  $\tau_2$  is lower than the one of  $-\tau_2$ , since the POF's response will be too attenuated if a torque of same magnitude as  $-\tau_2$  is applied. The region of Figure 4-6 related to  $\tau_0$  is the POF's response without the application of torsion stress. In addition, the peak between  $\tau_1$  and  $\tau_2$  is related to a torque relaxation on the process of applying the higher torque  $\tau_2$ .

Referring to Figure D-2, the response's transitions around 280 s and 400 s are related to the process of applying the torque on the fiber and due to its viscoelastic behavior. The polymer viscoelasticity causes the transient behavior of the response in 280 s and 420 s, in which there is a sudden increase followed by the

polymer relaxation when the torque is applied, as characterized in [34-35]. It is worth to mention that the polymer relaxation is an intrinsic behavior of the POF used, which occurs for all the torques tested. Since this effect becomes more evident with the strain increases, there is a larger variation of the POF's response in higher torsion angles. As long as the sensor is isolated from external mechanical disturbances, when the torsion angle  $\tau_1$  is applied there is a stabilization of the voltage after about 150 seconds. Since such polymer relaxation can be affected by the temperature, the temperature's level was kept at around 24°C, what led to a lower variation of the polymer's viscoelastic behavior.

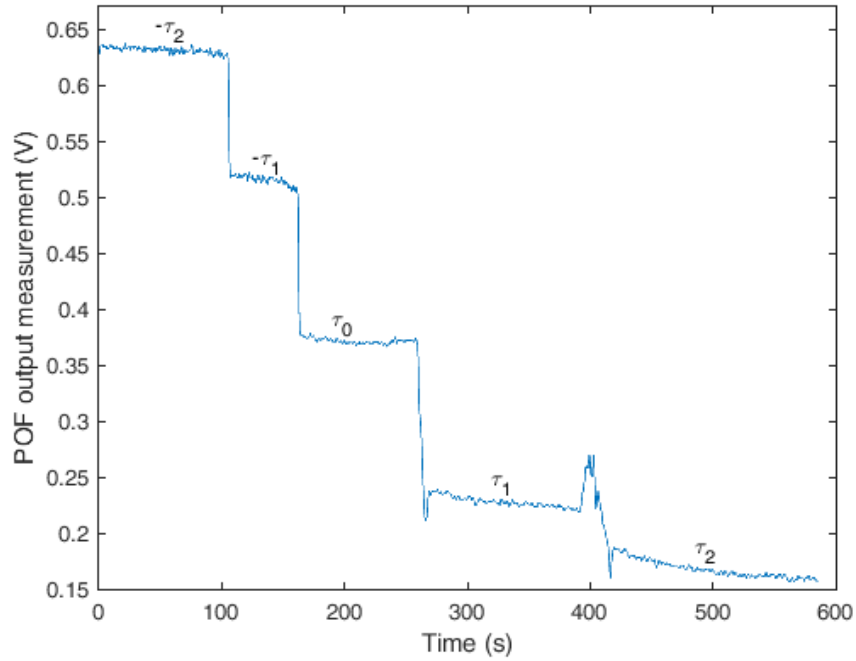


Figure D-2 POF response under different torques.

## Appendix E. POF-based Insole for In-shoe GRF Measurements During FES-assisted Gait

Aiming at the advantages of POFs in sensor development discussed and demonstrated in previous sections, this sub-section proposes the application of POF sensors in an insole for the vertical GRF measurement. The measuring system is based on four intensity variation based POF sensors positioned on an insole. The compensation for the polymer creep response developed in Section 6.3.2.2 is also applied in this case. Moreover, the sensor is based on the intensity variation with the response acquired by one photodetector, which means that the sensor response acquired by the single photodetector is the sum of the contribution of each sensor, instead of the individual response of each sensor that can be acquired if the number of photodetectors is equal to the number of sensors. For this reason, the sensors need to have similar sensitivity in order to reduce the errors and guarantee that each sensor has the same contribution on the response acquired by the photodetector with the advantage of lower cost than the FBG-based insoles presented in [50], [218], [227], [228]. After the characterization, the sensor is tested in two experimental setups. First, experimental are performed in quasi-static conditions for the assessment of the center of mass forward displacement. The proposed POF sensor response is compared with a commercial force platform as reference. The second setup involves dynamic conditions, where the subject is asked to walk with the device, demonstrating the advantages of the developed insole sensor for gait analysis purposes. Then, there is the application of the POF-based insole on the gait phase identification in an FES system for gait assistance, which is used to identify five gait events, assisting the actuation of the FES controller.

### Sensors operation principle and characterization

In this study, the POF employed is made of PMMA with a core diameter of 980  $\mu\text{m}$ , a cladding of fluorinated polymer with 20  $\mu\text{m}$  thickness and a polyethylene coating that results on a total diameter of 2.2 mm for the fiber considering its coating (as applied in the previous sections). The sensors are placed on the insole as shown in Figure E-1. Sensor positions on the insole are chosen based on the spots with higher plantar pressure during gait [228]. Each POF sensor has a lateral section, namely the sensitive zone, which is made by removing the cladding and part of the core to increase the sensor sensitivity. The lateral section length, depth and surface roughness, as well as the curvature radius have influence on the sensor sensitivity as shown in Appendix B. The curvature radius is defined here as the distance between the sensitive zone center and each support that fixes the fiber on the insole. These parameters are carefully chosen in order to obtain similar sensitivity in all four sensors. The side-polished region is placed facing the insole surface. When each sensor is pressed, there is a curvature on the sensitive zone, which leads an output power attenuation proportional to the angle of the curvature. Furthermore, when the sensor is under stress, there is a variation of the fiber refractive index due to the stress-optic effect [162]. The variation of the refractive index also leads to the power attenuation of the sensor as depicted in previous sections.

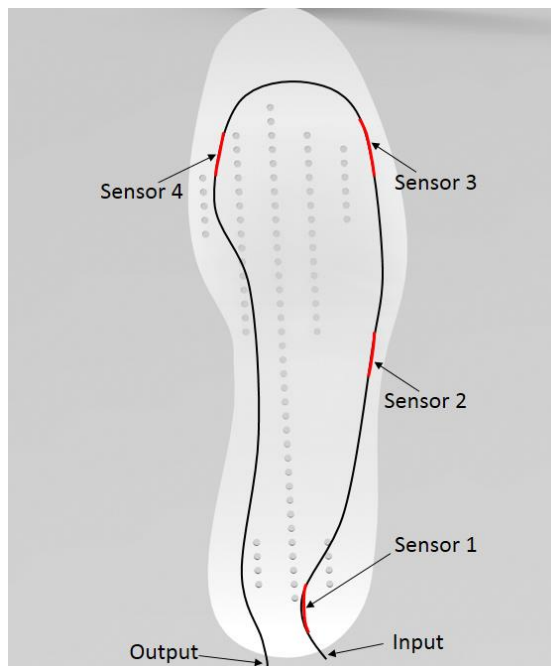


Figure E-1 Bottom of the insole with the POF sensors positions.

Since the POF sensors are attached to the insole, when the plantar pressure is applied on the insole, it will be a deformation of such material that causes a displacement of each POF sensor with respect to the insole. The displacement of the POF sensors lead to the optical power attenuation, where most of the stress is applied on the insole material, which is also a polymer. However, the polymer is a viscoelastic material and the response to the stress applied varies with time [19]. Nevertheless, the stress response of the POF can be divided in static and transient components through the Maxwell's Model (see Appendix A), where the same procedure depicted in Section 6.3.2.2 is applied on each sensor of the proposed instrumented insole.

After three consecutive tests with each sensor, the sensor normalized response after the load application is fitted in an exponential model to obtain the polymer time constant. By doing so, the inverse of the time constant obtained is  $0.0019 \pm 0.0005 \text{ s}^{-1}$ . Although the polymer time constant is a range of values instead of a single one, the time constants of the sensors 2, 3 and 4 are close and the highest difference on the time constant is due to the sensor 1. Figure E-2 shows the application of the viscoelastic compensation on sensor 2. The comparison between the reference signal from the force sensor, the uncompensated and compensated signals show the feasibility of the technique presented. Since the characterization of the sensor viscoelastic response is made with the sensor positioned on the insole, it also accounts for the viscoelastic response of the insole material. For this reason, this viscoelastic compensation technique can be applied to different insole materials, where the difference will be related to the time constant of each material.

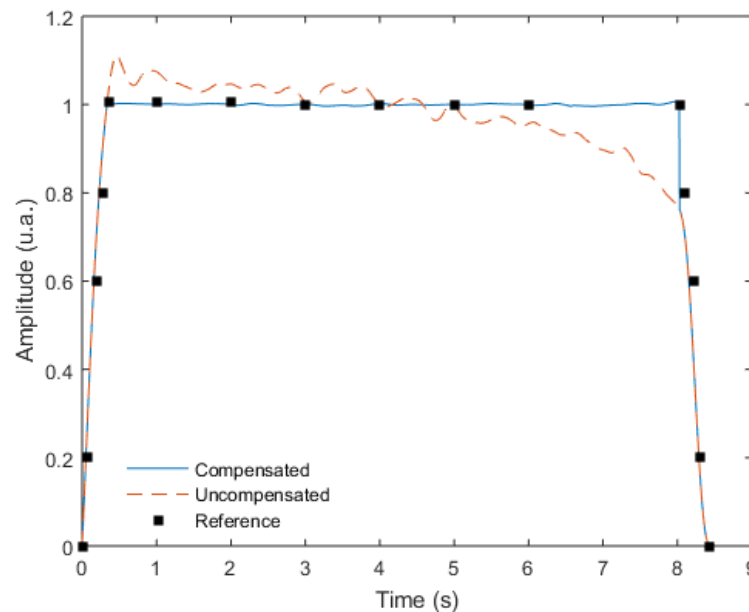


Figure E-2 Viscoelastic compensation technique applied on sensor 2.

Thereafter, the sensitivity of each sensor can be estimated. In order to obtain the sensor contribution of each sensor on the GRF response, it is desirable that they have similar sensitivities. For this reason, different forces are applied at each sensor to characterize its output power variation with an applied force on the range of 0 N to 50 N with steps of 10 N. The test is made by positioning calibrated weights on the top on each sensor. Figure E-3 shows the sensor's response to the loads employed.

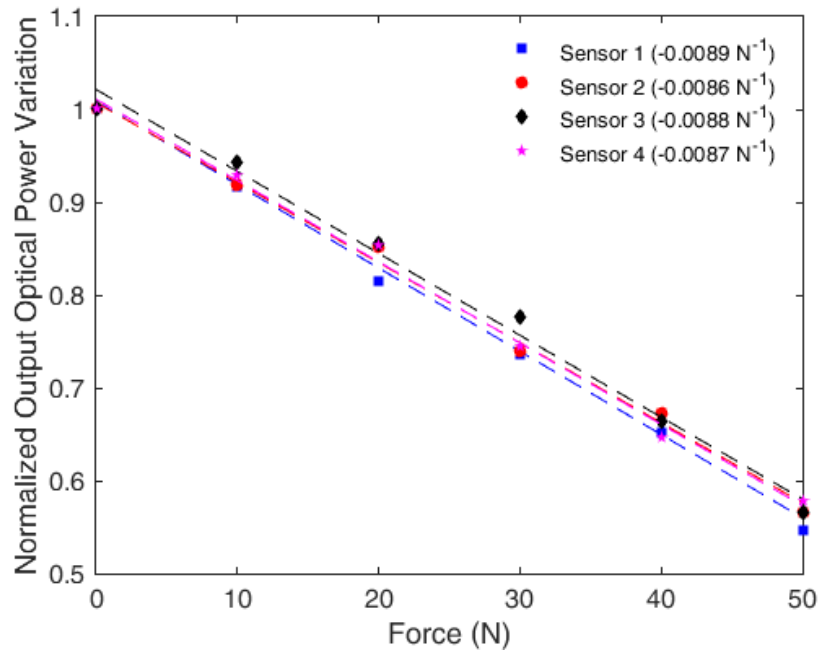


Figure E-3 Signal attenuation of the sensors under compression loads and the sensitivity of each sensor.

The sensitivity of each sensor is related to the slope of the sensors linear regression. Referring to Figure E-3, the sensor 1 has the highest sensitivity, whereas sensor 2, 3 and 4 have almost the same sensitivity. This behavior can explain the fact that sensor 1 has the higher deviation of the time constant when compared with the other sensors. Nevertheless, the sensitivity of the sensor 1 is close to the ones of the sensors 2, 3 and 4. Table E-1 shows the design parameters of each sensor.

Table E-1 POF sensors design parameters.

Sensor	Length	Depth	Curvature Radius
1	12.80 mm	0.66 mm	9.65 mm
2	10.50 mm	0.72 mm	17.25 mm
3	9.71 mm	0.60 mm	14.00 mm
4	11.00 mm	0.68 mm	8.70 mm

## Experimental setup for the POF-embedded insole validation

The sensors with design parameters presented in Table E-1 and with the positions and insole presented in Figure E-1 are positioned inside a shoe as presented in Figure E-4. The employed light source is a LED IF-E97 (Industrial Fiber Optics, USA) with central wavelength at 660 nm. The POF power variation is acquired by the photodiode IF-D91 (Industrial Fiber Optics, USA) with a transimpedance amplifier. The system is powered by a 9 V battery and the sensor response is acquired by a microcontroller that saves the data in a SD card. The system presented in Figure E-4 is employed on the dynamic tests as a portable solution for vertical GRF assessment.

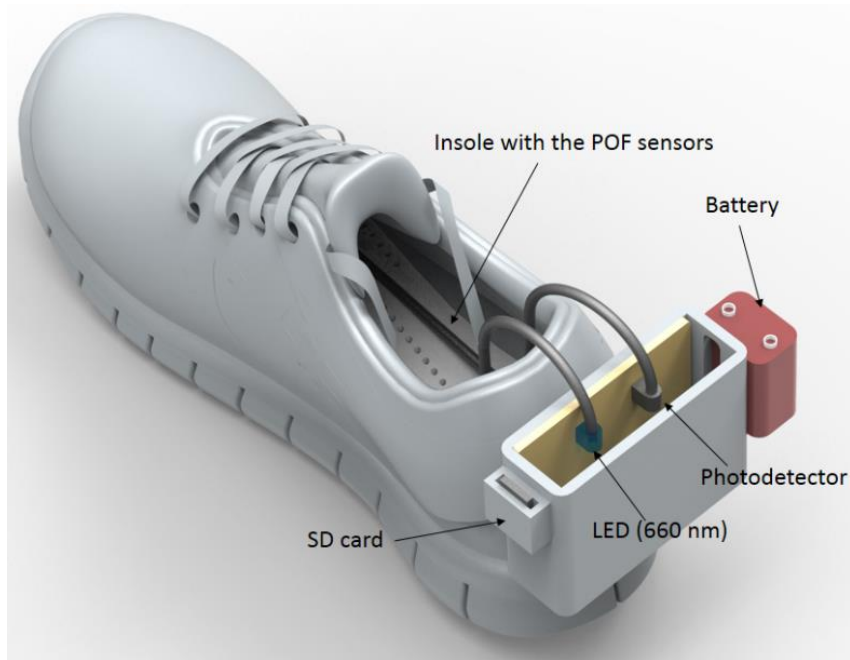


Figure E-4 POF sensors for in-shoe measurement of vertical GRF.

The presented system is applied in quasi-static tests for the assessment of the center of mass displacement and on dynamic tests for the gait analysis. Both quasi-static and dynamic tests were performed with two subjects: one male of 98 kg and one female of 54 kg to show that the POF-embedded insole is capable of operate with a large range of body mass.

Quasi-static tests are made to verify if the sensor is capable of track the center of mass movement on sagittal plane. The displacement of the center of mass generates a variation on the vertical GRF, which is measured by the sensors. In order to obtain a validation of the proposed instrumented insole, a commercial force platform (EMG system, Brazil) is employed on the quasi-static tests. Figure E-5 presents the experimental setup for the quasi-static tests, where the proposed insole is positioned on the center of the force platform.

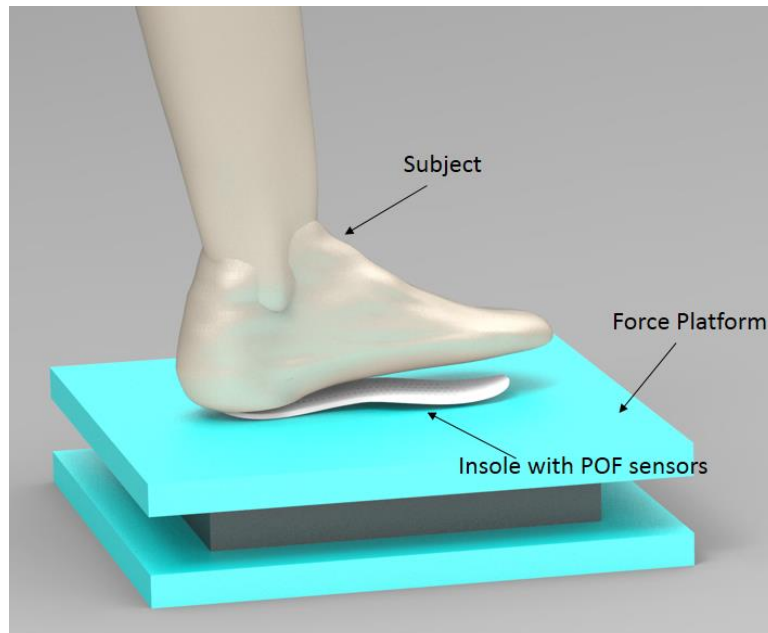


Figure E-5 Experimental setup for the quasi-static tests with the POF insole and the force platform.

The protocol for the quasi-static tests on the sensor comprises of three phases: the first phase is to place the foot on the ground with the heel strike position. The second phase is to lean the body forward to dislocate the center of mass forward. Then, the heel loses contact with the ground and the third phase takes place. Besides the evaluation of the feasibility of the sensors to detect the center of mass variation in sagittal plane, the quasi-

static test also can indicate if the sensor is capable of measuring the vertical GRF on a gait cycle. Since proposed the protocol has the forward movement of the body center of mass similar to the one presented in gait cycle, it is expected an M-shaped pattern, which is characteristic of the vertical GRF in gait cycles [155]. After the validation on the force platform, the in-shoe monitoring of the vertical GRF is made on dynamic tests. For these tests, both subjects are asked to walk on a straight line for about 60 m.

## Quasi-static tests

Figure E-6 shows the result obtained in this test. The protocol was repeated for 30 seconds and good repeatability was obtained. Moreover, the sensor presented the typical pattern of the vertical GRF during gait, but with higher times at each cycle, due to the nature of the test. Referring to Figure E-6, the POF sensors are capable of measuring the variation of the center of mass. However, it presents only the combined effects of the four sensors employed. For this reason, it may be not possible to separate the effects of each sensor on the total response, which means that the movement in both directions and on the lateral plane may not be assessed. If the goal is to define the movement of the center of mass in both planes, it is necessary to employ four photodetectors, one for each sensor, which results in a less compact system and increase the complexity of the signal acquisition and analysis. Therefore, there is a tradeoff on the application of these sensors. On the one hand, the application of only one photodetector for the signal acquisition limits the ability of the system to detect lateral and backward movements. On the other hand, the setup is more compact, less intrusive, easier to implement and has lower cost.

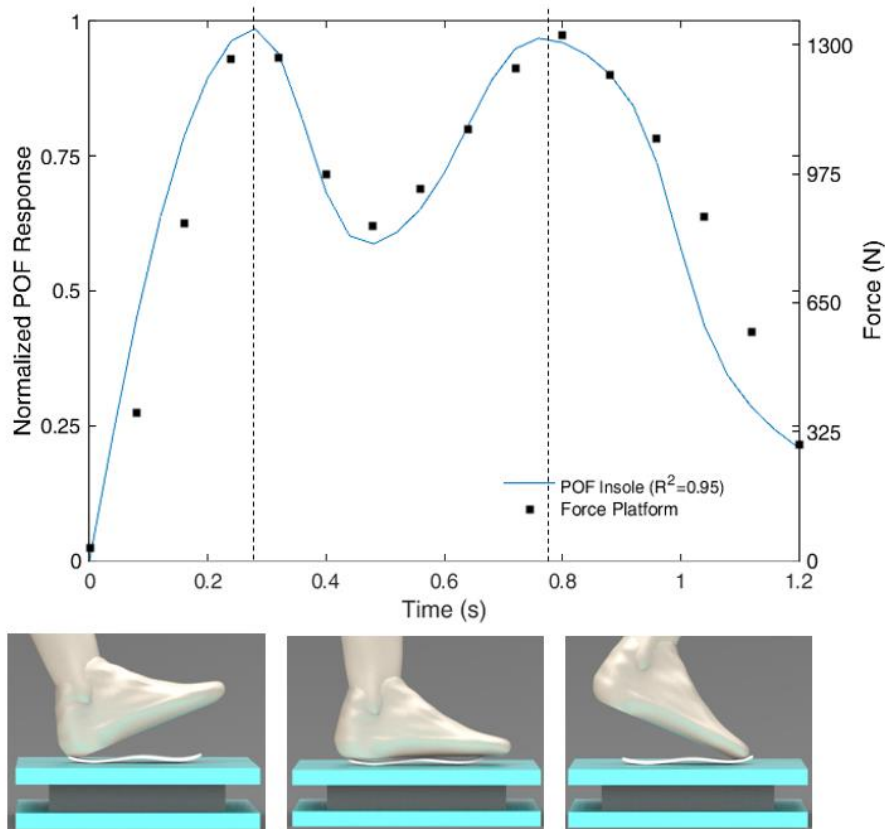


Figure E-6 POF sensors response and force platform measurement for the quasi-static tests with the male subject.

Since the body center of mass moves mainly forward on the gait cycle, the application of only one photodetector can track this movement and the vertical GRF during the gait can be estimated, which is the aim of this system. The test result presented in Figure E-6 was obtained with the male subject that has a body mass of 98 kg, which means a force of about 960 N. The dashed lines are an approximation of the regions that represent each of the three phases of the quasi-static test. The correlation coefficient ( $R^2$ ) between the force platform and the POF insole is 0.95, which means a strong correlation between both approaches. The test performed with the subject of 54 kg presented a RMSE of 7.48 N, which may be related to the differences of foot positioning on the platform during the tests. Although there are only four sensors on the POF insole, these sensors are positioned on the points of higher plantar pressure [15]. For this reason, the proposed sensor is capable of tracking the differences of the vertical GRF and may be used to detect gait events. In addition, the

POF insole can also be applied to monitoring the GRF of pathological gait, since it presents high correlation and low RMSE when compared with the force platforms, which are commonly applied to that end in pathologies such as knee osteoarthritis [229], low back pain [230] and patients after hip arthroplasty individuals [231]. Therefore, the proposed system may be suitable to track abnormal GRF patterns of such individuals.

## Gait analysis

For the gait analysis, the insole is positioned on the shoe as presented in Figure E-4. Figure E-7 presents the results obtained for the female subject. Since the ground reaction forces occur only on the stance phase, the measured normalized variation of the forces is plotted with respect to the stance phase. When the GRF is zero, at the end of the stance phase, the swing phase starts. The bottom of Figure E-7 presents the foot position at each subdivision of the stance phase.

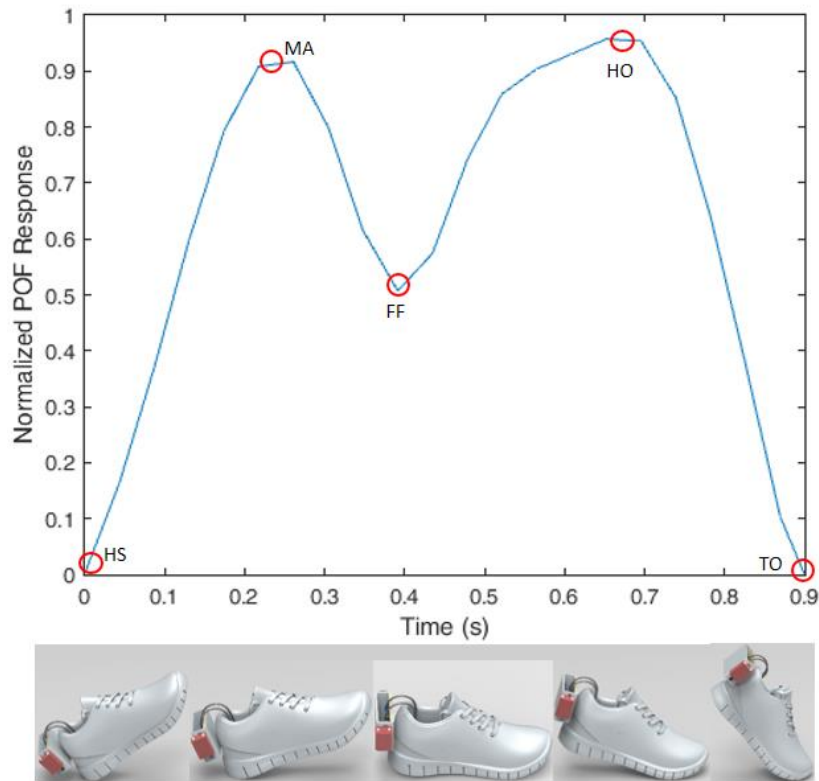


Figure E-7 Gait cycle analysis with the POF insole, where HS is the heel strike, MA is the maximum weight acceptance, FF is the flat foot phase, HO is heel off and TO, toe off.

The results shown in Figure E-7 demonstrate the feasibility of the system for the gait analysis. The vertical GRF presents the M-shape, which is the typical pattern broadly study throughout the years [155]. Moreover, it is possible to separate all the subdivisions of the stance phase. Although a marked point on Figure E-7 represents each phase, some phases can be represented as an interval due the dynamic behavior of a gait cycle. The HS phases starts when the heel touches the ground. When the first peak of load is measured, the MA phase is reached. Then, the foot starts to rotate with the ankle as a pivot until reaches the FF phase, where the foot is at straight position. The foot continues its rotation until the heel losses contact with the ground, which is referred as the HO phase. In this point, there is another peak of load, since all the body weight is transferred to the metatarsal region. The last phase is TO when the foot losses contact with the ground and the swing phase starts. Although Figure E-7 presents the test with the female subject, the same pattern was found for the male subject.

In order to show the system repeatability, Figure E-8 presents the first five gait cycles of the female subject on the dynamic tests for in-shoe vertical GRF monitoring. In this case, the stance phase represented more than 70% of the gait cycle due to the gait velocity of the subject on the test. If the velocity is slow, the stance phase takes higher percentage of the cycle, whereas, when the velocity starts to increase, the stance phase represents a smaller amount of the gait cycle [207]. The quasi-static and dynamic tests with subjects with such weight difference prove that the proposed insole can be applied to a higher range of subjects. Similar repeatability was found on the tests with the male subject of 98 kg.

Since POFs present a strain limit of about 10 times higher than the one of silica fibers [41], the proposed POF insole can be applied to people with higher body mass than the insole based on silica fibers, which is especially desirable due to the relation between obesity and pathologies that affect the gait [232], [233]. Furthermore, the proposed insole is compact, low cost, flexible and can be embedded on a shoe, which enables its application for healthcare [4] and soft robotics [234]. In addition, the higher resilience and fracture toughness of POFs also may enable its application on the assessment of jump kinematics.

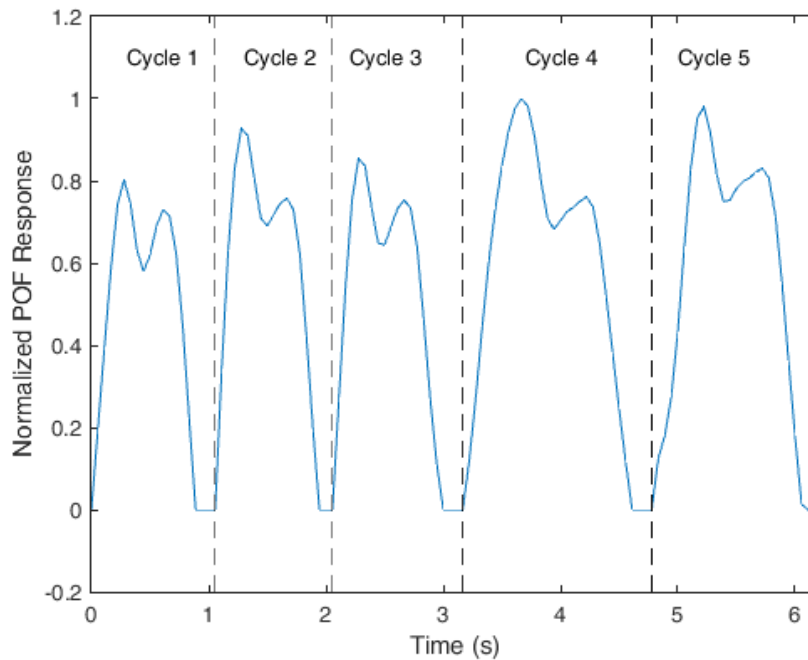


Figure E-8 In-shoe monitoring of sequential gait cycles

## Gait phase detection on gait assisted by FES

Different configurations of FES systems may be used for gait assistance. In one of the pioneering works, which has led to a commercial product, quadriceps stimulation for locking the knee during stance and peroneal nerve stimulation for leg flexion were employed [235]. In our work, bilateral FES-induced quadriceps and hamstrings contractions are used to emulate knee function during gait. A programmable multichannel stimulator is used (Rehastim 2, Hasomed, Germany), and electrical stimuli is applied using self-adhesive 5x10cm electrodes. Wearable sensors are used to detect gait cycle phases, enabling triggering stimulation at appropriate timing based on a finite state machine. After selecting individual FES parameters for each muscle, the test is performed on a treadmill with constant velocity. Figure E-9 shows the user with the electrodes and IMUs (3-space, Yost Labs, USA) positioned.

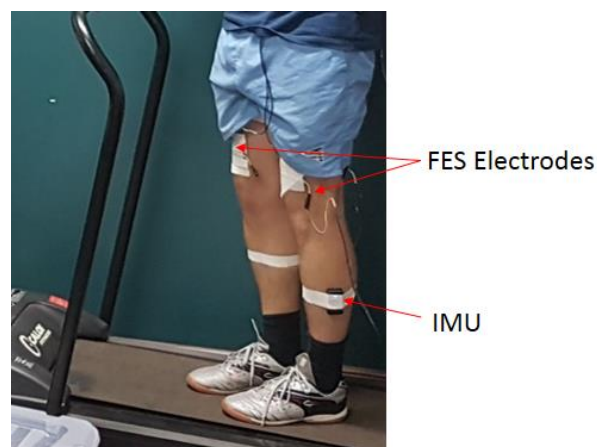


Figure E-9 FES system for gait assistance

The insole is then applied on the FES system. Since FES control is performed using a finite state machine based on each phase of the gait cycle, a low-cost and reliable system capable of identifying such gait events

will be of great benefit. Currently, the gait identification is accomplished with the positioning of two IMUs on each lower limb and the gait event is identified through the knee angles measured with the IMUs. However, IMUs presents sensitivity to electromagnetic fields [27], which is a major disadvantage in the case of the FES, since the electric current can harm the IMU operation. For the tests performed in a treadmill, the electromagnetic interference can be even higher due to the treadmill's electric motor activation. In addition, IMUs need to be calibrated and carefully attached on the subject's skin [27]. Since the FES electrodes also need to be carefully attached on the skin, the system preparation with FES electrodes and IMUs can be a time-consuming process. Aiming to overcome these limitations, a POF insole is applied on the FES system (see Figure E-9). The proposed POF sensor is able to acquire the ground reaction forces during gait, which can be applied to detect gait events [15]. The POF system presents immunity to the electromagnetic field that can be generated on the FES operation and enable an easy and fast system preparation, since the subject only needs to put-on the shoe with the embedded POF insole.

The POF insole is applied on the tests with the FES for gait assistance (see Figure E-9). The subject with the FES, IMU and POF insole positioned is asked to walk on a treadmill for about 2 minutes with the FES control system. Figure E-10 presents the results obtained for 3 sequential gait cycles, where each gait phase is represented on the figure. The proposed POF insole is able to identify more gait events. In addition, it presents high repeatability. The possibility of detecting more gait events can enhance the control of the FES system, since it will be possible to add more states on the finite state machine, potentially providing a more precise control for the FES.

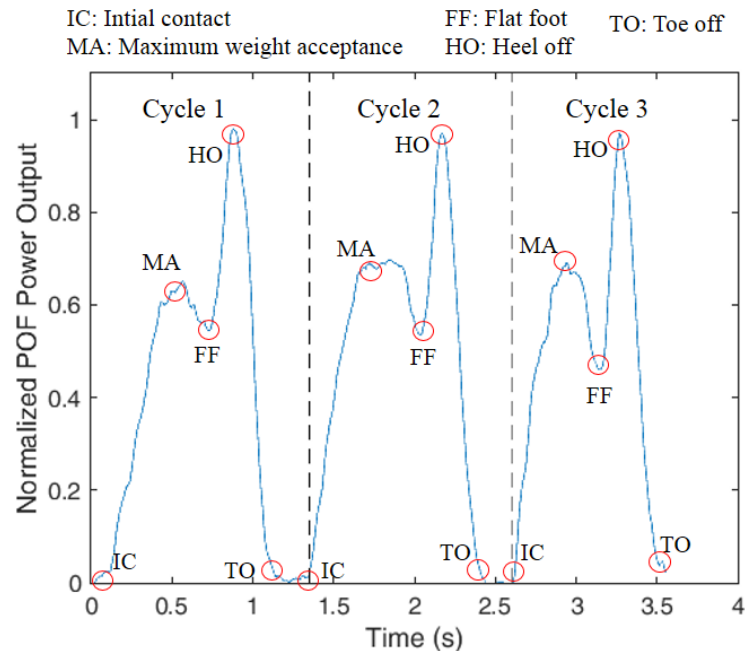


Figure E-10 POF insole for the gait phase detection during the FES assisted gait.

## Appendix F. Influence of the Stress-optic Effect on POF Intensity Variation-based Sensors

In order to verify this assumption, the POF sensor is bent in angles from 0 to 100°. Since the fiber is at straight position and the distance between the supports on both ends of the POF is 40 mm, the stress on the fiber is lower than in the condition of the spring deflection measurements presented in Figure F-1. In such conditions, the fiber is at 180° and the distance between the supports is about 9 mm, which leads to a higher stress on the fiber. Figure F-1 shows the response when the fiber is under a curvature of 0° to 100° with constant velocity of 0.0561 rad/s.

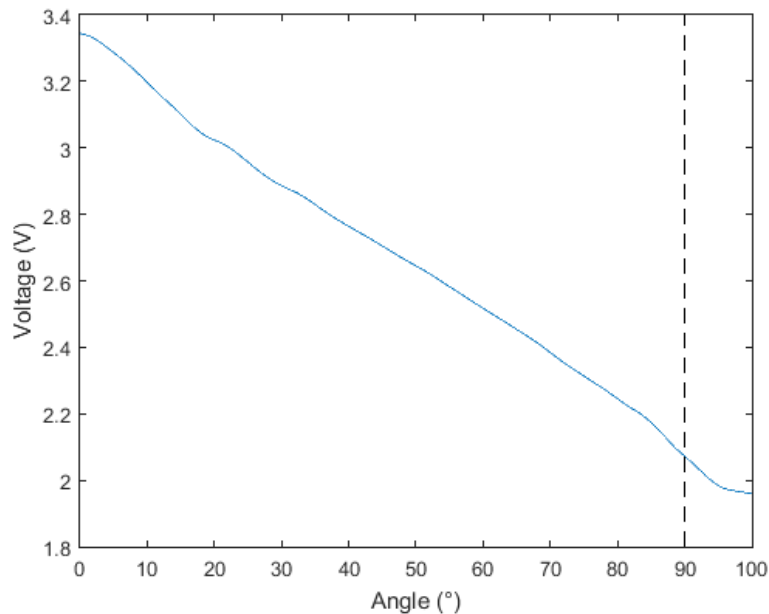


Figure F-1 POF sensor response in 0 to 100° bend with angular velocity 0.0561 rad/s. The dashed line represents the angle of 90°.

Referring to Figure F-1, there is a clearly saturation trend when the angle is higher than 90°. However, in Figure 6-15 the sensor has a response almost linear with the fiber under curvature angles of 180° of the POF positioning on the spring (see Figure 6-13) plus the 10° of the spring deflection. The assumption of the difference between the sensor behavior in Figure 6-15 and Figure 6-16 is a higher influence of the stress-optic effect on the sensor response when it is submitted to higher stress. Since there is a relation between the stress and the refractive index variation, it is expected that if the stress-optical effect is dominant, the sensor response will show high attenuation even if it is submitted to angles above 90°.

Another evidence for the assumption of stress-optic effect dominance is the static tests made on Section 6.3.2.2. In these tests, the sensor presents the characteristic response of viscoelastic materials on creep recovery or stress relaxation tests [59]. For obtaining the differences between static tests of the fiber placed on the spring (initial angle of 180°) and on the straight position, a static test is performed with the fiber on the straight position. In this test, the fiber is bent from straight position (0°) until 100° on steps of 5° and it remains at each position for 10 seconds. The results are shown in Figure F-2, which can be seen that the response does not show the characteristic response of viscoelastic material. When the fiber is at the straight position the stress-optic effect is not dominant and there is not an exponential decay of the POF response at each angle, which represent different levels of stress on the fiber. In other words, if the curvature angle increases, the stress over the fiber also increases. Therefore, Figure F-2 reinforces the assumption that the stress-optic effect is dominant on the response of the POF sensor placed on the torsional spring.

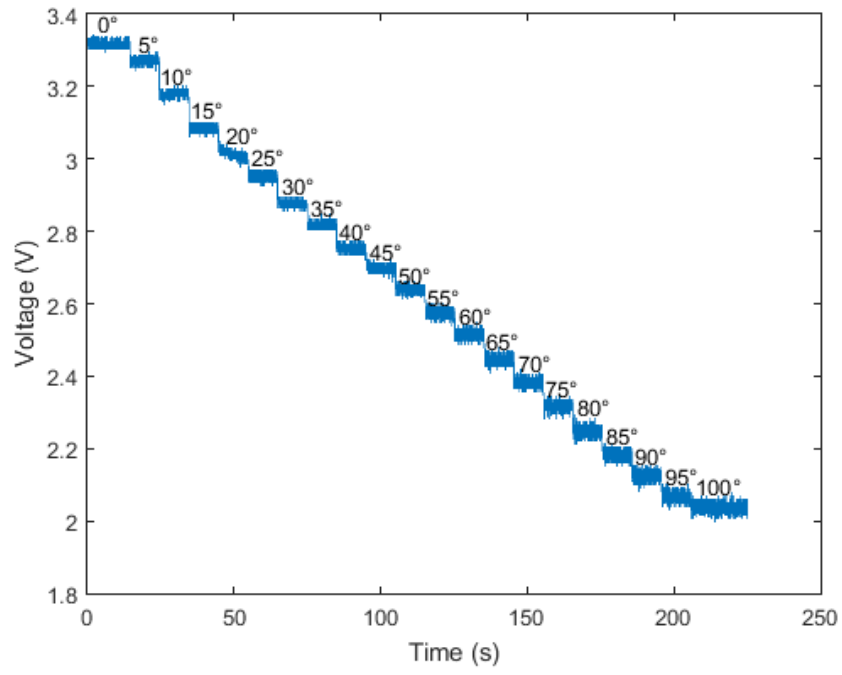


Figure F-2 POF sensor response on static tests with curvature angle between 0° and 100°.

## Appendix G. Results of Intensity Variation-based Microclimate and Force Sensors Characterizations

The results obtained in the characterization of the microclimate sensors 1 and 2 are presented in Figure G-1(a) and (b) for temperature and humidity conditions, respectively. The results are presented with respect to the normalized POF power attenuation, in order to better visualize the sensitivity difference between the microclimate sensors. Such difference may be related to the fabrication process of the sensor either on the lateral section of the fiber or on the embedding process in the ABS structure. Nevertheless, it presents repeatability in all performed tests.

Nevertheless, with the results presented in Figure G-1 it is possible to obtain the sensitivity of each sensor for temperature and humidity. Thus,  $K_{1,T}$  and  $K_{2,T}$  are  $0.00076 \text{ (}^\circ\text{C)}^{-1}$  and  $0.0037 \text{ (}^\circ\text{C)}^{-1}$ , whereas  $K_{1,H}$  and  $K_{2,H}$  are  $0.0021 \text{ (}\% \text{)}^{-1}$  and  $0.0012 \text{ (}\% \text{)}^{-1}$ , respectively. Substituting these values in the matrix shown in Eq. 6.6, a determinant of  $6.85 \times 10^{-6}$  is obtained for the resultant matrix. Since the determinant is not null, the matrix is invertible and it is possible to apply Eq. 6.6 on the microclimate sensor responses and obtain the temperature and humidity. Furthermore, such sensitivity difference between both sensors are related to not only the sensitive zone length and depth, but also to the embedment conditions of each sensor. The differences in the sensor embedment can lead to a condition where each sensor is subjected to higher or lower stress. The stress on the sensor is directly related to its temperature and humidity sensitivities [236]. Therefore, it is possible to infer that microclimate sensor 1 is subjected to lower axial stress condition (due to its lower temperature sensitivity) [47] and higher shear stress condition, since its humidity sensitivity is higher, whereas the opposite occurs for microclimate sensor 2.

Regarding the characterization of the force sensors, Figure G-2 shows the temperature and humidity responses of force sensors 1 and 2, where it can be seen that both sensors present temperature and humidity dependence, which lead to an offset on the force response of each sensor. Once again, the response of each sensor is presented as a function of the normalized power. In addition, the temperature characterization of both sensors is presented in Figure G-2(a), whereas the humidity response is depicted in Figure G-2(b). The linear regression of each sensor for temperature and humidity responses are also presented in Figure G-2(a) and (b), where  $b_{1,2}(T,H)$  is shown in Figure 6-20. The differences between the sensors sensitivities are also related to the fabrication process and their embedment in the TPU structure.

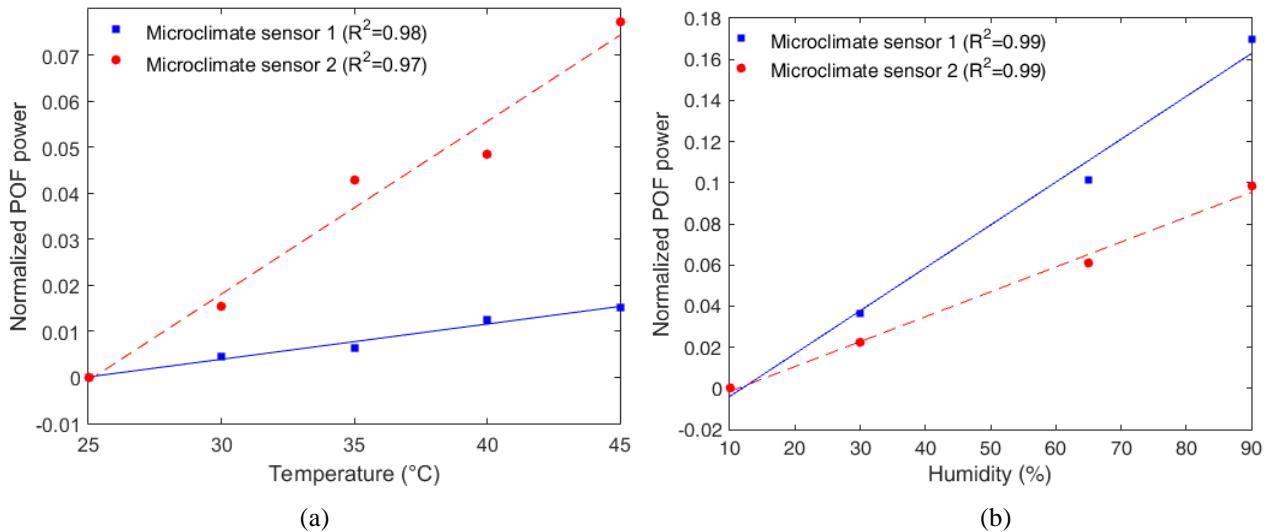


Figure G-1 (a) Temperature characterization for the microclimate sensors. (b) Humidity response for the microclimate sensors. All results normalized with respect to the initial power.

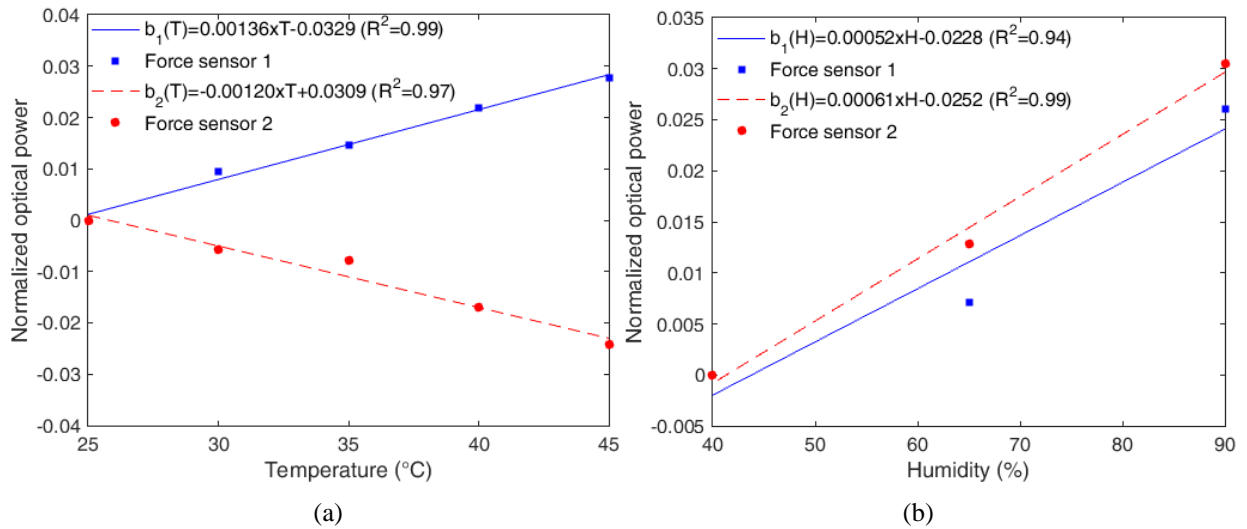


Figure G-2 (a) Temperature characterization for the force sensors. (b) Humidity response for the force sensors.

After characterizing the offset in the force sensor response due to environmental variations, the force response of each sensor is obtained in three different conditions: constant temperature and humidity, variation of temperature and in two different humidity conditions. In this way, it is possible to evaluate the influence of the temperature and humidity in the force sensor sensitivity. In Figure G-3, the force characterization in different temperature and humidity conditions is shown for force sensors 1 and 2.

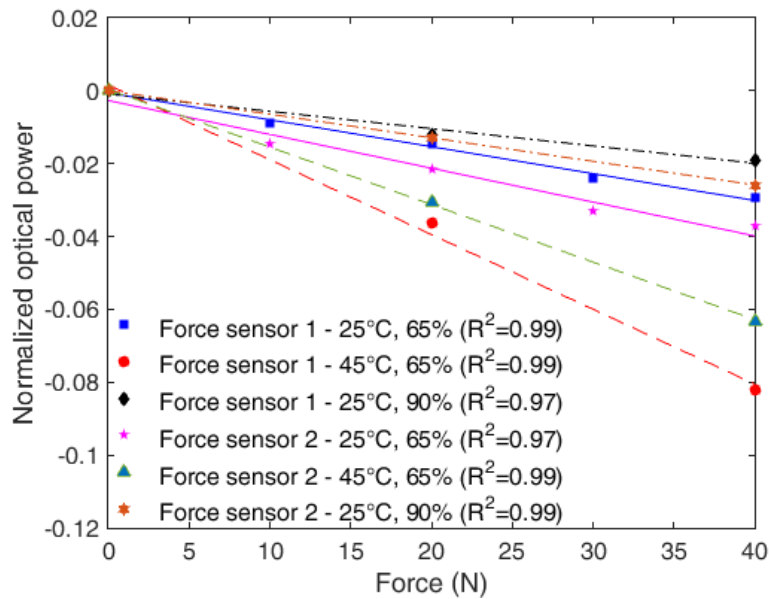


Figure G-3 Force characterization under different temperature and humidity conditions for Force sensor 1 and Force sensor 2.

The force characterization results show similar trend for both sensors 1 and 2 in which the increase in the temperature leads to an increase of the sensor force sensitivity, which was already anticipated in [197]. In contrast, the increase of the humidity results in a reduction of the sensor sensitivity with respect to the applied force. The reason for this behavior is related to the changes on the POF Young’s modulus under which environmental condition.

As presented in Chapter 3, when there is an increase of the temperature, the Young’s modulus reduces, which leads to an increase of the stress in the fiber, resulting in an increase of the sensor sensitivity. On the other hand, when the humidity increases, the opposite occurs, i.e., there is an increase of the POF Young’s modulus and the stress on the fiber is reduced and, thus, decreasing the sensor force sensitivity. Additional force tests in the humidity and temperature ranges used in the sensors characterization with respect to those environmental parameters show a second-order polynomial behavior between the sensor force sensitivity and the environmental parameters (as also shown in [197]). The results of such polynomial regression are the parameters  $a_{1,2}(T,H)$ , shown in Eq. G.1-G.4 as follows:

$$a_1(T) = -4.14 \times 10^{-6} T^2 + 2.17 \times 10^{-4} T - 2.93 \times 10^{-3}, \quad (\text{G.1})$$

$$a_2(T) = 1.81 \times 10^{-6} T^2 - 1.54 \times 10^{-4} T - 1.59 \times 10^{-3}, \quad (\text{G.2})$$

$$a_1(H) = -1.19 \times 10^{-7} H^2 + 2.08 \times 10^{-5} H - 1.32 \times 10^{-3}, \quad (\text{G.3})$$

$$a_2(H) = -1.11 \times 10^{-7} H^2 + 2.04 \times 10^{-5} H - 1.51 \times 10^{-3}. \quad (\text{G.4})$$

The last characterization for the force sensors is the creep response analysis, which is made by applying a constant load of 20 N on each sensor for 2 minutes. In this way, it is possible to analyze the stability of the sensors in an extended time period. By compensating the creep response, a POF sensor with higher stability can be obtained. The results are presented in Figure G-4, where an exponential regression was performed for each sensor response and the exponential term of Eq. 6.5 is obtained. In this way, the normalized sensor response is multiplied by an exponential term on the form  $\exp(\tau \times t)$ , where the time constant ( $\tau$ ) is obtained on the exponential regression of each sensor response and is also considered on the compensation of the creep response. There are some power fluctuations on the sensor responses, which can be due to slight deviations on temperature and humidity during the test. Nevertheless, the exponential regression on the responses of each sensor showed a correlation coefficient higher than 0.9 on both cases, which indicate that these fluctuations do not significantly affect the creep response evaluation. The time constant of each sensor is also presented in Figure G-4, where the constant for the force sensor 2 is higher than the one of force sensor 1. This difference can be related to the variations in the fiber embedment conditions, since force sensors 1 and 2 have different structures.

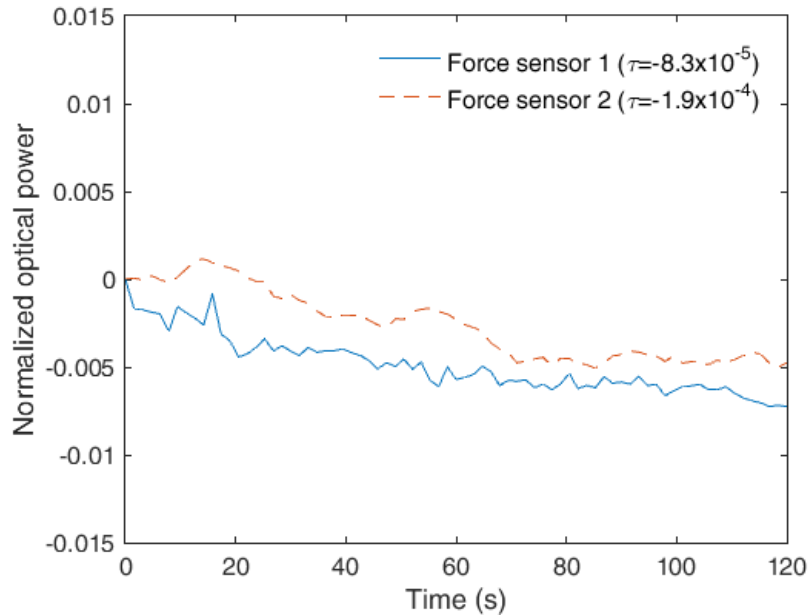


Figure G-4 Creep/relaxation tests with force sensors 1 and 2.

## Appendix H. Characterization of the FBG Array Embedded in TPU Structure for Human-robot Interaction Forces Assessment

The theoretical background (depicted in previous sections) has led to the development of the characterization methodology for the FBG-embedded force sensors, for which the sensors are characterized with respect to force, temperature and the simultaneous variation of both parameters. One may now evaluate the force sensitivity variation as a function of temperature, and enable the compensation of the temperature's influence on the sensor force response. The polymer response under a constant stress or strain is characterized by a creep (or recovery) that is described as a time-dependent viscous deformation when loading is applied [59]. An exponential regression was applied on the creep response, which was compensated by dividing the sensor response to the characterized time constant. It is worth to mention that the transverse force applied on the FBG also leads to birefringence and polarization effects, which causes a polarization dependent loss that increases linearly with the transverse force. Even though this principle was used on the development of

transverse force sensors [186], we considered only the wavelength shift caused by the applied force as shown in previous reported works for pressure [50] and force [212] sensors based on FBGs and described in Section 5.3 and 5.4.

As the POF is embedded in another polymer (TPU structure), the tests for the sensors' characterization have to be made for the whole structure in which the sensor is embedded. For this reason, each TPU structure (see Figure 6-40) with embedded FBGs is placed on the experimental setup shown in Figure H-1. The force is applied using calibrated weights positioned in the region indicated in Figure H-1, where the whole force is transmitted to the embedded FBG. These weights have a known mass and, thus, the applied force is also known. The range for the force characterization is up to 40 N (in 10 N steps) with a stabilization time of 5 minutes, whereas for the creep response characterization, a force of 20 N is applied and the sensor response is monitored over 10 minutes and the time constant of the FBG-embedded structure is experimentally obtained. For the temperature characterization, the TPU structure (with the setup for force characterization) is positioned on top of a Peltier plate (TEC1-12706, Hebei IT), which has its temperature controlled by a temperature controller (TED 200C, Thorlabs). The range of the temperature test is from 25°C to 45°C, in steps of 5°C with a stabilization time of about 5 minutes. This temperature range was chosen to ensure human comfort as described in [6], given that the proposed support will be in contact with the user. Additional force characterization tests are made at different temperatures (30 °C, 35 °C, 40 °C) to evaluate the sensitivity variation of the force sensor. Hence, by considering the sensitivity variation as a function of the temperature, it is possible to compensate the temperature effects on the sensor response, as described in Section 5.4.

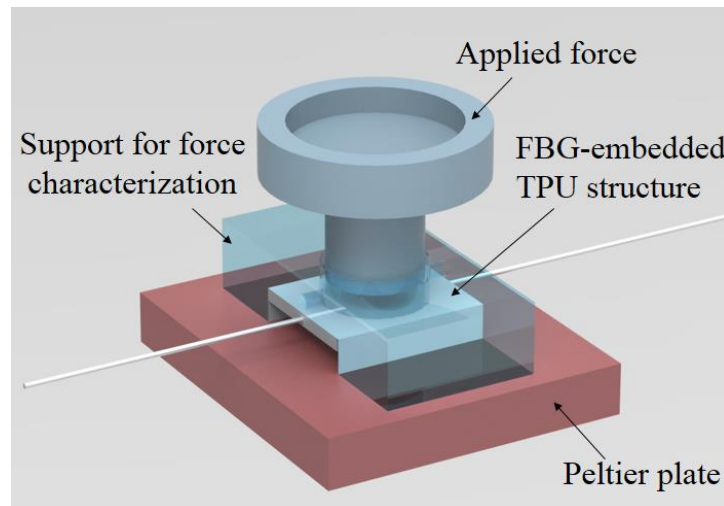


Figure H-1 Experimental setup for the FBG sensors (embedded in the TPU structure) characterization.

The results obtained in the force characterization at a constant temperature of 25 °C for FBG 1 and FBG 2 (embedded in shank support 1 and 2, respectively) are presented in Figure H-2, where the sensitivities of 57.8 pm/N and 63.1 pm/N were obtained for FBG 1 and FBG 2, respectively. In addition, the equations presented in Figure H-2 were obtained through the linear regression between the applied force and wavelength shift for FBGs 1 and 2. Compared to previous Section for which the force was directly applied on the fiber (without the 3D-printed structure), the obtained sensitivity was lower than the one without the TPU structure [196]. The reason for this behavior is the reduction of the strain transmitted to the fiber when it is embedded in a different structure. Moreover, the structure also influences the sensor linearity, which may be lower as a result of nonlinearities in the strain distribution along the TPU structure that are transmitted to the fiber. Comparing FBGs 1 and 2, the higher sensitivity of FBG 2 can be related either to the embedment process in the TPU structure or the differences on the material properties along the fiber, which may result from anisotropy and the annealing conditions. Although, the FBG 1 has lower force sensitivity, it also has higher linearity, which leads to lower errors in the force estimation.

The second step in the sensors' characterization is their temperature analysis without the influence of force. In this case, it is possible to estimate the offset that the temperature causes in the sensor's response. Figure H-3 shows the results of such temperature characterization for both FBGs. In contrast with the results obtained in force characterization, the temperature sensitivities for FBGs 1 and 2 (30.8 pm/°C, 27.8 pm/°C, respectively) are higher when compared with fiber that has not been embedded [44], [196]. Since the temperature increase also leads to a thermal expansion of the TPU structure, the thermally-induced strain in the structure is directly

transmitted to the FBG, which leads to an additional wavelength shift due to the TPU structure's thermal expansion, resulting in higher temperature sensitivity for the embedded sensor.

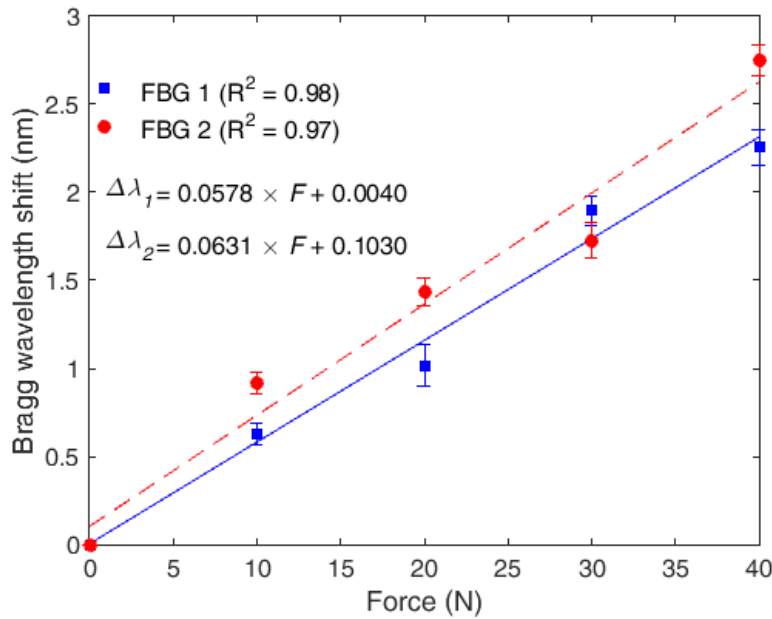


Figure H-2 Force characterization of FBG 1 (embedded in the shank flexible support 1) and FBG 2 (embedded in the shank flexible support 2) at constant temperature of 25 °C.

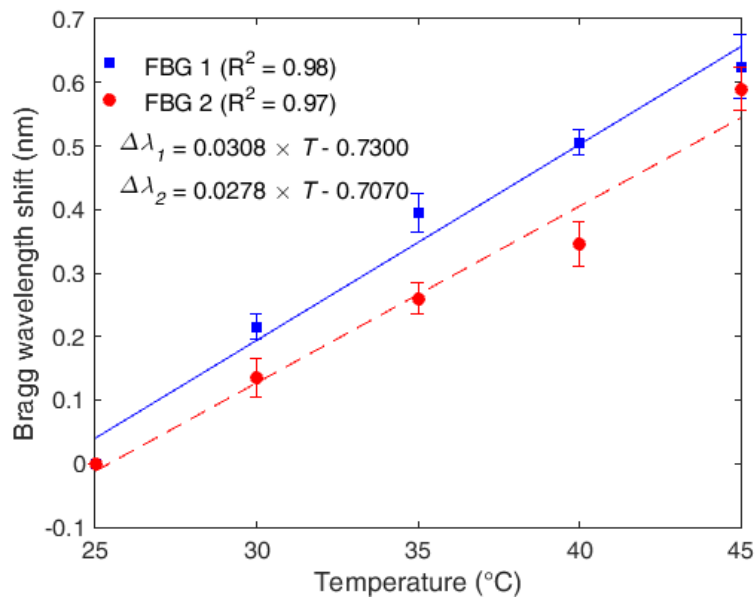


Figure H-3 Temperature characterization of FBG 1 (embedded in the shank flexible support 1) and FBG 2 (embedded in the shank flexible support 2).

After the temperature and force characterizations, each sensor is subjected to applied forces at different temperatures, in order to evaluate the force sensitivity variation as a function of temperature. Thus, the FBGs were characterized for different temperatures (30 °C, 35 °C and 40 °C) with the same force range (0 to 40 N) as used for the test at room temperature (25 °C). The results of the characterization at different temperatures for FBG 1 and 2 are presented in Figure H-4(a) and (b), respectively. In addition, the force sensitivity of both FBGs at each temperature is shown in Figure H-4(c). The results show an increase in the sensor sensitivity when the force is applied at higher temperature conditions, which is expected since the Young's modulus of the fiber is reduced as the temperature increases [197]. However, the POF is embedded in a structure made of another polymer (TPU, in this case), which also has its own Young's modulus dependency with temperature. For this reason, the sensitivity variation with respect to the temperature has some differences when compared with unembedded CYTOP (shown in Section 5.4). In this case, a linear regression for the sensors' force sensitivities was obtained for each FBG, where the coefficients presented in Figure H-4(c) show a higher

temperature dependency on the force response of FBG 2, which can be related to minor differences in the embedment conditions.

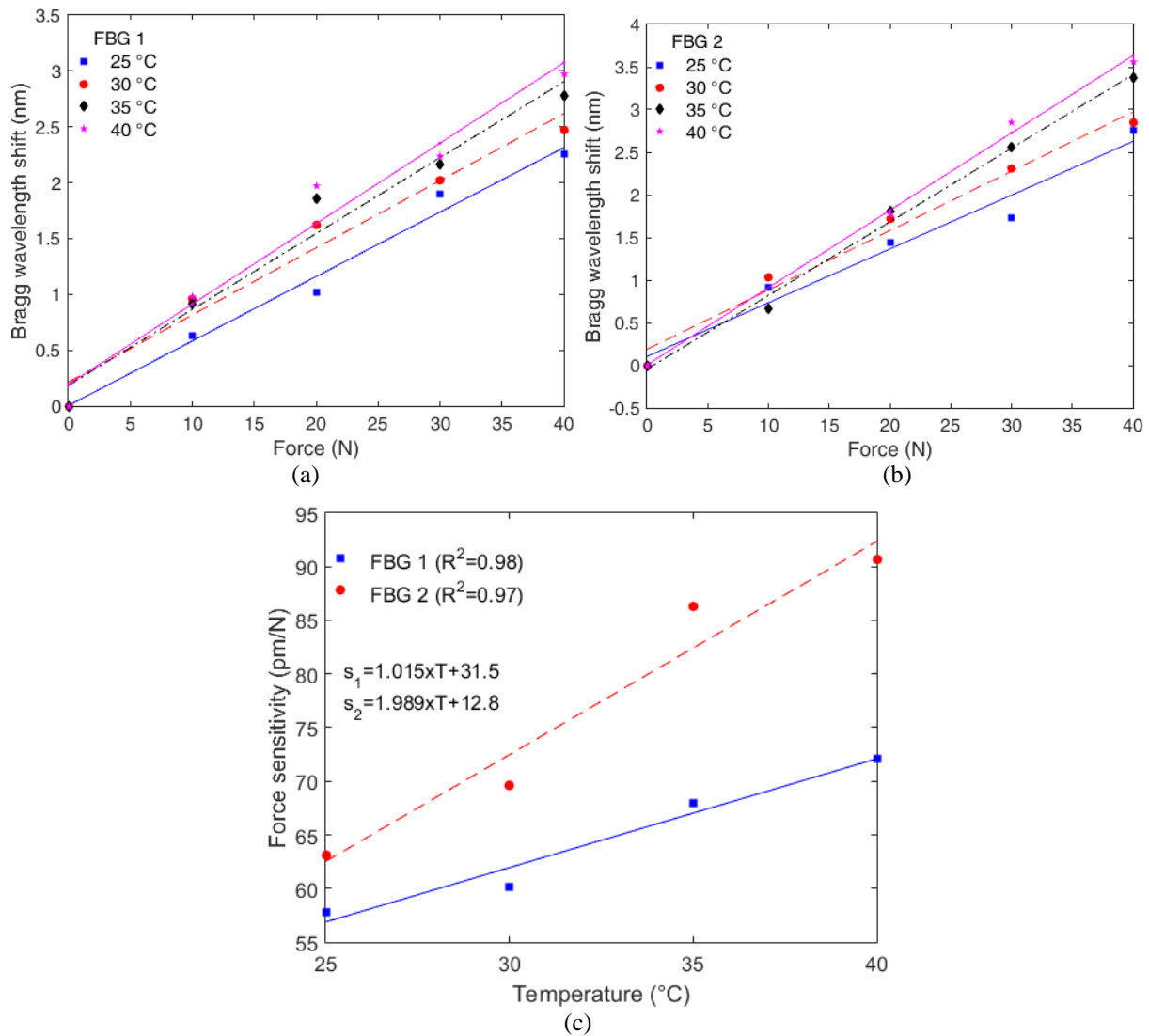


Figure H-4 (a) Force characterization at different temperatures for FBG 1. (b) Force characterization at different temperatures for FBG 2. (c) Force sensitivity as a function of the temperature for FBGs 1 and 2.

For the last set of characterization tests, the FBGs were positioned on the experimental setup of Figure H-1 and a constant force was applied on each FBG at constant temperature of  $\sim 22^\circ\text{C}$  (room temperature). The sensor response is monitored for 5 minutes and an exponential regression was performed on the response of each FBG, as shown in Figure H-5. The creep response characterization of FBG 1 and 2 was not made at the same time due to operational limitations. Thus, the reason for the slightly increase on the wavelength shift of FBG 1 is related to an increase at room temperature of about  $1^\circ\text{C}$  on its characterization. In addition, if the material is thermorheologically simple, temperature variations will only lead to an offset on the polymer viscoelastic response [59]. It was demonstrated in [58] that PMMA behaves as a thermorheologically simple on the time and temperature ranges used on the sensor characterization. Since PMMA and CYTOP have similarities on the molecular structure, one can assume for simplification that the CYTOP is also a thermorheologically simple material and the temperature variations will result in an offset of the material response.

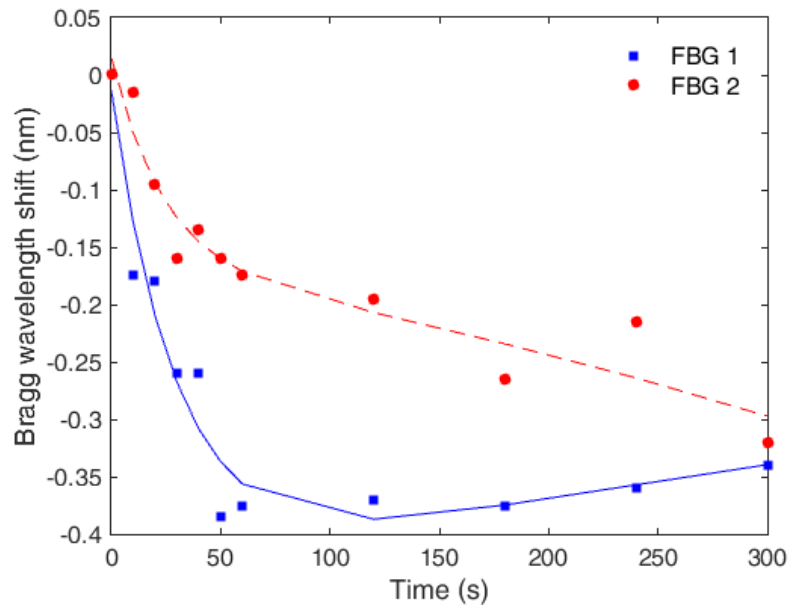


Figure H-5 Creep response and exponential regression for FBG 1 and 2 for 5 minutes.

Applying the results and regressions of each characterization, one can obtain a characterization equation for each FBG in which the effects of creep and temperature are compensated. For this reason, the linear regressions for force response at room temperature for FBGs 1 and 2 are applied with the isolation of the force term (see Figure H-2). Then, the compensation for the creep response is applied in the measured wavelength shift ( $\Delta\lambda_c$ ), whereas the force sensitivity as a function of the temperature, as shown in Figure H-4(c), is also applied. The offset in the force response due to the temperature ( $T_r$ ) is also considered by means of applying the temperature regression presented in Figure H-3.

## Appendix I. Numerical Analysis of the FBG Array on the Torsional Spring

In order to evaluate the spring deflection at each of the points where the FBG sensors are placed, a numerical simulation is performed on the spring through FEM analysis using the Ansys Workbench 15.0. In the analysis, the outer cylinder is fixed, whereas a torque is applied on the inner cylinder (the one where the output shaft is placed). Figure I-1 shows the results obtained in the simulation for flexion (Figure I-1(a)) and extension (Figure I-1(b)), where a torque with same magnitude (20 Nm), but different direction (flexion and extension) was applied.

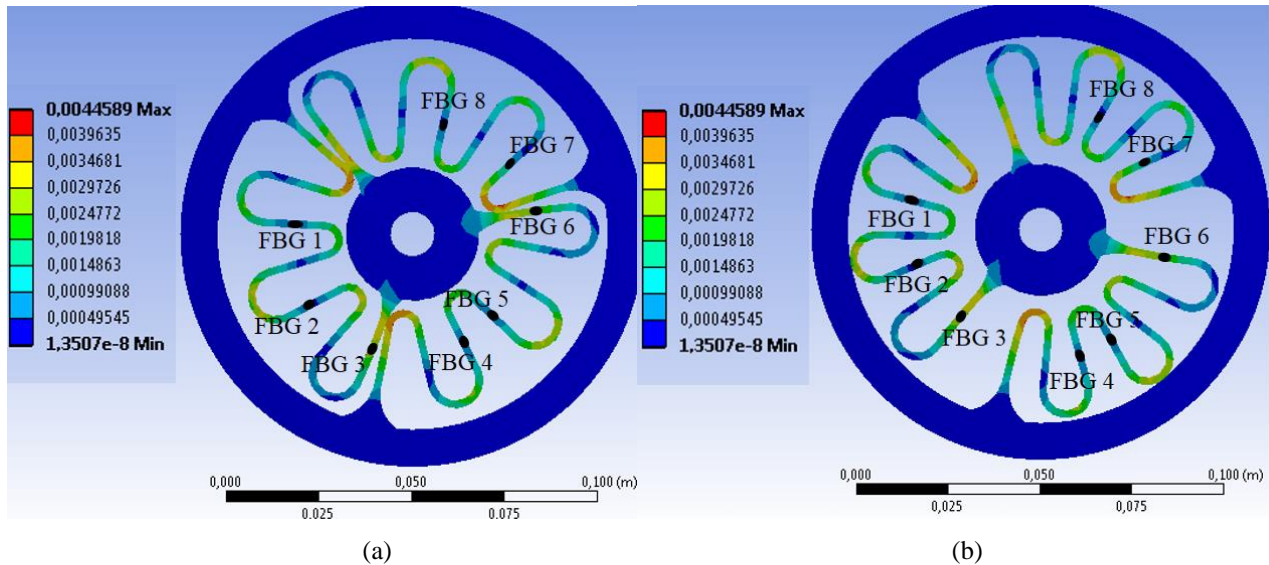


Figure I-1 Equivalent strain (m/m) on the spring under (a) flexion and (b) extension.

The simulation results from Figure I-1 indicate that there is a strain variation in all points analyzed proportional to the applied torque (following Hooke's law). It also shows the polarity of the strain, where the strain pattern is similar on flexion and extension cases, but with different directions. If the clockwise direction (flexion cycle) is attributed as the positive direction, the strain at the counter-clockwise direction has the same magnitude, but with the negative signal (indicating different direction). After verifying the spring behavior under flexion/extension cycles, another numerical analysis is made to verify the effect of an external force applied on the front plane of the spring (see Figure I-2). This transverse force acts as a mechanical disturbance on the system, which needs to be evaluated by the sensor array. Figure I-2 shows the strain on the spring after the application of an arbitrary transverse force, which has 5 N magnitude in the simulation.

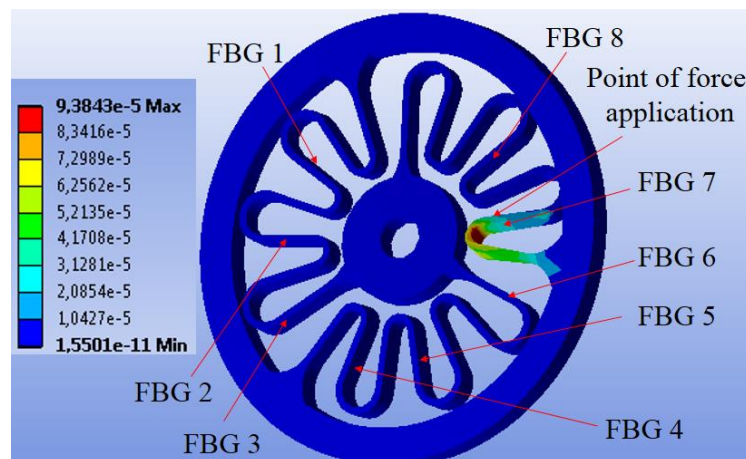


Figure I-2 Equivalent strain (m/m) on the spring under a transverse force of 5 N.

The transverse force simulation shows that there is a stress concentration on regions close to the point of force application, which leads to higher strain in the FBGs close to this region. Thus, by analyzing the response all FBGs in the spring, it is possible to infer if the strain is caused by a transverse force or by the flexion/extension, since the position of each FBG is known. In this way, a simple and straightforward manner to analyze if the spring deflection is due to flexion and extension or transverse mechanical disturbances is to analyze the

differences on the wavelength shift of FBGs positioned on the spring. Then, compare it with the case where only flexion and extension torques are applied on the spring.

## Bibliography

- [1] Source, Undesa, and Population, “Setting the scene Global population ageing,” 2012.
- [2] World Health Organization, “Key Facts,” *Ageing and health*, 2018. [Online]. Available: <http://www.who.int/news-room/fact-sheets/detail/ageing-and-health>. [Accessed: 22-Oct-2018].
- [3] W. Huo, S. Mohammed, J. C. Moreno, and Y. Amirat, “Lower Limb Wearable Robots for Assistance and Rehabilitation: A State of the Art,” *IEEE Syst. J.*, vol. 10, no. 3, pp. 1068–1081, 2016.
- [4] S. Majumder, T. Mondal, and M. Deen, “Wearable Sensors for Remote Health Monitoring,” *Sensors*, vol. 17, no. 12, p. 130, Jan. 2017.
- [5] M. M. Martins, C. P. Santos, A. Frizera-Neto, and R. Ceres, “Assistive mobility devices focusing on Smart Walkers: Classification and review,” *Rob. Auton. Syst.*, vol. 60, no. 4, pp. 548–562, 2012.
- [6] J. C. Moreno, L. Bueno, J. L. Pons, J. M. Baydal-Bertomeu, J. M. Belda-Lois, J. M. Prat, and R. Barberá, *Wearable Robot Technologies*. 2008.
- [7] K. H. Ha, H. A. Varol, and M. Goldfarb, “Volitional control of a prosthetic knee using surface electromyography,” *IEEE Trans. Biomed. Eng.*, vol. 58, no. 1, pp. 144–151, 2011.
- [8] C. Bayón, S. Lerma, O. Ramírez, J. I. Serrano, M. D. Del Castillo, R. Raya, J. M. Belda-Lois, I. Martínez, and E. Rocon, “Locomotor training through a novel robotic platform for gait rehabilitation in pediatric population: short report,” *J. Neuroeng. Rehabil.*, vol. 13, no. 1, p. 98, 2016.
- [9] W. M. dos Santos, G. A. P. Caurin, and A. A. G. Siqueira, “Design and control of an active knee orthosis driven by a rotary Series Elastic Actuator,” *Control Eng. Pract.*, pp. 1–12, 2015.
- [10] M. Martins, C. Santos, A. Frizera, and R. Ceres, “A review of the functionalities of smart walkers,” *Med. Eng. Phys.*, vol. 37, no. 10, pp. 917–928, 2015.
- [11] G. Kwakkel, B. J. Kollen, and H. I. Krebs, “Effects of Robot-Assisted Therapy on Upper Limb Recovery After Stroke: A Systematic Review,” *Neurorehabil. Neural Repair*, vol. 22, no. 2, pp. 111–121, Mar. 2008.
- [12] L. Bueno, F. Brunetti, A. Frizera, and J. L. Pons, *Human – robot cognitive interaction*, no. 1998. 2008.
- [13] A. H. Abdul Razak, A. Zayegh, R. K. Begg, and Y. Wahab, “Foot Plantar Pressure Measurement System: A Review,” *Sensors*, vol. 12, no. 7, pp. 9884–9912, Jul. 2012.
- [14] D. S. Teyhen, B. E. Stoltenberg, K. M. Collinsworth, C. L. Giesel, D. G. Williams, C. H. Kardouni, J. M. Molloy, S. L. Goffar, D. S. Christie, and T. McPoil, “Dynamic plantar pressure parameters associated with static arch height index during gait,” *Clin. Biomech.*, vol. 24, no. 4, pp. 391–396, 2009.
- [15] A. G. Leal-Junior, A. Frizera, L. M. Avellar, C. Marques, and M. J. Pontes, “Polymer Optical Fiber for In-Shoe Monitoring of Ground Reaction Forces During the Gait,” *IEEE Sens. J.*, vol. 18, no. 6, pp. 2362–2368, Mar. 2018.
- [16] J. Taborri, E. Palermo, S. Rossi, and P. Cappa, “Gait Partitioning Methods: A Systematic Review,” *Sensors*, vol. 16, no. 1, p. 66, Jan. 2016.
- [17] A. Villa-Parra, D. Delisle-Rodriguez, J. Souza Lima, A. Frizera-Neto, and T. Bastos, “Knee Impedance Modulation to Control an Active Orthosis Using Insole Sensors,” *Sensors*, vol. 17, no. 12, p. 2751, 2017.
- [18] A. G. Leal-Junior, A. Frizera, L. Vargas-Valencia, W. M. dos Santos, A. P. L. Bo, A. A. G. Siqueira, and M. J. Pontes, “Polymer Optical Fiber Sensors in Wearable Devices: Toward Novel Instrumentation Approaches for Gait Assistance Devices,” *IEEE Sens. J.*, vol. 18, no. 17, pp. 7085–7092, Sep. 2018.
- [19] H. Dejnabadi, B. M. Jolles, and K. Aminian, “A new approach to accurate measurement of uniaxial joint angles based on a combination of accelerometers and gyroscopes,” *IEEE Trans. Biomed. Eng.*, vol. 52, no. 8, pp. 1478–1484, 2005.
- [20] D. Hawkins, “A new instrumentation system for training rowers,” *J. Biomech.*, vol. 33, no. 2, pp. 241–245, 2000.
- [21] K. Tong and M. H. Granat, “A practical gait analysis system using gyroscopes.pdf,” *Med. Eng. Phys.*, vol. 21, pp. 87–94, 1999.
- [22] A. Nag, S. C. Mukhopadhyay, and J. Kosel, “Wearable Flexible Sensors: A Review,” *IEEE Sens. J.*, vol. 17, no. 13, pp. 3949–3960, Jul. 2017.
- [23] I. Korhonen, J. Pärkkä, and M. Van Gils, “Health Monitoring in the Home of the Future,” *IEEE Eng. Med. Biol. Mag.*, vol. 22, no. 3, pp. 66–73, 2003.
- [24] M. Böhm, J. C. Reil, P. Deedwania, J. B. Kim, and J. S. Borer, “Resting heart rate: Risk indicator and emerging

- risk factor in cardiovascular disease,” *Am. J. Med.*, vol. 128, no. 3, pp. 219–228, 2015.
- [25] M. Nishyama, M. Miyamoto, and K. Watanabe, “Respiration and body movement analysis during sleep in bed using hetero-core fiber optic pressure sensors without constraint to human activity,” *J. Biomed. Opt.*, vol. 16, no. 1, p. 17002, 2011.
- [26] R. Strauß, S. Ewig, K. Richter, T. König, G. Heller, and T. T. Bauer, “The Prognostic Significance of Respiratory Rate in Patients With Pneumonia,” *Dtsch. Aerzteblatt Online*, vol. 111, no. 29–30, pp. 503–508, Jul. 2014.
- [27] M. El-Gohary and J. McNames, “Shoulder and elbow joint angle tracking with inertial sensors,” *IEEE Trans. Biomed. Eng.*, vol. 59, no. 9, pp. 2635–2641, 2012.
- [28] A. G. Leal-Junior, A. Frizera, C. Marques, M. R. A. Sánchez, T. R. Botelho, M. V. Segatto, and M. J. Pontes, “Polymer optical fiber strain gauge for human-robot interaction forces assessment on an active knee orthosis,” *Opt. Fiber Technol.*, vol. 41, no. December 2017, pp. 205–211, 2018.
- [29] M. Manti, V. Cacucciolo, and M. Cianchetti, “Stiffening in soft robotics: A review of the state of the art,” *IEEE Robot. Autom. Mag.*, vol. 23, no. 3, pp. 93–106, 2016.
- [30] L. N. Awad, J. Bae, K. O’Donnell, S. M. M. De Rossi, K. Hendron, L. H. Slood, P. Kudzia, S. Allen, K. G. Holt, T. D. Ellis, and C. J. Walsh, “A soft robotic exosuit improves walking in patients after stroke,” *Sci. Transl. Med.*, vol. 9, no. 400, p. eaai9084, Jul. 2017.
- [31] C. Walsh, “Human-in-the-loop development of soft wearable robots,” *Nature Reviews Materials*, 02-Jun-2018. [Online]. Available: <http://dx.doi.org/10.1038/s41578-018-0011-1>.
- [32] C. A. Cifuentes, A. Frizera, R. Carelli, and T. Bastos, “Human-robot interaction based on wearable IMU sensor and laser range finder,” *Rob. Auton. Syst.*, vol. 62, no. 10, pp. 1425–1439, 2014.
- [33] C. A. Cifuentes, C. Rodriguez, A. Frizera-neto, T. F. Bastos-filho, R. Carelli, and S. Member, “Multimodal Human – Robot Interaction for Walker-Assisted Gait,” *Ieee Syst. J.*, pp. 1–11, 2014.
- [34] B. Culshaw, “Optical fibre sensors for industrial applications in safety and security,” *Opt. InfoBase Conf. Pap.*, pp. 1–3, 2013.
- [35] M. J. Mueller, K. E. Smith, P. K. Commean, D. D. Robertson, and J. E. Johnson, “Use of computed tomography and plantar pressure measurement for management of neuropathic ulcers in patients with diabetes,” *Phys. Ther.*, vol. 79, no. 3, pp. 296–307, 1999.
- [36] L. Ballaz, M. Raison, and C. Detrembleur, “Decomposition of the vertical ground reaction forces during gait on a single force plate,” *J. Musculoskelet. Neuronal Interact.*, vol. 13, no. 2, pp. 236–243, 2013.
- [37] L. Shu, T. Hua, Y. Wang, Q. Qiao Li, D. D. Feng, and X. Tao, “In-shoe plantar pressure measurement and analysis system based on fabric pressure sensing array,” *IEEE Trans. Inf. Technol. Biomed.*, vol. 14, no. 3, pp. 767–775, 2010.
- [38] S. C. Mukhopadhyay, “Wearable Sensors for Human Activity Monitoring : A Review,” vol. 15, no. 3, pp. 1321–1330, 2015.
- [39] D. J. Sanderson, I. M. Franks, and D. Elliott, “The effects of targeting on the ground reaction forces during level walking,” *Hum. Mov. Sci.*, vol. 12, no. 3, pp. 327–337, 1993.
- [40] A. G. Leal-Junior, A. Frizera, L. M. Avellar, C. Marques, and M. J. Pontes, “Polymer Optical Fiber for In-Shoe Monitoring of Ground Reaction Forces during the Gait,” *IEEE Sens. J.*, vol. 18, no. 6, pp. 2362–2368, 2018.
- [41] K. Peters, “Polymer optical fiber sensors—a review,” *Smart Mater. Struct.*, vol. 20, no. 1, p. 13002, 2011.
- [42] L. Alwis, T. Sun, and K. T. V Grattan, “Developments in optical fibre sensors for industrial applications,” *Opt. Laser Technol.*, vol. 78, pp. 62–66, 2016.
- [43] V. Mishra, N. Singh, U. Tiwari, and P. Kapur, “Fiber grating sensors in medicine: Current and emerging applications,” *Sensors Actuators, A Phys.*, vol. 167, no. 2, pp. 279–290, 2011.
- [44] A. Theodosiou, M. Komodromos, and K. Kalli, “Carbon Cantilever Beam Health Inspection Using a Polymer Fiber Bragg Grating Array,” *J. Light. Technol.*, vol. 36, no. 4, pp. 986–992, Feb. 2018.
- [45] A. G. Leal-Junior, A. Frizera, and M. José Pontes, “Sensitive zone parameters and curvature radius evaluation for polymer optical fiber curvature sensors,” *Opt. Laser Technol.*, vol. 100, pp. 272–281, 2018.
- [46] N. Zhong, Q. Liao, X. Zhu, M. Zhao, Y. Huang, and R. Chen, “Temperature-independent polymer optical fiber evanescent wave sensor,” *Sci. Rep.*, vol. 5, pp. 1–10, 2015.
- [47] A. Leal-Junior, A. Frizera-Neto, C. Marques, and M. Pontes, “A Polymer Optical Fiber Temperature Sensor Based on Material Features,” *Sensors*, vol. 18, no. 2, p. 301, Jan. 2018.

- [48] G. Rajan, Y. M. Noor, B. Liu, E. Ambikairaja, D. J. Webb, and G. D. Peng, "A fast response intrinsic humidity sensor based on an etched singlemode polymer fiber Bragg grating," *Sensors Actuators, A Phys.*, vol. 203, pp. 107–111, 2013.
- [49] A. Stefani, S. Andresen, W. Yuan, N. Herholdt-Rasmussen, and O. Bang, "High sensitivity polymer optical fiber-bragg-grating-based accelerometer," *IEEE Photonics Technol. Lett.*, vol. 24, no. 9, pp. 763–765, 2012.
- [50] D. Vilarinho, A. Theodosiou, C. Leitão, A. Leal-Junior, M. Domingues, K. Kalli, P. André, P. Antunes, and C. Marques, "POFBG-Embedded Cork Insole for Plantar Pressure Monitoring," *Sensors*, vol. 17, no. 12, p. 2924, Dec. 2017.
- [51] Z. Chen, D. Lau, J. T. Teo, S. H. Ng, X. Yang, and P. L. Kei, "Simultaneous measurement of breathing rate and heart rate using a microbend multimode fiber optic sensor," *J. Biomed. Opt.*, vol. 19, no. 5, p. 57001, 2014.
- [52] M. Krehel, M. Wolf, L. F. Boesel, R. M. Rossi, G.-L. Bona, and L. J. Scherer, "Development of a luminous textile for reflective pulse oximetry measurements," *Biomed. Opt. Express*, vol. 5, no. 8, p. 2537, 2014.
- [53] M. Krehel, M. Schmid, R. M. Rossi, L. F. Boesel, G. L. Bona, and L. J. Scherer, "An optical fibre-based sensor for respiratory monitoring," *Sensors (Switzerland)*, vol. 14, no. 7, pp. 13088–13101, 2014.
- [54] J. Z. Gul, M. Sajid, M. M. Rehman, G. U. Siddiqui, I. Shah, K.-H. Kim, J.-W. Lee, and K. H. Choi, "3D printing for soft robotics – a review," *Sci. Technol. Adv. Mater.*, vol. 19, no. 1, pp. 243–262, Dec. 2018.
- [55] L. Fang, T. Chen, R. Li, and S. Liu, "Application of Embedded Fiber Bragg Grating (FBG) Sensors in Monitoring Health to 3D Printing Structures," *IEEE Sens. J.*, vol. 16, no. 17, pp. 6604–6610, 2016.
- [56] Y.-F. Zhang, C.-Y. Hong, R. Ahmed, and Z. Ahmed, "A fiber Bragg grating based sensing platform fabricated by fused deposition modeling process for plantar pressure measurement," *Measurement*, vol. 112, no. April, pp. 74–79, 2017.
- [57] A. Leal-Junior, A. Theodosiou, A. Frizera-Neto, M. José Pontes, E. Shafir, O. Palchik, N. Tal, S. Zilberman, G. Berkovic, P. Antunes, P. André, K. Kalli, and C. Marques, "Characterization of a new polymer optical fiber with enhanced sensing capabilities using a Bragg grating," *Opt. Lett.*, vol. 43, no. 19, 2018.
- [58] A. G. Leal-Junior, C. Marques, A. Frizera, and M. J. Pontes, "Dynamic Mechanical Analysis on a PolyMethyl Methacrylate (PMMA) Polymer Optical Fiber," *IEEE Sens. J.*, vol. 18, no. 6, pp. 2353–2361, Mar. 2018.
- [59] R. Lakes, *Viscoelastic Materials*. Cambridge: Cambridge University Press, 2009.
- [60] A. Leal-Junior, A. Frizera, C. Marques, and M. José Pontes, "Polymer-optical-fiber-based sensor system for simultaneous measurement of angle and temperature," *Appl. Opt.*, vol. 57, no. 7, p. 1717, Mar. 2018.
- [61] A. Leal-Junior, A. Frizera, L. E. E. Heeyoung, Y. Mizuno, K. Nakamura, T. Paixão, C. Leitão, M. Fátima Domingues, N. Alberto, P. Antunes, P. Andre, C. Marques, and M. J. Pontes, "Strain, temperature, moisture, and transverse force sensing using fused polymer optical fibers," *Opt. Express*, vol. 26, no. 10, 2018.
- [62] R. da Silva Marques, A. R. Prado, P. F. da Costa Antunes, P. S. de Brito André, M. R. N. Ribeiro, A. Frizera-Neto, and M. J. Pontes, "Corrosion resistant FBG-based quasi-distributed sensor for crude oil tank dynamic temperature profile monitoring," *Sensors*, vol. 15, no. 12, pp. 30693–30703, 2015.
- [63] Y. Liu, W. Peng, Y. Liang, X. Zhang, X. Zhou, and L. Pan, "Fiber-optic Mach-Zehnder interferometric sensor for high-sensitivity high temperature measurement," *Opt. Commun.*, vol. 300, pp. 194–198, 2013.
- [64] A. Minardo, R. Bernini, and L. Zeni, "Distributed temperature sensing in polymer optical fiber by BOFDA," *IEEE Photonics Technol. Lett.*, vol. 26, no. 4, pp. 387–390, 2014.
- [65] A. Tapetado, P. J. Pinzon, J. Zubia, and C. Vazquez, "Polymer Optical Fiber Temperature Sensor With Dual-Wavelength Compensation of Power Fluctuations," *J. Light. Technol.*, vol. 33, no. 13, pp. 2716–2723, Jul. 2015.
- [66] L. Bilro, N. Alberto, J. L. Pinto, and R. Nogueira, "Optical sensors based on plastic fibers," *Sensors (Switzerland)*, vol. 12, no. 9, pp. 12184–12207, 2012.
- [67] A. T. Moraleda, C. V. Garcia, J. Z. Zaballa, and J. Arrue, "A temperature sensor based on a polymer optical fiber macro-bend," *Sensors (Basel)*, vol. 13, no. 10, pp. 13076–13089, 2013.
- [68] Y. Luo, B. Yan, Q. Zhang, G.-D. Peng, J. Wen, and J. Zhang, "Fabrication of Polymer Optical Fibre (POF) Gratings," *Sensors*, vol. 17, no. 3, p. 511, 2017.
- [69] A. Lacraz, A. Theodosiou, and K. Kalli, "Femtosecond laser inscribed Bragg grating arrays in long lengths of polymer optical fibres; a route to practical sensing with POF," *Electron. Lett.*, vol. 52, no. 19, pp. 1626–1627, Sep. 2016.
- [70] C. A. F. Marques, R. Min, A. Leal Junior, P. Antunes, A. Fasano, G. Woyessa, K. Nielsen, H. K. Rasmussen, B.

- Ortega, and O. Bang, "Fast and stable gratings inscription in POFs made of different materials with pulsed 248 nm KrF laser," *Opt. Express*, vol. 26, no. 2, p. 2013, Jan. 2018.
- [71] A. Lacraz, M. Polis, A. Theodosiou, C. Koutsides, and K. Kalli, "Femtosecond Laser Inscribed Bragg Gratings in Low Loss CYTOP Polymer Optical Fiber," *IEEE Photonics Technol. Lett.*, vol. 27, no. 7, pp. 693–696, 2015.
- [72] C. Marques, A. Leal-Junior, R. Min, M. Domingues, C. Leitão, P. Antunes, B. Ortega, and P. André, "Advances on Polymer Optical Fiber Gratings Using a KrF Pulsed Laser System Operating at 248 nm," *Fibers*, vol. 6, no. 1, p. 13, 2018.
- [73] Y. Koike and M. Asai, "The future of plastic optical fiber," *NPG Asia Mater.*, vol. 1, no. 1, pp. 22–28, 2009.
- [74] A. Theodosiou, A. Lacraz, A. Stassis, C. Koutsides, M. Komodromos, and K. Kalli, "Plane-by-Plane Femtosecond Laser Inscription Method for Single-Peak Bragg Gratings in Multimode CYTOP Polymer Optical Fiber," *J. Light. Technol.*, vol. 35, no. 24, pp. 5404–5410, Dec. 2017.
- [75] J. Zubia and J. Arrue, "Plastic Optical Fibers: An Introduction to Their Technological Processes and Applications," *Opt. Fiber Technol.*, vol. 7, no. 2, pp. 101–140, 2001.
- [76] O. Ziemann, J. Krauser, P. E. Zamzow, and W. Daum, *POF Handbook*. Berlin, Heidelberg: Springer Berlin Heidelberg, 2008.
- [77] C. Markos, J. C. Travers, A. Abdolvand, B. J. Eggleton, and O. Bang, "Hybrid photonic-crystal fiber," *Rev. Mod. Phys.*, vol. 89, no. 4, pp. 1–55, 2017.
- [78] M. C. J. Large, J. Moran, and L. Ye, "The role of viscoelastic properties in strain testing using microstructured polymer optical fibres (mPOF)," *Meas. Sci. Technol.*, vol. 20, no. 3, p. 34014, 2009.
- [79] C. Markos, A. Stefani, K. Nielsen, H. K. Rasmussen, W. Yuan, and O. Bang, "High-Tg TOPAS microstructured polymer optical fiber for fiber Bragg grating strain sensing at 110 degrees.," *Opt. Express*, vol. 21, no. 4, pp. 4758–65, 2013.
- [80] W. Yuan, L. Khan, D. J. Webb, K. Kalli, H. K. Rasmussen, A. Stefani, and O. Bang, "Humidity insensitive TOPAS polymer fiber Bragg grating sensor.," *Opt. Express*, vol. 19, no. 20, pp. 19731–9, 2011.
- [81] J. B. Jensen, P. E. Hoiby, G. Emilianov, O. Bang, L. H. Pedersen, and A. Bjarklev, "Selective detection of antibodies in microstructured polymer optical fibers," *Opt. Express*, vol. 13, no. 15, p. 5883, 2005.
- [82] R. Oliveira, L. Bilro, and R. Nogueira, "Bragg gratings in a few mode microstructured polymer optical fiber in less than 30 seconds," *Opt. Express*, vol. 23, no. 8, p. 10181, 2015.
- [83] D. J. Webb, "Fibre Bragg grating sensors in polymer optical fibres," *Meas. Sci. Technol.*, vol. 26, no. 9, p. 92004, 2015.
- [84] M. G. Kuzyk, U. C. Paek, and C. W. Dirk, "Guest-Host Fibers for Nonlinear Optics," *Appl. Phys. Lett.*, vol. 59, no. 8, p. 902, 1991.
- [85] G. Woyessa, A. Fasano, A. Stefani, C. Markos, K. Nielsen, H. K. Rasmussen, and O. Bang, "Single mode step-index polymer optical fiber for humidity insensitive high temperature fiber Bragg grating sensors," *Opt. Express*, vol. 24, no. 2, pp. 1253–1260, 2016.
- [86] A. G. Leal-Junior, A. Frizera, R. Min, M. J. Pontes, A. Fasano, G. T. Woyessa, O. Bang, and C. Marques, "Influence of the cladding structure in PMMA mPOFs mechanical properties for strain sensors applications," *IEEE Sens. J.*, vol. 18, no. 14, 2018.
- [87] C. A. F. Marques, D. J. Webb, and P. Andre, "Polymer optical fiber sensors in human life safety," *Opt. Fiber Technol.*, vol. 36, pp. 144–154, 2017.
- [88] A. Fasano, G. Woyessa, P. Stajanca, C. Markos, A. Stefani, K. Nielsen, H. K. Rasmussen, K. Krebber, and O. Bang, "Fabrication and characterization of polycarbonate microstructured polymer optical fibers for high-temperature-resistant fiber Bragg grating strain sensors," *Opt. Mater. Express*, vol. 6, no. 2, p. 649, 2016.
- [89] I. P. Johnson, W. Yuan, A. Stefani, K. Nielsen, H. K. Rasmussen, L. Khan, D. J. Webb, K. Kalli, and O. Bang, "Optical fibre Bragg grating recorded in TOPAS cyclic olefin copolymer," *Electron. Lett.*, vol. 47, no. 4, p. 271, 2011.
- [90] G. Woyessa, A. Fasano, C. Markos, A. Stefani, H. K. Rasmussen, and O. Bang, "Zeonex microstructured polymer optical fiber: fabrication friendly fibers for high temperature and humidity insensitive Bragg grating sensing," *Opt. Mater. Express*, vol. 7, no. 1, p. 286, 2017.
- [91] A. Stefani, K. Nielsen, H. K. Rasmussen, and O. Bang, "Cleaving of TOPAS and PMMA microstructured polymer optical fibers: Core-shift and statistical quality optimization," *Opt. Commun.*, vol. 285, no. 7, pp. 1825–1833, 2012.

- [92] K. Nielsen, H. K. Rasmussen, A. J. Adam, P. C. Planken, O. Bang, and P. U. Jepsen, "Bendable, low-loss Topas fibers for the terahertz frequency range," *Opt. Express*, vol. 17, no. 10, pp. 8592–8601, 2009.
- [93] K. Nielsen, H. K. Rasmussen, P. U. Jepsen, and O. Bang, "Broadband terahertz fiber directional coupler," *Opt. Lett.*, vol. 35, no. 17, pp. 2879–2881, 2010.
- [94] J. Anthony, R. Leonhardt, A. Argyros, and M. C. J. Large, "Characterization of a microstructured Zeonex terahertz fiber," *J. Opt. Soc. Am. B*, vol. 28, no. 5, p. 1013, May 2011.
- [95] G. Woyessa, A. Fasano, C. Markos, H. Rasmussen, and O. Bang, "Low loss polycarbonate polymer optical fiber for high temperature FBG humidity sensing," *IEEE Photonics Technol. Lett.*, vol. 29, no. 7, pp. 1–1, 2017.
- [96] D. Kinet, P. Mégret, K. Goossen, L. Qiu, D. Heider, and C. Caucheteur, "Fiber Bragg Grating Sensors toward Structural Health Monitoring in Composite Materials: Challenges and Solutions," *Sensors*, vol. 14, no. 4, pp. 7394–7419, 2014.
- [97] Y. Zhang, H. Peng, X. Qian, Y. Zhang, G. An, and Y. Zhao, "Recent advancements in optical fiber hydrogen sensors," *Sensors Actuators B Chem.*, vol. 244, pp. 393–416, 2017.
- [98] R. Oliveira, T. H. R. Marques, L. Bilro, R. Nogueira, and C. M. B. Cordeiro, "Multiparameter POF Sensing Based on Multimode Interference and Fiber Bragg Grating," *J. Light. Technol.*, vol. 35, no. 1, pp. 3–9, 2017.
- [99] Z. Bai, M. Li, J. Zhao, S. Cao, Y. Wang, C. Liao, and Y. Wang, "Influence of Side-Polished Fiber Surface Topography on Surface Plasmon Resonance Wavelengths and the Full Width at Half-Maximum," *IEEE Photonics J.*, vol. 9, no. 2, pp. 1–13, 2017.
- [100] W. S. Fegadolli, J. E. B. Oliveira, and V. R. Almeida, "Plastic Optical Fiber Microbend Sensors," *Electromagnetics*, pp. 842–845, 2008.
- [101] Z. Chen, J. T. Teo, S. H. Ng, and X. Yang, "Plastic optical fiber microbend sensor used as breathing sensor," *Proc. IEEE Sensors*, 2012.
- [102] K. S. C. Kuang, W. J. Cantwell, and P. J. Scully, "An evaluation of a novel plastic optical fibre sensor for axial strain and bend measurements," *Meas. Sci. Technol.*, vol. 13, no. 10, pp. 1523–1534, 2002.
- [103] Y. Hou, W.-Y. Liu, S. Su, H.-X. Zhang, J. Zhang, J. Liu, and J. Xiong, "Polymer optical fiber twisted macro-bend coupling system for liquid level detection," *Opt. Express*, vol. 22, no. 19, p. 23231, 2014.
- [104] H. Zhang, L. Feng, Y. Hou, S. Su, W. Liu, J. Liu, and J. Xiong, "Optical fiber liquid level sensor based on macro-bending coupling," *Opt. Fiber Technol.*, vol. 24, pp. 135–139, 2015.
- [105] P. F. C. Antunes, H. Varum, and P. S. Andre, "Intensity-encoded polymer optical fiber accelerometer," *IEEE Sens. J.*, vol. 13, no. 5, pp. 1716–1720, 2013.
- [106] a. Vallan, a. Carullo, M. L. Casalicchio, and G. Perrone, "Design and characterization of curvature sensors based on plastic optical fibers for structural monitoring," *2013 IEEE Int. Instrum. Meas. Technol. Conf.*, pp. 996–1000, 2013.
- [107] A. Vallan, A. Carullo, M. L. Casalicchio, and G. Perrone, "Static Characterization of Curvature Sensors Based on Plastic Optical Fibers," *IEEE Trans. Instrum. Meas.*, vol. 63, no. 5, pp. 1293–1300, 2014.
- [108] L. E. Dunne, P. Walsh, S. Hermann, B. Smyth, and B. Caulfield, "Wearable monitoring of seated spinal posture," *IEEE Trans. Biomed. Circuits Syst.*, vol. 2, no. 2, pp. 97–105, 2008.
- [109] J. M. Williams, I. Haq, and R. Y. Lee, "Dynamic measurement of lumbar curvature using fibre-optic sensors," *Med. Eng. Phys.*, vol. 32, no. 9, pp. 1043–1049, 2010.
- [110] M. Donno, E. Palange, F. Di Nicola, S. Member, G. Bucci, and F. Ciancetta, "A New Flexible Optical Fiber Goniometer for Dynamic Angular Measurements: Application to Human Joint Movement Monitoring," *Instrumentation*, vol. 57, no. 8, pp. 1614–1620, 2008.
- [111] L. Bilro, J. G. Oliveira, J. L. Pinto, and R. N. Nogueira, "A reliable low-cost wireless and wearable gait monitoring system based on a plastic optical fibre sensor," *Meas. Sci. Technol.*, vol. 22, no. 4, p. 45801, 2011.
- [112] A. Vallan, M. L. Casalicchio, M. Olivero, and G. Perrone, "Assessment of a Dual-Wavelength Compensation Technique for Displacement Sensors Using Plastic Optical Fibers," *Instrum. Meas. IEEE Trans.*, vol. 61, no. 5, pp. 1377–1383, 2012.
- [113] G. D. Peng, Z. Xiong, and P. L. Chu, "Photosensitivity and Gratings in Dye-Doped Polymer Optical Fibers," *Opt. Fiber Technol.*, vol. 5, no. 2, pp. 242–251, 1999.
- [114] Z. Xiong, G. D. Peng, B. Wu, and P. L. Chu, "Highly tunable Bragg gratings in single mode polymer optical fibers," *IEEE Photon. Technol. Lett.*, vol. vol, no. 3, p. 11pp352-354, 1999.

- [115] C. A. F. Marques, L. B. Bilro, N. J. Alberto, D. J. Webb, and R. N. Nogueira, "Narrow bandwidth Bragg gratings imprinted in polymer optical fibers for different spectral windows," *Opt. Commun.*, vol. 307, pp. 57–61, 2013.
- [116] W. Yuan, A. Stefani, and O. Bang, "Tunable polymer fiber Bragg grating (FBG) inscription: Fabrication of dual-FBG temperature compensated polymer optical fiber strain sensors," *IEEE Photonics Technol. Lett.*, vol. 24, no. 5, pp. 401–403, 2012.
- [117] I.-L. Bundalo, K. Nielsen, C. Markos, and O. Bang, "Bragg grating writing in PMMA microstructured polymer optical fibers in less than 7 minutes," *Opt. Express*, vol. 22, no. 5, p. 5270, 2014.
- [118] P. Stajanca, O. Cetinkaya, M. Schukar, P. Mergo, D. J. Webb, and K. Krebber, "Molecular alignment relaxation in polymer optical fibers for sensing applications," *Opt. Fiber Technol.*, vol. 28, pp. 11–17, 2016.
- [119] C. A. F. Marques, A. Pospori, G. Demirci, O. Çetinkaya, B. Gawdzik, P. Antunes, O. Bang, P. Mergo, P. André, and D. J. Webb, "Fast bragg grating inscription in PMMA polymer optical fibres: Impact of thermal pre-treatment of preforms," *Sensors (Switzerland)*, vol. 17, no. 4, pp. 1–8, 2017.
- [120] J. Yu, X. Tao, and H. Tam, "Trans-4-stilbenemethanol-doped photosensitive polymer fibers and gratings," *Opt. Lett.*, vol. 29, no. 2, p. 156, 2004.
- [121] X. Hu, C.-F. J. Pun, H.-Y. Tam, P. Mégret, and C. Caucheteur, "Highly reflective Bragg gratings in slightly etched step-index polymer optical fiber," *Opt. Express*, vol. 22, no. 15, p. 18807, 2014.
- [122] X. Hu, C.-F. J. Pun, H.-Y. Tam, P. Mégret, and C. Caucheteur, "Tilted Bragg gratings in step-index polymer optical fiber," *Opt. Lett.*, vol. 39, no. 24, p. 6835, Dec. 2014.
- [123] X. Hu, D. Kinet, P. Mégret, and C. Caucheteur, "Control over photo-inscription and thermal annealing to obtain high-quality Bragg gratings in doped PMMA optical fibers," *Opt. Lett.*, vol. 41, no. 13, p. 2930, 2016.
- [124] D. Sáez-Rodríguez, K. Nielsen, H. K. Rasmussen, O. Bang, and D. J. Webb, "Highly photosensitive polymethyl methacrylate microstructured polymer optical fiber with doped core," *Opt. Lett.*, vol. 38, no. 19, pp. 3769–3772, 2013.
- [125] L. Pereira, R. Min, X. Hu, C. Caucheteur, O. Bang, B. Ortega, C. Marques, P. Antunes, and J. L. Pinto, "Polymer optical fiber Bragg grating inscription with a single Nd:YAG laser pulse," *Opt. Express*, vol. 26, no. 14, p. 18096, 2018.
- [126] M. Koerdt, S. Kibben, J. Hesselbach, C. Brauner, A. S. Herrmann, F. Vollertsen, and L. Kroll, "Fabrication and Characterization of Bragg Gratings in a Graded-index Perfluorinated Polymer Optical Fiber," *Procedia Technol.*, vol. 15, pp. 138–146, 2014.
- [127] R. Min, B. Ortega, A. Leal-Junior, and C. Marques, "Fabrication and Characterization of Bragg Grating in CYTOP POF at 600-nm Wavelength," *IEEE Sensors Lett.*, vol. 2, no. 3, pp. 1–4, 2018.
- [128] R. Min, B. Ortega, X. Hu, C. Broadway, C. Caucheteur, C.-F. J. Pun, H.-Y. Tam, P. Antunes, and C. Marques, "Bragg Gratings Inscription in TS-Doped PMMA POF by Using 248-nm KrF Pulses," *IEEE Photonics Technol. Lett.*, vol. 30, no. 18, pp. 1609–1612, 2018.
- [129] R. R. Gattass and E. Mazur, "Femtosecond laser micromachining in transparent materials," *Nat. Photonics*, vol. 2, no. 4, pp. 219–225, Apr. 2008.
- [130] K. Sugioka and Y. Cheng, "Ultrafast lasers-reliable tools for advanced materials processing," *Light Sci. Appl.*, vol. 3, no. 390, pp. 1–12, 2014.
- [131] F. He, Y. Liao, J. Lin, J. Song, L. Qiao, Y. Cheng, F. He, and K. Sugioka, "Femtosecond laser fabrication of monolithically integrated microfluidic sensors in glass," *Sensors*, vol. 14, no. 10, pp. 19402–19440, 2014.
- [132] A. Cusano, A. Cutolo, and J. Albert, *Fiber Bragg Grating Sensors: Market Overview and New Perspectives*. Bentham Science Publishers: Potomac, 2009.
- [133] A. Theodosiou, M. Polis, A. Lacraz, K. Kalli, M. Komodromos, and A. Stassis, "Comparative study of multimode CYTOP graded index and single-mode silica fibre Bragg grating array for the mode shape capturing of a free-free metal beam," p. 988600, 2016.
- [134] M. G. Zubel, K. Sugden, D. Saez-Rodriguez, K. Nielsen, and O. Bang, "3D printed sensing patches with embedded polymer optical fibre Bragg gratings," in *Sixth European Workshop on Optical Fibre Sensors*, 2016, p. 99162E.
- [135] C. A. F. Marques, G.-D. Peng, and D. J. Webb, "Highly sensitive liquid level monitoring system utilizing polymer fiber Bragg gratings," *Opt. Express*, vol. 23, no. 5, pp. 6058–6072, 2015.
- [136] C. A. F. Marques, A. Pospori, D. Saez-Rodriguez, K. Nielsen, O. Bang, and D. J. Webb, "Aviation Fuel Gauging Sensor Utilizing Multiple Diaphragm Sensors Incorporating Polymer Optical Fiber Bragg Gratings," *IEEE Sens.*

- J., vol. 16, no. 15, pp. 6122–6129, 2016.
- [137] X. Qiao, Z. Shao, W. Bao, and Q. Rong, “Fiber Bragg Grating Sensors for the Oil Industry,” *Sensors*, vol. 17, no. 3, p. 429, 2017.
- [138] R. Ishikawa, H. Lee, A. Lacraz, A. Theodosiou, K. Kalli, Y. Mizuno, and K. Nakamura, “Pressure Dependence of Fiber Bragg Grating Inscribed in Perfluorinated Polymer Fiber,” *IEEE Photonics Technol. Lett.*, vol. 29, no. 24, pp. 2167–2170, Dec. 2017.
- [139] X. Chen, C. Zhang, D. J. Webb, G. D. Peng, and K. Kalli, “Bragg grating in a polymer optical fibre for strain, bend and temperature sensing,” *Meas. Sci. Technol.*, vol. 21, no. 9, 2010.
- [140] A. Leal-Junior, A. Frizera, M. J. Pontes, A. Fasano, G. Woyessa, O. Bang, and C. A. F. Marques, “Dynamic mechanical characterization with respect to temperature, humidity, frequency and strain in mPOFs made of different materials,” *Opt. Mater. Express*, vol. 8, no. 4, 2018.
- [141] W. Zhang and D. J. Webb, “Humidity responsivity of poly(methyl methacrylate)-based optical fiber Bragg grating sensors,” *Opt. Lett.*, vol. 39, no. 10, p. 3026, May 2014.
- [142] J. Bonafacino, H.-Y. Tam, T. S. Glen, X. Cheng, C.-F. J. Pun, J. Wang, P.-H. Lee, M.-L. V. Tse, and S. T. Boles, “Ultra-fast polymer optical fibre Bragg grating inscription for medical devices,” *Light Sci. Appl.*, vol. 7, no. 3, p. 17161, 2018.
- [143] C. Broadway, D. Gallego, A. Pospori, M. Zobel, D. J. Webb, K. Sugden, G. Carpintero, and H. Lamela, “A compact polymer optical fibre ultrasound detector,” *Proc. SPIE*, vol. 9708, no. March 2016, p. 970813, 2016.
- [144] T. A. Hamdalla and S. S. Nafee, “Bragg wavelength shift for irradiated polymer fiber Bragg grating,” *Opt. Laser Technol.*, vol. 74, pp. 167–172, 2015.
- [145] I. K. Lin, K. S. Ou, Y. M. Liao, Y. Liu, K. S. Chen, and X. Zhang, “Viscoelastic characterization and modeling of polymer transducers for biological applications,” *J. Microelectromechanical Syst.*, vol. 18, no. 5, pp. 1087–1099, 2009.
- [146] S. Ropers, M. Kardos, and T. A. Osswald, “A thermo-viscoelastic approach for the characterization and modeling of the bending behavior of thermoplastic composites,” *Compos. Part A Appl. Sci. Manuf.*, vol. 90, pp. 22–32, 2016.
- [147] T. C. Henry, C. E. Bakis, and E. C. Smith, “Viscoelastic characterization and self-heating behavior of laminated fiber composite driveshafts,” *Mater. Des.*, vol. 66, no. PA, pp. 346–355, 2015.
- [148] D. Celentano, D. Wimmer, L. Colabella, and A. P. Csilino, “Viscoelastic mechanical characterization of a short-fiber reinforced polyethylene tube: Experiments and modelling,” *Int. J. Press. Vessel. Pip.*, vol. 134, pp. 82–91, 2015.
- [149] G. Huang, B. Wang, and H. Lu, “Measurements of viscoelastic functions of polymers in the frequency-domain using nanoindentation,” *Mech. Time-Dependent Mater.*, vol. 8, no. 4, pp. 345–364, 2004.
- [150] A. Badawi, “Characterization of the optical and mechanical properties of CdSe QDs/PMMA nanocomposite films,” *J. Mater. Sci. Mater. Electron.*, vol. 26, no. 6, pp. 3450–3457, 2015.
- [151] K. Menard, *Dynamic Mechanical Analysis: A Practical Introduction*. Press, CRC, 1999.
- [152] “<https://www.iso.org/standard/56045.html>.” .
- [153] ASTM International, “ASTM D4065 - Standard Practice for Plastics : Dynamic Mechanical Properties : Determination and Report of Procedures,” *Annu. B. ASTM Stand.*, vol. i, pp. 1–7, 2012.
- [154] S. E. Zeltmann, B. R. Bharath Kumar, M. Doddamani, and N. Gupta, “Prediction of strain rate sensitivity of high density polyethylene using integral transform of dynamic mechanical analysis data,” *Polymer (Guildf)*, vol. 101, pp. 1–6, 2016.
- [155] C. Kirtley, *Clinical Gait Analysis: Theory and Practice*. Philadelphia: Elsevier, 2006.
- [156] A. Stefani, S. Andresen, W. Yuan, and O. Bang, “Dynamic characterization of polymer optical fibers,” *IEEE Sens. J.*, vol. 12, no. 10, pp. 3047–3053, 2012.
- [157] A. Leal-Junior, A. Frizera, M. J. Pontes, A. Fasano, G. Woyessa, O. Bang, and C. A. F. Marques, “Dynamic mechanical characterization with respect to temperature, humidity, frequency and strain in mPOFs made of different materials,” *Opt. Mater. Express*, vol. 8, no. 4, p. 804, Apr. 2018.
- [158] D. Sartiano and S. Sales, “Low cost plastic optical fiber pressure sensor embedded in mattress for vital signal monitoring,” *Sensors (Switzerland)*, vol. 17, no. 12, 2017.
- [159] M. A. Zawawi, S. O’Keeffe, and E. Lewis, “Plastic optical fibre sensor for spine bending monitoring with power

- fluctuation compensation.,” *Sensors (Basel)*, vol. 13, no. 11, pp. 14466–14483, 2013.
- [160] W. Qiu, X. Cheng, Y. Luo, Q. Zhang, and B. Zhu, “Simultaneous measurement of temperature and strain using a single bragg grating in a few-mode polymer optical fiber,” *J. Light. Technol.*, vol. 31, no. 14, pp. 2419–2425, 2013.
- [161] R. Liu, Z. Fu, Y. Zhao, Q. Cao, and S. Wang, “Operation principle of a bend enhanced curvature optical fiber sensor,” *IEEE Int. Conf. Intell. Robot. Syst.*, pp. 1966–1971, 2006.
- [162] J. Zubia, J. Arrue, and a. Mendioroz, “Theoretical Analysis of the Torsion-Induced Optical Effect in a Plastic Optical Fiber,” *Opt. Fiber Technol.*, vol. 3, no. 2, pp. 162–167, 1997.
- [163] P. Piriyaarasarth and M. E. Morris, “Psychometric properties of measurement tools for quantifying knee joint position and movement: A systematic review,” *Knee*, vol. 14, no. 1, pp. 2–8, 2007.
- [164] A. G. Leal-Junior, A. Frizera, and M. J. Pontes, “Dynamic Compensation Technique for POF Curvature Sensors,” *J. Light. Technol.*, vol. 36, no. 4, pp. 1112–1117, 2018.
- [165] D. Z. Stupar, J. S. Bajic, L. M. Manojlovic, M. P. Slankamenac, A. V. Joza, and M. B. Zivanov, “Wearable low-cost system for human joint movements monitoring based on fiber-optic curvature sensor,” *IEEE Sens. J.*, vol. 12, no. 12, pp. 3424–3431, 2012.
- [166] A. G. Leal-Junior, A. Frizera, and M. J. Pontes, “Dynamic Compensation Technique for POF Curvature Sensors,” *J. Light. Technol.*, vol. 36, no. 4, pp. 1112–1117, Feb. 2018.
- [167] W. Zhang, D. J. Webb, and G. D. Peng, “Investigation into time response of polymer fiber bragg grating based humidity sensors,” *J. Light. Technol.*, vol. 30, no. 8, pp. 1090–1096, 2012.
- [168] C. A. R. Diaz, A. G. Leal-Junior, P. S. B. Andre, P. F. da C. Antunes, M. J. Pontes, A. Frizera-Neto, and M. R. N. Ribeiro, “Liquid Level Measurement Based on FBG-Embedded Diaphragms With Temperature Compensation,” *IEEE Sens. J.*, vol. 18, no. 1, pp. 193–200, Jan. 2018.
- [169] C. Li, T. Ning, C. Zhang, J. Li, X. Wen, L. Pei, X. Gao, and H. Lin, “Liquid level measurement based on a no-core fiber with temperature compensation using a fiber Bragg grating,” *Sensors Actuators, A Phys.*, vol. 245, pp. 49–53, 2016.
- [170] A. Leal-Junior, A. Frizera, C. Marques, and M. J. Pontes, “Polymer-optical-fiber-based sensor system for simultaneous measurement of angle and temperature,” *Appl. Opt.*, vol. 57, no. 7, 2018.
- [171] W. Zhang and D. J. Webb, “PMMA Based Optical Fiber Bragg Grating for Measuring Moisture in Transformer Oil,” *IEEE Photonics Technol. Lett.*, vol. 28, no. 21, pp. 2427–2430, Nov. 2016.
- [172] A. Leal-Junior, A. Frizera, C. Marques, and M. J. Pontes, “Mechanical properties characterization of polymethyl methacrylate polymer optical fibers after thermal and chemical treatments,” *Opt. Fiber Technol.*, vol. 43, no. March, pp. 106–111, 2018.
- [173] Z. Ding, C. Wang, K. Liu, J. Jiang, D. Yang, G. Pan, Z. Pu, and T. Liu, “Distributed Optical Fiber Sensors Based on Optical Frequency Domain Reflectometry: A review,” *Sensors*, vol. 18, no. 4, p. 1072, 2018.
- [174] Y. Zhang, Y. Hou, Y. Zhang, Y. Hu, L. Zhang, X. Gao, H. Zhang, and W. Liu, “A cost-effective quasi-distributed liquid leakage sensor based on the polymer optical fiber and flexible lamp belt with LEDs,” *Opt. Express*, vol. 26, no. 8, p. 10152, Apr. 2018.
- [175] Y. Fu, H. Di, and R. Liu, “Light intensity modulation fiber-optic sensor for curvature measurement,” *Opt. Laser Technol.*, vol. 42, no. 4, pp. 594–599, 2010.
- [176] A. G. Leal-Junior, A. Frizera, and M. J. Pontes, “Analytical model for a polymer optical fiber under dynamic bending,” *Opt. Laser Technol.*, vol. 93, pp. 92–98, 2017.
- [177] A. Pospori, C. A. F. Marques, G. Sagias, H. Lamela-Rivera, and D. J. Webb, “Novel thermal annealing methodology for permanent tuning polymer optical fiber Bragg gratings to longer wavelengths,” *Opt. Express*, vol. 26, no. 2, p. 1411, 2018.
- [178] W. Yuan, A. Stefani, M. Bache, T. Jacobsen, B. Rose, N. Herholdt-Rasmussen, F. K. Nielsen, S. Andresen, O. B. Sørensen, K. S. Hansen, and O. Bang, “Improved thermal and strain performance of annealed polymer optical fiber Bragg gratings,” *Opt. Commun.*, vol. 284, no. 1, pp. 176–182, 2011.
- [179] A. Pospori, C. A. F. Marques, D. Sáez-Rodríguez, K. Nielsen, O. Bang, and D. J. Webb, “Thermal and chemical treatment of polymer optical fiber Bragg grating sensors for enhanced mechanical sensitivity,” *Opt. Fiber Technol.*, vol. 36, pp. 68–74, 2017.
- [180] G. Woyessa, K. Nielsen, A. Stefani, C. Markos, and O. Bang, “Temperature insensitive hysteresis free highly sensitive polymer optical fiber Bragg grating humidity sensor,” *Opt. Express*, vol. 24, no. 2, pp. 1206–13, 2016.

- [181] A. Leal-Junior, A. Frizera, M. J. Pontes, P. Antunes, N. Alberto, M. F. Domingues, H. Lee, R. Ishikawa, Y. Mizuno, K. Nakamura, P. André, and C. Marques, “Dynamic mechanical analysis on fused polymer optical fibers: towards sensor applications,” *Opt. Lett.*, vol. 43, no. 8, p. 1754, Apr. 2018.
- [182] A. G. Leal-Junior, A. Frizera, C. Marques, and M. J. Pontes, “Viscoelastic features based compensation technique for polymer optical fiber curvature sensors,” *Opt. Laser Technol.*, vol. 105, pp. 35–40, 2018.
- [183] L. Y. Shao, J. Canning, T. Wang, K. Cook, and H. Y. Tam, “Viscosity of silica optical fibres characterized using regenerated gratings,” *Acta Mater.*, vol. 61, no. 16, pp. 6071–6081, 2013.
- [184] I.-L. Bundalo, K. Nielsen, G. Woyessa, and O. Bang, “Long-term strain response of polymer optical fiber FBG sensors,” *Opt. Mater. Express*, vol. 7, no. 3, pp. 401–403, 2017.
- [185] AGC-Chemicals, “Amorphous Fluoropolymer CYTOP,” 2015. [Online]. Available: <https://www.agcchem.com/documentation/technical-data/cytop/513-cytop-brochure/file>. [Accessed: 06-Jun-2018].
- [186] X. Hu, D. Saez-Rodriguez, C. Marques, O. Bang, D. J. Webb, P. Mégret, and C. Caucheteur, “Polarization effects in polymer FBGs: study and use for transverse force sensing,” *Opt. Express*, vol. 23, no. 4, p. 4581, 2015.
- [187] M. F. Ashby, *Materials Selection in Mechanical Design*. Cambridge: Elsevier, 2005.
- [188] A. Pospori and D. J. Webb, “Stress Sensitivity Analysis of Optical Fiber Bragg Grating-Based Fabry–Pérot Interferometric Sensors,” *J. Light. Technol.*, vol. 35, no. 13, pp. 2654–2659, Jul. 2017.
- [189] A. G. Leal-Junior, A. Frizera-Neto, M. J. Pontes, and T. R. Botelho, “Hysteresis compensation technique applied to polymer optical fiber curvature sensor for lower limb exoskeletons,” *Meas. Sci. Technol.*, vol. 28, no. 12, p. 125103, Dec. 2017.
- [190] A. Leal-Junior, L. Vargas-Valencia, W. M. dos Santos, F. Schneider, A. A. G. Siqueira, M. J. Pontes, and A. Frizera, “POF-IMU sensor system: A fusion between inertial measurement units and POF sensors for low-cost and highly reliable systems,” *Opt. Fiber Technol.*, 2018.
- [191] A. G. Leal-Junior, A. Frizera, C. Marques, M. R. A. Sanchez, W. M. dos Santos, A. A. G. Siqueira, M. V. Segatto, and M. J. Pontes, “Polymer Optical Fiber for Angle and Torque Measurements of a Series Elastic Actuator’s Spring,” *J. Light. Technol.*, vol. 36, no. 9, pp. 1698–1705, May 2018.
- [192] C. Díaz, C. Leitão, C. Marques, M. Domingues, N. Alberto, M. Pontes, A. Frizera, M. Ribeiro, P. André, and P. Antunes, “Low-Cost Interrogation Technique for Dynamic Measurements with FBG-Based Devices,” *Sensors*, vol. 17, no. 10, p. 2414, 2017.
- [193] Y. Marin, T. Nannipieri, C. J. Oton, and F. Di Pasquale, “Fiber Bragg grating sensor interrogators on chip: challenges and opportunities,” in *25th International Conference on Optical Fiber Sensors, OFS 2017*, 2017, p. 103230D.
- [194] Redondo Optics Inc, “Fiber Bragg Gratings Transceivers,” *Fiber Bragg Gratings Transceivers*, 2018. [Online]. Available: [http://www.redondooptics.com/FBGT\\_060209.pdf](http://www.redondooptics.com/FBGT_060209.pdf). [Accessed: 30-Oct-2018].
- [195] C. A. Cifuentes and A. Frizera, *Human-Robot Interaction Strategies for Walker-Assisted Locomotion*, vol. 115, no. September. Cham: Springer International Publishing, 2016.
- [196] A. G. Leal-Junior, A. Theodosiou, C. Marques, M. J. Pontes, K. Kalli, and A. Frizera, “Thermal Treatments and Compensation Techniques for the Improved Response of FBG Sensors in POFs,” *J. Light. Technol.*, vol. 36, no. 17, pp. 3611–3617, Sep. 2018.
- [197] A. G. Leal-Junior, A. Theodosiou, C. Marques, M. J. Pontes, K. Kalli, and A. Frizera, “Compensation Method for Temperature Cross-Sensitivity in Transverse Force Applications With FBG Sensors in POFs,” *J. Light. Technol.*, vol. 36, no. 17, pp. 3660–3665, Sep. 2018.
- [198] B. Kehoe, S. Patil, P. Abbeel, and K. Goldberg, “A Survey of Research on Cloud Robotics and Automation,” *IEEE Trans. Autom. Sci. Eng.*, vol. 12, no. 2, pp. 398–409, Apr. 2015.
- [199] D. C. Berry and S. R. Seitz, “Educating the Educator: Use of Pulse Oximetry in Athletic Training,” *Athl. Train. Educ.*, vol. 7, no. 2, pp. 74–80, 2012.
- [200] H. Lee, H. Ko, and J. Lee, “Reflectance pulse oximetry: Practical issues and limitations,” *ICT Express*, vol. 2, no. 4, pp. 195–198, 2016.
- [201] Z. J. V Cohen, S. Haxha, and A. Aggoun, “Pulse oximetry optical sensor using oxygen-bound haemoglobin,” *Opt. Express*, vol. 24, no. 9, p. 10115, 2016.
- [202] M. Jyothish Kumar and V. Arun Kumar, “Reflectance pulse oximetry using single light source,” *Procedia Eng.*, vol. 38, pp. 2484–2490, 2012.

- [203] M. Rothmaier, B. Selm, S. Spichtig, D. Haensse, and M. Wolf, "Photonic textiles for pulse oximetry," *Opt. Express*, vol. 16, no. 17, p. 12973, 2008.
- [204] D. T. Delpy, M. Cope, and P. van der Zee, "Estimation of optical path length through tissue from direct time of flight measurement," *Physic Med. Biol.*, vol. 33, no. 12, pp. 1433–1442, 1988.
- [205] R. J. Abboud, "(i) Relevant foot biomechanics," pp. 165–179, 2002.
- [206] S. J. M. Bamberg, A. Y. Benbasat, D. M. Scarborough, D. E. Krebs, and J. A. Paradiso, "Gait analysis using a shoe-integrated wireless sensor system," *IEEE Trans. Inf. Technol. Biomed.*, vol. 12, no. 4, pp. 413–423, 2008.
- [207] Y. Liu, K. Lu, S. Yan, M. Sun, D. K. Lester, and K. Zhang, "Gait phase varies over velocities," *Gait Posture*, vol. 39, no. 2, pp. 756–760, 2014.
- [208] A. Karatsidis, G. Bellusci, H. M. Schepers, M. de Zee, M. S. Andersen, and P. H. Veltink, "Estimation of ground reaction forces and moments during gait using only inertial motion capture," *Sensors (Switzerland)*, vol. 17, no. 1, pp. 1–22, 2017.
- [209] S. H. Huang, P. Liu, A. Mokasdar, and L. Hou, "Additive manufacturing and its societal impact: A literature review," *Int. J. Adv. Manuf. Technol.*, vol. 67, no. 5–8, pp. 1191–1203, 2013.
- [210] R. Eguchi, A. Yorozu, T. Fukumoto, and M. Takahashi, "Ground reaction force estimation using insole plantar pressure measurement system from single-leg standing," *IEEE Int. Conf. Multisens. Fusion Integr. Intell. Syst.*, pp. 109–113, 2017.
- [211] W. H. Organization, "Who Can Benefit From Assistive Technology?," *Assistive technology*, 2015. [Online]. Available: <http://www.who.int/news-room/fact-sheets/detail/assistive-technology>. [Accessed: 29-Oct-2018].
- [212] A. G. Leal Junior, A. Theodosiou, C. Marques, M. J. Pontes, K. Kalli, and A. Frizera, "Compensation Method for Temperature Cross-sensitivity in Transverse Force Applications with FBG Sensors in POFs," *J. Light. Technol.*, vol. 8724, no. c, pp. 1–1, 2018.
- [213] M. K. Duong, H. Cheng, H. T. Tran, and Q. Jing, "Minimizing Human-Exoskeleton Interaction Force Using Compensation for Dynamic Uncertainty Error with Adaptive RBF Network," *J. Intell. Robot. Syst. Theory Appl.*, vol. 82, no. 3–4, pp. 413–433, 2016.
- [214] J. Z. Sasiadek and P. Hartana, "Sensor data fusion using Kalman filter," *Inf. Fusion, 2000. FUSION 2000. Proc. Third Int. Conf.*, vol. 2, p. WED5/19-WED5/25 vol.2, 2000.
- [215] B. Feng, M. Fu, H. Ma, Y. Xia, and B. Wang, "Kalman Filter With Recursive Covariance Estimation — Sequentially Estimating Process Noise Covariance," vol. 61, no. 11, pp. 6253–6263, 2014.
- [216] F. Auger, M. Hilaret, J. M. Guerrero, E. Monmasson, T. Orłowska-Kowalska, and S. Katsura, "Industrial applications of the kalman filter: A review," *IEEE Trans. Ind. Electron.*, vol. 60, no. 12, pp. 5458–5471, 2013.
- [217] A. Pospori, C. A. F. Marques, O. Bang, and D. J. Webb, "Polymer optical fiber Bragg grating inscription with a single UV laser pulse," *Opt. Express*, vol. 25, no. 8, pp. 9028–9038, 2017.
- [218] M. F. Domingues, C. Tavares, C. Leitão, A. Frizera-Neto, N. Alberto, C. Marques, A. Radwan, J. Rodriguez, O. Postolache, E. Rocon, P. André, and P. Antunes, "Insole optical fiber Bragg grating sensors network for dynamic vertical force monitoring," *J. Biomed. Opt.*, vol. 22, no. 9, p. 91507, 2017.
- [219] M. Kovacević, A. Djordjevich, and D. Nikezić, "An Analytical Approach and Optimization of Curvature Gauge," *J. Phys. Conf. Ser.*, vol. 48, no. 1, pp. 850–858, 2006.
- [220] L. Bilro, N. J. Alberto, L. M. Sá, J. De Lemos Pinto, and R. Nogueira, "Analytical analysis of side-polished plastic optical fiber as curvature and refractive index sensor," *J. Light. Technol.*, vol. 29, no. 6, pp. 864–870, 2011.
- [221] J. Dugas, I. Pierrejean, J. Farenc, and J. P. Peichot, "Birefringence and internal stress in polystyrene optical fibers," *Appl. Opt.*, vol. 33, no. 16, pp. 3545–8, 1994.
- [222] M. K. Szczurowski, T. Martynkien, S. B. Gabriela, W. Urbanczyk, L. Khan, and D. J. Webb, "Measurements of stress-optic coefficient in polymer optical fibers," *Opt. Lett.*, vol. 35, no. 12, pp. 2013–2015, 2010.
- [223] E. Riande, R. Diaz-Calleja, M. Prolongo, R. Masegosa, and C. Salom, *Polymer Viscoelasticity: Stress and Strain in Practice*. New York: Marcel Dekker, 2000.
- [224] K. Kalantar-Zadeh, *Sensors: An introductory course*. Springer US, 2013.
- [225] A. Konak, D. W. Coit, and A. E. Smith, "Multi-objective optimization using genetic algorithms: A tutorial," vol. 91, pp. 992–1007, 2006.
- [226] A. Fasano, G. Woyessa, J. Janting, H. K. Rasmussen, and O. Bang, "Solution-Mediated Annealing of Polymer Optical Fiber Bragg Gratings at Room Temperature," *IEEE Photonics Technol. Lett.*, vol. 29, no. 8, pp. 687–690,

2017.

- [227] R. Suresh, S. Bhalla, J. Hao, and C. Singh, "Development of a high resolution plantar pressure monitoring pad based on fiber Bragg grating ( FBG ) sensors," vol. 23, pp. 785–794, 2015.
- [228] T. Liang, J. Lin, and L. Guo, "Plantar Pressure Detection with Fiber Bragg Gratings Sensing System," *Sensors*, vol. 16, no. 10, p. 1766, Oct. 2016.
- [229] A. V. Wiik, A. Aqil, M. Brevadt, G. Jones, and J. Cobb, "Abnormal ground reaction forces lead to a general decline in gait speed in knee osteoarthritis patients," *World J. Orthop.*, vol. 8, no. 4, p. 322, 2017.
- [230] N. Farahpour, A. A. Jafarnezhad, M. Damavandi, A. Bakhtiari, and P. Allard, "Gait ground reaction force characteristics of low back pain patients with pronated foot and able-bodied individuals with and without foot pronation," *J. Biomech.*, vol. 49, no. 9, pp. 1705–1710, 2016.
- [231] J. L. McCrory, S. C. White, and R. M. Lifeso, "Vertical ground reaction forces: objective measures of gait following hip arthroplasty," *Gait Posture*, vol. 14, no. 2, pp. 104–109, 2001.
- [232] S. Ko, S. Steinhilf, and L. Ferrucci, "Characteristic Gait Patterns in Older Adults with Obesity - Results from the Baltimore Longitudinal Study of Aging," *J. Biomech.*, vol. 43, no. 6, pp. 1104–1110, 2011.
- [233] V. Cimolin, L. Vismara, M. Galli, F. Zaina, S. Negrini, and P. Capodaglio, "Effects of obesity and chronic low back pain on gait," *J. Neuroeng. Rehabil.*, vol. 8, no. 1, p. 55, 2011.
- [234] M. Cianchetti, C. Laschi, A. Menciassi, and P. Dario, "Biomedical applications of soft robotics," *Nat. Rev. Mater.*, vol. 3, no. 6, pp. 143–153, 2018.
- [235] D. Graupe and K. H. Kohn, "Transcutaneous functional neuromuscular stimulation of certain traumatic complete thoracic paraplegics for independent short-distance ambulation," *Neurol. Res.*, vol. 19, no. 3, pp. 323–333, 1997.
- [236] A. Leal-Junior, A. Frizera-Neto, C. Marques, and M. Pontes, "Measurement of Temperature and Relative Humidity with Polymer Optical Fiber Sensors Based on the Induced Stress-Optic Effect," *Sensors*, vol. 18, no. 3, p. 916, Mar. 2018.